OUKA
The University of Osaka
Institutional Knowledge Archive

Title	半導体の共鳴ブリルアン散乱とピエゾ複屈折に関する研究
Author(s)	伊藤, 寧夫
Citation	大阪大学, 1982, 博士論文
Version Type	VoR
URL	https://hdl.handle.net/11094/189
rights	
Note	

The University of Osaka Institutional Knowledge Archive : OUKA

https://ir.library.osaka-u.ac.jp/

The University of Osaka

Resonant Brillouin Scattering and Piezobirefringence in Semiconductors

Yasuo Itoh

Resonant Brillouin Scattering and Piezobirefringence in Semiconductors

(半導体における共鳴ブリルアン散乱とピエゾ複屈折に関する研究)

Yasuo Itoh

伊藤寧夫

ACKNOWLEDGMENTS

The auther would like to express his appreciation to Professor Y. Inuishi for helpful advice, stimulating throughout the course of his reserch and critical reading. He would also like to express his appreciation to Professor C. Hamaguchi for helpful advice, criticism and continual encourgement throughout the course of his work. He also thanks to Professors H. Kinoshita, C. Yamanaka, K. Fujii, U. Suzuki, M. Yokoyama, S. Nakai, T. Yamanaka and A. Mitsuishi for their critical readings of this thesis.

Special thanks are due to Professor R. Bray of Purdue University, U.S.A., for valuable discussions throughout the course of his work.

He appreciates Dr. K. Ando and Dr. S. Adachi, Musashino Electrical Communication Laboratory, NTT, Mr. K. Yamabe, Reserch & Developement Center, Toshiba Corporation, and Mr. Fujii, Nippon Electric Co., for his collaboration on the present work. He also wishes to thank Mr. W. C. Chang of Purdue University, for helpful advice and useful discussion on the work reported in Chapter 6.

He wishes to thank Professor J. Shirafuji and Professor K. Yoshino for helpful advice and useful discussions. He also wishes to thank Dr. M. Inoue, Dr. T. Taguchi and Dr. K. Kaneto and many memberes of the Semiconductor and Insulator Reserch Groups in Electrical Engineering, and the Semiconductor Reserch Group in Department of Electronics, for helpful and enjoyable discussions.

He is grateful to Dr. S. Fujita, Kyoto University, for his kind supply of cubic ZnS and Professor S. Nakashima, Osaka University, for his kind supply of HgI_2 crystals used in the present study. He would like to thank Dr. N. Kuroda, Tohoku University, and Dr. K. Uchinokura, Tsukuba

University, for his help in understanding the finer points of the resonant light scattering theory. He also wish to Mr. A. Terashima for showing him many powerful techniques in writing computer programs and graphics.

He grately acknowledges the financial support he has received from the Japan Scholarship Foundation.

TABLE OF CONTENTS

LIST OF TABLES

LIST OF FIGURES

Figure Page

VITA

August 1, 1953 - Born - Osaka City.

1977 - B. Eng., Osaka University, Department of Electronics.

1979 - M. Eng., Osaka University, Department of Electronics.

1982 - Ph. D., Osaka University, Electrical Enigineering.

PUBLICATIONS

"Resonant Brillouin Scattering Phenomena in Some II-VI Compounds," Solid State Electronics *21* (1978) 1585.

"Resonant Brillouin Scattering by LA Phonons in CdS," J. Phys. Soc. Jpn. *46* (1979) 542.

"Effect of Lifetime Broadening on Resonant Brillouin Scattering in ZnTe and ZnSe," Jpn. J. Appl. Phys. *18* (1979) 575.

"Analysis of Resonant Brillouin Scattering and Piezobirefringence in GaAs," Phys. Stat. Sol. (b) *93* (1979) 381.

"Quasi-Static Analysis of Resonant Brillouin Scattering in ZnSe, ZnTe and CdS," J. Phys. Soc. Jpn. *46* (1979) 1546.

"Brillouin Scattering by Injected Acoustic Domains in ZnS," *Proceedings of Phonon Scattering in Condensed Matter*, edited by Humphery J. Maris (Plenum Publishing Corporation, 1980), p. 433.

"Resonant Brillouin Scattering and Piezobirefringence in ZnS," J. Phys. Soc. Jpn. *48* (1980) 1972.

"Acoustic Domain Injection Method and Resonant Brillouin Scattering," Jpn. J. Appl. Phys. *20* (1981) Supplement 20-3, p. 259.

"Resonant Brillouin Scattering in Opaque Region of CdS," *Proceedings of the International Conference on Phonon Physics*, J. de Physique (in press).

"Resonant Brillouin Scattering by Elasto-Optic Mechanism in Opaque Region of CdS," (to be published).

"Resonant Brillouin Scattering by Injected Acoustic Domains in HgI_2," (to be published).

ABSTRACT

Yasuo Itoh, Doctor of Engineering, Osaka University, June 1982.

Resonant Brillouin Scattering and Piezobirefringence in Semiconductors.

The present work is a study of the resonant Brillouin scattering and piezobirefringence in several semiconductors in the region near the fundamental absorption edge. The thesis will be essentially devided into three subjects. One is concerned with the theoretical construction of the Brillouin scattering theory and piezobirefringence theory. The other is devoted to the experimental results of the Brillouin scattering by using the acoustoelectrically amplified phonon domains in several semiconductors such as CdS, ZnS, and HgI_2. The third is devoted to the measurement and analysis of the resonant Brillouin scattering in the range of photon energy above the fundamental absorption edge of CdS.

In Chapter 1, historical background of the resonant light scattering is reviewed and significance of the present work is explained.

In Chapter 2, classical and quantum mechanical theory of the Brillouin scattering are presented. Brillouin scattering cross sections near the M_0 critical point not only in the energy range below but also above the band gap are interpreted by the quantum mechanical theory of light scattering precess. Selection rules of the momentum matrix element and deformation potential scattering are discussed.

Chapter 3 deals with the basic concept of piezobirefringence and photo-elastic constants are derived theoretically by the piezobirefringence theory.

Chapter 4 deals with the experimental procedure and detailed explanations of the sample preparation used in the present work are presented. The experimental technique of the acoustic domain injection method and the some results are also presented.

In Chapter 5, the experimental results and discussion on the resonant

Brillouin scattering in CdS, GaAs, ZnS, HgI_2 are presented. In the observed spectra, one can find a sharp resonant enhancement and cancellation in the dispersion curves of the resonant Brillouin scattering cross sections by TA-mode phonons in CdS, GaAs and ZnS. Resonant features of the scattering efficiency by pure LA phonon is found to be quite different form that of TA-mode, where only a sharp resonant increase is observed. The resonant Brillouin scattering in cubic and polytype ZnS was investigated in a wide range of the photon energy and we found that the scattering cross sections exhibit ω^4 dependence as expected from the classical light scattering theory. Resonant Brillouin scattering experiment in layered compound HgI_2 was made by employing the acoustic domain injection method. The experimental data have a resonant cancellation, while no resonant enhancement has been found in the measured photon energy region.

Chapter 6 deals with the experimental results and discussions of the Brillouin scattering above the band gaps of CdS. A dispersion curves of the resonant Brillouin scattering cross seciton above the fundamental absorption edge was measured for the first time by using acoustoelectrically amplified phonon domains. It has been difficult to obtain the dispersion of the Brillouin scattering cross sections in opaque region when one adopts a transmission type of experiment. To overcome this restriction reflection type of experiment with Ar ion laser was used because the wavelength of the Ar ion laser locate in the region of the three energy bands in CdS. The experimental results have shown a resonant enhancement in the region and are analyzed on the basis of light scatteing theory and piezobirefringence theory extending the photon energy above the band gap. A good agreement between the experimental data and theory was found when we take into account both the real and imaginary part in Brillouin tensor and in piezobirefringence coefficient.

In Chapter 7, the conclusions obtained in the presnt study are summarized.

CHAPTER 1

INTRODUCTION

In the past dozen or so years, inelastic scattering of light has become one of the most powerful means of investigating elementary excitations in solids. Light scattering has been used in numerous ways to study both acoustic and optical phonon, electronic and magnetic excitations, and exciton polariton.[1,2] Traditionally, Ramman scattering refers to inelastic light scattering from optical phonons and Brillouin scattering, to scattering from acoustic phonons. However, in the modern context the distinction is made on the basis of the magnitude of the accompanying frequency shift of the scattered light and the experimental technique used in measureing the frequency shift in the scattering process. In Raman scattering experiments, one usually measures a frequency shift 1 cm^{-1} (1 meV = 8 cm^{-1}) or greater by using a grating spectrometer, while in Brillouin scattering the typical range of frequency shift is $10^{-3} cm^{-1}$(30 MHz) - 1 cm^{-1}(30 GHz) and standerd method of spectrum anlysis is a Fabry-Perot interferometer. Quasi-elastic light scattering with a frequency shift less than a few tens of MHz is referred to as Rayleigh scattering, and here a photon beating technique is employed.

Present dissertation is concernned with a study of the resonant Brillouin scattering and piezobirefringence in semiconductors. Before we go into a discussion of the specific advance in the field of the Brillouin scattering by acoustoelectrically amplified phonon domains, we shall review some recent advances in the study of light scattering in solids. The Brillouin scattering was first predicted by Brillouin in 1922.[3] Smekal[4] developed in 1923 the theory of light scattering by a system with two quantized energy levels: this theory contained the essential characteristics of the phenomena discovered by

Raman[5] and independently by Lansberg and Mandelstam[6] in 1928. The Brillouin doublets were first obseved experimentally by Gross[7] in 1930 and later cofirmed by Mayer and Raman,[8] Debye and Sears,[9] and by Lucas and Biquard[10] in 1932. Later many studies, both theoretical and experimental, were devoted to those phenomena, and the characteristics of the vibrational spectra of crystals, fluctuation phenomena, and other physical properties of solids and liquids were investigated. In the 1940's emphasis shifted to systematic investigation of single crystals in order to obtain information for the semi-empirical treatment of their crystal dynamics. Because of the small scattering cross sections, however, experments were difficult and remained in the hands of relatively few groups. The possibilities of the light scattering studies have drastically expanded in 1960's because of the developement of laser. Its monochrimacity, coherence, collimation and power quickly made the old mercury arcs obsolete as sources for light scattering spectroscopy. Ever since the discovery of the laser one could easily obtained the detailed experimental data enough to be compared with detailed theory. In the early days of Raman scattering experiments, work was only possible with materials transparent to the scattering radiation. The scattering volume, limitted by absorption length, was too small in opaque samples to make observation possible. The first measurement of the Raman scattering in the opaque region was observed by Russell[11] for Si with a He-Ne laser in 1965. The measurements were performed in the back-scattering configuration which has later become standerd for studies of resonance effects. Later, Raman scattering in the opaque region was made by Parker et al.[12] in Si and Ge with the 488.0 nm line of Ar ion laser in 1967. On the other hand. the first measurement of the Brillouin scattering in the opaque region was made by Sandercock[13] in Si by thanks to the use of multi-pass Fabry-Perot interferometer. In 1960's these two

spectroscopies, Raman and Brillouin scattering, have developed into powerful technique for studying phonons and other kinds of elementaly excitations in solids.[2] However, their potential for studying excitations has expanded recently. The ability of these scattering technique to probe electronic transition lies in the dependence of scattering cross section on the exciting photon energy. Such excitation spectroscopies are known as resonant Brillouin scattering (RBS) and resonant Raman scattering (RRS).

The first experiment of the resonant Raman scattering has been performed by Leite and Parto[14] in 1966 for CdS by using discrete lines of Ar ion laser, which cover the range between 2.38 and 2.73 eV. Subsequently, in 1970, Ralston et al.[15] have comfirmed the resonance enhancement in CdS and also established the existance of an antiresonance of the Raman-scattering cross section for TO phonons immediately below the fundamental absorption edge. Such a structure is now understood as a cancellation (anti-resonance) between the contribution of the band edge and of higher transition: these contribution must have opposite signs.

Measurement taken with a few discrete lines, however, may sometimes miss sharp structure between discrete point. The slight mismatch in frequency between the band gap and the nearest laser can be minimized by varying the temperature or pressure of the sample. By this method, Pinczuk and Burstein[16] were able to detect a resonance near the E_1 gap of InSb. This resonance was studied in greater detail by Leite and Scott[17] for InAs using lines of Ar ion laser. However such tuning techniques have limitations and pitfalls. A breakthrough occurred in the field of resonance scattering with the advent of the tunable dye lasers.[18] The dye laser with its ability to tune over a wide range of wavelengths naturally became the best source of radiation for resonant light scattering studies. The tuning range of existing dyes capable of lasing in continuous (CW) mode is approximately 410 nm to 965 nm.[19] This

tuning range is sufficient for studying the resonant scattering in a large number of semiconductors such as: III-V compound : GaAs, GaP and AlAs; II-VI compound: ZnTe, ZnSe, ZnO, CdTe, and CdS: layered semiconductors: GaS,GaSe, and HgI_2. With the help of ion laser and dye laser, Cardona and coworkers have extensively and systematically investigate the resonant Raman scattering in Ge, Si, diamond, III-V compound and II-VI compound.[20-25)]

The first measurement of the resonant Brillouin scattering has been performed by Tell et al.[26)] in 1965 using transduser driven LA phonons along the a-axis of CdS and ZnO. The incident light was tuned over several hundred nm to the transparency limit of the crystals. Over this range they observed almost decade dispersion in the P_{31}, P_{21} and P_{11} tensor confugurations. The second experiment of the resonant Brillouin scattering has been performed by Pine[27)] in 1972 for CdS by employing the high contrast Fabry-Perot interferometer. The resonant condition has been achieved by thermally tuning the fundamental absorption edge of this sample through the incident radiation at 514.5 nm Ar laser light between 100 K and 300 K. The data show a strong resonant enhancement in the vicinity of the fundamental absorption edge. The new experimental technique of resonant Brillouin scattering by making use of the strong amplified acoustic domains through the acoustoelectric effect in piezoelectric semiconductors was proposed by Garrod and Bray[28,29)] in 1972. Scattering from acoustoelectrically or piezoelectrically driven ultrasonic waves is easily observed with lasers or conventional light sources and angular dependence establishes the sound frequency. Thermal phonon Brillouin scattering is much weaker, so laser sources are generally used with interferometric spectral analysis. They have used a particularly simple and versatile apparatus of this kind because the acoustoelectrically amplified phonon domains provide strong Brillouin scattering signal with high S/N ratio and permit the use of conventional light source dispersed with a single

monochrometer. They demonstrated a sharp dip in the scattering dispersion about 30 meV below the gap and resonant enhancement near the fundamental absorption edge of GaAs. This measurement is the starting point of the investigation in resonant Brillouin scattering by making use of the high density acoustic domains. Subsequently, similar resonace behaviours have been observed in CdS from acoustoelectrical domains by Hamaguchi and coworkers[30] and independently by Gelbert and Many.[31] Resonant Brillouin scattering has also been performed from the acoustoelectrical domains in CdS and ZnO by Berkowicz and Skettrup[32] and CdSe by Yamamoto et al.[33] The experimental results have also clearly shown enhancement and cancellation in the region near the fundamental absorption edge. Such studies were restricted to only crystals in which the acoustoelectrical instability can occur by the application of a high electron field. This disadvantage was successfully overcome by employing the acoustic domain injection method by Ando and Hamaguchi.[34] This method enables us to inject the intense acousto-electrical domains amplified in CdS into other end-bonded semiconductors through the thin indium layer with a high transmission efficiency.[35] This method made us possible to investigate the resonant Brillouin scattering in the non-piezoelectric semiconductors or even in insulators such as ZnSe[34] ZnTe,[36] ZnCdTe,[37] CdS,[38] GaP,[39,40] GaSe and GaS.[41] The experimental data show a resonant enhancement and a resonant cancellation by shear acoustic waves of direct gap semiconductors, while by longitudinal acoustic waves or by shear waves in GaSe, GaS and GaP, no resonant cancellation has been observed.

In these studies, the incident photon energies were limitted to the region in which the samples were transparent. Because of the strong absorption near the fundamental absorption edge, it has been difficult to obtain the dispersion of the Brillouin scattering cross section in the highly

opaque region when we adopt a transmission type of experiment. To overcome this restriction Chang et al.[42] used reflection type experiment.[43] In the opaque region, the scattered light intensity is considerably weak even if we use a high density acoustic domains, so it is necessary to use laser. They used several lines of Ar ion laser with a Fabry-Perot interferometer. In their experiments, two kinds of Brillouin scattering were studied. One is scattering from ripple, which involves dinamic corrugation generated on the sample surface and the other is those from the elasto-optic mechanism, which is based on phonon induced modulation. The ripple mechanism, which is the well known mechanism, shows no dispersion above the band gap, while the elasto-optic mechanism shows explicit resonant enhancement in the opaque side of the absorption edge.

The objective of the present study is to present the dispersion curves of the resonant Brillouin scattering in various semiconductors such as II-VI and III-V compound, and analyze these data by the light scattering theory and piezobirefringence theory. Especially, in the present study, we shall extensively discuss the results of the resonant Brillouin scattering and piezobirefringence in cubic and polytype ZnS, theoretical analysis of the resonant Brillouin scattering in GaAs, resonant Brillouin scattering and piezobirefringence in CdS, and resonant Brillouin scattering in layered compound HgI_2. Also theoretical point of view, we shall constract the most complete expression of the Brillouin (Raman) tensor extending the existing light scattering theory to the three band process, which enables us to analyze the experimental data. The second motibation of the present study is to investigate the dispersion curves of the resonant Brillouin scattering cross section above the band gap and analyze the mechanism in the region theoretically.

CHAPTER 2

BRILLOUIN SCATTERING THEORY

2.1 Introduction

In this chapter, we shall be concerned with a theoretical treatment of the resonant Brillouin scattering, which permit us to make a quantitative calculation of the Brillouin scattering cross section.

The microscopic theory of the Brillouin scattering was first derived by Benedek and Fritsch[44] and Born and Huang.[45] They dealt thouroughly with the scattering cross sections in cubic crystals by incorporating the photoelastic constant. Such an analysis has been extended to the case of anisotropic media by Nelson et al.[46] Hope[47] and Hamaguchi[48] by taking into account the intrinsic birefringence. In the present study, the expressions of the Brillouin scattering cross section derived by Benedek and Fritsch[44] is used in the case of cubic materials and that of Hamaguchi[48] is applied to the case of anisotropic materials such as CdS and hexagonal ZnS. It should be noted that the formulation mentioned above is valid only in the transparent optical frequency range, so in the long wavelength region, where the incident photons never excite the electronic excitations in the crystals. In the photon energy region near the band gap energy the macroscopic treatment of Brillouin scattering is not useful because such treatments never take into account the effect of electronic excitations.

The microscopic (quantum-mechanical) expression for first-order Brillouin (Raman) scattering is obtained by 3rd order time-dependent perturbation calculation including the effect of electronic excitation by Loudon.[49] He predicted that the scattering efficiency should increase

drastically, kown as the resonant Brillouin (Raman) effect, when the incident or scattered photon energy approaches the band gap energy. It is also found that the deformation potential scattering of intermediate virtual states (electronic - excitaitons) by acoustic phonons plays an important role in the discussion of resonant effect. After his prediction, a considerable number of theoretical investigations on the dispersion of the resonance effect in semiconductors have been carried out.[50-57] The formulations of the first and second order Brillouin (Raman) scattering efficiency for the case in which the intermediate electron hole pair state are Wannier-Mott excitons have been given by Ganguly and Birman.[50] Later, more explicit calculation for Wannier-Mott excitons (allowed and forbidden scattering for transparent and absorbing frequency regions) was derived by Zeyher et al.[57] The final results of the above two calculations satisfactorily explains the resonant characteristics below and above the band gap. These results, however, contain some minor mistakes, arising from the calculation of the integration in the continuum part of the Brillouin (Raman) tensor. These mistakes have been corrected and completed formulation of the Brillouin (Raman) tensor has been presented by Peuker[58] and Bechstedt.[59] They gave a detailed discussion of the role of the imaginary and real parts, involving the discrete and continuum part of the Brillouin (Raman) tensor. It has been found in the present calculation that Coulomb interaction between electron and hole causes a strong asymmetry in the Brillouin (Raman) efficency with respect to the band gap, a strong enhancement only occurs below the gap. Section 2.2 is devoted to show the explanation of macroscopic treatment in the Brillouin scattering and scattering cross section for each acoustic mode in cubic and wurtzite materials are derived. In Section 2.3, microscopic theories are discussed based on the Loudon's and Birman's formulation.

In Section 2.4, deformation potential scattering and momentum matrix element are presented.

2.2 Basic Theory of Brillouin Scattering

2.2.1 Basic Concept of the Light Scattering

The kinetics of any scattering process is usually governed by two conservation laws, namely those of energy and momentum. For the light scattering process represented schematicallay in Fig. 2.1, these two laws reduces to these two equations[60)]

$$\text{energy conservation} \quad \hbar\omega_i = \hbar\omega_s \pm \hbar\omega_q \tag{2.1}$$

$$\text{momentum conservation} \quad \hbar\vec{k}_i = \hbar\vec{k}_s \pm \hbar\vec{q} \tag{2.2}$$

where $\hbar\omega_i$, $\hbar\omega_s$ are, respectively, the energy of the incident and scattered phonons; $\hbar\vec{k}_i$ and $\hbar\vec{k}_s$ are their momenta and $\hbar\omega_q$ and $\hbar\vec{q}$ are, respectively, the energy and momentum of the phonon scattered. The +(-) sign in eqs. (2.1) and (2.2) corresponds to phonon emission (absorption) and the scattering process is called a Stokes (anti-Stokes) process.

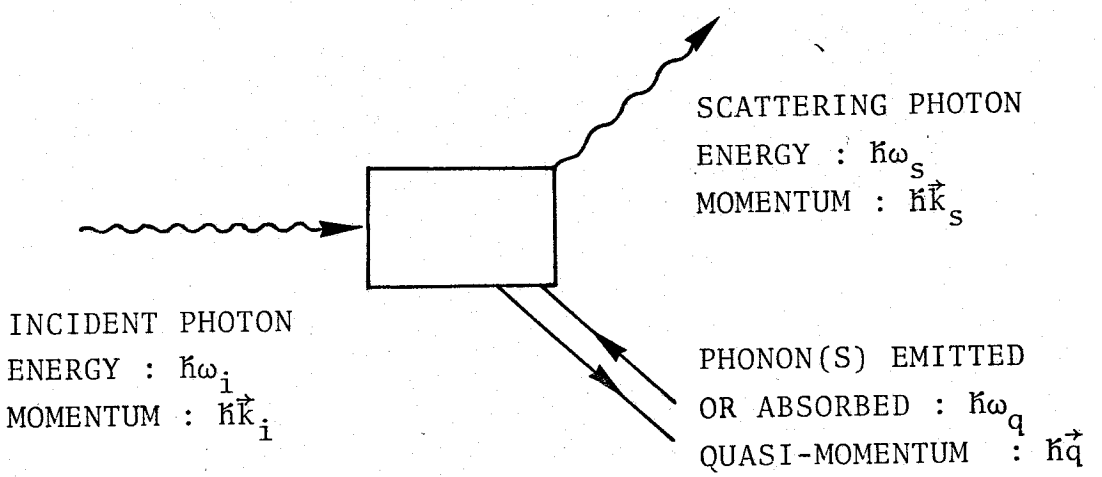

Fig. 2-1. Graphcal description of the scattering of light by phonons

In most light scattering experiment $\vec{k}_i$ and $\vec{k}_s$ are the order of 10^5 cm^{-1} (wave vector = $2\pi \times$ refractive index $\times$ wavenumber), so that q is also around 10^5 cm^{-1} or less. In crystals the size of Brillouin zone is typically $\simeq 10^8$ cm^{-1}. This implies that one-phonon scattering process, only small momentum phonons can be excited. In multi-phonon scattering this restriction is relaxed although the vector sum of the momenta of the phonons scattered still has to be small. For example two-phonon Raman scattering, the two phonons can have momenta $\hbar\vec{q}_1$ and $\hbar\vec{q}_2$ provided $\vec{q}_1 + \vec{q}_2 = \vec{k}_1 - \vec{k}_2$. Since $\vec{k}_i - \vec{k}_s \simeq 0$, we conclude that $\vec{q}_1 \simeq -\vec{q}_2$. If these two phonons belong to some branch (overtone scattering), the Raman frequency $\omega_i - \omega_s$ is equal to $2\omega_q$. This is the reason why zone edge phonon energies can be deduced from two-phonon Raman scattering. In Brillouin scattering, since the acoustic phonon frequency is given by $\omega_q = v_s q$ (where v_s is the sound velocity), it is not possible to neglect $\vec{k}_i - \vec{k}_s$.

In addition to the above consevation laws, the symmetry of the crystal also imposes restriction on the phonon(s) which can be observed by light scattering techniques. In the scattering process a photon of energy $\hbar\omega_i$ and polarization $\vec{e}_i$ is converted into a photon of energy $\hbar\omega_s$ and polarization $\vec{e}_s$. If the small difference in energy between $\hbar\omega_i$ and $\hbar\omega_s$ is neglected, the scattering can be described in terms of a second-rank tensor known as Raman tensor.[1)]

2.2.2 Macroscopic Theory of Brillouin Scattering in Cubic Crystals

Macroscopic treatments of Brillouin scattering from isotropic crystals has been derived by Benedek and Fritsch,[44)] in which the integral equations are solved. The theory predicts the scattering intensity, incident and scattered light polarization, in the cubic crystals. In the case of anisotropic crystals such as wurtzite crystals, Nelson [46)] and Hamaguchi[48)] have extended the theory of Benedek and Fritsch[44)] by taking into account the

effect of intrinsic birefringence. In the following, we will discuss the expression of the Brillouin scattering intensities in isotropic (zincblende) matrials.

A light wave passing through solid or liquid medium produces an oscillating dipole moment per unit or polarization $\vec{P}(\vec{r},t)$ at each point $\vec{r}$. The oscillating moments in turn radiate or scatter electromagnetic energy in all directions. The electric field $d\vec{E}'$ scttered to the field point $\vec{R}$ by the oscillating polarization within a volume $|d\vec{r}| \ll \lambda^3$ is

$$d\vec{E}'(\vec{R},t) = \left[\frac{\vec{1}_{\vec{R}-\vec{r}} \times (\vec{1}_{\vec{R}-\vec{r}} \times \partial^2 \vec{P}(\vec{r},t')/\partial t'^2)}{c^2 |\vec{R} - \vec{r}|} |d\vec{r}| \right]_{t' = t - |\vec{R} - \vec{r}|/c} \cdot \quad (2.3)$$

In eq. (2.3) $\vec{1}_{\vec{R}-\vec{r}}$ is a unit vector parallel to the vector $\vec{R} - \vec{r}$ connecting the source point $\vec{r}$ and the field point $\vec{R}$. t' is the retarded time $t - |\vec{R} - \vec{r}|/c_m$, calculated using as velocity the speed of light inside the medium (c_m) rather than that in a vacuum (c).

For low-intensity incident radiation, the local polarization is linearly proportional to the electric field, the proportionality factor being the polarizability tensor $\vec{\alpha}$. In analyzing the origin of the scattering we have separated the time average part of the polarizability $\langle\vec{\alpha}\rangle$ from the time-space fluctuation part $\delta\vec{\alpha}(\vec{r},t)$. This assumption is justified if only a negligible amount of light is scattered and no absorption is present. In cubic crystals the time average polarizability $\langle\vec{\alpha}\rangle$ is a scalar times the unity tensor, and the index of the refractive index n is independent of the direction of propagation. The thermal fluctuations in a crystal, however, cause off-diagonal component to appear in the polarizability tensor. Writting the electric field of the incident wave within the medium as

$$\vec{E}(\vec{r},t) = \vec{E}_0 \, e^{i(\vec{k}_i \cdot \vec{r} - \omega_i t)}, \quad (2.4)$$

We obtain that the polarization at each point in the medium is

$$\vec{P}(\vec{r},t) = (\langle\vec{\alpha}\rangle + \delta\vec{\alpha}(\vec{r},t))\cdot\vec{E}_0\, e^{i(\vec{k}_i\cdot\vec{r} - \omega_i t)}. \qquad (2.5)$$

To evaluate the second derivative of $\vec{P}$, as required by eq. (2.3), we must realize that the characteristic frequency for thermal fluctuations are small ($< 10^{12}$ s^{-1}) compared to the frequency in the optical region ($\simeq 5\cdot 10^{14}$ s^{-1}). We may therefore regard $\delta\vec{\alpha}(\vec{r},t)$ as a very weak function of the time and write

$$\frac{\partial^2\vec{P}(\vec{r},t)}{\partial t^2} \simeq - \omega_i^2\, \vec{P}(\vec{r},t)\ , \qquad (2.6)$$

On substituting eqs. (2.5) and (2.6) into (2.3) and carrying out the integration over the illumination volume V at the retarded time t', one obtains that $\vec{R} \gg \vec{r}$,

$$\vec{E}'(\vec{R},t) = -(\frac{\omega_i}{c})^2 \frac{e^{i(\vec{k}'\cdot\vec{R} - \omega_i t)}}{|\vec{R}|}\, \vec{1}_{\vec{k}} \times [\vec{1}_{\vec{k}} \times \int_V (\langle\vec{\alpha}\rangle + \delta\vec{\alpha}(\vec{r},t'))\cdot\vec{E}_0\, e^{i(\vec{k}_i - \vec{k}')\cdot\vec{r}}|d\vec{r}|] \qquad (2.7)$$

where $\vec{1}_{\vec{k}}$ is a unit vector parallel to $\vec{R}$ which is the direction of scattering and

$$\vec{k}_i = \frac{n_i\omega_i}{c}\vec{1}_i, \qquad \vec{k}_s = \frac{n_s\omega_s}{c}\vec{1}_{\vec{k}}\ , \qquad (2.8)$$

where n_s is the refractive index in direction E'. The integral in eq.(2.7) represents the superposition of phases of waves scattered from each illuminated point in the medium. In the absence of the fluctuations($\delta\vec{\alpha}$) this superposition leads to a complete cancellation of the scattered waves. The contribution to the integral from $\langle\vec{\alpha}\rangle$ term is zero except in the forword direction, because of,

$$\int_{V\to\infty} e^{i(\vec{k}_i - \vec{k}')\cdot\vec{r}}\, |d\vec{r}| = (2\pi)^3\, \delta(\vec{k}_i - \vec{k}') \quad . \qquad (2.9)$$

Scattering out of the incident direction ($\vec{k}' = \vec{k}_i$) results entirely from the fluctuations ($\delta\vec{\alpha}$). The fluctuating component can be expressed in terms of their spacial components:

$$\delta\vec{\alpha}(\vec{r},t) = \frac{1}{(2\pi)^{3/2}}\sum_{\mu}\int |d\vec{q}|\, \delta\vec{\alpha}^{\mu}(q) e^{i(\vec{q}\cdot\vec{r} \pm \omega_{\mu}(\vec{q})t')} \quad . \tag{2.10}$$

In this expansion $2\pi/|\vec{q}|$ is the wavelength of the fluctuation, $\omega_{\mu}(\vec{q})$ is the angular frequency of the fluctuation corresponding to this wavelength. The index μ denotes the posibility of a number of branches of the dispersion relation connecting the wave vector $\vec{q}$ and the corresponding angular frequency $\omega_{\mu}(\vec{q})$. $\omega_{\mu}(\vec{q})$ is double valued with ($\pm$) to account for the degeneracy in the dispersion relation for positive and negative running waves. Substituting eq.(2.10) into eq.(2.7) one obtains

$$\vec{E}'(\vec{R},t) = -\left(\frac{\omega_i}{c}\right)^2 \sum_{\mu} \vec{1}_{\vec{k}} \times \vec{1}_{\vec{k}} \times \int |d\vec{q}|\, (\delta\alpha^{\mu}(\vec{q})\cdot\vec{E}_0) \frac{e^{i(\vec{k}_s\cdot\vec{R} - (\omega_i \pm \omega_{\mu}(\vec{q})t)}}{|\vec{R}|}$$

$$\times \frac{1}{(2\pi)^{3/2}} \int_V |d\vec{r}|\; e^{i(\vec{k}_i - \vec{k}_s + \vec{q})\cdot\vec{r}} \quad , \tag{2.11}$$

where

$$\vec{k}_s = \left(\frac{n_s}{c}\right)(\omega_i \pm \omega_{\mu}(\vec{q}))\vec{1}_{\vec{k}} \quad . \tag{2.12}$$

The last integral in eq. (2.11) is a delta function provided that the integration volume is large compared to the wavelength of light,

$$\int_{V \to \infty} |d\vec{r}|\; e^{i(\vec{k}_i - \vec{k}_s + \vec{q})\cdot\vec{r}} = (2\pi)^3\, \delta(\vec{k}_i - \vec{k}_s + \vec{q}) \quad . \tag{2.13}$$

Thus the wavevector of the fluctuation which produces the scattering in the

direction $\vec{1}_{\vec{k}}$ is that which satisfies the implicit equation

$$\vec{q} = \vec{k}_s - \vec{k}_i \equiv \vec{K} \quad . \tag{2.14}$$

The solution of this equation is denoted by $\vec{K}$ and is called the scattering vector. Equation (2.12) indicates that the frequency of the scattered wave ($\omega_s = k_s c/n_d$) is shifted by amount $\pm \omega_\mu(q)$, and therefore eqs.(2.12) and (2.14) represent the conservation of energy and momentum among the incident, the scattered photons and scattering fluctuations (phonons). From eqs. (2.8), (2.12) and (2.13) the angles of incident and scattered light may be calculated as follows (Fig. 2.2),

$$\sin \theta_i' = \frac{\lambda_0}{2n_i v_\mu}\left[f_s + \frac{v_\mu^2}{f_s \lambda_0^2} (n_i^2 - n_d^2)\right] \quad , \tag{2.15}$$

$$\sin \theta_d' = \frac{\lambda_0}{2n_d v_\mu}\left[f_s - \frac{v_\mu^2}{f_s \lambda_0^2} (n_i^2 - n_d^2)\right] \quad , \tag{2.16}$$

where the subscript "i" and "d" denote "incident" and "deflected" or (scattered), respectively, λ_0 the wavelength of the incident light in free space, v_μ the sound velocity and f_s the frequency of the acoustic waves. The angles θ_i' and θ_d' are the internal angles in the medium. The scattering angle θ_s' is defined by

$$\theta_s' = \theta_i' + \theta_d' \quad . \tag{2.17}$$

If the scattering medium is isotropic one obtains, $n_i = n_d = n_0$ and in the case, eqs.(2.15) and (2.16) reduce to the simple isotropic form

$$\theta_s'/2 = \theta_i' = \theta_d' \tag{2.18}$$

and

$$\sin \frac{\theta_s'}{2} = \frac{\lambda_0 f_s}{2n_0 v_\mu} \tag{2.19}$$

where we have to note that θ_s' is the scattering angle in the medium.

In the Brillouin scattering measurements by acoustoelectically

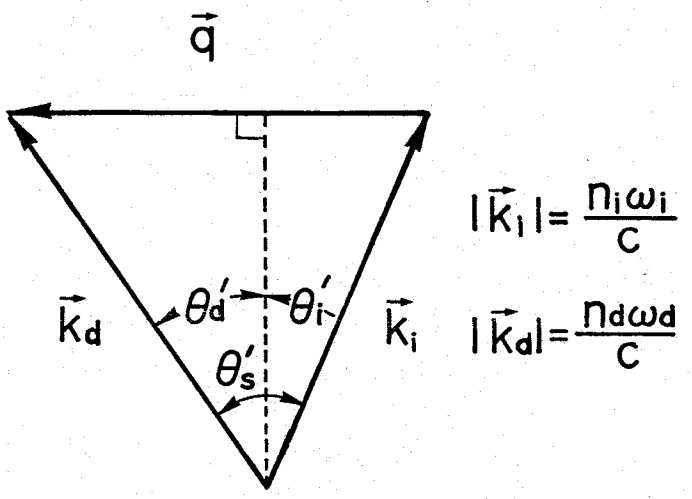

Fig. 2-2. Schematic diagram showing the wave vector construction between the incident light ($k_i = n_i\omega_i/c$), the scattered light ($k_d = n_s(\omega_i + \omega_\mu)/c$), and the acoustic wave ($q = \omega_\mu/v_\mu$).

amplified phonons, we employ the geometry shown in Fig. 2-3. In the case we measure the external angles θ_i and θ_d (or $\theta_s = \theta_i + \theta_d$) instead of θ_i' and θ_d'. Therefore we have to use Snell's low to derive the incident and scattering angles outside the specimen (in air). The result for the anti-Stokes process is[48]

$$\sin\theta_i = n_i \sin\left[\sin^{-1}\left\{\frac{\lambda_0}{2n_i v_\mu} \times \left[f_s + \frac{v_\mu^2}{f_s \lambda_0^2}(n_i^2 - n_d^2)\right]\right\} + \delta\right], \quad (2.20)$$

$$\sin\theta_d = n_d \sin\left[\sin^{-1}\left\{\frac{\lambda_0}{2n_d v_\mu} \times \left[f_s - \frac{v_\mu^2}{f_s \lambda_0^2}(n_i^2 - n_d^2)\right]\right\} + \delta\right], \quad (2.21)$$

where δ is the propagation angle of the acoustic waves with respect to the direction parallel to the slab faces. For the isotropic material and for $\delta = 0$ we have

$$\theta_s/2 = \theta_i = \theta_d \quad , \quad (2.22)$$

with

$$\sin\frac{\theta_s}{2} = \frac{\lambda_0 f_s}{2v_\mu} \quad . \quad (2.23)$$

In the case of CdS the refractive indices are $n_0 = 2.460$ for ordinary

waves and $n_e = 2.477$ for extraordinary waves. The acoustoelectric domains (T2-mode) in CdS consist of the transverse aoustic waves propagationg in the c-plane with its polarization vector parallel to the c-axis. When the polarization vector of the incident light is perpendicular to the c-axis, the scattered light is polarized parallel to the c-axis. On Fig. 2-4. is shown the angle of incident light (θ_i), and the angles of diffracted light (θ_d) as a function of acoustic frequency of CdS. For comparison is also shown the frequency dependence of $\theta_i = \theta_d = (\theta_0)$ for the isotropic case ($n = \frac{1}{2}(n_e + n_0)$). In the calculation we have used the following data: λ_0 =632.8 nm(vacuum wavelength of He-Ne laser), $v_\mu = 1.76 \times 10^5$ cm/sec

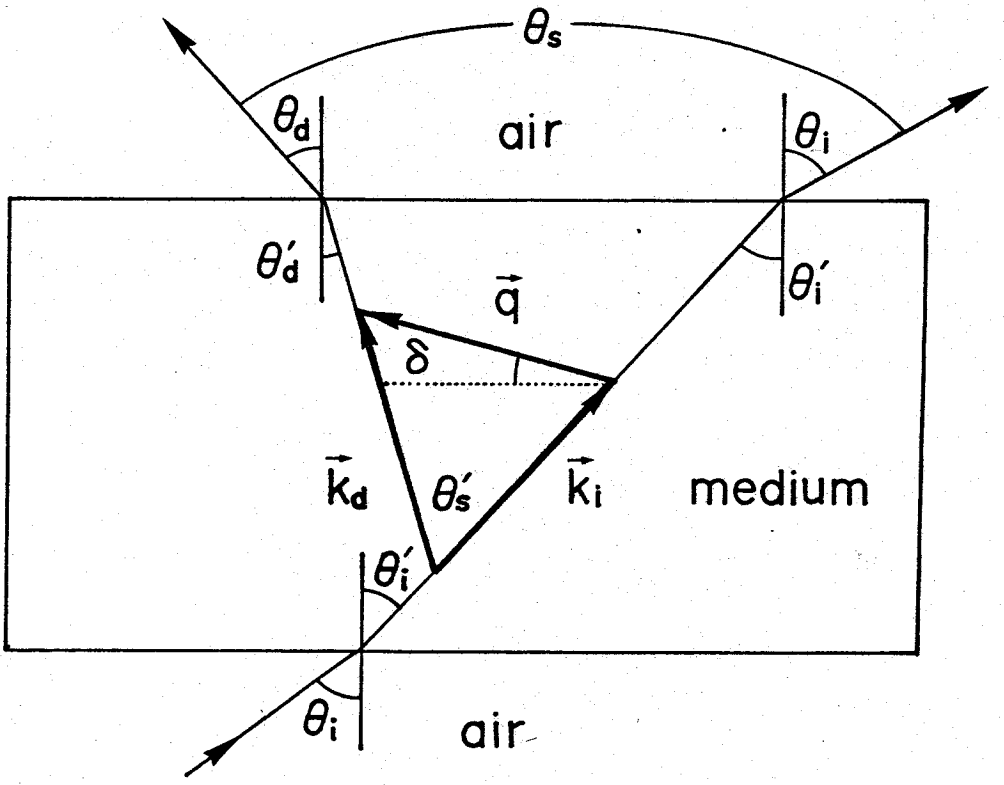

Fig. 2-3. Interaction geometry for optical diffraction by an off-axis elastic wave. $\vec{k}_0$:wave vector of the incident light. $\vec{k}$:wave vector of the scattered light. q:wave vector of the acoustic wave. θ_i:external incident angle. θ_d:external diffracted angle. θ_s:external scattering angle. δ:propagation angle of the acoustic wave with respect to the slab faces of the specimen.

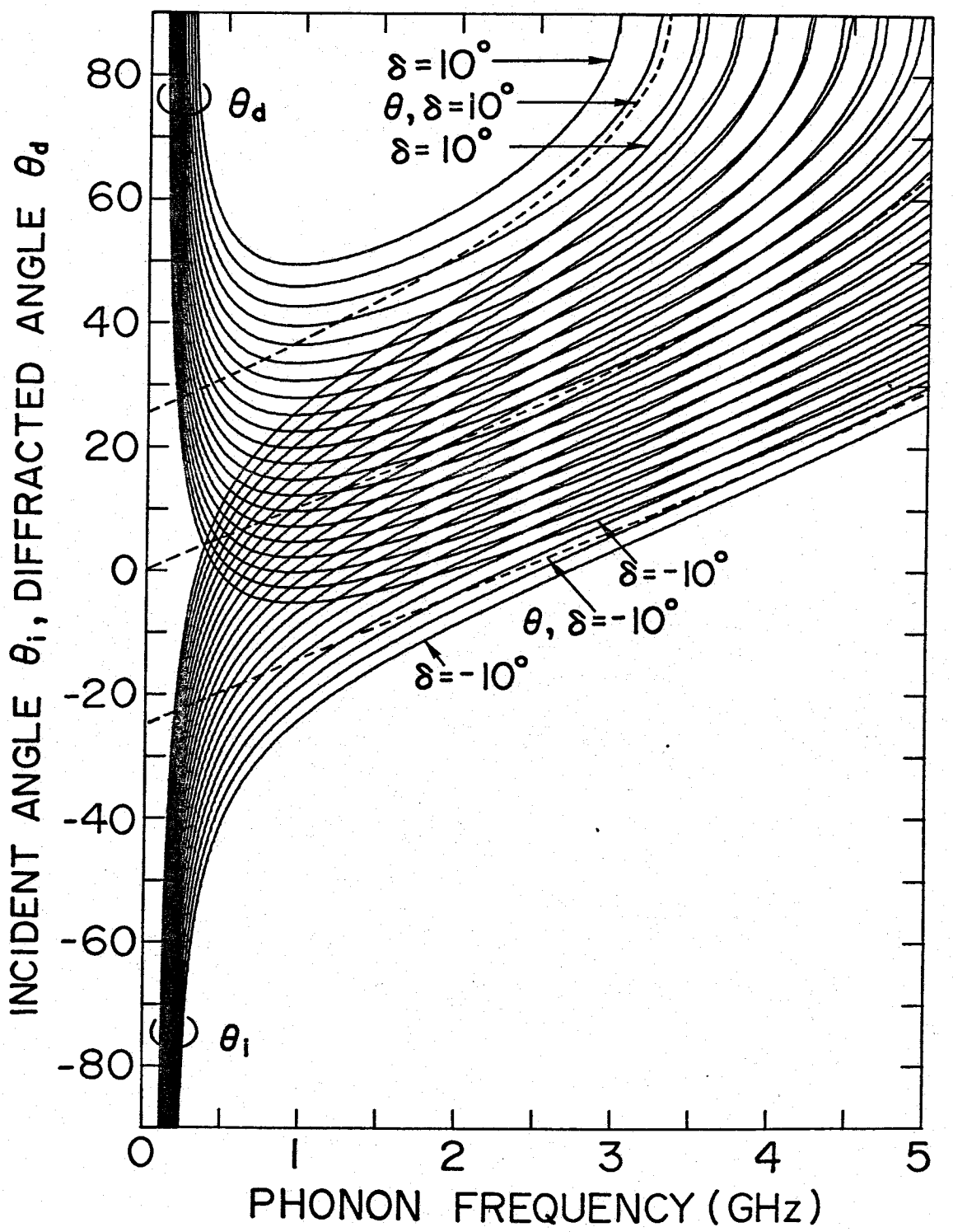

Fig. 2-4. Angles of incident light (θ_i) and that of diffracted light (θ_d) outside the crystal as a function of acoustic phonon frequency (f_s) in CdS with the off-axis angle (δ) of the acoustic wave vector as parameter, where the incident plane is perpendicular to the c-axis of the crystal. The incident light polarized perpendicular to the c-axis is scattered by the transverse acoustic waves propagating in the c-plane with the polarization vector parallel to the c-axis, and the scattered light is polarized to the c-axis. Isotropic case is shown in the dashed curves.

(sound velocity of the acoustoelectric domain in CdS). It should be noted that there exsists a remarkable difference between the two cases; optically isotropic materials and anisotropic materials. Substituting eq.(2.10) into eq. (2.11) and replacing $\delta\vec{\alpha}$ by $\delta\vec{\varepsilon}/4\pi$, where $\delta\vec{\varepsilon}$ is the fluctuation in the dielectric constant tensor, we obtain the expression for the amplitude of the electric field scattered by the mode μ of the fluctuation having the wave vector $\vec{K}$,

$$E'(\vec{K},t) = -(\frac{\omega_i}{c})\frac{2(2\pi)^{3/2}}{4\pi R}\sum_{\mu} e^{i\{\vec{k}\cdot\vec{R} - [\omega_i \pm \omega_\mu(\vec{K})]t\}} \vec{1}_{\vec{k}}\times[\vec{1}_{\vec{k}}\times(\delta\vec{\varepsilon}^{\mu}(\vec{K})\cdot\vec{E}_0)] \quad . \tag{2.24}$$

As follows from the eq. (2.24) the scattered light has the frequency $\omega_0 + \omega_\mu$, where the plus sign corresponds to the aiti-Stokes component and the minus sign to the Stokes component. The direction of the scattered light is given by the unit vector $\vec{1}_{\vec{k}}$ and the wave vector is given by eq. (2.12).

The total power $dP'(\vec{q},\vec{R})$ in all frequencies scattered into a solid angle $d\Omega'$ at the field point $\vec{R}$ is proportional to the mean squared field strength,

$$dP'(\vec{q},\vec{R}) = \frac{c}{8\pi}\langle|\vec{E}'(\vec{q},t)|^2\rangle R^2 d\Omega' \quad . \tag{2.25}$$

The spectrum of scattered radiation is derived using the autocorrelation function for $\vec{E}'(\vec{q},t)$. The fluctuation in the dielectric constant tensor components results from the fact that those components depend on the state of strain of the solid. A fluctuation produces a corresponding fluctuation in the electric displacement vector $\delta\vec{D}(\vec{q},t) = \delta\vec{\varepsilon}^{\mu}(\vec{q},t)\cdot\vec{E}_0$. The fluctuation in the dielectric constant tensor $e_{kl} = (1/2)(\partial u_k/\partial r_l + \partial u_l/\partial r_k)$, $\vec{u}$ and $\vec{r}$ being the displacement and position vectors, respectively, of an element of the crystal. The fluctuation of strains are produced by the passage of sound waves. In general, for small strains, the change in the dielectric

tensor component $\delta\varepsilon_{ij}(\vec{r},t)$ as a linear function of the elestic strain component $e_{kl}(\vec{r},t)$,

$$-\frac{\delta\varepsilon_{ij}(\vec{r},t)}{\varepsilon_{ii}\varepsilon_{jj}} \equiv \sum_{k,l} p_{ijkl} e_{kl}(\vec{r},t) \quad , \tag{2.26}$$

where p_{ijkl} is the components of the photoelastic tensor. Each tensor for the zincblende-type crystals has the following form:

dielectric constant tensor:[ε]

$$[\varepsilon] = \begin{bmatrix} \varepsilon_{11} & 0 & 0 \\ 0 & \varepsilon_{11} & 0 \\ 0 & 0 & \varepsilon_{11} \end{bmatrix} \qquad \varepsilon_{11} = n^2 \tag{2.27}$$

strain tensir :[e]

$$[e] = \begin{bmatrix} e_{11} & e_{12} & e_{13} \\ e_{21} & e_{22} & e_{23} \\ e_{31} & e_{32} & e_{33} \end{bmatrix} \tag{2.28}$$

photoelastic constant tensor:[p]

$$[p] = \begin{bmatrix} p_{11} & p_{12} & p_{13} & 0 & 0 & 0 \\ p_{12} & p_{11} & p_{12} & 0 & 0 & 0 \\ p_{13} & p_{12} & p_{11} & 0 & 0 & 0 \\ 0 & 0 & 0 & p_{44} & 0 & 0 \\ 0 & 0 & 0 & 0 & p_{44} & 0 \\ 0 & 0 & 0 & 0 & 0 & p_{44} \end{bmatrix} \tag{2.29}$$

In eq. (2.27), n is the refractive index of the crystal. Note that the strain [e] is the symmetric tensor. One can write $\delta\varepsilon_{ij}(\vec{r},t)$ using eq.(2.26) as

$$\delta\varepsilon_{ij}(\vec{r},t) = \varepsilon_{ii}\varepsilon_{jj}\sum_{k,l} p_{ijkl}\, e(\vec{r},t) \quad . \tag{2.30}$$

From the Fourier transformation of $e_{kl}(\vec{r},t)$ into $e_{kl}(\vec{q},t)$, we obtain for the fluctuation of the electric displacement in the crystal

$$\begin{aligned}\delta D_i &\equiv \delta\varepsilon^{\mu}_{ij}\ (\vec{K},t)\cdot E_j \\ &= \varepsilon_{im}\varepsilon_{nj}p_{mnkl}e_{kl}(\vec{K},t)E_j \\ &= \frac{\varepsilon_{11}^2}{i}\, E_j \cdot Ku^{\mu}(\vec{K},t)\vec{\xi}_j \quad .\end{aligned} \tag{2.31}$$

It can be seen from eq. (2.31) that in the light scattering experiment one observes not $\vec{\zeta}$ but the component of $\vec{\xi}$ in the plane perpendicular to the scattered wave vector $\vec{k}$ given by

$$\vec{\xi}^{\mu} = \vec{1}_{\vec{k}} \times (\vec{1}_{\vec{k}} \times \vec{\zeta}^{\mu}) \quad . \tag{2.32}$$

The vector $\vec{\xi}^{\mu}$ therefore determines explicitly the polarization of the light scattered from each acoustic mode μ. From eqs.(2.24), (2.25) and (2.31) we obtain

$$dP' = \frac{cE_0^2}{8\pi}\left(\frac{\omega_0}{c}\right)^4 \varepsilon_{11}^4 \frac{V}{(4\pi)^2}\frac{k_B T}{\rho}\sum_{\mu=1}^{3}\frac{|\vec{\xi}^{\mu}|^2}{[\omega_{\mu}(\vec{q})]^2}\, d\Omega' \quad . \tag{2.33}$$

The result of eq.(2.33) is valid provided that $\hbar\omega_{\mu} \ll k_B T$. The correct form for eq.(2.33) at all temperature is

$$dP' = \frac{cE_0^2}{8\pi}\left(\frac{\omega_0}{c}\right)^4 \varepsilon_{11}^4 \frac{V}{(4\pi)^2}\sum_{\mu=1}^{3}\frac{|\vec{\xi}^{\mu}|}{2\rho v_{\mu}^2}\hbar\omega_q(\vec{q})\,[(<n_{\mu}(\vec{q})+1>+<n_{\mu}(q)>]\, d\Omega' \ , \tag{2.34}$$

where

$$<n_{\mu}(\vec{q})> = \frac{1}{\exp(\hbar\omega_{\mu}(\vec{q})/k_B T - 1)} \quad . \tag{2.35}$$

The two terms in the square brackets at right hand side of eq.(2.34) correspond to the so-called Stokes component and anti-Stokes component, respectively. The intensity of light scattered into the solid angle Ω'

during the optical path length r is given by

$$dP'(\Omega') = I_0 \frac{\pi^2 n_0^8}{\lambda_0^4} \sum_{\mu=1}^{3} \frac{|\vec{\xi}^{\mu}|^2}{\rho v_{\mu}^2} \frac{\hbar\omega_{\mu}}{2} [(<n_{\mu}> + 1) + <n_{\mu}>] d\Omega' \cdot r \quad , \qquad (2.36)$$

where I_0 is the incident intensity and λ_0 is the wavelength of the light in vacuum. The summation in eq. (2.34) indicate that one must include contributions from three different acoustical phonon mode, i.e., these from two transverse modes and one longitudinal phonon mode.

In the case of $\hbar\omega_{\mu} \ll k_B T$, eq. (2.34) can be written in good approximation as

$$n_{\mu} \simeq k_B T / \hbar\omega_{\mu}(\vec{q}) \quad . \qquad (2.37)$$

Thus, the energy density of eq. (2.34) can be replaced by $k_B T$ in the case of Brillouin scattering by thermal phonons [$\Phi^{\mu} = n_{\mu}(\vec{q})\hbar\omega_{\mu}(\vec{q}) \simeq k_B T$].

The intensity of light scattering through anti-Stokes or Stokes process is given by

$$dP'(\Omega') = I_0 \sum_{\mu=1}^{3} \frac{\pi^2 n_0^8}{\lambda_0^4} \frac{\Phi^{\mu}}{2} \frac{|\vec{\xi}^{\mu}|^2}{\rho v_{\mu}^2} r \cdot d\Omega' \quad . \qquad (2.38)$$

It should be noted here that the solid angle Ω' is the internal solid angle in the sample. In Brillouin scattering measurement an aperture is usually placed in front of the detector, which determines an external collection angle Ω, not the internal cone Ω' given in eq. (2.34) and eq. (2.38). For small cone angles one obtains[48]

$$d\Omega \simeq \frac{\cos\theta_d}{n_d \sqrt{n_d^2 - \sin^2\theta_d}} d\Omega' \quad , \qquad (2.39)$$

where θ_d is the external scattering angle. The scattering cross section σ_B is

$$\sigma_B = \frac{\pi^2 n_0^8}{\lambda_0^4} \sum_{\mu=1}^{3} \frac{\Phi^{\mu}}{2} \frac{|\vec{\xi}^{\mu}|^2}{\rho v_{\mu}^2} \frac{\cos\theta_d}{n_d \sqrt{n_d^2 - \sin^2\theta_d}} \qquad (2.40)$$

where σ_B is defined as the Brillouin scattering intensity per unit path length per unit external solid angle.

According to the eq. (2.31), light scattered by acoustic waves should exhibit certain distinguishing characteristics which should depend strongly upon the polarization and propagation direction of incident light beam relative to those of acoustic waves. To evaluate the intensity of Brillouin scattering, one has to calculate $|\xi^{\mu}|^2/\rho v_{\mu}^2$ for the conditions appropriate to one's experiments.

Case 1 (T1-Mode Acoustic Phonons in Cubic Materials)

The T1-mode phonons propagate in the $[1\bar{1}0]$ direction with shear polarization parallel to the [110] direction. We adopt the configuration that the incident light polarization is parallel to the [110] direction.

$$\text{Acoustical polarization: } \vec{\pi} = (1/\sqrt{2},\ 1/\sqrt{2},\ 0)\ , \qquad (2.41a)$$

$$\text{Acoustical propagation: } \vec{1}_q = (1/\sqrt{2},\ -1/\sqrt{2},\ 0)\ , \qquad (2.41b)$$

$$\text{Incident light polarization: } \vec{1}_E = (1/\sqrt{2},\ 1/\sqrt{2},\ 0)\ . \qquad (2.41c)$$

Substituting eq. (2.41) into eqs.(2.31) and (2.32), one obtains $\vec{\zeta}^{T1}$ as

$$\vec{\zeta}^{T1} = \frac{1}{2}(p_{11} - p_{12})\vec{1}_q\ , \qquad (2.42)$$

and $\vec{\xi}^{T1}$ as

$$\vec{\xi}^{T1} = \frac{1}{2}(p_{11} - p_{12})\cos\theta_i' \cdot \vec{1}_S\ , \qquad (2.43)$$

where θ_i' is the incident angle inside the specimen, and the vector $\vec{1}_S$ stands for the unit vector lying the scattering plane. The scalar product of $\vec{1}_S$ and $\vec{1}_E$ is given by

$$\vec{1}_S \cdot \vec{1}_E = 0\ , \qquad (2.44)$$

which means that the scattered light polarization is explicitly perpendicular to the incident light polarization. Substituting eq. (2.42) into eq.(2.40) we can obtain the Brillouin scattering cross sections for T1-mode phonons as

$$\sigma_B = \frac{\pi^2 \varepsilon_{11}^4}{\lambda^4} \frac{\Phi^{T1}}{C_{11} - C_{12}} \left[\frac{1}{2}(P_{11} - P_{12}) \cos\theta_i' |\vec{1}_S| \right]^2 \frac{\cos\theta_d}{n\sqrt{n^2 - \sin^2\theta_d}} \quad , \tag{2.45}$$

where C_{ij} is the component of the elastic stiffness tensor. In eq.(2.45), we used the following relation:

$$v_{T1} = [(C_{11} - C_{12})/2\ ]^{1/2} \quad . \tag{2.46}$$

Case 2 (T2-Mode Acoustic Phonons in Cubic Materials)

The T2 -mode phonons propagate in the [110] direction with shear polarization parallel to the [110] direction. We adopt the configulation that the incident polarization is parallel to the [110] direction.

The vectors $\vec{\pi}$, $\vec{1}_q$ and $\vec{1}_E$ are, thus written as

$$\text{Acoustical polarization: } \vec{\pi} = (1/\sqrt{2},\ 1/\sqrt{2},\ 0) \ , \tag{2.47a}$$

$$\text{Acoustical propagation: } \vec{1}_q = (\ 0\ ,\ 0\ ,\ 1) \ , \tag{2.47b}$$

$$\text{Incident light polarization: } \vec{1}_E = (1/\sqrt{2},\ 1/\sqrt{2},\ 0) \ . \tag{2.47c}$$

Substituting eq.(2.46) into eq.(2.31) and (2.32), one obtains $\vec{\zeta}^{T2}$ as

$$\vec{\zeta}^{T2} = p_{44} \vec{1}_q \tag{2.48}$$

and $\vec{\xi}^{T2}$ as

$$\vec{\xi}^{T2} = p_{44} \cos\theta_i \vec{1}_S \quad . \tag{2.49}$$

The scattered light polarization is also explicitly perpendiculatr to the incident light polarization, because $\vec{1}_s \cdot \vec{1}_E = 0$. Substituting eq.(2.48) into eq.(2.40), we obtain

$$\sigma_B = \frac{\pi^2 \varepsilon_{11}^2}{\lambda_0^4} \frac{\Phi^{T2}}{2C_{44}} [p_{44} \cos\theta_i' |\vec{1}_s|^2] \frac{\cos\theta_d}{n\sqrt{n^2 - \sin^2\theta_d}} \quad , \tag{2.50}$$

where C_{44} is the component of the elastic stiffness tensor, and we used the following relation:

$$v_{T2} = (C_{44}/\rho)^{1/2} \quad . \tag{2.51}$$

2.2.3 Macroscopic Theory of Brillouin Scattering in Wurtzite Crystals

The macroscopical theory of Brillouin scattering in the wurtzite-type crystals offeres the closest analogy with that in the zincblende-type crystals. One must, however, take into account the anisotripic nature of the optical properties [i.e., birefringence and dichroism] in these crystals, since the scattered and incident lights have sometimes different polarizations. For the crystals with crystal symmetry of 6mm, $\bar{6}$m2, 622, or 6/mmm, the dielectric constant tensor [ε], strain tensor [e] and photoelastic constant tensor [p] can be written as

$$[\varepsilon] = \begin{bmatrix} \varepsilon_{11} & 0 & 0 \\ 0 & \varepsilon_{11} & 0 \\ 0 & 0 & \varepsilon_{33} \end{bmatrix} \tag{2.52}$$

with

$$\varepsilon_{11} = n_o^2 \quad \text{and} \quad \varepsilon_{33} = n_e^2 \tag{2.53}$$

and

$$[p] = \begin{bmatrix} p_{11} & p_{12} & p_{13} & 0 & 0 & 0 \\ p_{12} & p_{11} & p_{13} & 0 & 0 & 0 \\ p_{31} & p_{31} & p_{33} & 0 & 0 & 0 \\ 0 & 0 & 0 & p_{44} & 0 & 0 \\ 0 & 0 & 0 & 0 & p_{44} & 0 \\ 0 & 0 & 0 & 0 & 0 & p_{66} \end{bmatrix} \tag{2.54}$$

with

$$p_{66} = \frac{1}{2}(p_{11} - p_{12}) \tag{2.55}$$

where n_o and n_e are the refractive indices for the ordinary and extraordinaly rays, respectively. If the birefringence effect is taken into account, the wave vectors k_i[eq.(2.8)], k_d[eq.(2.8)] appeared in 2.2.2 becomes[48)]

$$\vec{k}_i = \frac{n_i \omega_i}{c} \vec{l}_i \ , \tag{2.55}$$

$$\vec{k}_s = \frac{n_d \omega_s}{c} \vec{l}_k \ , \tag{2.56}$$

where n_i and n_d are the refractive indices for the polarization of the incident light and for that of the scattered light, and $\vec{l}_k$ is a unit vector in the direction of the scattered wave vector $\vec{k}$.

One can write eq.(2.26) by using the formulation of [p] in eq.(2.54),

$$-\delta\varepsilon_{ij}(\vec{r},t) = \varepsilon_{im}\varepsilon_{nj}p_{mnkl}e_{kl} \tag{2.58}$$

and thus the fluctuation in the electric displacement vector in the crystal δD is written

$$\delta D^{\mu}(\vec{q},t) = \delta\varepsilon^{\mu}(\vec{q},t)\cdot E_0 = \frac{\varepsilon_{11}^2}{i} E_0 q u^{\mu}(\vec{q},t)\vec{\zeta}^{\mu} \ . \tag{2.59}$$

The vector $\vec{\xi}$, which determines the polarization of the scattered light is given by the same form as eq.(2.32), one obtain the Brillouin scattering cross section in the wurtzite type crystal as

$$\sigma_B = \frac{\pi^2 \varepsilon_{11}^4}{\lambda_0^4} \sum_{\mu=1}^{3} \frac{\Phi^{\mu}}{2\rho v_{\mu}^2} |\vec{\xi}^{\mu}|^2 \frac{\cos\theta_d}{n_d \sqrt{n_d^2 - \sin^2\theta_d}} \ . \tag{2.60}$$

In the following, we evaluate the Brillouin scattering cross section in the wurtzite type crystals for three special phonon modes;(1) T1-mode acoustic phonons, (2) T2-mode acoustic phonons and (3) LA-mode acoustic phonons by the aid of the above results.

Case 1 (T1-Mode Acoustic Phonons in Wurtzite Materials)

The T1-mode phonons propagate in the direction perpendicular to the

c-axis with shear polaization perpendicular to the c-axis. We adopt the configulaiton that the incident light polarization is perpendicular to the c-axis and parallel to the shear polarizaiton. The vectors $\vec{\pi}$, $\vec{1}_{\vec{q}}$ and $\vec{1}_{\vec{E}}$, thus, become[48]

$$\text{Acoustical polarization: } \vec{\pi} = (0, 1, 0) , \tag{2.61a}$$

$$\text{Acoustical propagation: } \vec{1}_{\vec{q}} = (1, 0, 0) , \tag{2.61b}$$

$$\text{Incident light polarization: } \vec{1}_{\vec{E}} = (0, 1, 0) . \tag{2.61c}$$

Substituting eq.(2.61) into eqs.(2.59) and (2.32), one obtains $\vec{\xi}^{T1}$ as

$$\vec{\xi}^{T1} = \frac{1}{2}(p_{11} - p_{12})(\vec{1}_{\vec{k}})_3 \vec{1}_{xz} , \tag{2.62}$$

where $\vec{1}_{xz}$ is the unit vector in the $OX_1 - OX_3$ plane, and then

$$\frac{|\vec{\xi}^{T1}|^2}{2\rho v_{T1}^2} = \frac{(p_{11}-p_{12})^2}{2(c_{11}-c_{12})}(\vec{1}_{\vec{k}})_3^2 |\vec{1}_{xz}|^2 , \tag{2.63}$$

where the sound velocity v_{T1} of this phonon mode is given by the same form as eq.(2.46). The elastic stiffness tensor [c] has the similar form as eq.(2.54). The Brillouin scattering cross section can be obtained by substituting eq.(2.63) into eq.(2.60). Thus we find that the polarization of the scattered light is perpendicular to the incident polarizaion for the scattering by the T1-mode acousitc phonon.

Case 2 (T2-Mode Acoustic Phonons in Wurtzite Materials)

The T2-mode phonons propagate in the direction perpendicular to the c-axis with shear polarization parallel to the c-axis. We adopt the configuration that the incident light polarization is parallel to the c-axis. The vectors $\vec{\pi}$, $\vec{1}_{\vec{q}}$, and $\vec{1}_{\vec{E}}$ are, thus, written as

$$\text{Acoustical polarization: } \vec{\pi} = (0, 0, 1) , \tag{2.64a}$$

$$\text{Acoustical propagation: } \vec{1}_{\vec{q}} = (1, 0, 0) , \tag{2.64b}$$

$$\text{Incident light polarization: } \vec{1}_{\vec{E}} = (0, 0, 1) . \tag{2.64c}$$

It is clear from eq.(2.64) that

$$\vec{\pi}\cdot\vec{1}_{\vec{q}}=0, \quad \vec{1}_{\vec{q}}\cdot\vec{1}_{\vec{E}}=0 \quad \text{and} \quad (\vec{\pi}^{\mu})_1(\vec{1}_q)_1(\vec{1}_E)=0,$$

so that eq.(2.59) can be reduced to as

$$\vec{\zeta}^{T2}=p_{44}\left(\frac{\varepsilon_{33}}{\varepsilon_{11}}\right)^2\vec{1}_q \ . \tag{2.65}$$

Then, one obtains

$$\vec{\xi}^{T2}=p_{44}\left(\frac{\varepsilon_{33}}{\varepsilon_{11}}\right)^2|\vec{1}_{\vec{k}}\times\vec{1}_{\vec{q}}|\vec{1}_{\perp c} \ , \tag{2.66}$$

where the vector $\vec{1}_{\perp c}$ in eq.(2.66) is the unit vector perpendicular to the c-axis of the crystal. Thus we find that the scattered light is polarized perpendicular to the incident beam. One can finally obtain

$$\frac{|\vec{\xi}^{T2}|^2}{\rho v_{T2}^2}=\frac{p_{44}^2}{2c_{44}}\left(\frac{\varepsilon_{33}}{\varepsilon_{11}}\right)^4|\vec{1}_{\vec{k}}\times\vec{1}_{\vec{q}}|^2|\vec{1}_{\perp c}|^2 . \tag{2.67}$$

The sound velocity v_{T2} is given by the same form as eq.(2.50). The Brillouin scattering cross section can be obtained by substituting eq.(2.67) into eq.(2.60).

Case 3 (LA-Mode Acoustic Phonons in Wurtzite Materials)

The LA-mode (pure longitudinal) phonons propagate in the direction perpendicular to the c-axis with acoustical polarization perpendicular to the c-axis We adopt the configuration that the incident light polarization is parallel to the c-axis. The vectors $\vec{\pi}$, $\vec{1}_{\vec{q}}$ and $\vec{1}_{\vec{E}}$, thus become

$$\text{Acoustical polarization: } \vec{\pi}=(1,\ 0,\ 0) , \tag{2.68a}$$

$$\text{Acoustical propagation: } \vec{1}_{\vec{q}}=(1,\ 0,\ 0) , \tag{2.68b}$$

$$\text{Incident light polarization: } \vec{1}_{\vec{E}}=(0,\ 0,\ 0) . \tag{2.68c}$$

Thus, eq.(2.59) can be reduced to as

$$\vec{\xi}^{LA}=p_{31}\left(\frac{\varepsilon_{33}}{\varepsilon_{11}}\right)^2\vec{1}_{\parallel c} \ , \tag{2.69}$$

where the vector $\vec{1}_{\parallel c}$ is the unit vector parallel to the c-axis. It can be

seen that the polarization vector of the light does not change after being the Brillouin scattering process. Finally, one obtains

$$\frac{|\vec{\xi}^{LA}|^2}{2\rho v_{LA}^2} = \frac{p_{31}}{2c_{11}}\left(\frac{\varepsilon_{33}}{\varepsilon_{11}}\right)^4 |\vec{1}_{\parallel c}|^2 \tag{2.70}$$

In eq. (2.70), we used the following relation:

$$v_{LA} = (c_{11}/\rho)^{1/2} \tag{2.71}$$

The Brillouin scattering cross section can also be obtained by substituting eq.(2.70) into (2.60).

2.3 Quantum Mechanical Theory

2.3.1 Brillouin Scattering for Uncorrelated Electron-Hole Pairs

The detailed nature of the resonant light scattering mechanism of the Brillouin (Raman) scattering is examined by quantum mechanical theory. Expression for the Brillouin (Raman) cross section, σ_B, can be derived by the application of time-dependent perturbation theory by Loudon.[49] Using time-dependent perturbation theory, the Brillouin (Raman) scattering probability per unit time is given by[61]

$$P(\omega_i;\omega_s) = (2\pi/\hbar^6)\sum_f \left| \sum_{j,k} \frac{\langle f|H_1|k\rangle\langle k|H_1|j\rangle\langle j|H_1|i\rangle}{(\omega_j - \omega_i)(\omega_k - \omega_s)} \right|^2$$

$$\times\delta(\omega_i - \omega_s - \omega_q) \tag{2.72}$$

where $|i\rangle$ is the initial state consisting of a crystal in its ground state plus an incident photon;and $|f\rangle$ is an additional phonon $\hbar\omega_q$;$|j\rangle$ and $|k\rangle$ denote intermediate states in which excitons are excited in the solid. H_1

is the interaction Hamiltonian, assumed to the sum of the exciton-radiation Hamiltonial (H_{ER}) and the exciton-phonon (H_{EP}) interaction as follows;

$$H_1 = H_{ER} + H_{EP} \quad . \tag{2.73}$$

By permuting the order in which H_{ER} and H_{EP} occur in eq. (2.72) one obtains the following six terms contributing to the scattering probability.[49)]

$$\begin{aligned} P(\omega_i;\omega_s) = (2\pi/\hbar^6)\sum_f \Bigg| \sum_{\alpha,\beta} \Bigg(& \frac{\langle 0|H_{ER}(\omega_s)|\beta\rangle\langle\beta|H_{EP}|\alpha\rangle\langle\alpha|H_{ER}(\omega_i)|0\rangle}{(\omega_\beta + \omega_0 + \omega_s)(\omega_\alpha + \omega_s)} \\ & + \frac{\langle 0|H_{ER}(\omega_i)|\beta\rangle\langle\beta|H_{EP}|\alpha\rangle\langle\alpha|H_{ER}(\omega_s)|0\rangle}{(\omega_\beta + \omega_0 + \omega_s)(\omega_\alpha + \omega_s)} \\ & + \frac{\langle 0|H_{ER}(\omega_s)|\beta\rangle\langle\beta|H_{ER}(\omega_i)|\alpha\rangle\langle\alpha|H_{EP}|0\rangle}{(\omega_\beta + \omega_0 - \omega_i)(\omega_\alpha + \omega_0)} \\ & + \frac{\langle 0|H_{ER}(\omega_i)|\beta\rangle\langle\beta|H_{ER}(\omega_s)|\alpha\rangle\langle\alpha|H_{EP}|0\rangle}{(\omega_\beta + \omega_0 + \omega_s)(\omega_\alpha + \omega_0)} \\ & + \frac{\langle 0|H_{EP}|\beta\rangle\langle\beta|H_{ER}(\omega_s)|\alpha\rangle\langle\alpha|H_{ER}(\omega_i)|0\rangle}{(\omega_\beta + \omega_s - \omega_i)(\omega_\alpha - \omega_i)} \\ & + \frac{\langle 0|H_{EP}|\beta\rangle\langle\beta|H_{ER}(\omega_i)|\alpha\rangle\langle\alpha|H_{ER}(\omega_s)|0\rangle}{(\omega_\beta + \omega_s - \omega)(\omega_\alpha + \omega)} \Bigg|^2 \delta(\omega_i - \omega_s - \omega_q) \end{aligned} \tag{2.74}$$

To simplify the notation, only exciton states are shown in eq. (2.74). $|0\rangle$ denotes the ground state in which no excitons are excited. $|\alpha\rangle$ and $|\beta\rangle$ represent states in which excitons α and β are excited, respectively. The Brillouin (Raman)cross section is taken related to the scattering rate P by the equation

$$\sigma(\omega_i;\omega_s) = VP/v = nPV/c \quad , \tag{2.75}$$

where v and c are, respectively, the velocity of light inside the medium and in vacuo; n is the refractive index of the scattering medium and V its volume. In studying resonant scattering, one usually tunes $\hbar\omega_i$, close to

some excitation energies, $\hbar\omega_\alpha$, so of the six terms in eq.(2.74), the first one becomes the strongest component to reminding terms which can be taken to be equal to a constant C. Thus in resonant light scattering the Brillouin tensor R_{is} can be written as

$$R_{is} = \frac{1}{V}\sum_{\alpha,\beta}\frac{\langle 0|H_{ER}(\omega_s)|\beta\rangle\langle\beta|H_{EP}|\alpha\rangle\langle\alpha|H_{ER}(\omega_i)|0\rangle}{(\omega_\beta + \omega_q - \omega_i)(\omega_\alpha - \omega_i)} + C \qquad (2.76)$$

where V is the crystal volume. In most cases the constant C is much smaller than the resonant term and can be neglected. $\langle 0|H_{ER}(\omega_s)|\beta\rangle$ and $\langle\alpha|H_{EP}|0\rangle$ are known as the p-matrix elements and information on $\langle\beta|H_{EP}|\alpha\rangle$ can be obtained by the deformation potential scattering. The electron-phonon interaction $\langle\beta|H_{EP}|\alpha\rangle$ is reprented by

$$\langle\beta|H_{EP}|\alpha\rangle = \Xi^{ij}_{\alpha\beta}\bar{S}_{ij} \qquad (2.77)$$

where $\Xi^{ij}_{\alpha\beta}$ is the matrix element of the deformation potential, and i and j refer to the coordinates axis (x, y and Z) and $\bar{S}_{ij}$ is the strain tensor. The Brillouin scattering cross section σ_B has the form

$$\sigma_B \propto \left(\frac{e}{\hbar mc}\right)^2 \frac{\Phi}{2\rho v_\mu^2}\frac{\omega_s}{\omega_i}|R_{is}|^2, \qquad (2.78)$$

where the energy density Φ can be replaced by k_BT in the case of Brillouin scattering by thermal phonons. v_μ is the sound velocity in acoustic mode μ. The dominant term in eq.(2.74) (=eq.(2.76)) can be written as

$$R_{is} = \frac{1}{V}\sum_{\alpha,\beta}\frac{P_{0\beta}\Xi_{\beta\alpha}P_{\alpha 0}}{(\omega_\beta - \omega_s)(\omega_\alpha - \omega_i)}, \quad \omega_s = \omega_i \pm \omega_q \qquad (2.79)$$

where $\Xi_{\beta\alpha}$ is the matrix element of deformation potential scattering and $P_{0\beta}$ and $P_{\alpha 0}$ are the appropriate momentum matrix elements, where subscript α and β stand for single electron hole pair states. The mechanism of the light scattering can be described from a phenomenological aspect as follows:

a photon incident on a crystal in a ground state $|0\rangle$ creates a virtual intermediate electron hole pair in a state $|\alpha\rangle$, the electron or the hole of the state $|\alpha\rangle$ will be scattered to a state $|\beta\rangle$ by phonon via deformation potential, and finally the electron and hole in the state $|\beta\rangle$ recombine to emit a scattered photon (return to the ground state $|0\rangle$). The scattering efficiency is expected to resonate when the incident or the scattered photon energy approaches one of the resonance energies ($\hbar\omega_\alpha$ or $\hbar\omega_\beta$).

Loudon[49] has constructed the theory assuming the intermediate state as non-interacting electron hole pair states. It is usually a good approximation to assume that the band edge in semiconductor is parabolic in k space, i.e.,

$$\omega_\alpha(k) = \omega_{g\alpha}(0) + \hbar^2k^2/2\mu \tag{2.80}$$

$$\omega_\beta(k) = \omega_{g\beta}(0) + \hbar^2k^2/2\mu \tag{2.81}$$

where μ is the reduced effctive mass, which is assumed to be equal for the $|\alpha\rangle$ and $|\beta\rangle$ pair states for simplicity, $\hbar\omega_{g\alpha}(0)$ and $\hbar\omega_{g\beta}(0)$ are the optical band gaps at $k = 0$ for pair states α and β corresponding to the incident and scattered light, respectively. Then with prescription

$$\frac{1}{V}\sum_k \longrightarrow \frac{2}{(2\pi)^2}\int_0^{k_{max}} k^2dk \tag{2.82}$$

Equation (2.79) can be written as

$$R_{is} = \frac{2P_{0\beta}\Xi_{\beta\alpha}P_{\alpha 0}}{(2\pi)^2}\int_0^{k_{max}} \frac{k^2dk}{(\omega_{g\beta} + \frac{\hbar k^2}{2\mu} - \omega_i + \omega_q)(\omega_{g\alpha} + \frac{\hbar k^2}{2\mu} - \omega_i)} \tag{2.83}$$

where the momentum matrix element P and deformation potential Ξ-matrix elements are assumed to be independent of k. The integral eq.(2.83) can be performed from $k = 0$ to k_{max}. One obtains the following results.[30]

$$R_{is} = \frac{2}{(2\pi)^2}\left(\frac{2\pi}{\hbar}\right)^{3/2} \frac{P_{0\beta}\Xi_{\beta\alpha}P_{\alpha 0}}{\omega_{g\beta} - \omega_{g\alpha} + \omega_q}\left[(\omega_{g\beta} - \omega_s)^{1/2}\tan^{-1}\left(\frac{\Delta\omega_{g\beta}}{\omega_{g\beta} - \omega_s}\right)^{1/2}\right.$$

$$\left. - (\omega_{g\alpha} - \omega_i)^{1/2}\tan^{-1}\left(\frac{\Delta\omega_{g\alpha}}{\omega_{g\alpha} - \omega_i}\right)^{1/2}\right] , \qquad (2.84)$$

where $\hbar\Delta\omega_\alpha$ (or $\hbar\Delta\omega_\beta$) is the combined width of the conduction and valence bands, which is given by

$$\Delta\omega_{g\alpha} = \Delta\omega_{g\beta} = \hbar k_{max}^2 \quad . \qquad (2.85)$$

In the limit when $k_{max} \to \infty$, then one obtains the well-known expression

$$R_{is} = \frac{2}{(2\pi)^2} \frac{P_{0\beta}\Xi_{\beta\alpha}P_{\alpha 0}}{\omega_{g\beta} - \omega_{g\alpha} + \omega_q}\left[(\omega_{g\beta} - \omega_s)^{1/2} - (\omega_{g\alpha} - \omega_i)^{1/2}\right] \qquad (2.86)$$

with

$$\mathrm{Re.}(R_{is}) = \frac{2}{(2\pi)^2} \frac{P_{0\beta}\Xi_{\beta\alpha}P_{\alpha 0}}{\omega_{g\beta} - \omega_{g\alpha} + \omega_q} \times$$

$$\left[|\omega_{g\beta} - \omega_s|^{1/2}\theta(\omega_{g\beta} - \omega_s) - |\omega_{g\alpha} - \omega_i|^{1/2}\theta(\omega_{g\alpha} - \omega_i)\right] \qquad (2.87)$$

and

$$\mathrm{Im.}(R_{is}) = \frac{2}{(2\pi)^2} \frac{P_{0\beta}\Xi_{\beta\alpha}P_{\alpha 0}}{\omega_{g\beta} - \omega_{g\alpha} + \omega_q} \times$$

$$\left[|\omega_{g\beta} - \omega_s|^{1/2}\theta(\omega_s - \omega_{g\beta}) - |\omega_{g\alpha} - \omega_i|^{1/2}\theta(\omega_i - \omega_{g\alpha})\right] \qquad (2.88)$$

where $\theta(z)$ is the step function.

If $\omega_{g\alpha}$ is equal to $\omega_{g\beta}$, eq.(2.86) reduces to the simple form (two band model) as

$$R_{is} = \frac{2}{(2\pi)^2} P_{0\alpha}\Xi_{\alpha\alpha}P_{\alpha 0} \cdot (\omega_{g\alpha} - \omega_i)^{-1/2} \qquad (2.89)$$

with

$$\mathrm{Re.}(R_{is}) = \frac{2}{(2\pi)^2} P_{0\alpha}\Xi_{\alpha\alpha}P_{\alpha 0}|\omega_{g\alpha} - \omega_i|^{-1/2}\theta(\omega_{g\alpha} - \omega_i) \qquad (2.90)$$

and

$$\mathrm{Im.}(R_{is}) = \frac{2}{(2\pi)^2} P_{0\alpha}\Xi_{\alpha\alpha}P_{\alpha 0}|\omega_{g\alpha} - \omega_i|^{-1/2}\theta(-\omega_{g\alpha} + \omega_i) \qquad (2.91)$$

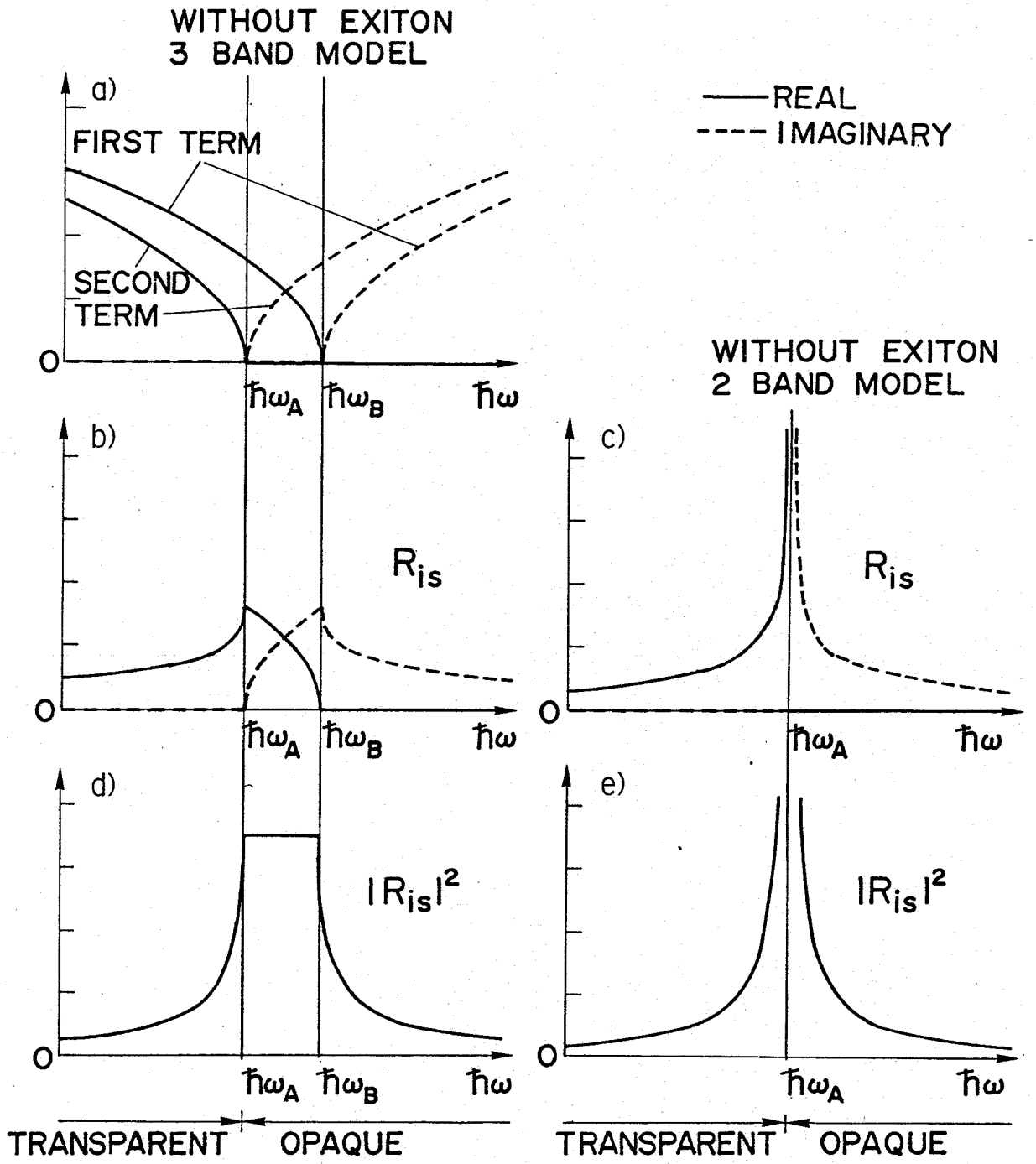

Fig. 2-5. a) Real and imaginary part of the first and second term of Brillouin tensor R_{is} (eq.(2.86)). b),c) Frequency dependence of the Brillouin tensor R_{is} calculated for real(solid line) and imaginary(dashed line) part for three band(eq.(2.86)) and two band (eq.(2.89)) process. d),e) Frequency dependence of the squared modulus of Brillouin tensor $|R_{is}|^2$ for three and two band process. ω is the incident frequency, ω_A and ω_B are the gap frequency.

The ω_i-dependence of the real and imaginary parts of the Brillouin tensor and the scattering amplitude are illustrated graphically in Fig. 2-5. The squared modulus $|R_{is}|^2$ which shows the essential spectral dependence of the scattering cross section is also represented there. Inspection of eqs.(2.86) and (2.89) shows at once two important propaerties of the Brillouin tensor, calculated for non-interacting electron-hole pairs: a) $|R_{is}|^2$ as function of ω is symmetric with respect to the frequency $\frac{1}{2}(\omega_A + \omega_B)$ (ω_A for the two band case). Fig. 2-5 d) and e) show graphically this symmetry; R_{is} is real for $\omega < \omega_A$ expressing the fact that only virtual electronic process can take place in that frequency region. R_{is} is pure imaginary for $\omega > \omega_B$ and reflects the fact that ingoing and outgoing photons are resonance with electronic states. For $\omega_A < \omega < \omega_B$, R_{is} is in general complex. In other word, the imaginary part of the Brillouin tensor reflects the density of states. The above result disagrees with that of Jain and Choudhury [62] who obviously omitted the imaginary part of the Brillouin (Raman) tensor.

2.3.2 Brillouin Tensor for Electron-Hole Pairs with Coulomb Interaction

In the following we consider the first-order Brillouin scatteing process and that the virtual intermediate states are assumed to be Wannier-Mott exciton,[57] and polariton picture is not introduced in the calculation for simplicity. The first step is to write the total Hamiltonian for a bounded crystal. The Hamiltonial consists of free photon, exciton, and phonon fields plus the bilinear exciton-photon and trilinear excion-phonon couplings.[50]

The total Hamiltonian H can be split into a polariton part H^{Pol}, a (harmonic) phonon part H^L, and exciton-phonon interaction H':

$$H = H^{Pol} + H^L + H', \tag{2.92}$$

$$H^{Pol} = \sum_{\vec{k},\gamma} \hbar c|\vec{k}| (\hat{a}^{\dagger}_{\vec{k}\gamma} \hat{a}_{\vec{k}\gamma} + \frac{1}{2}) + \sum_{i} \hbar\omega_i (\hat{b}^{\dagger}_i \hat{b}_i + \frac{1}{2})$$

$$+ i \sum_{i,\vec{k},\gamma} g_{i,\vec{k}\gamma} \left(\frac{2\pi\hbar\omega_i}{c|\vec{k}|}\right)^{1/2} \hat{b}_i (\hat{a}^{\dagger}_{\vec{k}\gamma} + \hat{a}_{-\vec{k}\gamma}) + c.c.$$

$$+ \sum_{\vec{k},\gamma} \frac{\omega_p^2}{|\vec{k}|} \frac{\hbar}{4c} (\hat{a}^{\dagger}_{\vec{k}\gamma} + \hat{a}_{-\vec{k}\gamma})(\hat{a}^{\dagger}_{-\vec{k}\gamma} + \hat{a}_{\vec{k}\gamma}), \tag{2.93}$$

$$H^{L} = \sum_{\vec{q}} \hbar\Omega(\vec{q}) \ (\hat{c}^{\dagger}_{\vec{q}} \hat{c}_{\vec{q}} + \frac{1}{2}), \tag{2.94}$$

$$H' = \sum_{i,j,\vec{q}} f_{ij}(\vec{q}) \hat{b}^{\dagger}_i \hat{b}_j \hat{c}^{\dagger}_{\vec{q}} + c.c. \tag{2.95}$$

$\hat{a}^{\dagger}_{\vec{k}\gamma}$, $\hat{b}^{\dagger}_i$, $\hat{c}^{\dagger}_{\vec{q}}$ are creation operators for photon, excition, and phonon, respectively. $\vec{k}$ denotes the momentum of photon and γ a polarization lebel; i and $\vec{q}$ are quantum labels which characterize the exciton and phonon states for a bound crystal, respectively. The exciton label i consists of quantum numbers for the relative and center-of-mass of the exciton as well as band indices for the electron and hole band. In eq.(2.93), $g_{i,\vec{k}}$ is the bilinear exciton-photon coupling coefficient, which can be expressed as matrix element $\langle i|\vec{A}_{\vec{k}} \cdot \vec{p}|0\rangle$, where $|i\rangle$ is the exciton state; $|0\rangle$ is the ground state, with no exciton present; $\vec{A}_{\vec{k}}$ is the vector potential for photon $\vec{k}$; $\vec{p}$ is the relevant momentum operator. We shall implicitly assume that the optical transition $0 \to i$ is dipole allowed; $f_{ij}(q)$ is the exciton-phonon coupling coefficient. We now turn to the polariton Hamiltonian and its eigenstates. H^{Pol} is a bilinear form in the photon and exciton operators, and can be therefore be diagonalized by a linear transformation to give

$$H^{Pol} = \sum_{\vec{k}_0\gamma} \hbar c|\vec{k}_0| \hat{B}^{\dagger}_{k_0\gamma} \hat{B}_{k_0\gamma} \ . \tag{2.96}$$

The vacuum state $|0\rangle$ of H^{Pol} is defined by $\hat{B}_{\vec{k}\gamma}|0\rangle = 0$ for all $\vec{k}_0$ and γ. Note that we use label $k_0^{\rightarrow}$ of the external photon to label the polariton state. We shall discuss this more fully below, and also later for the scattering cross section we shall need to specify asmptotic "incoming" and "outgoing" photon state and we shall then affix "in" and "out" to the $\hat{B}^{\dagger}$ and $\hat{B}$ operators. The operators $\hat{B}$ are linear combinations of the $\hat{a}$ (operator for photon) and $\hat{b}$ (operator for phonon). It is convenient for the following to begin with linear combination of the $\hat{a}$ and $\hat{b}$ operators which correspond to the classical field and momentum variable:

$$A_{\vec{k}\gamma} = \frac{\hat{a}^{\dagger}_{\vec{k}\gamma} + \hat{a}_{-\vec{k}\gamma}}{(c|\vec{k}|)^{1/2}}, \qquad \hat{P}_{\vec{k}\gamma} = i(c|\vec{k}|)^{1/2}(\hat{a}^{\dagger}_{\vec{k}\gamma} - \hat{a}_{-\vec{k}\gamma}), \tag{2.97}$$

$$\hat{\alpha}_i = \frac{\hat{b}_i + \hat{b}_i^{\dagger}}{(\omega_i)^{1/2}}, \qquad \hat{\Pi}_i = i(\omega_i)^{1/2}(\hat{b}_i^{\dagger} - \hat{b}_i). \tag{2.98}$$

In terms of these auxiliary operators, we write the $\hat{B}^{\dagger}$ operator as

$$\hat{B}^{\dagger}_{\vec{k}_0\gamma} = \sum_{\vec{k}\gamma'} (A^{\vec{k}_0\gamma}_{\vec{k}'\gamma'} \hat{A}_{\vec{k}'\gamma'} + P^{\vec{k}_0\gamma}_{\vec{k}'\gamma'} \hat{P}_{\vec{k}'\gamma'}) + \sum_i (\alpha_i^{\vec{k}_0\gamma} \hat{\alpha}_i + \Pi_i^{\vec{k}_0\gamma} \hat{\Pi}_i), \tag{2.99}$$

and likewise for Hamailtonian adjoint. Scalar amplitude are written everywhere without caret, the corresponding operators are written with caret. To find the correct linear combinations eq.(2.99) the equation of motion is used.

$$i\hbar \dot{\hat{B}}^{\dagger}_{\vec{k}\gamma} = [\hat{B}^{\dagger}_{\vec{k}_0\gamma}, H^{Pol}] = \hbar c|\vec{k}_0| \hat{B}^{\dagger}_{\vec{k}_0\gamma} = \hbar\omega \hat{B}^{\dagger}_{\vec{k}_0\gamma} \tag{2.100}$$

This can be written as a system of equation for the scalar amplitudes

$$i\omega_i^2 \Pi_i - \omega\alpha_i = 0, \tag{2.101}$$

$$-i\omega P_{k',\gamma'} + A_{\vec{k}',\gamma'} = 0 \tag{2.102}$$

$$(\omega_i - \omega^2)\alpha_i = 2i \frac{\omega_i^2}{\omega} \left(\frac{2\pi}{\hbar}\right)^{1/2} \sum_{\vec{k}',\gamma'} g_{i,\vec{k}',\gamma'} A_{\vec{k}',\gamma'} \quad , \tag{2.103}$$

$$(-\omega^2 + c^2 k'^2 + \omega_p^2) A_{\vec{k}',\gamma'} = -2i\omega \left(\frac{2\pi}{\hbar}\right)^{1/2} \sum_i g_{i,-\vec{k}'} \alpha_i \quad . \tag{2.104}$$

Inserting eq. (2.103) into eq. (2.104) gives

$$\{-\omega^2 + c^2 k^2 + \omega_p^2\} A_{\vec{k}\gamma} = \frac{8\pi}{\hbar} \times \sum_{i,\vec{k}',\gamma'} \frac{g_{i,-\vec{k}',\gamma'} g_{i,\vec{k}',\gamma'}}{\omega_i^2 - \omega^2} \omega_i^2 A_{\vec{k}',\gamma'} \tag{2.105}$$

For simplicity we drop the subscript $(k_0\gamma)$ on $A^{\vec{k}}_{\vec{k}',\gamma'}$, $P^{\vec{k}}_{\vec{k}',\gamma'}$, $\alpha_i^{\vec{k}}$, and $\Pi^{\vec{k}}$ defined from eq. (2.99). The quantum label i for the exciton can be decomposed into two labels λ and s which are quantum exciton wave function is a product of a wave function for the center-of-mass motion $\Psi_s(\vec{r})$ and a wave function for the relative motion.

Now we specialize to the case of no spectral dispersion, which means in particular neglect of the dependence of the exciton frequency $\omega_i \equiv \omega_{\lambda,s}$ upon the center-of-mass quantum number s, and also neglect s dependence in any matrix elements. This will permit us to evaluate the sums over $i \equiv (\lambda,s)$ in eq. (2.105) and so obtain simplified expressions. In the case of infinite crystals s stands for the momentum $\vec{k}$, $\Psi_s(\vec{r})$ is simply a plane wave and the coupling function has well known from

$$g_{\lambda\vec{k},\vec{k}',\gamma'} = g_\lambda^{\gamma'} \delta_{k,k'} \quad . \tag{2.106}$$

In the case of a bound medium, the coupling function $g_{\lambda s,\vec{k}}$, can be caluculated by expanding $\Psi_s(\vec{r})$ in pla ne waves and using eq. (2.106). The result is

$$g_{\lambda s,\vec{k}',\gamma'} = g_\lambda^{\gamma'} \Psi_s(\vec{k}) \quad , \tag{2.107}$$

where $\Psi_s(\vec{k})$ is the Fourier transform of $\Psi_s(\vec{r})$. Using the f sum rule

$$\omega_p^2 = \frac{8\pi}{\hbar} \sum_\lambda |g_\lambda^{\gamma'}| \tag{2.108}$$

which permit us to eliminate ω_p^2 in the left-hand side of eq. (2.105). Next we use the completeness of the set of $\Psi_s(\vec{r})$ which states

$$\sum_s \Psi_s^*(\vec{r})\Psi_s(\vec{r}') = \begin{cases} \delta(\vec{r}-\vec{r}'), & \text{if both arguments are in} \\ & \text{the crystal region;} \\ 0 \quad , & \text{otherwise} \end{cases} \tag{2.109}$$

Then the Fourier transform of eq.(2.105) can be written

$$(-\omega^2 - c^2\nabla^2)A_\gamma(\vec{r}) = 4\pi\omega^2 \int d\vec{r}\chi(\vec{r},\vec{r}')A_\gamma(\vec{r}') \tag{2.110}$$

which is Maxwell's equation for $\vec{A}(\vec{r})$ in a medium with

$$\delta(\vec{r},\vec{r}') = \begin{cases} \delta(\vec{r},\vec{r}')\frac{2}{\hbar}\sum_\lambda \frac{|g_\lambda^\gamma|^2}{\omega_\lambda^2 - (\omega \pm i\eta)^2} \quad , & \text{if the both} \\ & \text{arguments are in the crystal region;} \\ 0 \ , & \text{otherwise.} \end{cases} \tag{2.111}$$

It is clear from eqs. (2.110) and (2.111) that this case the integro-differential equation (2.110) needs to be solved subject to specifying asmptotic conditions on the homogeneous equation (right-hand side zero), which physically corresponds to vanishing exciton-photon coupling coefficient, i.e., $g_\lambda^\gamma=0$. For this reason, $\pm i\eta$ is put in the denominator in eq. (2.111), with η a real positive infinitesimal quantity. The positive sign (negative sign) in front of $i\eta$ corresponds to "out" ("in") boundary conditions. The polarition operators $\hat{B}^\dagger_{\vec{k}_0\gamma}$ and $\hat{B}_{\vec{k}_0\gamma}$ can correspondingly be labeled with "in" and "out" to regulate the asmptotic photon solution as either incoming or outgoing .

Summarizing, we have solved Maxwell's equation eq. (2.110) with susceptibility equation eq.(2.111) via diagonalizing $H^{Pol.}$ Once $A(\vec{r})$ is known the other amplitudes can be determined from eqs. (2.103) and (.104). Equation (2.103) gives, in particular,

$$\alpha(\vec{r}) = \frac{2i}{\omega}\left(\frac{2\pi}{\hbar}\right)^{1/2} \sum_{\gamma} \frac{\omega_\lambda^2 \, g_\lambda^\gamma}{\omega_\lambda^2 - (\omega \pm i\eta)^2} \vec{A}_\lambda(r), \tag{2.112}$$

if $\vec{r}$ is in the crystal region and 0 otherwise.

The differential cross section per unit volume, per unit scattered frequency interval for scattering of a photon with wave vector $\vec{k}_0$ into a photon with wave vector $\vec{k}_0'$ exciting a phonon $\vec{q}$ in the crystal is[63]

$$\frac{d^2\sigma}{d\Omega d\omega'} = \left(\frac{k_0'}{2\pi\hbar c}\right)^2 \sum_{\vec{q}} \delta[\omega - \omega' - \Omega(\vec{q})] \times \left| T_{\vec{k}_0, \gamma, \vec{q}, \vec{k}_0 \gamma}(\omega + i\eta) \right|^2, \tag{2.113}$$

with

$$T_{k_0' \gamma' \vec{q} \; k_0 \gamma}(\omega + i\eta) = \langle \bar{0} | \hat{a}_{\vec{k}_0', \gamma'} \hat{c}_{\vec{q}} \times T^{H^{PE}, H'}(\omega + i\eta) \hat{a}^\dagger_{\vec{k}_0 \gamma} | \bar{0} \rangle \; . \tag{2.114}$$

H^{PE} is the photon-exciton interaction in the polariton Hamiltonian eq. (2.93) and $|0\rangle$ is the product of the free photon, exciton, and phonon vacuum states. The T operator is

$$T^{H^{PE}, H'}(\omega + i\eta) = (H^{PE} + H') + (H^{PE} + H') \frac{1}{\hbar(\omega + i\eta) - H} (H^{PE} + H') \tag{2.115}$$

The T operator in eq. (2.115) describes the scattering of photons by two potentials H^{PE} and H'. Equation (2.115) can be written as follows by using an operator indicating which can be established after some algebra

$$\begin{aligned} T^{H^{PE}, H'}(z) = {} & H^{PE} \frac{1}{z - H + H'} (z - H + H' + H^{PE}) \\ & + (1 + H^{PE} \frac{1}{z - H + H'}) T^{H'}(z) \\ & (1 + \frac{1}{z - H + H'} H^{PE}) \; . \end{aligned} \tag{2.116}$$

The operator in parentheses in the second term when applied as in eq.(2.114) will permit us to introduce new states. The application of this operator to the ket $a^\dagger_{\vec{k}_0} |0\rangle$ will produce a new state which we call $|\phi_{\vec{k}_0}\rangle$, which can be labeled by the "in" and "out" labels. This state can be identified as an

eigen state of H^{Pol}. Thus let the new state be[64)]

$$|\phi^{out}_{\vec{k}_0\gamma}\rangle = (1+\frac{1}{\hbar(\omega+i\eta)-H^{Pol}}H^{PE})\hat{a}^{\dagger}_{\vec{k}_0\gamma}|\bar{0}\rangle \ ,$$
$$|\phi^{in}_{\vec{k}_0\gamma}\rangle = (1+\frac{1}{\hbar(\omega-i\eta)-H^{Pol}}H^{PE})\hat{a}^{\dagger}_{\vec{k}_0\gamma}|\bar{0}\rangle \ . \qquad (2.117)$$

For vanishing exciton-photon coupling equation (2.117) reduces to a photon plane wave. Choosing the plus (+) or minus (-) sign with ($i\eta$) in eq.(2.117) produces "out" or "in" going scattered waves. For vanishing exciton-photon coupling $\alpha = 0$ and the $\hat{B}^{\dagger}_{\vec{k}\gamma}$ operator reduces to $\hat{A}^{\dagger}_{\vec{k}_0\gamma}$. Depending on chose of $\pm i\eta$ in eq. (2.111), these operators become the $B^{\dagger out}_{\vec{k}_0\gamma}$ and correspondingly the "in" operators which describe "out" and "in" scattered waves.

However a solution of the Schrödinger equation which describes scattering of a particle in a potential is uniquely determined by the incident wave vector of the particle (here photon) and the asymptotic behaviour. Thus they are identified

$$|\phi^{out}_{\vec{k}_0\gamma}\rangle \equiv \hat{B}^{\dagger out}_{\vec{k}_0\gamma}|0\rangle \qquad (2.118)$$
$$|\phi^{in}_{\vec{k}_0\gamma}\rangle \equiv \hat{B}^{\dagger in}_{\vec{k}_0\gamma}|0\rangle \ . \qquad (2.119)$$

This important step permits us to rewrite the original transition matrix element between bare photons as a matrix element between appropriate polariton states. Then eq. (2.114) becomes

$$T_{\vec{k}_0\gamma,\vec{q},\vec{k}_0\gamma} = \langle 0|\hat{B}^{in}_{\vec{k}_0\gamma}, \hat{c}_{\vec{q}}\, H, \hat{B}^{\dagger out}_{\vec{k}_0\gamma}|0\rangle = \sum_{ij} f_{ij}(\vec{q})\langle 0|\hat{B}^{in}_{\vec{k}_0\gamma}, \hat{b}^{\dagger}_i\hat{b}_j\hat{B}^{\dagger out}_{\vec{k}_0\gamma}|0\rangle$$
$$= \sum_{ij} f_{ij}(\vec{q})\{\langle 0|[\hat{B}^{in}_{\vec{k}_0\gamma}, b^{\dagger}_i][\hat{b}_j, B^{\dagger out}_{\vec{k}_0\gamma}] + [B^{in}_{\vec{k}_0\gamma}, \hat{b}_j][\hat{b}^{\dagger}_i, B^{\dagger out}_{\vec{k}_0\gamma}]|0\rangle \ , \qquad (2.120)$$

and using eq.(2.112) this becomes

$$T_{\vec{k}_0\gamma',\vec{q}\,\vec{k}_0} = \sum_{ij} (\alpha_i^{\vec{k}_0'\gamma'})^{*in} (\alpha_j^{\vec{k}_0\gamma})^{out} \times \frac{f_{ij}(\vec{q})(\omega_i+\omega')(\omega_j+\omega) + f_{ij}(\vec{q})(\omega-\omega_j)(\omega'-\omega_i)}{\omega_i^{3/2}\omega_j^{3/2}}, \quad (2.120)$$

If we trnasform the $\vec{k}$ label in $i \equiv (\lambda,\vec{k})$ into $\vec{r}$ space, eq.(2.120) becomes

$$\frac{d^2\sigma}{d\Omega d\omega'} = k_0 k_0'^3 \sum_{\vec{q}} \delta[\omega-\omega'-\Omega(\vec{q})] \Big| \sum_{\gamma\gamma'} R_{\gamma\gamma'}(\vec{q},\omega) S_{\gamma\gamma'}(\vec{q}) \Big|^2 , \quad (2.122)$$

$$R_{\gamma\gamma'}(\vec{q},\omega) = \sum_{\lambda\lambda'} \frac{\omega_\lambda^{1/2} g_\lambda^\gamma f_{\lambda\lambda'}(\vec{q}) g_\lambda^{\gamma'*} \omega_{\lambda'}^{1/2}}{\omega\,\omega'} \times \left(\frac{1}{[\hbar\omega_\lambda - \hbar(\omega+i\eta)][\hbar\omega_{\lambda'} - \hbar(\omega'+i\eta)]} + \frac{1}{[\hbar\omega_\lambda + \hbar(\omega+i\eta)][\hbar\omega_{\lambda'} + \hbar(\omega'+i\eta)]} \right), \quad (2.123)$$

$$S_{\gamma\gamma'}(\vec{q}) = \int_C d\vec{r}\; e^{-i\vec{q}\cdot\vec{r}} A^{\vec{k}_0'\gamma',in*}(\vec{r})\, A^{\vec{k}_0\gamma,out}(\vec{r}). \quad (2.124)$$

The vector potential A in eq. (2.124) is determined by Maxwell's equation eq. (2.110) and the condition that outside the crystal the incident or scattered wave $\vec{k}$ taken to be unit amplitude. The prefactor in eq. (2.122) is calculated using this boundary condition. The letter C in eq. (2.124) means that the r integral runs only over the crystal. One obtains the scattering efficiency {dimension [1/(length times frequency)]} from the cross section $d^2\sigma/d\Omega d\omega'$ [dimension (length squared/frequency)] by calculating the latter for unit volume.

Next we consider a simple insulator and we limit ourselves to one valence and one conduction band and the corresponding discrete and continuous exciton state. The bands are assumed to be parabolic and the band masses

negative and positive for the valence and conduction band, respectively. The quantum number λ is then determined by the internal exciton momentum $\vec{k}$ and a discrete variable $n = 1$, The oscillator strength g_λ^γ is [65]

$$g_\lambda^\gamma = (e/m)\langle P_\gamma \rangle (\omega_\lambda)^{-1/2} \psi_\lambda(0) \ , \tag{2.125}$$

$$\langle P_\lambda \rangle = \int d\vec{r} \phi_v^*(\vec{r}) P_\gamma \phi_c(\vec{r}) \tag{2.126}$$

where ϕ is a Bloch function at the zero center. The momentum matrix element is assumed to be nonzero. For free electron-hole pairs

$$|\psi_{\vec{k}}(0)|^2 = 1 \ , \tag{2.127}$$

while for Coulomb correlated pairs

$$|\psi_n(0)|^2 = \frac{1}{\pi r^3 n^3} \ , \quad |\psi_{\vec{k}}(0)|^2 = \frac{\pi}{r_0|\vec{k}|} \frac{e^{\pi/r_0|\vec{k}|}}{\sinh(\pi/r_0|\vec{k}|)} \tag{2.128}$$

where r_0 is the 1s exciton radius. The Brillouin tensor for correlated electron-hole pairs becomes

$$R_{\gamma\gamma'}(\omega) = \left(\frac{r_0}{V}\right)^{1/2} \frac{e^2 \langle P_\gamma \rangle \langle P_{\gamma'} \rangle^* (C_{cc} - C_{vv})}{\omega \omega' m^2}$$

$$\times \left(\sum_{n=1}^{\infty} \frac{1}{\pi r^3 n^3} \frac{1}{[\hbar(\omega + i\eta) + E_B/n^2 - E_g][\hbar(\omega' + i\eta) + E_B/n^2 - E_g]} \right.$$

$$\left. \frac{1}{2\pi r_0} \int_0^\infty dk k \frac{e^{\pi/r_0|\vec{k}|}/\sinh(\pi/r_0|\vec{k}|)}{[\hbar(\omega + i\eta) - \hbar^2 k^2/2\mu - E_g][\hbar(\omega' + i\eta) - \hbar^2 k^2/2\mu - E_g]} \right) . \tag{2.129}$$

Here E_B is the exciton binding energy $\hbar^2/2\mu r_0^2$ of the 1s exciton, μ is the reduced mass. In eq. (2.129), the first term is the contribution from descrete exciton levels and the second term is the contribution from continuum exciton levels. Writing the numerator in the more symmetric way as follows:

$$e^{\pi/r_0|\vec{k}|}/\sinh(\pi/r_0|\vec{k}|)$$

$$= 1 + \coth(\pi/r_0|\vec{k}|)$$

$$= 1 + \coth(\pi/\sqrt{E_B/E_k}) \qquad (2.130)$$

By using these relation one obtains

$$R^{\text{cont.}}_{\gamma\gamma'}(\omega) = \frac{A}{2\pi r_0}\int_0^\infty kdk \frac{1+\coth(\pi\sqrt{E_B/E_k})}{[\hbar(\omega+i\eta) - E_k - E_g][\hbar(\omega'+i\eta) - E_k - E_g]} \quad . \qquad (2.131)$$

where $E_k = \hbar^2k^2/2\mu$, A is the prefactor appeared in eq.(2.129). The integral in eq.(2.131) can be splitted into two parts in accordance with the numerator $1+\coth(\pi\sqrt{E_B/E_k})$. Here the complete integration in the second term is performed by contour integration in the complex E_k plane.[59] The first integration is trivial. The second integral can be performed by contour integration in the complex plane as shown in Fig. 2-6. There are

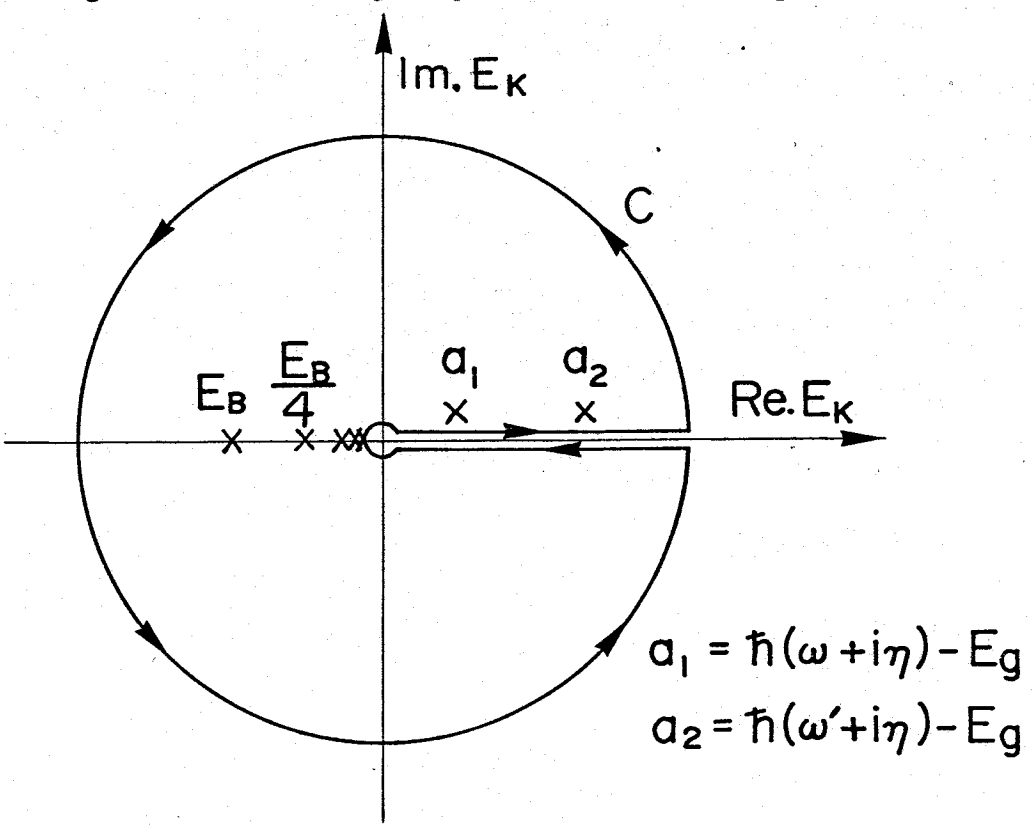

Fig. 2-6. Contour for the evaluation of eq.(2.131)

single poles at $E_k = a_1 = \hbar(\omega + i\eta) - E_g, E_k = a_2 = \hbar(\omega' + i\eta) - E_g$ and at the singularities of $E_k = -E_B/n^2$ ($n = 1, 2, 3, \cdots$) arising from $\coth(\pi\sqrt{E_B/E_k})$

Using the formula

$$\coth(\pi\sqrt{E_B/E_k}) = \frac{1}{\pi}\sqrt{\frac{E_k}{E_B}}\left(1 + 2\sum_{n=1}^{\infty}\frac{1}{n^2}\frac{1}{E_k + \frac{E_B}{n^2}}\right) \tag{2.132}$$

one obtains

$$R_{\gamma\gamma'}^{\text{cont.}}(\omega) = \frac{A}{4E_B\hbar\omega_q}\left[\ln\left|\frac{\hbar(\omega + i\eta) - E_g}{\hbar(\omega' + i\eta) - E_g}\right|\right.$$

$$+ i\{\tan^{-1}[(\hbar\omega - E_g)/\hbar\eta] - \tan^{-1}[(\hbar\omega' - E_g)/\hbar\eta]\}$$

$$+\pi i\left\{\coth\left(\pi\sqrt{\frac{E_B}{\hbar(\omega + i\eta) - E_g}}\right) - \coth\left(\pi\sqrt{\frac{E_B}{\hbar(\omega' + i\eta) - E_g}}\right)\right\}$$

$$\left. - \frac{1}{2}\sum_{n=1}^{\infty}\frac{1}{n^3}\frac{1}{[\hbar(\omega + i\eta) + E_B/n^2 - E_g][\hbar(\omega' + i\eta) + E_B/n^2 - E_g]}\right] \tag{2.133}$$

Then eq.(2.129) can be extended to the case of three band process (one conduction band and two valence bands). By using eqs.(2.129) and (2.133)

$$R_{is} \equiv \frac{\omega\omega'}{4\pi a_0^2}\sum_{\gamma\gamma'} R_{\gamma\gamma'} = \sum_{\alpha,\beta}\left(\frac{a_0}{V}\right)^{1/2}\frac{e^2 P_{0\beta}\Xi_{\beta\alpha}P_{\alpha 0}}{4\, a_0^2 m}$$

$$\times\left[\left[\sum_{n=1}^{\infty}\frac{1}{n^3}\frac{1}{[\hbar(\omega_i + i\eta_D) + E_B/n^2 - E_{g\alpha}][\hbar(\omega_s + i\eta_D) + E_B/n^2 - E_{g\beta}]}\right.\right.$$

$$+ \frac{1}{4E_B(E_{g\beta} - E_{g\alpha} + \hbar\omega_q)}\left[\ln\left|\frac{\hbar(\omega_s + i\eta_C) - E_{g\beta}}{\hbar(\omega_i + i\eta_C) - E_{g\alpha}}\right|\right.$$

$$+ i\{\tan^{-1}[(\hbar\omega_i - E_{g\alpha})/\hbar\eta_C] - \tan^{-1}[(\hbar\omega_s - E_{g\beta})/\hbar\eta_C]\}$$

$$\left.\left. + i\pi\left\{\coth\left(\pi\sqrt{\frac{E_B}{\hbar(\omega_i + i\eta_C) - E_{g\alpha}}}\right) - \coth\left(\pi\sqrt{\frac{E_B}{\hbar(\omega_s + i\eta_C) - E_{g\beta}}}\right)\right\}\right]\right.$$

$$\left. - \sum_{n=1}^{\infty}\frac{1}{2n^3}\frac{1}{[\hbar(\omega_i + i\eta_C) + E_B/n^2 - E_{g\alpha}][\hbar(\omega_s + i\eta_D) + E_B/n^2 - E_{g\beta}]}\right] \tag{2.134}$$

In eq.(2.134) the first term corresponds to the n-th discrete exciton contribution and rest four terms correspond to the unbound continuum exciton contributions. $E_{g\alpha}(=\hbar\omega_{g\alpha})$ and $E_{g\beta}(=\hbar\omega_{g\beta})$ are optical energy gaps for incident and scattered light, respectively, η_D and η_C the phenomenological damping factor for the discrete and continuum exciton levels, respectively. The broadening effect removes the divergence at critical points in the Brillouin tensor. For simplicity we assume $\eta_D = \eta_C = \Gamma$ and no incident light frequency dependence in the present calculation. Detailed discussion about the damping factor (life time broadening effect) is presented in Capter 6.

In the limit $E_B \to 0$, which condition corresponds to the no Coulomb interaction (free exciton model), the hyperbolic contribution in eq.(2.134) yields for following expanssion given in eq. (2.137). Using the formula[66]

$$\coth z = \frac{1}{z} + \frac{z}{3} - \frac{z^3}{45} + \cdots , \tag{2.135}$$

with

$$\coth z \longrightarrow \frac{1}{z} \quad (\text{if } z \to 0) , \tag{2.136}$$

one obtains

$$\coth \pi \sqrt{\frac{E_B}{\hbar(\omega_i + i\eta) - E_{g\alpha}}} \xrightarrow{E_B \to 0} \frac{1}{\pi\sqrt{E_B}} [\hbar(\omega + i\eta) - E_{g\alpha}]^{1/2} , \tag{2.137}$$

and the other part of eq. (2.134) vanish asymptotically when $E_B \to 0$.

Using the above relation, eq. (2.134) reaches asymptotically the expression for the Brillouin tensor for free electron-hole pairs given in eq.(2.86). Inspection of eqs. (2.134) and (2.86) shows several important properties of the Brillouin tensor in the case of Coulomb interaction. Brillouin tensor is, in general, a complex function and consists of real and imaginary part and eq.(2.134) is expressed as follows:

$$R_{is} \equiv R_{is}^r + iR_{is}^i , \tag{2.138}$$

where r and i indicate real and imaginaly part of R_{is}, respectively. It is

convenient to decompose the discrete and continuum part of R_{is}^{r} and R_{is}^{i} as follows:

$$R_{is}^{r} = \text{Re.}\ (R_{is}^{\text{disc.}} + R_{is}^{\text{cont.}}) \ , \tag{2.139a}$$

$$R_{is}^{i} = \text{Im.}\ (R_{is}^{\text{disc.}} + R_{is}^{\text{cont.}}) \ . \tag{2.139b}$$

By using eq. (2.86) we have already presented the dispersion curves of R_{is} near the direct gap semiconductors in Fig. 2-5, based on the simplified 2- and 3- band model (one conduction band and two valence bands; $E_{g\alpha} = E_0$, $E_{g\beta} = E_0 + \Delta_0$, where Δ_0 is the separation of the valence bands). From Figs. 2-7 to 2-13, we shall discuss the dispersion of R_{is} where exciton effect is taken into account (with exciton case). Our numerical calculation of Figs. 2-7 to 2-13 using the formulas of Brillouin tensor was carried out on the HP 9825A desk-top computer. It may be worth nothing however that the numerical summation shows that the n sum rapidly converges; taking 10 terms is sufficient for an accuracy of 10^{-6}. The number of calculated points is 1400 (0.5 meV interval) and the total calculation time is about half an hour. The calculated data are stored in the memory and drawn by a plotter (WATANABE WX 4675 Type).

First of all, we compared the continuum part of R_{is} (with exciton) and R_{is} of no exciton case. The results are shown in Fig. 2-7. In Fig. 2-7, four different curves are calculated; a) real part of the continuum part of R_{is} in the case of the Coulomb interaction ($E_B = 28$ meV, $\Gamma = 0$ meV); b) imaginary part of the continuum part of R_{is} in the case of Coulomb interaction ($E_B = 28$ meV, $\Gamma = 0$ meV); c) real part of R_{is} in the case of no Coulomb interaction ($E_B = 0$ meV, $\Gamma = 0$ meV); d) imaginary part of R_{is} in the case of no Coulomb interaction ($E_B = 28$ meV, $\Gamma = 0$ meV). The effect of Coulomb interaction on Re. ($R_{is}^{\text{cont.}}$) consists mainly in the appearance of logarithmic singularities at $E = E_0$ and $E = E_0 + \Delta_0$. On the other hand the

imaginary part of $R_{is}^{cont.}$ shows dominant peak between the resonance energies. This result manifests that the contribution of the imaginary part of Brillouin tensor is important, especially in the region near the band gaps. On the contrary the real and imaginary part of the Brillouin tensor in the case of no exciton (curves c and d, respectively) shows mirror symmetry respect to $E = E_0 + (1/2)\Delta_0$. Figure 2-8 shows the calculated curves of the continuum part of R_{is} ($=R_{is}^{cont.}$) based on the three band process with three different broadening paramenters ($\Gamma = 0$ meV, 20 meV, and 40 meV). Below the band gap, real continuum part shows resonant enhancement. Above the gap, the real continuum part is the same order of magnitude as below but different sign. When the excited states have an infinite lifetime ($\Gamma = 0$meV), the real part of $R_{is}^{cont.}$ shows divergence at the band gap energies, while the imaginary part of $R_{is}^{cont.}$ is zero when the incident photon energy E is lower than that of E_0 , and nerly zero when the incident photon energy E is higher than that of $E_0 + \Delta_0$, and has positive non-zero value between E_0 and $E_0 + \Delta_0$. The broadening paramenters broaden the resonant features and decrease the intensity of R_{is}. In Figs. 2-9 and 2-10, we show the discrete part of R_{is} which was calcualted by using the first term of eq. (2.134). In Fig. 2-9, we show the real part of $R_{is}^{disc.}$, where we find divergence at ground state exciton energy (dashed curve) and narrow resonant peaks arising from higher order exciton states ($n \geq 2$). The damping parameters broaden the resonance feature. In Fig. 2-10, we show the imaginary part of $R_{is}^{disc.}$. It is important to point out that if the photon enegy is resonance with exciton state, real part of R_{is} is completely zero and imaginary part is infinite when $\Gamma=0$. The spectral positons of the infinite peaks correspond to the $n = 1$ and $n = 2$ exciton states. In Figs. 2-11 and 2-12, we show the real and imaginary part ot R_{is} which was calculated by using eq. (2.134). The discrete and continuum contribution add up constructively below the band gap leading

to a strongly increased Brillouin efficiency due to the Coulomb correlation. Above the gap the discrete and the real part of the continuum contribution have different sign and roughly of the same sign of magnitude. The resulting cancellation makes the total real part of R_{is} (Fig. 2-11) rather small in the continuum. This destructive interference is also discussed in ref. 55. Figure 2-12 also shows that the Coulomb correlation tends to diminish somewhat the imaginary part of the Brillouin tensor. In total as shown in Fig. 2-13, the Coulomb attraction between electron and hole causes strong asymmetry in the Brillouin efficiency $|R_{is}|^2$ with respect to the gap, a strong enhancement occurs at n=1 exciton state. These resonant features are in contrast to those shown in the case of no exciton, where the Brillouin scattering efficiency $|R_{is}|^2$ shows symmetric form with respect to the band gap.

The resonant cancellation can be explained by the following relation;

$$\sigma_B = C|R_{is} + R_0|^2 , \qquad (2.140)$$

in which C is the prefactor appering on the right-hand side of eq. (2.134), R_{is} is the resonant contribution given by eq. (2.134), arising from the M_0 critical point, and R_0 is a non-resonant contribution arising from the other far off critical points in the band structur. The resonant contribution R_{is} is opposite in sign to the nonresonant contribution R_0 in the longer-wavelength region. The resonant cancellation, therefore, occurs at a wavelength when $R_{is} + R_0 = 0$. The experimental results of resonant cancellation will be discussed in Chapter 5 and 6.

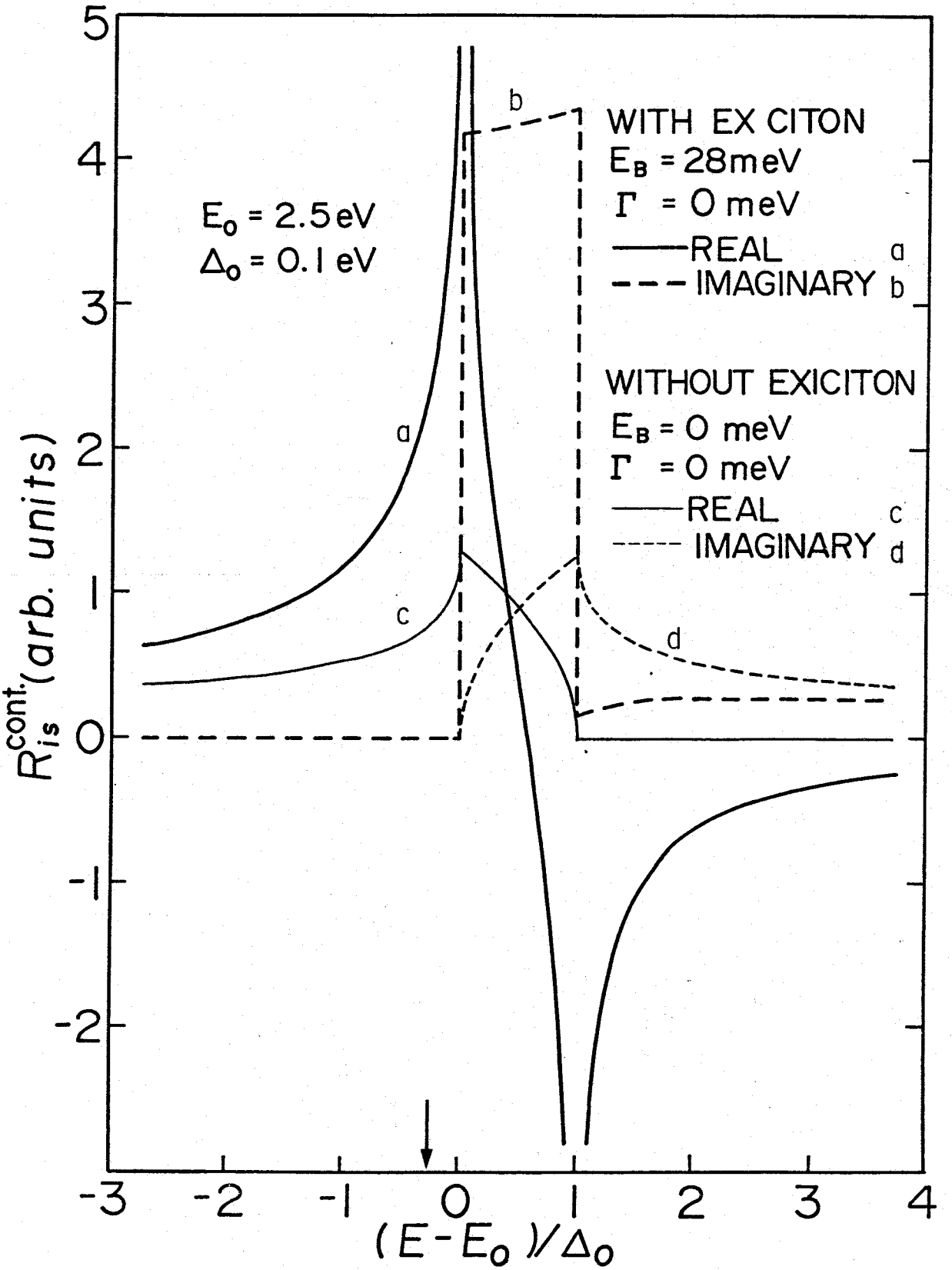

Fig. 2-7. Real and imaginary part of the continuum contribution of R_{is} for M_0 crytical point in the case of non-interacting (without exciton) and interacting (with exciton) electron-hole pairs. The vertical arrow indicates the position of the ground state exciton energy.

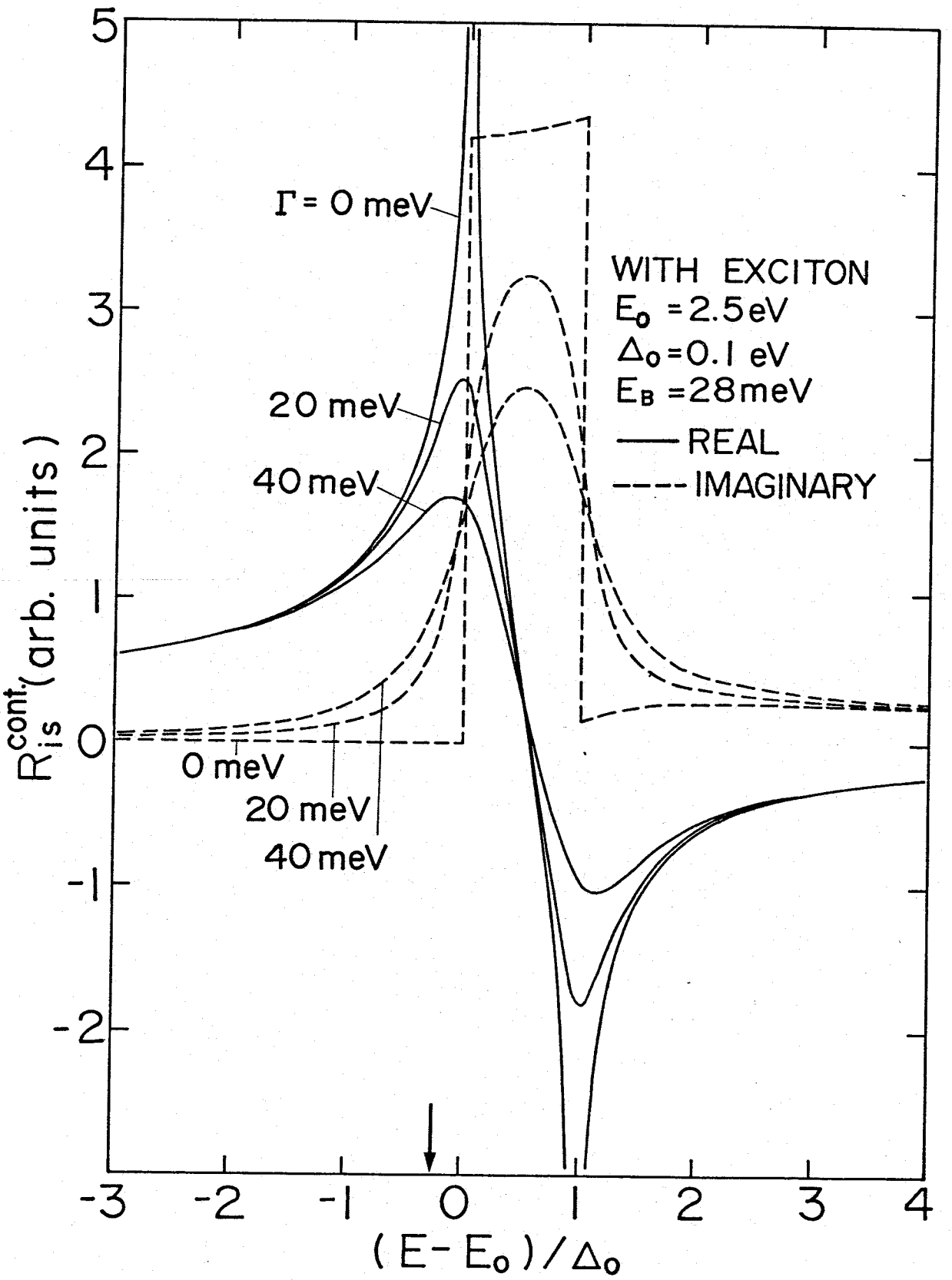

Fig. 2-8. Real and imaginary part of the continuum contribution of R_{is} in the case of Coulomb interaction for various broadening factors; Γ = 0, 20, 40 meV.

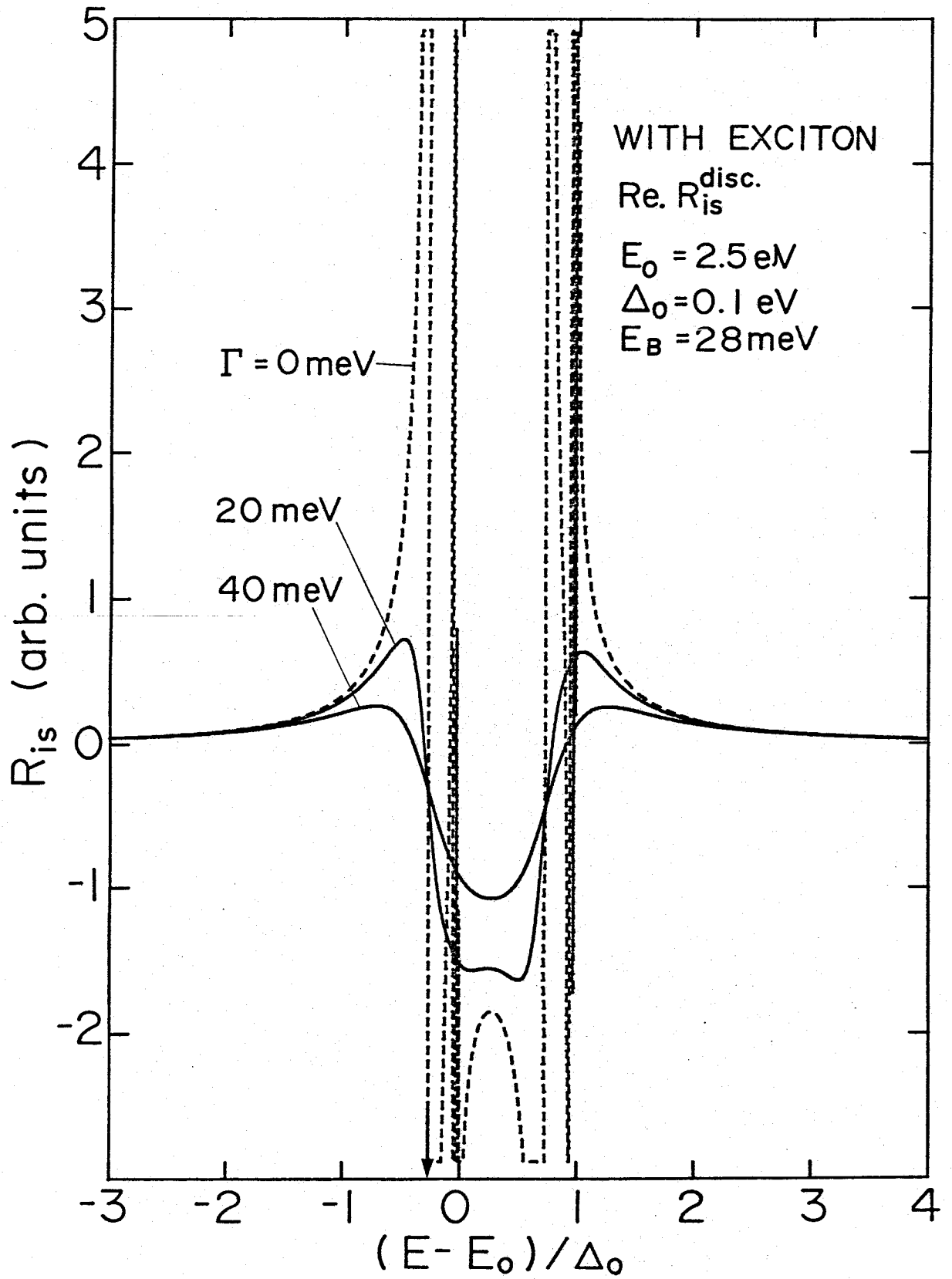

Fig. 2-9. Real part of the discrete exciton contribution of the Brillouin tensor R_{is} in the case of Coulomb interaction for various broadening factors; Γ = 0, 20 40 meV.

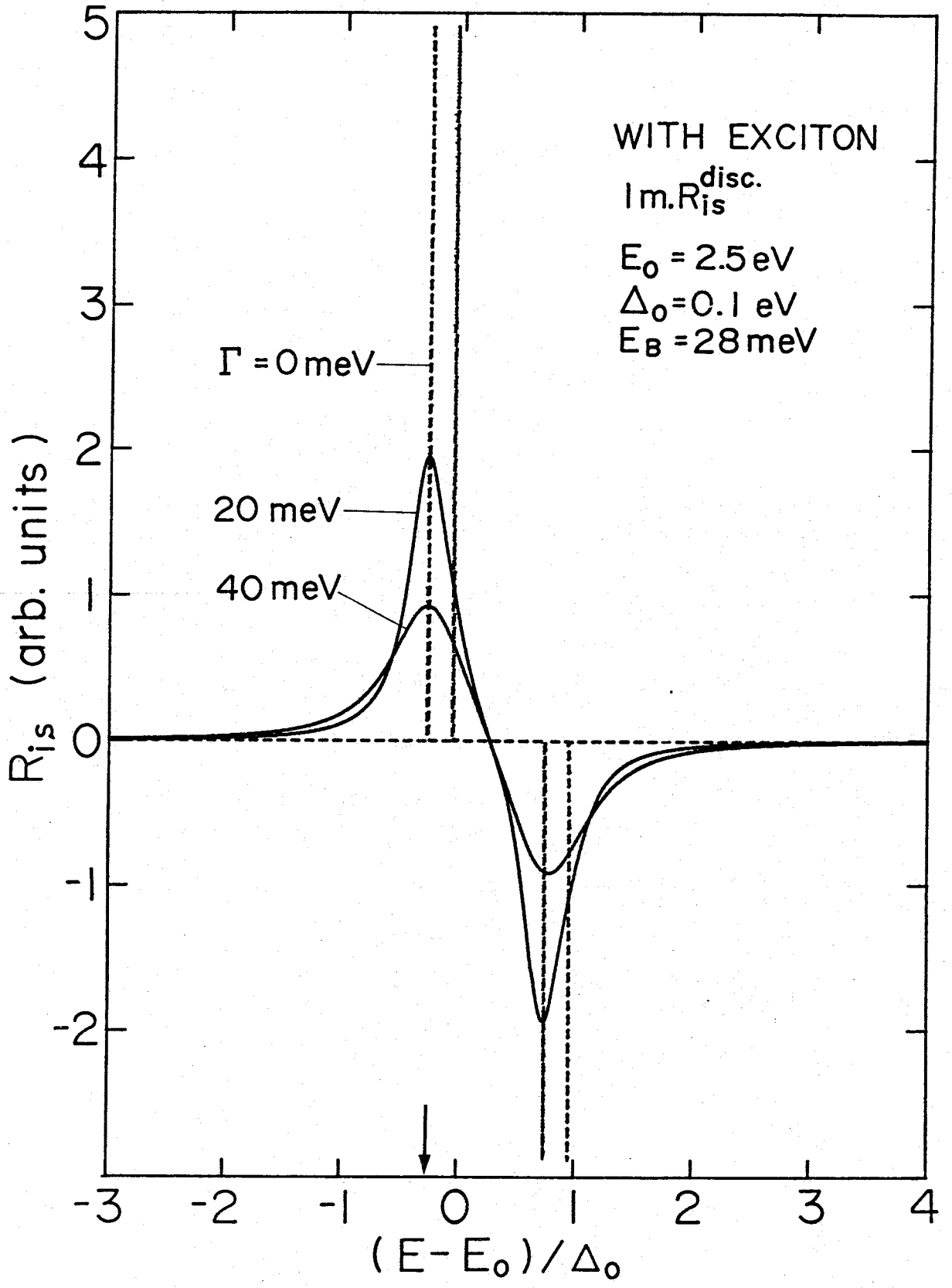

Fig. 2-10. Imaginary part of the discrete exciton contribution of the Brillouin tensor R_{is} in the case of Coulomb interaction for various broadening factors; $\Gamma = 0$, 20, 40 meV.

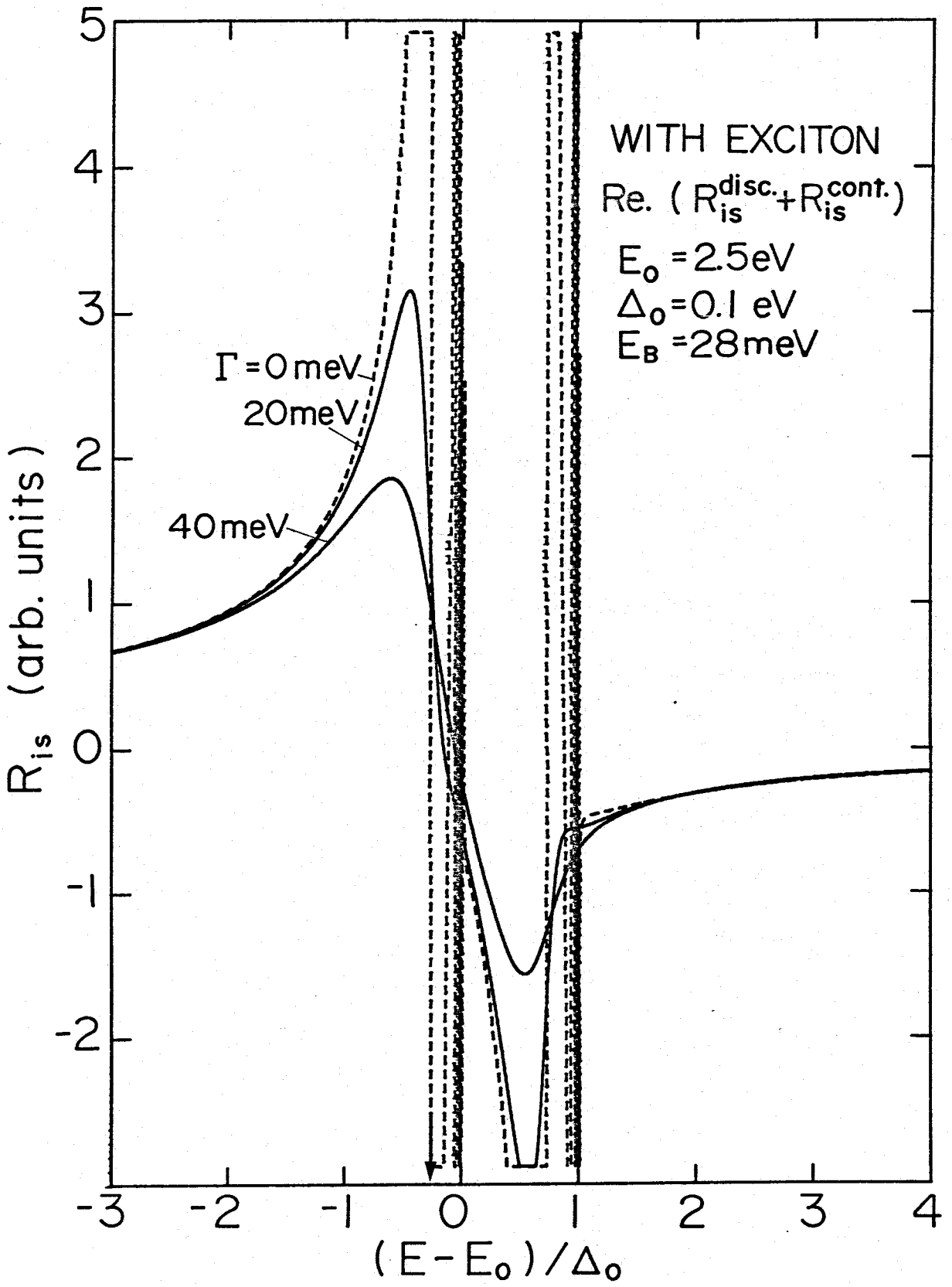

Fig. 2-11. Real part of the Brillouin tensor R_{is} in the case of Coulomb interaction for various broadening factors; $\Gamma = 0$, 20, 40 meV.

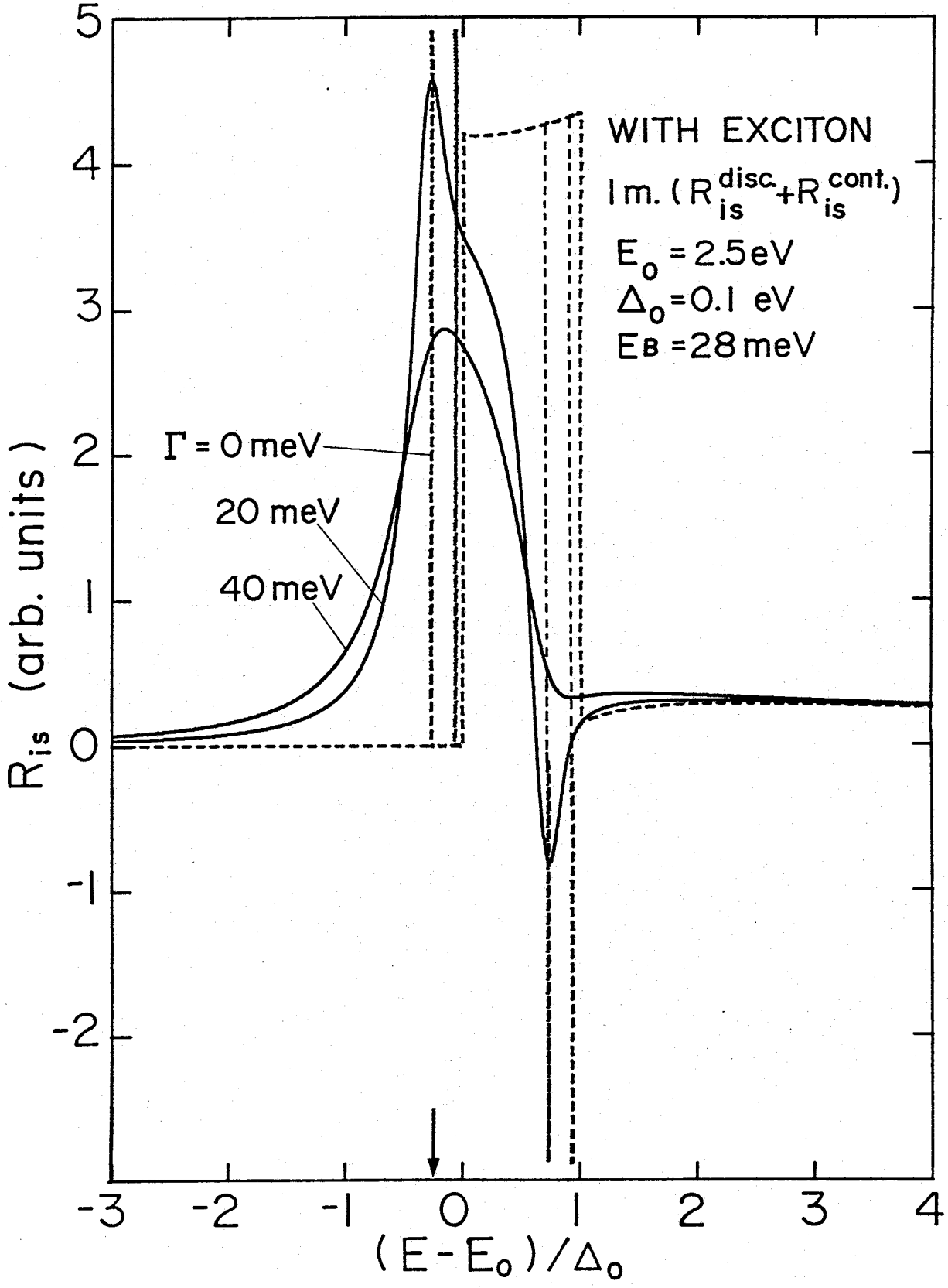

Fig. 2-12. Imaginary part of the Brillouin tensor in the case of Coulomb interaction for various broadening factors; Γ = 0, 20, 40 meV.

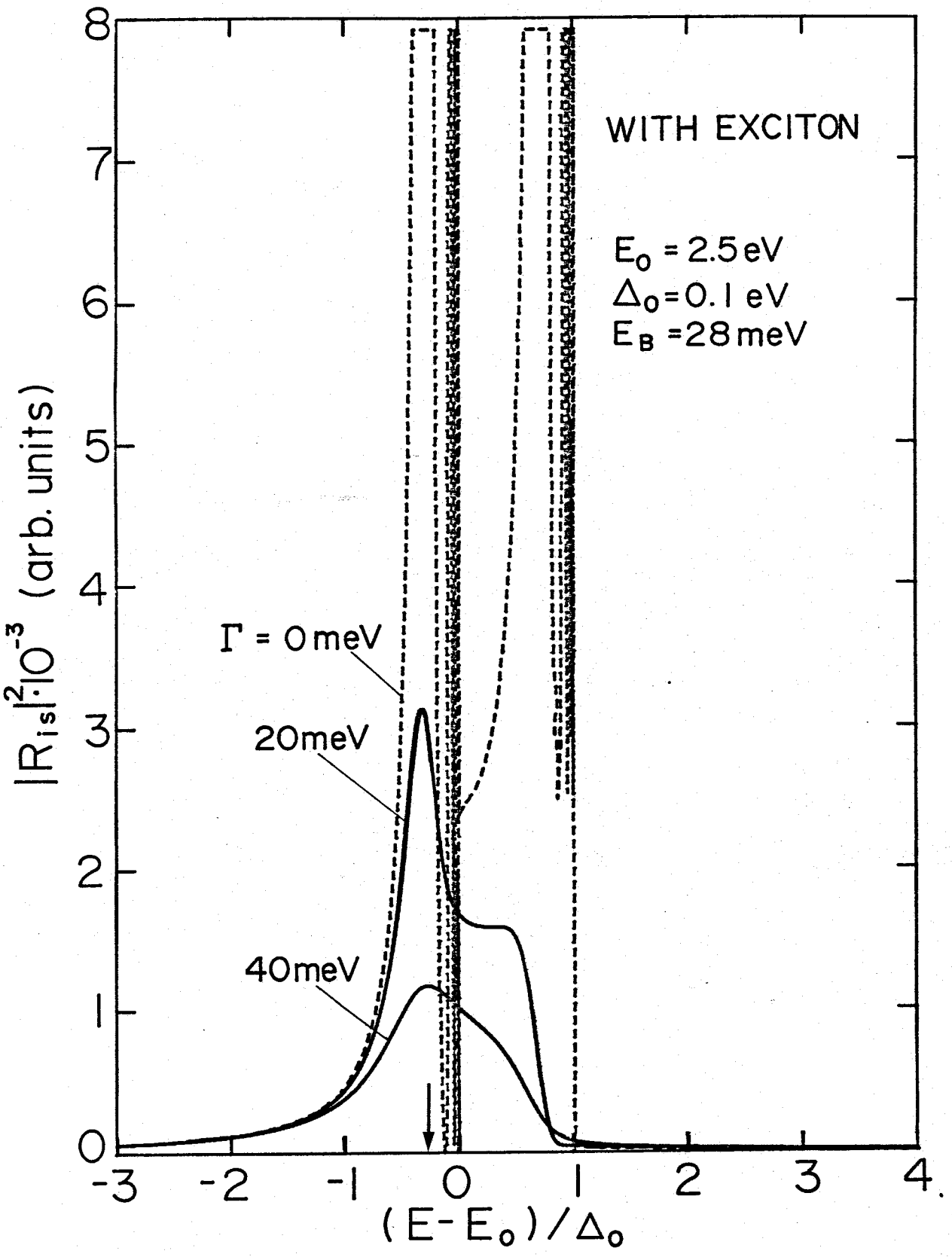

Fig. 2-13. Scattering cross section for an M_0 critical point in the presence of Coulomb interaction for various broadening factors: Γ = 0, 20, 40 meV.

2.4 Deformation Potential Scattering and Momentum Matrix Element

The intermediate electronic states produced by the incident light interact with the acoustical phonon via deformation potential interaction, resulting in a change in their electronic states. The transitions of the intermediate electronic states are determined by the transformation properties of the excited states and relevant acoustical phonon modes in crystals. Such a selection rule of the deformation potential scattering determines the electronic transition process (inter- or intra-band process) which plays an important role in the resonant Brillouin scattering process. The excitation of an acoustic phonon produces a displacement of the atoms of the lattice, and this displacement perturbes the periodic potential, leading to the electron-phonon interaction energy H_{EP}. The electron-phonon interaction is linear in the component u of the relative displacememt,[49] and a matrix element of H_{EP} is written as

$$\langle\alpha|H_{EP}|\beta\rangle = \Xi_{\beta\alpha}\, u/a \quad , \tag{2.141}$$

where a is the lattice constant, included to give a convinent normalization. The deformation potential $\Xi_{\beta\alpha}$ is a matrix element of the perturbed periodic potential with respect to u.

In this section we shall present the non-vanishing matrix elements of deformation potential scattering of hole (or electron) in zincblende and wurtzite crystals.

2.4.1 Zincblende Type Crystals

As shown in Fig. 2-14, the band structure of the zincblende type crystals consists of twofold degenerate s-like conduction band with double symmetry Γ_6 and a fourfould degenerate p-like multiplet ($J = \pm 3/2$, $m_J = \pm 3/2$, $\pm 1/2$ in angular momentum notation) with Γ_8 symmetry and a spin-orbit-

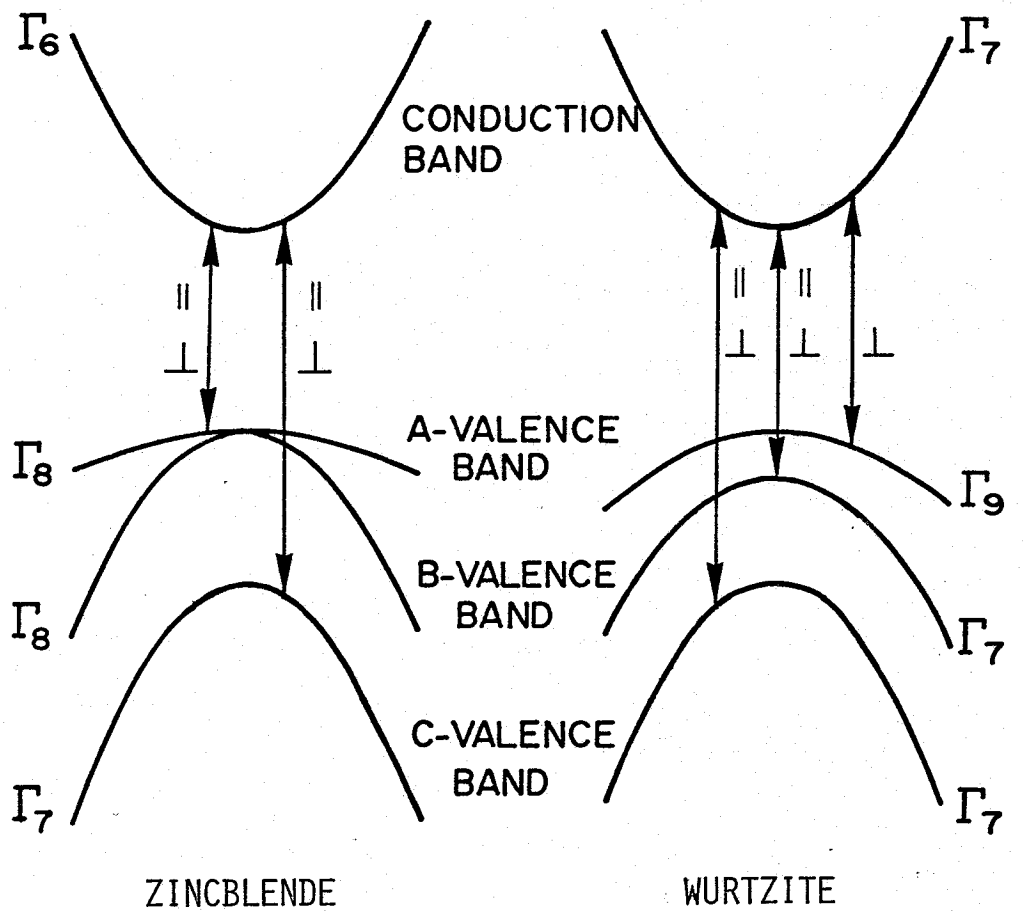

Fig. 2-14. Schematic illustration of the lowest conduction band and upper valence bands in zincblende and wurtzite type materials. Selection rule of the dipole transition is also shown, where $\parallel$ and $\perp$ indicate the polarization parallel and perpendicular to the c-axis (or z-aixs), respectively.

splitting energy Δ_0. The dipole transition is allowed between conduction band and any valence bands in any case of the incident light with linear polarizaziton. The unperturbed wave functions of three valence bands are given by[67]

$$\Phi_{VA} = \frac{1}{\sqrt{6}}|2Z\uparrow+(X+iY)\downarrow , \tag{2.142}$$

$$\Phi_{VB} = \frac{1}{\sqrt{2}}|(X+iY)\uparrow> , \tag{2.143}$$

$$\Phi_{VC} = \frac{1}{\sqrt{3}}|Z\uparrow-(X+iY)\downarrow> , \tag{2.144}$$

$$\Phi_{VA'} = \frac{1}{\sqrt{6}}|2Z\downarrow-(X-iY)\uparrow> , \tag{2.145}$$

$$\Phi_{VB'} = \frac{1}{\sqrt{2}}|(X-iY)\downarrow> , \tag{2.146}$$

$$\Phi_{VC'} = \frac{1}{\sqrt{3}}|Z\downarrow+(X-iY)\uparrow> , \tag{2.147}$$

where $\uparrow$ and $\downarrow$ indicate spin up and spin down, respectively, and subscript A, B, C of $\Phi_{V\alpha}$ indicate the corresponding A, B, C valence bands, respectively and A', B', and C' indicate the Kramers conjugates of the corresponding wave functions. X, Y, Z are the valence-band wave functions which transform as atomic p functions under the operations of the group of tetrahedron and S is the conduction band wave function which transforms as an atomic S function under the same operators. In order to calculate eq.(2.141), we use Picus and Bir's strain orbital Hamiltonian.[68]

$$H_{xC} = a'(e_{xx}+e_{yy}+e_{zz}) \tag{2.148}$$

for the conduciton band at $\vec{k}=0$, and

$$H_{xV} = -a(e_{xx}+e_{yy}+e_{zz}) - 3b[(L_x^2-\frac{1}{3}\mathbb{L}^2)e_{xx}+c.p.] - \frac{6d}{\sqrt{3}}\{[L_x,L_y]+c.p.\} \tag{2.149}$$

for the valence bands at $\vec{k}=0$, In eqs.(2.148) and (2.149), the parameter a' and a are the hydrostatic-pressure deformaiton potentials for the conduction

and valence bands, respectively, and b and d are the uniaxial deformation potential appropriate to strains of tetragonal and rhombohedral symmetry, respectively. e_{ij} is the component of the strain tensor, L_i the orbital angular momentum operator given by[69]

$$L_x = \frac{\hbar}{\sqrt{2}}\begin{bmatrix}0 & 1 & 0\\ 1 & 0 & 1\\ 0 & 1 & 0\end{bmatrix}, \qquad L_y = \frac{\hbar}{\sqrt{2}}\begin{bmatrix}0 & i & 0\\ i & 0 & i\\ 0 & i & 0\end{bmatrix}, \qquad L_z = \frac{\hbar}{\sqrt{2}}\begin{bmatrix}1 & 0 & 0\\ 0 & 0 & 0\\ 0 & 0 & -1\end{bmatrix}, \tag{2.150}$$

and

$$\mathbb{L}^2 = L_x^2 + L_y^2 + L_z^2 = 2\hbar\begin{bmatrix}1 & 0 & 0\\ 0 & 1 & 0\\ 0 & 0 & 1\end{bmatrix} . \tag{2.151}$$

"c.p" in the right-hand side of eq.(2.149) indicates cyclic permutations with respect to the indices x, y, and z, and the quantity in the square bracket denotes the symmetrized product:

$$[L_x, L_y] = \frac{1}{2}(L_x L_y + L_y L_x) . \tag{2.152}$$

In the case of the presence of all strain components, the strain-orbital Hamiltonian matrix for the valence bands can be written in Table 2-1.

The acoustic waves produce a displacement $u(\vec{r},t)$, which can be given by the following plane-wave form:

$$u_l(\vec{r},t) = \pi_l u_0 \exp[i(\vec{q}\cdot t - \omega t)] , \tag{1.153}$$

where $\vec{\pi}$ is a unit vector in the direction of the polarization of the sound wave, and subscript l represents the component of the direction x, y, or z. The strain components $e_{ij}(\vec{r},t)$ are related to the elastic displacememts $u(\vec{r},t)$ by[44]

$$e_{ij} = \frac{1}{2}\left(\frac{\partial u_i}{\partial r_j} + \frac{\partial u_j}{\partial r_i}\right) . \tag{2.154}$$

The non-zero component of the strain tensor can be obtained from eq.(2.154) The corresponding non-vanishing strain components obtained from eq.(2.154) are as follows,(See,eq.(2.41));

For T1-mode acoustic phonons:

$$e_{xx} \text{ and } e_{yy}, \text{ with } e_{xx} = -e_{yy} \quad , \tag{2.155}$$

For T2-mode acoustic phonons:

$$e_{yz} \text{ and } e_{zx}, \text{ with } e_{yz} = e_{zx} \quad , \tag{2.156}$$

where the T1- and T2-mode acoustic phonons propagation in the $[1\bar{1}0]$ and [001] directions, respectively, with shear polarization to the [110] direction. The strain-orbital Hamiltonians [eqs. (2.148) and (2.149)], thus, become

$$H_{xC} = 0 \tag{2.157}$$

$$H_{xV} = -3b[(L_x^2 - \frac{1}{3}\mathbb{L}^2)e_{xx} + (L_y^2 - \frac{1}{3}\mathbb{L}^2)]e_{yy} \tag{2.158}$$

for the T1-mode acoustic phonons, and

$$H_{xC} = 0 \tag{2.159}$$

$$H_{xV} = -\frac{6}{\sqrt{3}} d\{[L_y, L_z]e_{yz} + [L_z, L_x]e_{zx}\} \tag{2.160}$$

for the T2-mode acoustic phonons. It is noted from eqs(2.157) and (2.159) that the deformation-potential scattering of electron in the conduction bands disappears for both the T1- and T2-mode acoustic phonons. The wave functions of the p-like valence bands can be now in the matrix representation as follows:

$$\Phi_{VA} = \frac{1}{\sqrt{3}}(\sqrt{2}\begin{bmatrix}0\\1\\0\end{bmatrix}\alpha + \begin{bmatrix}1\\0\\0\end{bmatrix}\beta) \tag{2.161}$$

$$\Phi_{VB} = -\begin{bmatrix}1\\0\\0\end{bmatrix}\alpha \tag{2.162}$$

$$\Phi_{VC} = \frac{1}{\sqrt{3}}(\begin{bmatrix}0\\1\\0\end{bmatrix}\alpha - \sqrt{2}\begin{bmatrix}1\\0\\0\end{bmatrix}\beta) \tag{2.163}$$

$$\Phi_{VA'} = \frac{1}{\sqrt{3}}(\sqrt{2}\begin{bmatrix}0\\1\\0\end{bmatrix}\beta - \begin{bmatrix}0\\0\\1\end{bmatrix}\alpha \tag{3.164}$$

$$\Phi_{VB'} = \begin{bmatrix} 0 \\ 0 \\ 1 \end{bmatrix} \beta \tag{2.165}$$

$$\Phi_{VC'} = \frac{1}{\sqrt{3}} \left(\begin{bmatrix} 0 \\ 1 \\ 0 \end{bmatrix} \beta + \sqrt{2} \begin{bmatrix} 0 \\ 0 \\ 1 \end{bmatrix} \alpha \right) \tag{2.166}$$

where α and β indicate spin-up and spin-down, respectively. Substituting eqs. (2.158) and (2.160), and eqs. (2.161) to (2.166) into eq.(2.141), one can find the deformation potential scattering of holes in the valence bands. We obtain the following results:

$$\begin{aligned} &\Xi_{AA} = \Xi_{BB} = \Xi_{CC} = 0 \\ &\Xi_{B'A} = \sqrt{3}b, \quad \Xi_{C'B} = \sqrt{6}b, \quad \Xi_{AC} = 0 \end{aligned} \tag{2.167}$$

for T1-mode acoustic phonons, and

$$\begin{aligned} &\Phi_{AA} = \Xi_{BB} = \Xi_{CC} = 0 \\ &\Phi_{BA} = d \ , \quad \Xi_{CB} = d/\sqrt{2}, \ \Xi_{AC'} = \sqrt{6}/\sqrt{2} \end{aligned} \tag{2.168}$$

for T2-mode acoustic phonons. It is clear from above results that the interband deformation-potential scattering is forbidden for both the T1- and T2-mode acoustic phonons. Fiure 2-15 shows the schematic diagram of the electronic transitions which plays an important role in the first-order Brillouin scattering process. $\Xi_{\beta\alpha}$ means that the excited holes in the α valence band (α exciton) are scattered by the deformation potential to the β valence band (β excitons). Note that $\Xi_{\beta\alpha}$ has the symmetric property:

$$\Xi_{\beta\alpha} = \Xi_{\alpha\beta} \tag{2.169}$$

2.4.2 Wurtzite Type Crystals

We shall obtain the matrix element $\Xi_{\beta\alpha}$ in the case of the wurtzite type crystals based on the quasi-cubic model[70,71] It has been pointed out by Hopfield[71] that the direct-gap of wurtzite can be obtained from that of zincblende by the action of a small hexagonal crystal field.

H_{xv}	Φ_A	Φ_B	Φ_C	$\Phi_{A'}$	$\Phi_{B'}$	$\Phi_{C'}$
Φ_A	$A - \frac{b}{2} e_A$	de_{+z}	$-\frac{b}{\sqrt{2}} e_A$	0	$\frac{\sqrt{3}}{2} be_B - ide_{xy}$	$\frac{\sqrt{6}}{2} de_{-z}$
Φ_B	de_{-z}	$A + \frac{b}{2} e_A$	$\frac{d}{\sqrt{2}} e_{-z}$	$-\frac{\sqrt{3}}{2} be_B + ide_{xy}$	0	$\frac{\sqrt{6}}{2} be_B - i\sqrt{2} de_{xy}$
Φ_C	$-\frac{b}{\sqrt{2}} e_A$	$\frac{d}{\sqrt{2}} e_{+z}$	A	$-\frac{\sqrt{6}}{2} de_{-z}$	$\frac{\sqrt{6}}{2} be_B + i\sqrt{2} de_{xy}$	0
$\Phi_{A'}$	0	$-\frac{\sqrt{3}}{2} be_B - ide_{xy}$	$-\frac{\sqrt{6}}{2} de_{+z}$	$A - \frac{b}{2}$	de_{-z}	$-\frac{b}{\sqrt{2}} e_A$
$\Phi_{B'}$	$\frac{\sqrt{3}}{2} be_B + ide_{xy}$	0	$\frac{\sqrt{6}}{2} be_B - i\sqrt{2} de_{xy}$	de_{+z}	$A + \frac{b}{2} e_A$	$\frac{d}{\sqrt{2}} e_{+z}$
$\Phi_{C'}$	$\frac{\sqrt{6}}{2} de_{+z}$	$\frac{\sqrt{6}}{2} be_B + i\sqrt{2} de_{xy}$	0	$-\frac{b}{\sqrt{2}} e_A$	$\frac{d}{\sqrt{2}} e_{-z}$	A

Table 2-1. The strain Hamiltonian matrix for the valence bands in the case of the presence of all strain components in the zincblende type crystals. A parameter a is a hydrostatic pressure-deformation potential, quantities b and d are uniaxial-deformation potentials, e_{ij}'s are components of the strain tensor with $e_A = e_{xx} + e_{yy} - 2e_{zz}$, $e_B = e_{xx} - e_{yy}$ and $e_{+z} = e_{zx} \pm ie_{yz}$, and quantity A is defined by $A = -(e_{xx} + e_{yy} + e_{zz})$.

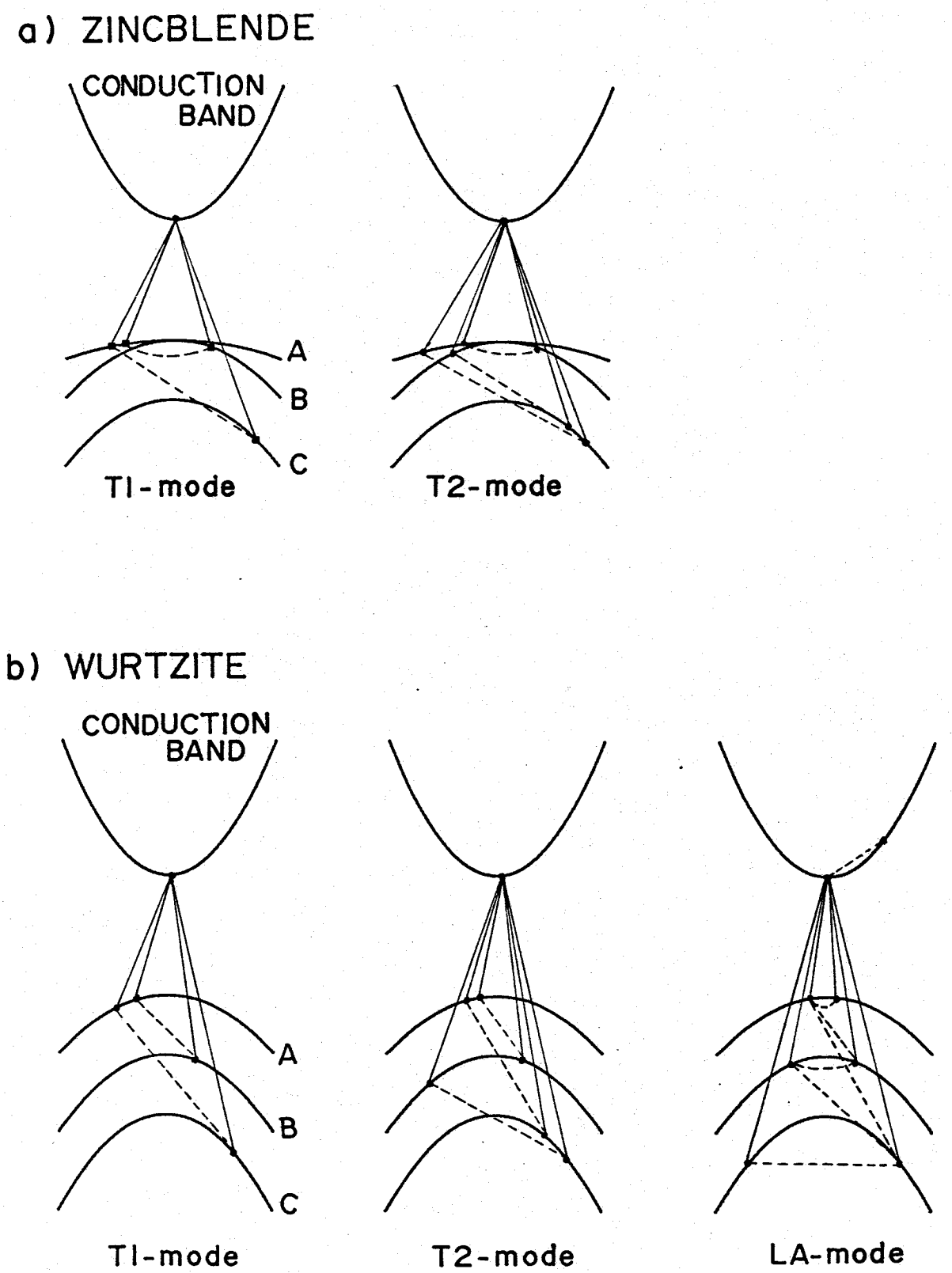

Fig. 2-15. Schematic diagram of the allowed transition process for holes in valence bands in the case of a) zincblende and b) wurtzite crystals.

Under the spin-orbit interaction and crystal field interaction, the energy difference of the split valence bands (correspond to the A, B, and C valence bands) are given by[71]

$$E_{BA} = E_{gB} - E_{gA} = \frac{\Delta_{so} + \Delta_c}{2} - \sqrt{(\frac{\Delta_{so} + \Delta_c}{2})^2 - \frac{2}{3}\Delta_{so}\Delta_c} \qquad (2.170)$$

$$E_{CA} = E_{gC} - E_{gA} = \frac{\Delta_{so} + \Delta_c}{2} + \sqrt{(\frac{\Delta_{so} + \Delta_c}{2})^2 - \frac{2}{3}\Delta_{so}\Delta_c} \qquad (2.172)$$

$$E_{CB} = E_{gC} - E_{gB} = 2\sqrt{(\frac{\Delta_{so}+\Delta_c}{2})^2 - \frac{2}{3}\Delta_{so}\Delta_c} \qquad (2.172)$$

where Δ_{so} and Δ_c are the spin-orbit energy and crystal field parameter, respectively. The corresponding wave functions of the three split valence bands are

$$\Phi_{VA} = S_+\uparrow \ , \qquad (2.173)$$

$$\Phi_{VB} = a_B S_-\uparrow + a_C S_0\downarrow \ , \qquad (2.174)$$

$$\Phi_{VC} = a_C S_-\uparrow - a_B S_0\downarrow \ , \qquad (2.175)$$

$$\Phi_{VA'} = S_-\downarrow \ , \qquad (2.176)$$

$$\Phi_{VB'} = a_B S_+\downarrow - a_C S_0\uparrow \ , \qquad (2.177)$$

$$\Phi_{VC'} = a_C S_+\downarrow + a_B S_0\uparrow \ , \qquad (2.178)$$

where $\uparrow$ and $\downarrow$ represent spin-up and spin-down, respectively, and S_+, S_- and S_0 are defined by using the p-like basis functions X, Y, Z as follows.

$$S_+ = (X + iY)/\sqrt{2} \ , \quad S_- = (X - iY)/\sqrt{2} \ , \quad S_0 = Z \qquad (2.179)$$

The admixture coefficients a_B and a_C are

$$a_B = [1 + \frac{1}{2}(2 - \frac{3}{\Delta_{so}}E_{BA})^2]^{-1/2} \ , \qquad (2.180)$$

$$a_C = [1 + \frac{1}{2}(2 - \frac{3}{\Delta_{so}}E_{CA})^2]^{-1/2} \ , \qquad (2.181)$$

$$a_B^2 + a_C^2 = 1 \ . \qquad (2.182)$$

The wave function of the conduction band is s-like in character:

$$\Psi_C = |S> \quad . \tag{2.183}$$

It has been shown that the strain-orbital Hamiltonian H_x for the s-like conduction band of wurtzite crystals at $\vec{k} = 0$ is given by[72)]

$$H_{xc} = d_1 e_{zz} + d_2(e_{xx} + e_{yy}) \quad , \tag{2.184}$$

for the p-like valence bands by

$$H_{xv} = (C_1 + C_3 L_z^2) e_{zz} + (C_2 + C_4 L_z^2)(e_{xx} + e_{yy}) + C_5(L_-^2 e_+ + L_+^2 e_-)$$

$$+ C_6([L_z, L_+]e_{-z} + [L_z, L_-]e_{+z}) \quad , \tag{2.185}$$

where the coefficient C_i and d_i are the deformation potential, e_{ij} is the component of strain tensor $e_\pm = e_{xx} - e_{yy} \pm 2ie_{xy}$, and $e_{\pm z} = e_{xz} \pm ie_{yz}$, and L_i is the strain-orbital momentum operator having the same form as eq. (2.150) and $L_\pm = (L_x \pm iL_y)/\sqrt{2}$. In the case of the presence of all strain tensor component, the strain-orbital Hamiltonian matrix element for the valence bands can be written as shown in Table 2-2.

The non-vanishing strain components of wurtzite-type crystals are obtained from eq.(2.154) as

T1-mode acoustical phonons:

$$e_{xy} \tag{2.186}$$

T2-mode acoustical phonons:

$$e_{zx} \text{ and } e_{yz} \text{ with } e_{zx} = e_{yz} \tag{2.187}$$

The strain-orbital Hamiltonian eqs.(2.184) and (2.185), hence, become

$$H_{xC} = 0 \tag{2.188}$$

$$H_{xV} = C_5(L_-^2 e_+ + L_+^2 e_-) = 2C_5(L_x L_y + L_y L_x)e_{xy} \tag{2.189}$$

for the T1-mode acoustical phonons and

$$H_{xC} = 0 \tag{2.190}$$

$$H_{xV} = C_6([L_z, L_+]e_{-z} + [L_z, L_-]e_{+z}) \tag{2.191}$$
$$= 2C_6(L_x L_z + L_z L_x)e_{xz}$$

H_{xv}	Φ_A	Φ_B	Φ_C	$\Phi_{A'}$	$\Phi_{B'}$	$\Phi_{C'}$
Φ_A	$A + B$	$-C_5 e_- a_B$	$-C_5 e_- a_C$	0	$\frac{C_6}{2} e_{-z} a_C$	$-\frac{C_6}{2} e_{-z} a_B$
Φ_B	$-C_5 e_+ a_B$	$A + Ba_B^2$	$Ba_B a_C$	$-\frac{C_6}{2} e_{-z} a_C$	0	$-\frac{C_6}{2} e_{+z}$
Φ_C	$-C_5 e_+ a_C$	$Ba_B a_C$	$A + Ba_C^2$	$\frac{C_6}{2} e_{-z} a_B$	$\frac{C_6}{2} e_{+z}$	0
$\Phi_{A'}$	0	$-\frac{C_6}{2} e_{+z} a_C$	$\frac{c_6}{2} e_{+z} a_B$	$A + B$	$-C_5 e_+ a_B$	$-C_5 e_+ a_C$
$\Phi_{B'}$	$\frac{C_6}{2} e_{+z} a_C$	0	$\frac{C_6}{2} e_{-z}$	$-C_5 e_- a_B$	$A + Ba_B^2$	$Ba_B a_C$
$\Phi_{C'}$	$-\frac{C_6}{2} e_{+z} a_B$	$-\frac{C_6}{2} e_{-z}$	0	$-C_5 e_- a_C$	$Ba_B a_C$	$A + Ba_C^2$

Table 2-2. The strain Hamiltonian matrix for the valence bands in the case of the presence of all strain components in the wurtzite type crystals. C_i's are the deformation potentials, e_{ij}'s are components of the strain tensor with $e_\pm = e_{xx} - e_{yy} \pm 2ie_{xy}$ and $e_{\pm z} = e_{zx} \pm ie_{yz}$, a_B and a_C are admixture coefficients, and A and B are defined by $A = C_1 e_{zz} + C_2(e_{xx} + C_{yy})$ and $B = C_3 e_{zz} + C_4(e_{xx} + e_{yy})$, respectively.

for the T2-mode acoustical phonons. It is clear from eqs. (2.188) and (2.190) that the deformation potential scattering of electrons in the conduction bands disappear for both T1- and T2-mode acoustical phonons, as similar to the case for the zincblende-type crystals. The wave functions of the p-like valence bands [eqs. (2.173) to (2.178)] can be written in the matrix representation as

$$\Phi_{VA} = \begin{bmatrix} 1 \\ 0 \\ 0 \end{bmatrix} \alpha \ , \tag{2.192}$$

$$\Phi_{VB} = a_B \begin{bmatrix} 0 \\ 0 \\ 1 \end{bmatrix} \alpha + a_C \begin{bmatrix} 0 \\ 1 \\ 0 \end{bmatrix} \beta \ , \tag{2.193}$$

$$\Phi_{VC} = a_C \begin{bmatrix} 0 \\ 0 \\ 1 \end{bmatrix} \alpha - a_B \begin{bmatrix} 0 \\ 1 \\ 0 \end{bmatrix} \beta \ , \tag{2.194}$$

$$\Phi_{VA'} = \begin{bmatrix} 0 \\ 0 \\ 1 \end{bmatrix} \beta \ , \tag{2.195}$$

$$\Phi_{VB'} = a_B \begin{bmatrix} 1 \\ 0 \\ 0 \end{bmatrix} \beta - a_C \begin{bmatrix} 0 \\ 1 \\ 0 \end{bmatrix} \alpha \ , \tag{2.196}$$

$$\Phi_{VC'} = a_C \begin{bmatrix} 1 \\ 0 \\ 0 \end{bmatrix} \beta + a_B \begin{bmatrix} 0 \\ 1 \\ 0 \end{bmatrix} \alpha \ . \tag{2.197}$$

Substituting eqs.(2.189) and (2.191), and eqs.(2.192) to (2.197) into eq.(2.141), one can obtain the deformation-potential scattering of holes in the valence bands of wurtzite-type crystals. We finally obtain the following results:

$$\Xi_{AA} = \Xi_{BB} = \Xi_{CC} = 0$$
$$\Xi_{BA} = a_B C_5, \ \Xi_{CB} = 0 \ , \ \Xi_{AC} = a_C C_5 \tag{2.198}$$

for T1-mode acoustical phonons and

$$\Xi_{AA} = \Xi_{BB} = \Xi_{CC} = 0$$
$$\Xi_{BA'} = -(1/2) a_C C_6, \ \Xi_{CB'} = (1/2) C_6 \ , \ \Xi_{A'C} = (1/2) a_B C_6 \tag{2.199}$$

for T2-mode acoustical phonons.[73] It can be found that form the above result that the interband deformaiton-potential scattering is forbidden for both the T1- and T2-mode acoustical phonons.

The matrix elements of the deformation-potential scattering for longitudinal acoustical phonons in wurtzite crystals can be also be obtained by the same procedure mentioned above. Now, we present the matrix elements of the deformation potential scatteing for longitudinal acoustic phonons (LA-mode). From eq.(2.68) and (2.154), the atomic displacement of LA-mode phonon produces the non-vanishing strain component e_{xx}. The strain-orbital Hamiltonian of eq.(2.184) and (2.185), thus, become

$$H_{xC} = d_2 e_{xx} \tag{2.200}$$

$$H_{xV} = (C_2 + C_4 L_z^2) e_{xx} + C_5 (L_-^2 e_+ + L_+^2 e_-) = [C_2 + 2C_5 (L_x^2 - L_y^2) + C_4 L_z^2] e_{xx} \tag{2.201}$$

Substituting eqs. (2.200), (2.201) and eqs. (2.192) - (2.197) into eq. (2.141), one obtains the following matrix elements:

$$\Xi_{AA} = d_2 - (C_2 + C_4) \ , \quad \Xi_{BB} = d_2 - (C_2 + a_B^2 C_4) \ , \quad \Xi_{CC} = d_2 - (C_2 + a_C^2 C_4)$$

$$\Xi_{BA} = a_B C_5, \quad \Xi_{CB} = a_C C_5 \ , \ \Xi_{AC} = a_B a_C C_4 \tag{2.202}$$

It should be noted that the interband deformaiton potential scattering $\Xi_{\alpha\alpha}$ is allowed in the case of LA phonons, in contrast to those for the transverse acoustical phonons.

In order to determine the Brillouin scattering process, we have to take into accousnt the selection rules of optical transiton (dipole transitions) in addition to those of the deformation potential scattering. The p-matrix elements in zincblende and wurtzite crystals are calculated by using the wave functions shown in eqs.(2.142) to (2.147), and eqs.(2.173) to (2.178), respectively. The results ars shown in Table 2-3, where S is the s-like conduction band, $P_x = \langle X\uparrow | P_x | S \rangle = \langle X\uparrow | P_x | S \rangle$ and P_y and P_z are also defined similarly.

Table. 2-3. Momentum matrix elements of the zincblende and wurtzite

a) Zincblende

P_x	S↑	S↓	P_x	S↑	S↓
Φ_{VA}	0	$P_x/\sqrt{6}$	$\Phi_{VA'}$	$-P_x/\sqrt{6}$	0
Φ_{VB}	$P_x/\sqrt{2}$	0	$\Phi_{VB'}$	0	$P_x/\sqrt{2}$
Φ_{VC}	0	$-P_x/\sqrt{3}$	$\Phi_{VC'}$	$P_x/\sqrt{3}$	0

P_y	S↑	S↓	P_y	S↑	S↓
Φ_{VA}	0	$-iP_y/\sqrt{6}$	$\Phi_{VA'}$	$-iP_y/\sqrt{6}$	0
Φ_{VB}	$-iP_y/\sqrt{2}$	0	$\Phi_{VB'}$	0	$iP_y/\sqrt{2}$
Φ_{VC}	0	$iP_y/\sqrt{3}$	$\Phi_{VC'}$	$iP_y/\sqrt{3}$	0

P_z	S↑	S↓	P_z	S↑	S↓
Φ_{VA}	$\sqrt{6}P_z/3$	0	$\Phi_{VA'}$	0	$\sqrt{6}P_z/3$
Φ_{VB}	0	0	$\Phi_{VB'}$	0	0
Φ_{VC}	$\sqrt{3}P_z/3$	0	$\Phi_{VC'}$	0	$\sqrt{3}P_z/3$

b) Wurtzite

P_x	S↑	S↓	P_x	S↑	S↓
Φ_{VA}	$P_x/\sqrt{2}$	0	$\Phi_{VA'}$	0	$P_x/\sqrt{2}$
Φ_{VB}	$a_B P_x/\sqrt{2}$	0	$\Phi_{VB'}$	0	$a_B P_x/\sqrt{2}$
Φ_{VC}	$a_C P_x/\sqrt{2}$	0	$\Phi_{VC'}$	0	$a_C P_x/\sqrt{2}$

P_y	S↑	S↓	P_y	S↑	S↓
Φ_{VA}	$-iP_y/\sqrt{2}$	0	$\Phi_{VA'}$	0	$iP_y/\sqrt{2}$
Φ_{VB}	$ia_B P_y/\sqrt{2}$	0	$\Phi_{VB'}$	0	$-ia_B P_y/\sqrt{2}$
Φ_{VC}	$ia_C P_y/\sqrt{2}$	0	$\Phi_{VC'}$	0	$-ia_C P_y/\sqrt{2}$

P_z	S↑	S↓	P_z	S↑	S↓
Φ_{VA}	0	0	$\Phi_{VA'}$	0	0
Φ_{VB}	0	$a_C P_z$	$\Phi_{VB'}$	$-a_C P_z$	0
Φ_{VC}	0	$-a_B P_z$	$\Phi_{VC'}$	$a_B P_z$	0

2.5 Summary

In this chapter, we gave a detailed description of the theoretical treatment of the resonant Brillouin scattering. We presented both macroscopic (classical) and microscopic (quantum-mechanical) theory. We learned from the quantum mechanical theory how resonant enhancement and cancellation occur in the dispersion curves of resonant Brillouin scattering cross section. We exammined carefully the resonant characteristics of the scattering cross section both below and above the fundamental absorption edge. From the present theory, we find the Coulomb interaction between electron and hole causes a strong asymmetry in the Brillouin efficiency with respect to the band gap, a strong resonant enhancement only occurs below the gap. It is also found, not only the real but the imaginary part of the Brillouin tensor as well plays an important role in determining the dispersion curves of the resonant Brillouin scattering cross section near the fundamental absoption edge. From the analysis of deformation potential scattering of intermediate virtual states by acoustic phonons, we showed that the observed resonant feature is interpreted in terms of the three band model.

CHAPTER 3

PIEZOBIREFRINGENCE THEORY

3.1 Introduction

In this chapter we shall discuss the theory of the photoelastic constants in zincblende and wurtzite materials. From a macroscopical point of view, the Brillouin scattering cross section is known to be proportional to the square of the photoelastic constant. Such constants can be obtained independently from the stress induced birefringence experiment (piezobirefringence, P.B). This is evident if we consider the situation that the piezobirefringence is characterized by the change in the dielectric constant induced by the static stress (uniaxial stress), whereas the Brillouin scattering is caused by the change in the dielectric constant by the dynamic stress (lattice vibration or travelling acoustic waves). Therefore both effects are characterized by the magnitude of the photoelastic constant.

In Section 3.2, we shall present the basic concept of the piezobirefringence and briefly discuss the method to determine the piezobirefringence. In Section 3.3, we present a experimental method of the piezobirefringence. In Section 3.4, we shall derive a theoretical expression of the dielectric functions, which are used to construct theoretical expressions of the photoelastic constants. In Section 3.5, we obtain the theoretical expression of the photoelastic constants by using the model dielectric constant, strain-orbital Hamiltonian and wave functions in the valence bands.

3.2 Basic Concept of the Photoelastic Constant

The application of a uniaxial stress to a crystal produces a change in the optical properties due to a change in energy gaps and momentum matrix elements.[74] The complex photoelastic (elasto-optic) constant P_{ijkl} and piezo-optic constant π_{ijkl} are defined through[75]

$$\Delta\left(\frac{1}{\varepsilon_{ij}}\right) = P_{ijkl}e_{kl} = \pi_{ijkl}X_{kl} \quad , \tag{3.1}$$

where ε_{ij} is the dielectric tensor, e_{kl} the strain and X_{kl} the stress tensor. Writting ε_{ij} as $\varepsilon^r_{ij} + i\varepsilon^i_{ij}$, eq. (3.1) can be rewritten as [76]

$$-\frac{(\Delta\varepsilon^r_{ij} + i\Delta\varepsilon^i_{ij})}{\varepsilon_{ii}\varepsilon_{jj}} = P_{ijkl}e_{kl} \quad . \tag{3.2}$$

In the region where $\varepsilon^i < \varepsilon^r$ the denominator of the left hand side can be approximated by $\varepsilon^r_{ii}\varepsilon^r_{jj}$ and the real and imaginaly part of P_{ijkl} are related directly to the corresponding change in ε_{ij}.

The piezobirefringence coefficient α is also defined by the following equation [77]

$$\alpha = \frac{\Delta\varepsilon_{ij}}{X_{mn}} = -\varepsilon_{ii}\varepsilon_{jj}P_{ijkl}S_{klmn} \quad , \tag{3.3}$$

where S_{klmn} is the elastic compliance tensor.

A cubic semiconductor which is optically isotropic if unstressed become birefringent when a uniaxial stress is applied.[74, 78] Such a birefringence induced by a uniaxial stress is called piezobirefringence and characterized by the difference in the refractive indices between the light polarized parallel and perpendicular to the stress direction. In cubic crystals the difference in the refractive indices is

$$n_{\parallel} - n_{\perp} = -\frac{1}{2} n_0^3 (P_{44}/C_{44}) X \ , \tag{3.4}$$

for the [111] stress, and

$$n_{\parallel} - n_{\perp} = -\frac{1}{2} n_0^3 \frac{P_{11} - P_{12}}{C_{11} - C_{12}} X \ , \tag{3.5}$$

for the [100] stress, where X is the stress magnitude, n_0 is the refractive index at zero stress, and C_{ij} is the elastic stiffness constnat.

On the other hand, for wurtzite crystals the birefringence induced by a stress along $[11\bar{2}0]$ direction is given by

$$n_{\parallel} - n_{\perp} = -\frac{1}{2} n_o^3 \frac{P_{11} - P_{12}}{C_{11} - C_{12}} \ , \tag{3.6}$$

where the light is assumed to propagate along $[1\bar{1}00]$ direction and n_o is the refractive index of the ordinary wave at zero stress.

It is clear from eqs. (3.4) - (3.6) that the photoelastic constants are experimentally determined by the change of the refractive index (Δn).

3.3 Piezobirefringence

One of the experimental method used to determine the photoelastic constant is based on the measurements of the piezobirefringence. The term piezobirefringence denotes the effect of change in the optical birefringence induced by an elastic deformation. If the crystal is optically anisotropic, two optical waves with different velocity but the same wavenormal, will in general be propagated through the crystal. The polarization of these waves will be perpendicular to each other (see Fig. 3-1). If the propagation direction corresponds to one of the principal axis (X_k), the polarization of these waves will be along the two other principal axis (X_i and X_j). The principal axis are the directions which if chosen as the coordinate

system make the dielectric constant diagonal. We consider a plane polarized optical wave at normal incidence on a sample cut in the form of a plane-parallel slab and one of the principal axis be perpendicular to the plane of incidence. In the region of transparency, where the absorption can be neglected, two different lineary polarizrd waves (p-polarization) with amplitude E_i and E_j will propagate through the crystal.

The electric vector of these waves, as a function of the position x_k in the crystal can be written

$$E_i(x_k) = E_0 \cos\phi \sin(\omega t - \frac{2\pi n_i}{\lambda} x_k) \quad , \tag{3.7}$$

$$E_j(x_k) = E_0 \cos\phi \sin(\omega t - \frac{2\pi n_j}{\lambda} x_k) \quad , \tag{3.8}$$

where ϕ is the angle between the polarization of the incident wave and the principal axis. The amplitude of the incident wave is E_0, and ω and λ are angular frequency and the wavelength in vacuum, respectively. n_i and n_j are the refractive indices along the optic axis. If in the experiment the sample is placed between two crossed polarizers, respect to the optic axis, the transmitted light intensity I_t through the second polarizer will be given by the equation

$$I_t/I_0 = \sin^2(2\phi)\sin^2(\Delta n \frac{\pi b}{\lambda}) \quad , \tag{3.9}$$

where I_0 is the intensity of the incident light, b is the thickness of the crystal, and $\Delta n = n_i - n_j$. By measureing the ratio (I_t/I_0), one can determine the crystal birefringence Δn. From eq.(3.9), the best condition of this experiment is made by putting $\phi = 45°$, because the transmitted intensity is maximum. The transmitted intensity had a minimum when

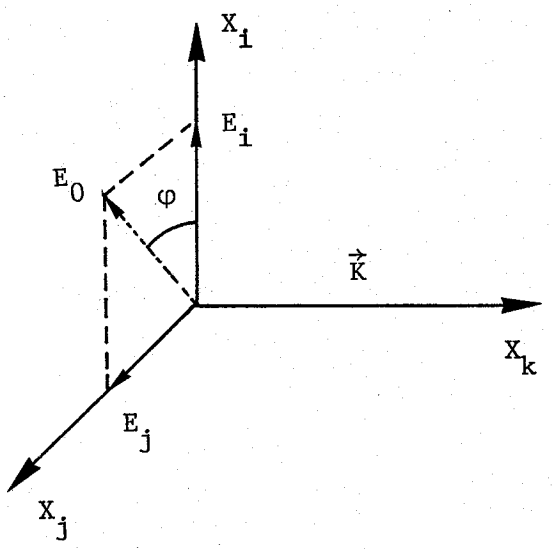

Fig. 3-1. The geometric configuration used in measurements of the optical birefringence. $\vec{K}$ is the wavevector of the incident light. X_i and X_j are the optical axis and E_0 is the amplitude of the incident light.

$$\Delta n \frac{\pi b}{\lambda} = m\pi \quad , \tag{3.10}$$

where m (the order of the interference) is an integer with positive or negative. The transmitted intensity would be zero if the light beam would be exactly monochromatic and collimated. From eq.(3.10) one obtains

$$\Delta n = \frac{m\lambda}{b} \quad . \tag{3.11}$$

On the other hand, the transmitted intensity has maximum when,

$$\Delta n \frac{\pi b}{\lambda} = (m+\frac{1}{2})\pi \quad , \tag{3.12}$$

$$\Delta n = (m+\frac{1}{2})\frac{\lambda}{b} \quad . \tag{3.13}$$

The dispersion of the birefringence $\Delta n(\lambda)$ can be determined from positons of the successive maxima and minima. In the region near the fundamental absorption edge, the effect of the dichroism (i.e., the anisotropy of the absorption coefficient) must be taken into account. If the polarization of the light forms the angle ϕ with respect to the optic axis, the

intensity of thr light transimitted through two crossed polarizers is:

$$I_t = I_0[\exp\{-(1/2)(\alpha_{\parallel}+\alpha_{\perp})b\}\sin^2(\Delta n \frac{\pi b}{\lambda}) +$$

$$\frac{1}{4}(\exp\{-(1/2)\alpha_{\parallel}b\}-\exp\{-(1/2)\alpha_{\perp}b\}]\sin^2 2\phi \ , \qquad (3.14)$$

where $\alpha_{\parallel}$ and $\alpha_{\perp}$ is the absorption coefficients for the two principal directions. From eq.(3.14) it follows that the intensity of the transmitted light is modulated by the factor $\sin^2(\Delta n \frac{\pi b}{\lambda})$. The modulation arising from the dichroism is much slower than that caused by birefringence. The spectral positons of the maxima and minima of the transmitted intensity will be same as those given in eq. (3.11) and eq. (3.13).

3.4 Dielectric Constant

For the purpose of determining the photoelastic constant, we have to obtain the theoretical expression of the model dielectric constant. In this subsection we shall discuss theoretical expression of the frequency-dependent dielectric constant derived by Cardona.[79] First of all, we consider the contribution to $\varepsilon_2(\omega)$ of the E_0 gap is

$$[\varepsilon_2(\omega)] \quad = \sum_{i=A,B,C} A|\langle c|P(\vec{k})|v_i\rangle|^2 \frac{1}{\omega^2}(\omega - \omega_{0i})^{1/2} \ , \qquad (3.15)$$

with

$$A = (2e^2\hbar^{1/2}/m^2)(2m^*/h^2)^{3/2} \ . \qquad (2.16)$$

In eq.(3.15) m^* is the combined density-of-state mass, and $\langle|p(\vec{k})|\rangle^2$ is the dipole transition between the i-valence band (i = A,B or C) and conduction bands and ω_{0i} is the energy difference between the i-valence and conduction band. For simplicity we assumed that the matrix element P is $\vec{k}$-independent quantity. The real part of the dielectric constant can

also be calculated from eq.(3.15) by using following Kramers-Kronig relations;

$$\varepsilon_1(\omega) - \varepsilon_\infty = \frac{2}{\pi} P\int_0^\infty \frac{\omega'\varepsilon_2(\omega')}{(\omega')^2 - \omega^2}\, d\omega' \quad , \tag{3.17}$$

$$\varepsilon_2(\omega) = -\frac{2}{\pi} P\int_0^\infty \frac{\varepsilon_1(\omega')}{(\omega')^2 - \omega^2}\, d\omega' , \tag{3.18}$$

where ε_∞ is the high-frequency dielectric constant and P represents the Cauchy's principal value.

Substituting eq.(3.15) into eq.(3.17), we obtain the following equation by using the contour shown in Fig. 3-2.

$$\varepsilon_1(\omega) - 1 = \sum_{i=A,B,C} A|<|p|>|^2\, \omega_0^{-3/2} f(x_{0i}) \quad , \tag{3.19}$$

where

$$f(x) = (1/x^2)[2 - (1+x)^{1/2} - (1-x)^{1/2}] \quad . \tag{3.20}$$

f(x) is, in general, a complex function and f(x) can be divided by real and imaginary part as follows;

$$f(x) \equiv f_r(x) + i f_i(x) \tag{3.21}$$

where the subscript r and i indicate the real and imaginary part of f(x), respectively.

$$f_r(x) = \begin{cases} (1/x^2)[2 - (1-x)^{1/2} - (1+x)^{1/2}] & 0 < x \le 1 \quad (3.22a) \\ (1/x^2)[2 - (1+x)^{1/2}] & x > 1 \quad (3.22b) \end{cases}$$

$$f_i(x) = \begin{cases} 0 & 0 < x \le 1 \quad (3.23a) \\ (1/x^2)(x-1)^{1/2} & x > 1 \quad (3.23b) \end{cases}$$

Figure 3-3 shows the calculated line shape of $f_r(x)$ and $f_i(x)$. Note that imaginary part of f(x) is zero below the band gap ($x < 1$).

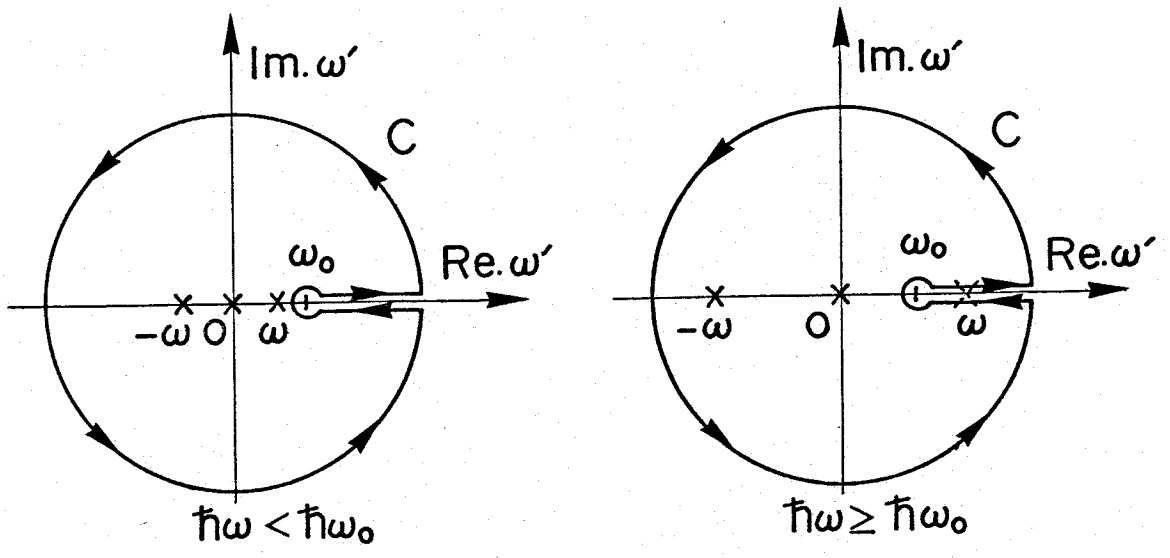

Fig. 3-2. Contour for the calculation of the real part of the dielectric function f(x).

For zincblende-type crystals the dispersion in the dielectric constant of Ge and III-V compounds can be interpreted with the parabolic band model (PBM).[74] In this model the dielectric constant below the edge is the sum of the contribution of the E_0 and $E_0+\Delta_0$ edge plus a constant D which corresponds to the effect of the avarage gap E_g.[80] In the II-VI compounds the effect of the exciton is strong and exciton modificaiton of the interband absorption edge is taken into accousnt. If we include the contribution of the ground state of the E_0 exciton:

$$\frac{C''_{ex}}{E_{ex}^2 - (\hbar\omega)^2} \tag{3.24}$$

we can write the dielectric constant as follows:

$$\varepsilon(\omega) = C''_{ex} \frac{1}{E_{ex}^2 - E} + C''_0 \left[f\left(\frac{\omega}{\omega_0}\right) + \frac{1}{2}\left(\frac{\omega}{\omega_{0s}}\right) f\left(\frac{\omega}{\omega_{os}}\right) \right] + D \tag{3.25}$$

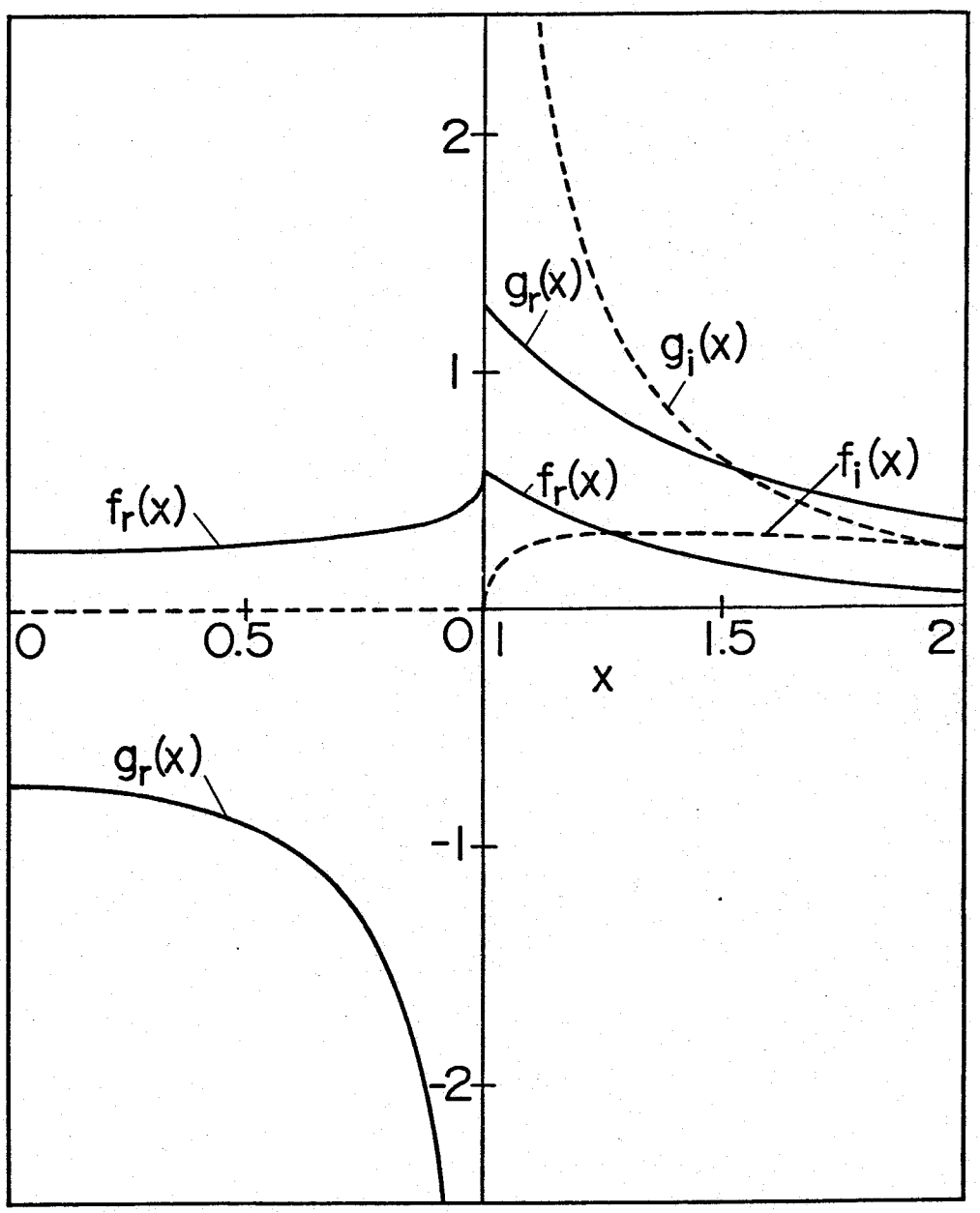

Fig. 3-3. Real and imaginary part of the dielectric functions f(x) and g(x).

where C_{ex}, and C_0 are the fitting parameters and E_{ex} is the energy of the ground state exciton.

3.5 Photoelastic Constant

In this subsection we shall represent a theoretical expression of the photoelestic constnat in zincblende and wurtzite materials. Now we show the effect of [001] and [111] stress for zincblende-type crystals.

For [001] stress, the strain components are derived from eq.(3.1) as

$$\begin{aligned} e_{zz} &= S_{11}X \ , \\ e_{xx} &= e_{yy} = S_{12}X \ , \\ e_{xy} &= e_{xz} = e_{yz} = 0 \ , \end{aligned} \tag{3.26}$$

where S_{11} and S_{12} are elastic compliance constants. The strain-orbital Hamiltonian for the energy difference between conduction and valence band becomes

$$\begin{aligned} H_\varepsilon &= -a(S_{11}+2S_{12})X - 3b(S_{11}-S_{12})X(L_z^{\,2} - \tfrac{1}{3}\mathbb{L}) \\ &= -\delta E_H - \tfrac{3}{2}\delta E_{001}(L_z^{\,2} - \tfrac{1}{3}\mathbb{L}) \ , \end{aligned} \tag{3.27}$$

where $\delta E_H = a(S_{11}+2S_{12})X = (\partial E_g/\partial P)\times P$ is the shift of the gap E_g, due to the hydrostatic component of the strain, and $\delta E_{001} = 2b(S_{11}-S_{12})X$ is the linear splitting of the $p_{3/2}$ multiplet. From eq.(3.26) and (3.27) the Hamiltonian matrix for the valence bands can be written as [81]

$$\begin{array}{c} \\ |\tfrac{3}{2},\tfrac{3}{2}\rangle_{001} \\ |\tfrac{3}{2},\tfrac{1}{2}\rangle_{001} \\ |\tfrac{1}{2},\tfrac{1}{2}\rangle_{001} \end{array} \begin{array}{c} \begin{array}{ccc} |\tfrac{3}{2},\tfrac{3}{2}\rangle_{001} & |\tfrac{3}{2},\tfrac{1}{2}\rangle_{001} & |\tfrac{1}{2},\tfrac{1}{2}\rangle_{001} \end{array} \\ \begin{bmatrix} \tfrac{1}{3}\Delta_0 - \delta E_H - \tfrac{1}{2}\delta E_{001} & 0 & 0 \\ 0 & \tfrac{1}{3}\Delta_0 - \delta E_H + \tfrac{1}{2}\delta E_{001} & \tfrac{1}{2}\sqrt{2}\delta E_{001} \\ 0 & \tfrac{1}{2}\sqrt{2}\delta E_{001} & -\tfrac{2}{3}\Delta_0 - \delta E_H \end{bmatrix} \end{array} \tag{3.28}$$

where Δ_0 is the spin-splitting of the valence bands at $\vec{k} = 0$. Diagonalizing the above Hamiltonian matrix, one obtains, for the change in the energy difference between the conduciton and valence band at $\vec{k} = 0$;

$$\Delta(E_c - E_{v2}) = -\frac{1}{3}\Delta_0 + \delta E_H + \frac{1}{2}\delta E_{001} ,$$

$$\Delta(E_c - E_{v1}) = \frac{1}{6}\Delta 0 + \delta E_H - \frac{1}{4}\delta E_{001} - \frac{1}{2}[\Delta_0{}^2 + \Delta_0 \delta E_{001} + (9/4)(\delta E_{001})^2]^{1/2} ,$$

$$\Delta(E_c - E_{v3}) = \frac{1}{6}\Delta 0 + \delta E_H - \frac{1}{4}\delta E_{001} + \frac{1}{2}[\Delta_0{}^2 + \Delta_0 \delta E_{001} + (9/4)(\delta E_{001})^2]^{1/2} . \tag{3.29}$$

For $\delta E_{001} \ll \Delta_0$, eq.(3.29) can be explained in power of $\delta E_{001}/\Delta_0$ to give

$$\Delta(E_c - E_{v2}) = -\frac{1}{3}\Delta 0 + \delta E_H + \frac{1}{2}\delta E_{001} ,$$

$$\Delta(E_c - E_{v1}) = -\frac{1}{3}\Delta 0 + \delta E_H - \frac{1}{2}\delta E_{001} - \frac{1}{2}(\delta E_{001})^2/\Delta_0 , \tag{3.30}$$

$$\Delta(E_c - E_{v3}) = \frac{2}{3}\Delta 0 + \delta E_H + \frac{1}{2}(\delta E_{001})^2/\Delta_0 .$$

It should be noted that since the state $|\frac{3}{2},\frac{3}{2}\rangle$ is not coupled by the stress to other two valence bands it has a linear stress dependence while the states with $m_J = 1/2$ have a nonlinear stress dependence caused by the off-diagonal term in eq.(3.28). From the unperturbed wave functions of the valence band state at $\vec{k} = 0$, to the first order in $\alpha_0(E_{001}/\Delta_0)$ have been calculated to first order X ;

$$u_{v2,X} = |\tfrac{3}{2},\tfrac{3}{2}\rangle_{001} ,$$

$$u_{v1,X} = |\tfrac{3}{2},\tfrac{1}{2}\rangle_{001} + \frac{1}{\sqrt{2}}\alpha_0 |\tfrac{1}{2},\tfrac{1}{2}\rangle_{001} , \tag{3.31}$$

$$u_{v3,X} = |\tfrac{1}{2},\tfrac{1}{2}\rangle_{001} + \frac{1}{\sqrt{2}}\alpha_0 |\tfrac{1}{2},\tfrac{1}{2}\rangle_{001} .$$

It should be shown that the intensity of optical transition is proportional to

$$|\langle\Psi_1|\vec{e}\cdot\vec{p}|\Psi_2\rangle| \ , \tag{3.32}$$

where $\vec{e}$ is the unit polarizaiton vector of the electric field of the incident radiaition and $\vec{p}$ is the linear momentum. For symmetry consideration,[82,83] it can be shown that the only nonzero matix elements of $\vec{p}$ between $\Gamma_{25'}$ and Γ_2 are

$$P = \langle X\uparrow|P_x|S\uparrow\rangle = \langle Y\uparrow|P_y|S\uparrow\rangle = \langle Z\uparrow|P_z|S\uparrow\rangle \ , \tag{3.33}$$

with similar expressions for spin down. The p-matrix elements for zincblende- and wurtzite-type crystals at $\vec{k} = 0$ are shown in Table 2-1 in Chapter 2. From wavefunctions shown in eq.(3.31), selection rules and relative intensities for transition to Γ_2 have been calculated, as a function of X for light polarized parallel and perpendicular to the stress axis. These intensities are given by

$$\begin{aligned}
&\langle c|P_{\parallel}|v_1\rangle^2 = \tfrac{2}{3}P^2(1+\alpha_0-\tfrac{3}{4}\alpha_0^2+\cdots) \ , \\
&\langle c|P_{\perp}|v_1\rangle^2 = \tfrac{1}{6}P^2(1-2\alpha_0+\tfrac{3}{2}\alpha_0^2+\cdots) \ , \\
&\langle c|P_{\parallel}|v_2\rangle^2 = 0 \ , \\
&\langle c|P_{\perp}|v_2\rangle^2 = \tfrac{1}{2}P^2 \ , \\
&\langle c|P_{\parallel}|v_3\rangle^2 = \tfrac{1}{3}P^2(1-2\alpha_0+\tfrac{3}{2}\alpha_0^2+\cdots) \ , \\
&\langle c|P_{\perp}|v_3\rangle^2 = \tfrac{1}{3}P^2(1+\alpha_0-\tfrac{3}{4}\alpha_0^2+\cdots) \ .
\end{aligned} \tag{2.34}$$

For a [111] stress, the analysis is almost identical to that for the stress along [001]. The strain components are given by[81]

$$e_{xx} = e_{yy} = e_{zz} = (S_{11}+2S_{12})(\tfrac{1}{3}X) \ , \tag{3.35}$$

$$e_{xy} = e_{yz} = e_{zx} = (\tfrac{1}{2}S_{44})(\tfrac{1}{3}X) \ , \tag{3.36}$$

where S_{44} is an elastic compliance constant. The strain Hamailtonian of eq.(2.149) now has the form

$$\begin{aligned}
H_\varepsilon = &-a(S_{11}+2S_{12})X - (6d/\sqrt{3}) \\
&\times [\{L_xL_y\}+\{L_yL_z\}+\{L_xL_z\}](\tfrac{1}{2}S_{44})(\tfrac{1}{3}X) \ .
\end{aligned} \tag{3.37}$$

The problem of diagonalizing H_ε can be simplified if we make a transformation such that the [111] direction becomes z axis. For stress parallel to [111] direction it is convenient to make a rotation so that [111] direction becomes the z axis. The wave functions of the valence band then have the form[81]

$$|\tfrac{3}{2},\tfrac{3}{2}\rangle_{111} = |\,(\tfrac{1}{2})^{1/2}\ (\bar{X}+i\bar{Y})\uparrow\rangle\ , \tag{3.38}$$

$$|\tfrac{3}{2},\tfrac{1}{2}\rangle_{111} = |\,(\tfrac{1}{6})^{1/2}[2\bar{Z}\uparrow + (\bar{X}+i\bar{Y})\downarrow]\rangle\ , \tag{3.39}$$

$$|\tfrac{1}{2},\tfrac{1}{2}\rangle_{111} = |\,(\tfrac{1}{3})^{1/2}[\bar{Z}\uparrow - (\bar{X}-i\bar{Y})\downarrow]\rangle\ , \tag{3.40}$$

where

$$\bar{X} = (\tfrac{1}{2})^{1/2}(X-Y)\ , \tag{3.41}$$

$$\bar{Y} = (\tfrac{1}{6})^{1/2}(X+Y-2Z)\ , \tag{3.42}$$

$$\bar{Z} = (\tfrac{1}{3})^{1/2}(X+Y+Z)\ . \tag{3.43}$$

The stress independent wave functions have the same form as eq.(3.31) with α_0 replaced by α_1 $(=\delta E_{111}/\Delta_0)$. Under this rotation the Hamiltonian matrix for this stress direction has the same form as the matrix for along the [001] direction [eq.(3.28)], with the quantity $\delta E_{111} = (d/\sqrt{3})S_{44}X$ replacing δE_{001}. Therefore, from eqs.(3.30) and (3.34) one can write for enegry change between the conduction and valence bands, and the momentum matix elements for [111] stress to first order in stress as

$$\begin{aligned}
\Delta(E_c - E_{v1}) &= \tfrac{1}{3}\Delta_0 + \delta E_H - \tfrac{1}{2}\delta E_{111} + \cdots\ , \\
\Delta(E_c - E_{v2}) &= -\tfrac{1}{3}\Delta_0 + \delta E_H + \tfrac{1}{2}\delta E_{111} + \cdots\ , \\
\Delta(E_c - E_{v3}) &= \tfrac{2}{3}\Delta_0 + \delta E_H + \tfrac{1}{2}\delta E_{111} + \cdots\ ,
\end{aligned} \tag{3.44}$$

$$
\begin{aligned}
&|\langle c|P_{\parallel}|v_1\rangle|^2 = \frac{2}{3}P^2(1+\alpha_1+\cdots)\ ,\\
&|\langle c|P_{\perp}|v_1\rangle|^2 = \frac{1}{6}P^2(1-2\alpha_1+\cdots)\ ,\\
&|\langle c|P_{\parallel}|v_2\rangle|^2 = 0\ ,\\
&|\langle c|P_{\perp}|v_2\rangle|^2 = \frac{1}{2}P^2\ ,\\
&|\langle c|P_{\parallel}|v_3\rangle|^2 = \frac{1}{3}P^2(1-2\alpha_1+\cdots)\ ,\\
&|\langle c|P_{\perp}|v_3\rangle|^2 = \frac{1}{3}P^2(1+\alpha_1+\cdots)\ .
\end{aligned}
\tag{3.45}
$$

To first order in stress, the change in $\varepsilon(\omega)$ can be expressed by[74]

$$
\Delta\varepsilon(\omega) = \frac{\partial\varepsilon}{\partial X}X = \sum_{i=A,B,C}\left(\frac{\partial\varepsilon}{\partial P_i}\Delta P_i + \frac{\partial\varepsilon}{\partial\omega_{gi}}\Delta\omega_{gi}\right)\ , \tag{3.46}
$$

where $P = |\langle|p|\rangle|^2$ is the squared p-matirx element and summation indicate that contribution from three valence bands must included. The first term on the right-hand side of eq.(3.46) corresponds to the contribution from the first order change in the squared p-matrix elements and interband transition energies, respectively.

Substitiuting eqs.(3.30) and (3.34) into eq.(3.46) and using the model dielectric constant of eq. (3.20), one obtains the expression of the photoelastic constant $P_{11}-P_{12}$ in the following expression:[77]

$$
\begin{aligned}
P_{11}-P_{12} = {} & \frac{C}{4n_0}\{-g(x_0)+4\frac{E_0}{\Delta_0}[f(x_0)-(\frac{\omega_0}{\omega_{0s}})^{3/2}f(x_{0s})]\}\\
& + \frac{C_{ex}}{4n_0}\{\frac{3-x_{ex}}{(1-x_{ex}^2)^2}+\frac{E_0}{\Delta_0}[\frac{1}{1-x_{ex}^2}+(\frac{E_{ex}}{E_{ex}+\Delta_0})^3\frac{1}{1-x_{exs}^2}]\}+D\ ,
\end{aligned}
\tag{3.47}
$$

where $g(x)$ are defined by [see Fig. 3-3]

$$
g(x) = (1/x^2)[2-(1+x)^{-1/2}-(1-x)^{-1/2}]\ . \tag{3.48}
$$

and

$$C = -(3m_e^*/2)^{3/2}P^2 b\omega_0^{-5/2} , \tag{3.49}$$

$$C_{ex} = -3(4\pi N f_1)b/E_{ex}^2 . \tag{3.50}$$

The photoelastic constant P_{44} can be obtained by the same procedure in the case of $P_{11} - P_{12}$. Substituting eqs.(3.44) and (3.45) into eq.(3.46) and using model dielectric constant of eq.(3.20), one obtains the expression of the photoelastic constant P_{44} in the following expression: [78]

$$P_{44} = \{\frac{C}{n_0^4} - g(x) + 4\frac{E_0}{\Delta_0}[f(x_0) - (\frac{\omega_0}{\omega_{os}})^{3/2} f(x_{0s})]\}$$
$$+ \frac{C_{ex}}{n_0^4}\{\frac{3 - x_{ex}}{(1 - x_{ex}^2)^2} + \frac{E_0}{\Delta_0}[\frac{1}{1 - x_{ex}^2} + (\frac{E_{ex}}{E_{ex} + \Delta_0})^3 \frac{1}{1 - x_{exs}^2}]\} + D, \tag{3.51}$$

where

$$C = -(3m_e^*/2)^{3/2}P^2 d\omega_0^{-5/2} , \tag{3.52}$$

$$C_{ex} = -3(4\pi N f_1)d/E_{ex}^2 . \tag{3.53}$$

In eqs.(3.47) to (3.53), we used the following notation; $x_0 = \hbar\omega/E_0$, $x_{0s} = \hbar\omega/(E_0 + \Delta_0)$, $x_{ex} = \hbar\omega/E_{x1}$, $x_{exs} = \hbar\omega/(E_{x1} + \Delta_0)$ with $\hbar\omega_0 = E_0$ and $\hbar\omega_{0s} = E_0 + \Delta_0$, $\hbar\omega$ the photon energy, Δ_0 the spin-orbit splitting energy, E_{x1} the ground-state exciton energy, P the momentum matrix element, and N and f_1 are the number of molecules per unit volume and oscillator strength of the exciton respectively. The term D is the non-dispersive contribution arising from the E_1, $E_1 + \Delta_1$ and E_2 gaps. Long-wavelength dielectric properties of semiconductors have been treated quite successfully by Van Vechten [84] with the Penn model, [80] a simple model of an insulator in which an average isotropic gap at the edge of spherical Brillouin zone is assumed. It is well known that ε_i (the imaginary part of the ε) in zincblende materials has a strong peak (E_2) in the neighbourhood of which most of the

optical density of state is concentrated. [85] The corresponding transition occur over a large number of the Brillouin zone, close to its boundaries. For the purpose of represent this fact Penn [80] suggested the model of non-physical spherical Brillouin zone with an isotropic gap (ω_g) at its bounderies. Penn obtained with this model the static dielectric constant for a finite wavevector q. The result can be approximated by the analytic form.[85]

$$\varepsilon(\omega = 0, q) = 1 + (\frac{\omega_p}{\omega_g})^2 \; F \; \{1 + \frac{\omega_F}{\omega_g} \frac{q}{k_F} F^{1/2}\}^{-2} \quad , \tag{3.54}$$

with

$$F = 1 - \frac{\omega_g}{\omega_F} + \frac{1}{3} (\frac{\omega_g}{\omega_F})^2 \quad . \tag{3.55}$$

In eq.(3.54) ω_p is the plasma frequency obtained for the density of valence electron and ω_F and k_F the corresponding free electron Fermi energy and wave number. The dimensionless quantity F is usually close to one. Equation (3.54) yields two contribution to the change in $\varepsilon(0)$ due to the stress (X): One arises from the change in plasma frequency and the other from that in the Penn gap, as follows;

$$\frac{1}{\varepsilon_0} \frac{d\varepsilon_0}{dX} = 2(\frac{d \ln\omega_p}{dX} - \frac{d \ln\omega_g}{dX}) \quad . \tag{3.56}$$

The first term in the braket should not exist for pure shear stress. According to Vechten, [84] ω_g for C, Ge, Si is proportional to $(a_0^{-2.5})$ where a_0 is the lattice constant. If one makes the assumption that this law gives also the change in ω_g with lattice constant for a given material when a stress is applied one can calculate the volume dependence of ε_0

$$\frac{1}{\varepsilon_0} \frac{d\varepsilon_0}{dX} = 2(0 - \frac{d \ln(X^{-2.5})}{dX}) = 5/X \, . \tag{3.57}$$

Equation (3.57) become the following relation

$$\Delta\tilde{\varepsilon}(0)/\tilde{\varepsilon}(0) = 5 \; \tilde{e} \quad , \tag{3.58}$$

where $\tilde{\varepsilon}$ and $\tilde{e}$ are the static dielectric constant and strain tensors, respsctively. Using eq.(3.58) one obtains the non-dispersive photoelastic constant[78)]

$$D = \frac{1}{n_0^4} 5\varepsilon(0) \qquad \text{for } P_{11} - P_{12} , \tag{3.59}$$

$$D' = \frac{1}{n_0^4} \frac{5}{2} \varepsilon(0) \qquad \text{for } P_{44} . \tag{3.60}$$

Equations (3.59) and (3.60) predict the correct sign for D and D', but a magnitude which is several times too large. This is because the contribution of the E_0, E_1, E_2 gaps to the photoelastic constant do not have the same signs. The effect of damping was taken into account by replacing $\hbar\omega$ with $\hbar\omega + i\Gamma$ in the above equations of the photoelastic constant.

The piezobirefringence analysis of the wurtzite-type crystals is almost identical to the zincblende-type crystals. The stress-induced changes in the band gap energies and squared p-matrix elements can be obtained by solving the eigenvalue problem as similar to those in the case of zincblende. We now present the component of dielectric tensor by taking into acount the exciton effect in the following form:

$$\varepsilon_{ij}^{\alpha}(E) = A_{ij}^{\alpha} \left(\frac{C_{ij}^{ex\alpha}}{1 - x_{ex\alpha}^2} + f(x_{0\alpha}) \right) , \tag{3.61}$$

with

$$A_{ij}^{\alpha} = F_{ij}^{\alpha} E_{ex} (GE_{g\alpha})^{3/2} / 8 , \tag{3.62}$$

and

$$C_{ij}^{ex\alpha} = 8(GE_{g\alpha})^{3/2} / (F_{ij}^{\alpha} E_{ex}^4) . \tag{3.63}$$

Here α labels the three valence bands A,B, and C, F_{ij} is the streigth parameter(eV^2) related to the oscillator strength, and G is the exciton binding energy. The first and second terms in the right-hand side of eq.(3.61) correspond to the cotributions from the discrete excitons and the

unbound continuum excitons transitons, respectively.

Case 1. Photoelastic Constant $P_{11} - P_{21}$ for Wurtzite-Type Crystals

Using the strain-orbital Hamiltonian of eq.(2.185) and three wave functions in valence bands of eqs.(2.173) to (2.178), the stress induced change in the band gap energys and strength parameters are obtained as follows (first order in stress X)

$$\Delta E_{gA} = [\, E_{gA}(X) - E_{gA}(0) \,] = 0 \,, \tag{3.64a}$$

$$\Delta E_{gB} = [\, E_{gB}(X) - E_{gB}(0) \,] = 0 \,, \tag{3.64b}$$

$$\Delta E_{gC} = [\, E_{gC}(X) - E_{gC}(0) \,] = 0 \,, \tag{3.64c}$$

$$\Delta F^{A}_{xy}/F^{A}_{xx}(0) = [\Delta F^{A}_{xx} - \Delta F^{A}_{yy}]/F^{A}_{xx}(0) = 4\left(\frac{a_B^2}{E_{BA}} + \frac{a_C^2}{E_{CA}}\right)C_5(S_{11} - S_{12})X \,, \tag{3.64d}$$

$$\Delta F^{B}_{xy}/F^{B}_{xx}(0) = [\Delta F^{B}_{xx} - \Delta F^{B}_{yy}]/F^{B}_{xx}(0) = -\frac{4}{E_{BA}}C_5(S_{11} - S_{12})X \,, \tag{3.64e}$$

$$\Delta F^{C}_{xy}/F^{C}_{xx}(0) = [\Delta F^{C}_{xx} - \Delta F^{C}_{yy}]\, F^{C}_{xx}(0) = -\frac{4}{E_{CA}}C_5(S_{11} - S_{12})X \,, \tag{3.64f}$$

where C_5 is the deformation potential, E_{BA} and E_{CA} are defined in eq. (2.170) to eq. (2.172). Substituting eq. (3.64) into eq. (3.46), one obtains the expression of the photoelestic constant P_{66} $(= \frac{1}{2}(P_{11} - P_{12}))$ in the following form:

$$P_{66} = \frac{1}{\varepsilon_{11}}\left(\frac{1}{2} D_{66} + C_5 F_{66}\right) , \tag{3.65}$$

with

$$F_{66} = 2\left(\frac{a_B^2}{E_{BA}} + \frac{a_C^2}{E_{CA}}\right)\varepsilon^{A}_{xx} - 2\frac{1}{E_{BA}}\varepsilon^{B}_{xx} - 2\frac{1}{E_{CA}}\varepsilon^{C}_{xx} . \tag{3.66}$$

In eq.(3.65) D_{66} is the non-dispersive contribution arising from the higher lying critical points. In accordance with the previous discussion, we can introduce the lifetime broadening effect in the calculation of the photoelastic constant by replacing E of eq.(3.61) by $E + i\Gamma$.

Case 2. Photoelastic Constant P_{44} for Wurtzite-Type Crystals

The photoelastic constant P_{44} can be obtained by using the strain-orbital Hamiltonian of eq.(2.185) and three wave functions in valence bands of eqs.(2.173) and (2.178), the stress induced change in the band gap energy and strength parameters are obtained as follows;

$$\Delta E_{gA} = [\, E_{gA}(X) - E_{gA}(0) \,] = 0 \,, \tag{3.67a}$$

$$\Delta E_{gB} = [\, E_{gB}(X) - E_{gB}(0) \,] = 0 \,, \tag{3.67b}$$

$$\Delta E_{gC} = [\, E_{gC}(X) - E_{gB}(0) \,] = 0 \,, \tag{3.67c}$$

$$\Delta F^{A}_{xz}/F^{A}_{xx}(0) = \frac{1}{\sqrt{2}} C_6 \, T \left(\frac{a_C^2}{E_{BA}} + \frac{a_B^2}{E_{CA}} \right) , \tag{3.67d}$$

$$\Delta F^{B}_{xz}/F^{B}_{xx}(0) = -\frac{1}{\sqrt{2}} C_6 \frac{T}{a_B^2} \left(\frac{a_C^2}{E_{BA}} - \frac{1}{E_{CB}} \right) , \tag{3.67e}$$

$$\Delta F^{C}_{xz}/F^{C}_{xx}(0) = -\frac{1}{\sqrt{2}} C_6 \frac{T}{a_C^2} \left(\frac{a_B^2}{E_{CA}} + \frac{1}{E_{CB}} \right) , \tag{3.67f}$$

where C_6 is the shear deformation potential, and

$$T = \left[\frac{a_B^2 F^{B}_{zz}(0)}{2a_C^2 F^{B}_{xx}(0)} \right]^{1/2} = \left[\frac{a_C^2 F^{C}_{zz}(0)}{2a_B^2 F^{C}_{xx}(0)} \right]^{1/2} . \tag{3.68}$$

Substituting eq.(3.67) into eq.(3.46), we obtain

$$P_{44} = \frac{1}{\varepsilon_{11}\varepsilon_{33}} (D_{44} + C_6 F_{44}) \,, \tag{3.69}$$

where

$$F_{44} = \frac{T}{2\sqrt{2}} \left[\left(\frac{a_C^2}{E_{BA}} + \frac{a_B^2}{E_{CA}} \right) \varepsilon^{A}_{xx} - \left(\frac{a_C^2}{a_B^2 E_{BA}} - \frac{1}{a_B^2 E_{CB}} \right) \varepsilon^{B}_{xx} \right.$$

$$\left. - \left(\frac{a_B^2}{a_C^2 E_{CA}} + \frac{1}{a_C^2 E_{CB}} \right) \varepsilon^{C}_{xx} \right] . \tag{3.70}$$

In eq.(3.70), D_{44} is the non-dispersive contribution arising from the higher lying gaps.

Case 3. Photoelastic Constant P_{31} for Wurtzite-Type Crystals

According to the Brillouin scattering scattering geometry for LA mode phonons, non-zero strain component is only e_{xx} (we can replace $e_{xx}+e_{yy}$ with e_{xx} without any loss of generality) and the other components vanish. Using the strain-orbital Hamiltonian of eqs.(2.184) and (2.185) and three wave functions in valence bands of eqs.(2.173) and (2.178), the stress induced change in the band gap energy and strength patameters are obtained as follows:

$$\Delta E_{gA} = [\ (C_2 - d_2) + C_4]e_{xx}\ , \tag{3.71a}$$

$$\Delta E_{gB} = [\ (C_2 - d_2) + a_B^2 C_4]e_{xx}\ , \tag{3.71b}$$

$$\Delta E_{gC} = [\ (C_2 - d_2) + a_C^2 C_4]e_{xx}\ , \tag{3.71c}$$

$$\Delta F_{xx}^{A}/F_{xx}^{A}(0) = 0\ , \tag{3.72a}$$

$$\Delta F_{xx}^{B}/F_{xx}^{B}(0) = -2\ C_4 \frac{a_B^2}{E_{CB}}\ , \tag{3.72b}$$

$$\Delta F_{xx}^{C}/F_{xx}^{C}(0) = 2\ C_4 \frac{a_C^2}{E_{CB}}\ . \tag{3.72c}$$

Substituting eq.(3.71) into eq.(3.46), we obtain the expression of the photoelastic constant p_{31} in the following form:

$$P_{31} = \frac{1}{\varepsilon_{33}\varepsilon_{33}}[\ D_{31} + C_4 F_{31}^{(A)} + (C_2 - d_2)F_{31}^{(B)}\ ]\ , \tag{3.73}$$

where

$$F_{31}^{(A)} = -2[\ \frac{a_B^2\varepsilon_{xx}^B - a_C^2\varepsilon_{xx}^C}{E_{CB}}] + [\ \frac{\partial\varepsilon_{xx}^A}{\partial E_{gA}} + a_B^2 \frac{\partial\varepsilon_{xx}^B}{\partial E_{gA}} + a_C^2 \frac{\partial\varepsilon_{xx}^C}{\partial E_{gC}}]\ , \tag{3.74}$$

$$F_{31}^{(B)} = (\frac{\partial\varepsilon_{xx}^A}{\partial E_{gA}} + \frac{\partial\varepsilon_{xx}^B}{\partial E_{gB}} + \frac{\partial\varepsilon_{xx}^C}{\partial E_{gC}})\ , \tag{3.75}$$

where $\frac{\partial \varepsilon_{ij}^{\alpha}}{\partial E_{g\alpha}}$ is the first derivative of the dielectic function $\varepsilon_{ij}^{\alpha}$ by the energy gap $E_{g\alpha}$ and given by the following equation:

$$\frac{\partial \varepsilon_{ij}^{\alpha}}{\partial E_{g\alpha}} = B_{ij}^{\alpha} \{ \frac{C_{ij}^{ex\alpha}(3-x_{ex\alpha})}{(1-x_{ex\alpha}^2)^2} - g(x_{0\alpha}) \} , \tag{3.76}$$

with

$$B_{ij}^{\alpha} = -F_{ij}^{\alpha}(GE_{g\alpha})^{3/2}/16 . \tag{3.77}$$

In eq.(3.73), D_{31} is the nondispersive contribution arising from the higher-lying gap transitions.

Next we consider the relation between the Brillouin-scattering cross section and the photoelastic constant. From the result of Nelson et. al.[46] we find the power ratio of the scattered light P^{φ} to the incident light P^{φ} as

$$\frac{P^{\varphi}}{P^{\theta}} = \frac{\omega^4 \Phi l_D \Delta\Omega_D (n^{\varphi} n^{\theta})^3 \cos\delta \ (\cos\delta^{\theta}) \tau^{\varphi} \tau^{\theta}}{32\pi^2 c^4 \rho v^2 \sin\theta_s} |d_m^{\varphi} p_{mnkl}^{eff} d_n^{\theta} b_k a_l|^2 \equiv \sigma_B l_D \Delta\Omega_D \tau^{\varphi} \tau^{\theta}, \tag{3.78}$$

where the notation is the same as used by Nelson et al.,[46] and $k_B T$ is replaced by Φ. In the present strudy we used three types of acoustic waves, T1- , T2- and LA modes as defined in Chapter 2.2. The relation between the Brillouin scattering cross section for the three modes of acoustic waves are

$$\sigma_B(T1) = A_1 n_0^6 \omega^4 (P_{11} - P_{12})^2 , \tag{3.79}$$

$$\sigma_B(T2) = A_2 n_0^6 \omega^4 P_{44}^2 , \tag{3.80}$$

for the zincblende-type crystals, and

$$\sigma_B(T1) = B_1 n_o^6 \omega^4 (P_{11} - P_{12})^2 , \tag{3.81}$$

$$\sigma_B(T2) = B_2 n_o^3 n_e^3 \omega^4 P_{44}^2 , \tag{3.82}$$

$$\sigma_B(LA) = B_3 n_e^3 n_e^3 \omega^4 P_{31}^2 \ , \tag{3.83}$$

for the wurtzite or polytype crystals, where A_i and B_i are frequency independent factors involved in eq.(3.78). Using these relations we are able to compare the wavelength dependence of the Brillouin-scattering cross sections with that of photoelastic constants determined from the piezo-birefringence measurements.

CHAPTER 4

EXPERIMENTAL TECHNIQUE

4.1 Introduction

We have largely concerned ourselves up to this point in the dissertation, with the theoretical aspect of the Brillouin scattering and piezobirefringence. In this chapter, we discuss the experimental aspects of our work. The intense phonon domains amplified by acoustoelectric instabilities are very useful to investigate the dispersion spectra of the resonant Brillouin scattering near the fundamental absorption edge of semiconductors. They consists of intense ultrasonic waves with various frequency components from 0.1 to 4 GHz, concentrated spatially with about 0.5 mm width.[86 - 88] The acoustic waves in domains are amplified by a factor of 10^6 to 10^9 above thermal equilibrium value. These amplified waves consists of piezoelectrically active shear waves in a narrow cone ($<10°$) along the direction of the electron drift. The wide frequency range and high energy density provide great advantages in investigating phonon-phonon interaction, electron-phonon-photon interaction in semiconductors. The generation of acoustic domains , however, are restricted to piezoelectric semiconductors such as GaAs,[89] CdS,[90] GaSb,[91] CdSe,[92] and ZnO.[93] To overcome this restriction, acoustic domain injection method is introduced in which the acoustic domains are injected from CdS to other semiconducters or insulators. This acoustic domain injection technique has also successfully extended by us to semiconductors such as ZnS and layered compound HgI_2. In these experiments, the incident photon energies, however, were restricted to the region in which the samples

were transparent due to the strong absorption near the band gap. Therefore it has been difficult to obtain the dispersion of the Brillouin scattering cross section in the opaque region (above the fundamental absoption edge) when we use a conventional light source (Xe flash lamp) and transmission type of experiment. To overcome this limitation, we employed the reflection scattering geometry and a high intensity Ar ion laser between 457.9 and 514.5 nm. It should be noted that we investigated the Brillouin scattering not by ripple mechanism but by the elasto-optic mechanism. The Brillouin scattering by the ripple mechanism, which is caused by the dynamic corrugation on the surface, show no dispersion. However the Brillouin scattering by the elasto-optic mechanism, which is caused by the change in the dielectric constant by the phonons, shows dispersion. Our main interest of the present study is the latter mechanism (elasto-optic mechanism) in the opaque region of the materials.

As is shown in the previous Section, Brillouin scattering cross section is proportional to the relevant photoelastic constant. Therefore we can obtain the dispersion of the photoelastic constant by the Brillouin scattering experiment. It is impossible, however, to determine the absolute value of the photoelastic constant only by the Brillouin scattering experiment. In order to determine the sign and absolute value of the photo-elastic constants, we performend the piezobirefringence measurements.

In section 4.2 we present some of the physical poperties of the materials used in the present study and sample preparation method. In Section 4.3, we discuss the Brillouin scattering technique below and above the fundamental absorption edge. In Section 4.4, we discuss the piezo-birefringence technique. In Section 4.5, we describe the acoustic domain injection method.

4.2 Material and Sample Preparation

In the present study we used bulk single crystals, CdS, ZnS, and HgI_2. The CdS crystals used were ultra-high purity (UHP grade) and purchased from Eagle Picher Company. We used two kinds of ZnS crystals; i) synthesized by melt-grown at Eagle Picher Company (UHP grade) ii) grown by I_2 chemical transport method. The melt-grown ZnS contains ≃ 10 % stacking faults along the c-direction of the axis, while ZnS grown by I_2 chemical transport is pure cubic and shows no optical anisotropy. The HgI_2 crystals were grown by the DMSO (dimethylsulfoxide) solution growth. In Table 4-1 are listed the crystal structure, growth method, electrical properties for each crystal.

All the samples used in the present study were cut in the form of rectangular parallelepipeds with typical dimensions of about $0.7 \times 1.5 \times 6.0$ mm^3. The crystal orientation of sample was determined by means of light figure method [94,95] with the accuracy of one degree. They were lapped on a glass plate using 3000 grit Cr_2O_3 powder, and subsequently polished by 8000 grit Al_2O_3. Final optical polishing was done by using 0.3 μm Al_3O_2 powder and polish-etched by Syton for 10 minutes. The optical flat surfaces of layered compound HgI_2 were obtained by cleavage with Cellotape and used for the measurement without any additional treatment. In order to obtain ohmic contacts, indium is deposited by evaporation on the both ends of the samples at $\sim 10^{-6}$ Torr and copper wires are soldered on them. The ZnS samples (polytype and cubic) used in the piezobirefringence experiments were parallelepiped of typical dimensions of $1.2 \times 1.3 \times 6.0$ mm^3 cut from the same crystals used in the Brillouin scattering experiments.

Table 4-1. Electrical and physical properties of the samples used in the present study.

Sample	Crystal Structure	Crystal-Growth Method	Resistivity ($\Omega \cdot$cm)	Conduction Type	Carrier Density (cm^{-3})	Mobility (cm^2/V-sec)
CdS (UHP)[a]	Wurtzite (C_{6v})	Melt-grown	~ 20	n	$\sim 3 \times 10^{15}$	300
ZnS (UHP)[a]	Polytype ($\alpha \simeq 0.1$) (C_{3v})	Melt-grown	$> 10^8$	n	——	——
ZnS [b]	Zincblende (T_d^2)	I_2 chemical transport	1.2	n	$\sim 4.8 \times 10^{16}$	107
HgI_2 [c]	Tetragonal (D_{4h}^{15})	DMSO[d] solution growth	——	——	——	——

a) Purchased from Eagle Picher Company.

b) Provided by Dr. S. Fujita (Kyoto University).

c) Provided by Prof. S. Nakashima (Osaka University).

d) Dimethylsulfoxide (DMSO).

4.3 Brillouin Scattering Technique

4.3.1 Transmission-Type Experiment

The experimental setup of the Brillouin scattering for transmission type of experiment is shown Fig. 4-1. The arrangement was used in the measurements in the photon energy region where the photon energy is below the fundamental absorption edge. Experimental technique in the opaque region by using Ar ion laser are touched upon in the next subsection *4.3.2*.

A high intensity light source of a continuous spectrum is obtained from a Xe-flash tube (Sunpack Strobo GTPRO 4011). The light source enabled us to measure Brillouin scattering signal in the wide spectral range from 300 nm to 900 nm. The spectrometer is a conventional monochromator (JASCO CF-50), 50 cm focal length system. We used gratings blazed for 750 nm and 300 nm (1200 lines per mm). This was calibrated with the emission lines from a mercury arc and a He-Ne laser line. The resolution is about 0.5 - 1 nm in the range of the present experiment. The incident light dispersed with the monochrometer was polarized by a Gran-Thompson prism (P_1) and collimated by lens (L_1) and then focused into the sample. The typical size of light spot at the surface of the specimens was about 0.5 mm in diameter. The scattered beam was analyzed by a film polarizer (Polaroid HN 32 for visible wavelength region, HNB'P for ultra-violet region). The scattered light was detected by a photomultiplier tube. We used at present a photomultiplier tube with an S-20 cathod (RCA-7265), which has approximately 20 % quantum efficiency at 400 nm wavelength and drops to appriximately 2 % q.e. at 720 nm, The detected signal was displayed on a storage oscilloscope (Tecktronics 7623A). A typical Brillouin scattering signal and current wave form in the sample are shown in Figs. 4-2 and 4-3. The experimental configurations of

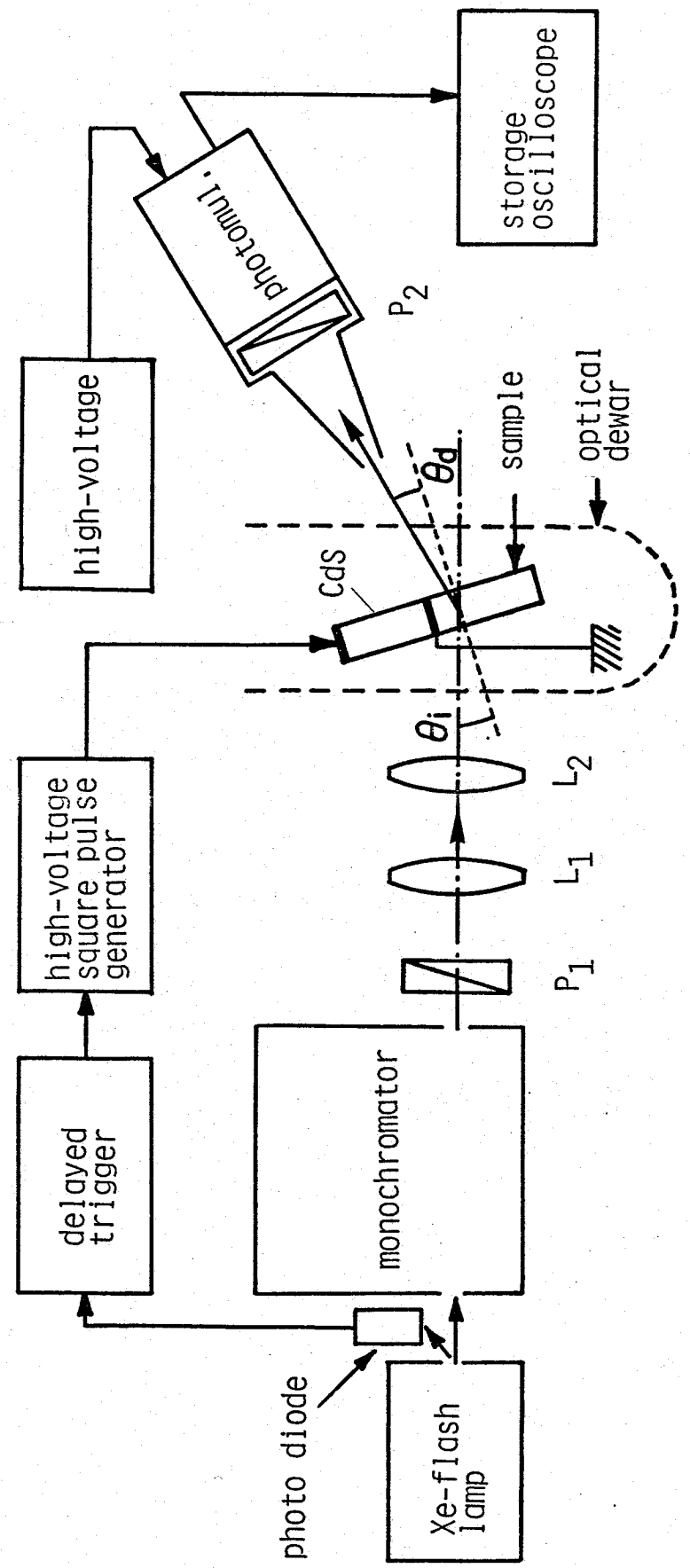

Fig. 4-1. Schematic diagram of the experimental setup used for the Brillouin scattering in the transparent region of the materials

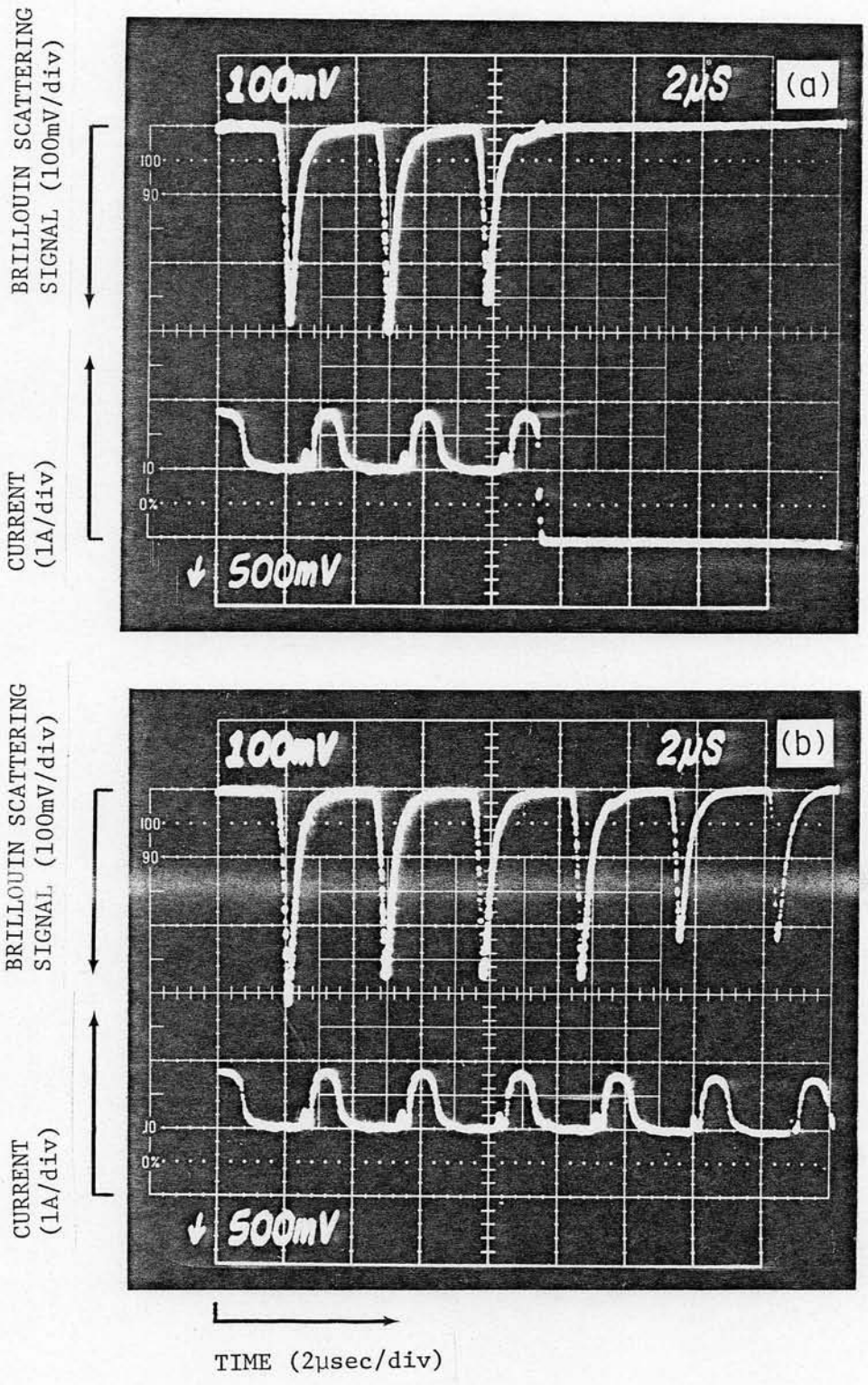

Fig. 4-2. Some typical example of the current-oscillation patterns (lower trace) and Brillouin scattering signals (upper trace) for two different pulse width; (a) 4.6 μs, (b) > 9 μs.

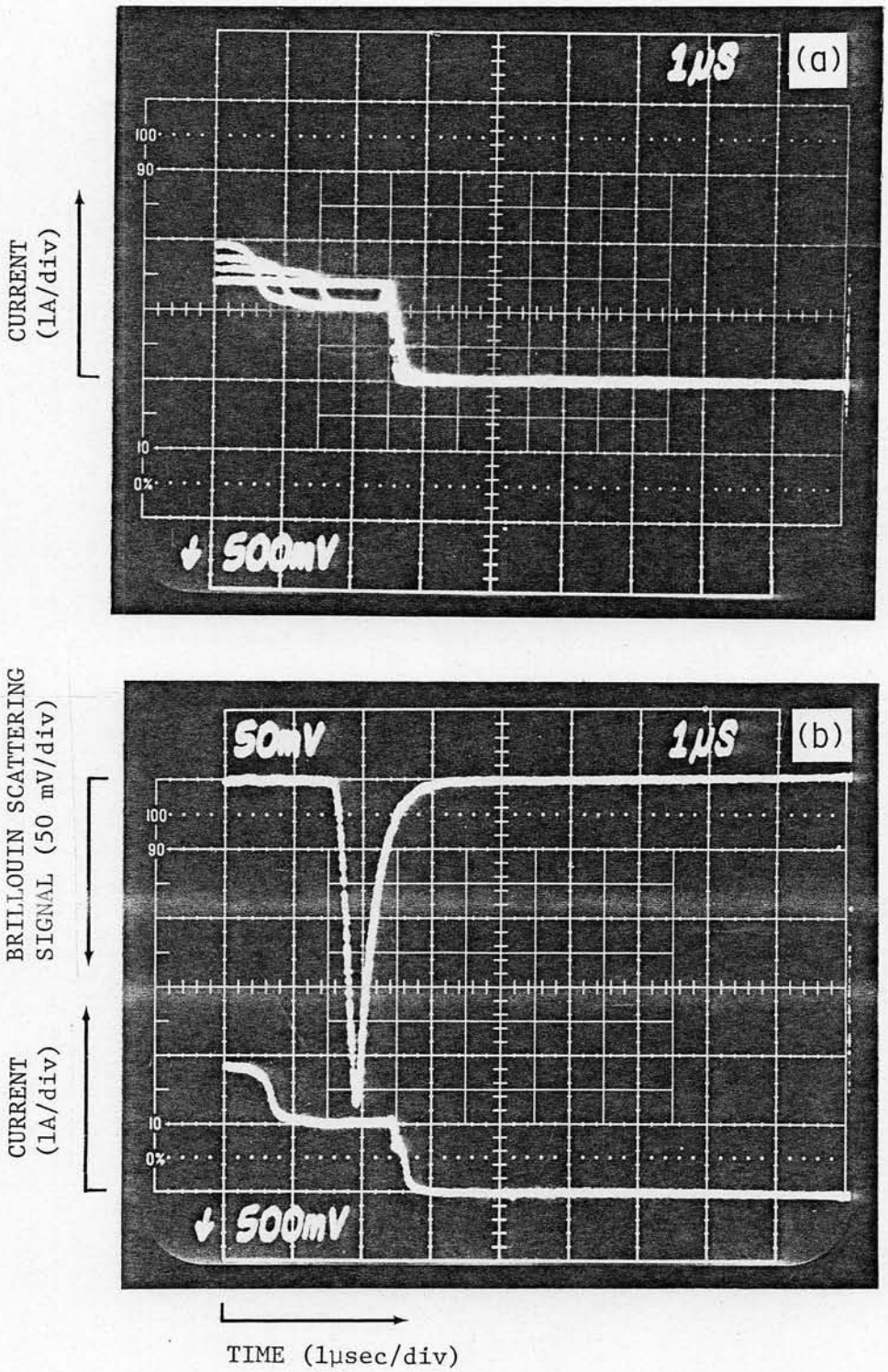

Fig. 4-3. (a) Some typical examples of the acoustic current-oscillation patterns for four different applied voltages. (b) Brillouin scattering signal by an acoustic domain in CdS.

Table 4-2. Experimental configuration for the Brillouin scattering measurements in cubic(zincblende) and wurtzite(or polytype ZnS) crystals.

Crystal structure	Acoustic mode	Acoustical propagation: 1_k	Acoustical polarization: π	Incident light polarization: 1_E	Scattering light polarization: 1_s
Zincblende	T1	$1_k \parallel [1\bar{1}0]$	$\pi \parallel [001]$	$1_E \parallel [110]$	$1_s \perp 1_E$
	T2	$1_k \parallel [001]$	$\pi \parallel [1\bar{1}0]$	$1_E \parallel [110]$	$1_s \perp 1_E$
Wurtzite a) (Polytype)	T1	$1_k \perp$ c-axis	$\pi \perp$ c-axis	$1_E \perp$ c-axis	$1_s \perp 1_E$
	T2	$1_k \perp$ c-axis	$\pi \perp$ c-axis	$1_E \parallel$ c-axis	$1_s \perp 1_E$
	LA	$1_k \perp$ c-axis	$\pi \perp$ c-axis	$1_E \parallel$ c-axis	$1_s \parallel 1_E$

a) The c-axis in wurtzite is equivalent to the [111] direction of cubic and thus we regard the c-axis of polytype ZnS as equivalent to the [111] direction of cubic ZnS

Brillouin scattering measurement for T1-, T2- and LA-mode phonons for zincblende and wurtzite crystals are listed in Table 4-2. In order to obtain the strong signals, synchronization of optical and electrical pulses was employed to measure the scattering from traveling acoustic domain when the pulsed light source was at the peak intensity. The acoustical domains was generated by an application to the high voltage pulse of $0.6 \sim 1.5$ kV with several μsec duration. The high-voltage pulses were generated from a Velonex, Model 350, high power pulse generator.

4.3.2 Reflection-Type Experiment

For the purpose of studying the resonant Brillouin scattering above the fundamental absorption edge in CdS, we employed reflection type of experiment[42,43] that extends measurement into the region where the sample is opaque. The difference between the transmission and reflection type experiments is shown in Fig. 4-4. It should be noted that in the case of reflection type of experiment only the k component parallel to the scattering surface is conserved because the interaction between phonon and photon is localized within the penetration depth ($\simeq \alpha^{-1}$). We used the single line mode of Ar ion laser (NEC GLG 3200) in which we may select eight different available operating wavelenghts, with different output power levels for each wavelength. These wavelength, and the maximum power available at each wavelength are:

514.5 nm (2.410 eV) 800 mW ,
501.7 nm (2.471 eV) 150 mW ,
496.5 nm (2.497 eV) 300 mW ,
488.0 nm (2.541 eV) 700 mW ,
476.5 nm (2.602 eV) 330 mW ,
472.7 nm (2.623 eV) 50 mW ,
465.8 nm (2.662 eV) 30 mW ,
457.9 nm (2.708 eV) 140 mW .

Figure 4-5 shows the schematic diagram of the experimental setup used in the Brillouin scattering in the opaque region. The Ar ion laser light was polarized by a Gran-Thompson or Rochon prism and focused onto the scattering surface by lens. We would like to point out here that the good S/N ratio of scattering light depends strongly on the surface condition of the sample. In order to obtain a reliable data we polished the scattering surface by Syton for 10 minutes. We find that Syton etching is a excellent method to obtain a optically flat surface for the measurement of the reflection scattering configuration.† The scattering light was detected by a photo-multiplier (RCA-7265) without using a Fabry-Perot interferometer. We used same detection system as was used in the transmission type of experiments.

4.4 Piezobirefringence Technique

Piezobirefringence spectra were measured with standerd optical and phase-sensitive electronic detection thchnique. The block diagram of the system is shown in Fig. 4-6. The optical system consists of a halogen lamp, double spectrometer, chopper, crossed polarizers, and detector. The light source was a tungsten-filament halogen lamp. Measurements were performed in the wavelength region 900 nm to the absorption edge of material. Polaroid HNP'B sheet polarizers were used as polarizer and anlyzer. Monochromatic light was obtained by Spex 1401 double spectro-meter with a 1200 line/mm reflection gratings blazed at 500 nm. We widened the slits to give a resolution 0.5 Å since high resolution was not

---

† Very recently, Aspnes and Studna reported that bromine-methanol is better agent than Syton in Ge, Si and some III-V compounds, for removing oxide and residual amorphous layer from the surface. [D. E. Aspnes and A. A. Studna: Appl. Phys. Lett. *39*(1981)316.]

usually required for the measurement of the piezobirefringence. The light was chopped at ≃ 200 Hz and the signal detected with a PAR model 126 lock-in amplifier. The output from the lock-in was applied to the x input of an xt recorder (YEW type 3056 vertical penrecorder), while the marker output from double spectrometer (100 cm^{-1}) was conected to the recorder. The samples were alined by light-figure method as described in Section 4.3 to better than 2° and cut to dimensions approximately $1.2 \times 1.3 \times 6$ mm. After cutting, the samples were polished, etched, and mounted on the stress appratus. The sample was placed between two pushing pistons and uniaxial stress was applied from a spring which was compressed by means of rotating the nob of the micrometer-head. The compression of the spring was measured by the scale of the micrometer-head and uniaxial up to 1.0 kbar was used.

The polarizer was oriented so that the beam incident on the sample was polarized at 45° to the stress axis (shown in Fig. 4-7). Under these condition, the light components polarized parallel and perpendicular to the stress are equal. The measurements were carried out at room temperature.

4.5 Acoustic Domain Injection Method

In this section we will discuss the acoustic domain injection method. Figure 4-8 is a schematic illustration of the experimental configulation of acoustic injection from CdS to ZnS. The two specimens are bonded together through the vacuum evaporated thin film of indium. The intensity of the acoustic waves of the domain excited in CdS and those transmitted to ZnS are estimated by the Brillouin scattering thechnique mentioned in the previous Section 4.3. Note that the acoustic phonon intensity is proportional to the Brillouin scattering efficiency, if the light

wavelength, optical path and scattering solid angle are constant. Therefore we can estimate the acoustic energy from the Brillouin efficiency at a wavelength, for example , using a He-Ne laser of several mW intensity.

We considered a case of CdS-ZnS, shown in Fig. 4-8, to estimate the transmission efficiency. For simplicity we neglected the indium layer at the bounded surface. It is well known that the acoustic waves amplified in CdS through acoustoelectric effect travel in a direction parallel to the c-plane with atomic displacement parallel to the c-axis. In Fig. 4-8, therefore, the excited acoustic waves are the transverse waves with the atomic displacement parallel to the [110] axis and wave vector along the [001] direction. The transmission efficiency T_P is given by[35)]

$$T_P = \frac{[P_{ac}]_T}{[P_{ac}]_I} = \frac{4(\rho C_{44})^{1/2}(\rho' C'_{44})^{1/2}}{\{(\rho C_{44})^{1/2}+(\rho' C'_{44})^{1/2}\}} , \qquad (4.1)$$

where ρ and C_{44} are crystal mass density and elastic stiffness constant in CdS and the corresponding values with prime are for other samples bonded to CdS. Here $[P_{ac}]_T$ and $[P_{ac}]_I$ are acoustic Pointing vector for transmittited and incident waves, respectively. We oftain from eq.(4.1) $T_P = 0.94$ for CdS-ZnS, $T_P = 0.94$ for CdS-ZnSe and $T_P = 0.95$ for CdS-ZnTe which are appreciably high. The experimental value of the transmission efficiency can be measured by the Brillouin scattering, as stated in ref.96. We measured the Brillouin scattering intensity in CdS and bonded specimen ZnS as function of position and the intensity at the bonded surface was estimated by extrapolation. In Fig. 4-9 , we show an example of the oscilloscope display of the Brillouin scattering signal by the injected acoustic domains obtained from the CdS-ZnS system (upper trace). The current waveform exhibitting the acoustical instability is also shown in the lower trace of the figure. The Brillouin scattering signal P_1 is produced by the injected forward-traveling acoustic domain, while the signal P_2 is produced by the reflected domain at the end surface of the injected crystal.

The experimental transmission efficiency was obtained using the extrapolated values, which are shown in Fig. 4-10 by solid circles for CdS-ZnS. Similar experiments were carried out for CdS- ZnTe and CdS-ZnSe and the results are also shown in Fig. 4-10. We find that the efficiency for CdS-ZnS sample is about 85 %. at the frequency f = 0.35 GHz. and decreases with the increase in frequency of acoustic waves. The decrease in efficiency at higher frequencies is mainly due to the acoustic mismatch of the waves in the three layer structure CdS-In-ZnS.

The attenuation coefficient of the transmitted acoustic waves can be obtained from the measurement of the Brillouin scatteirng intensity as a function of probing position. The acoustic frequency dependence of the attenuation coeffient is given by: $\alpha_L \propto f^{1.45}$ in ZnSe and $\alpha_L \propto f^{1.2}$ in ZnTe.[35,96] Experimental results show that the frequency dependence of attenuation coefficient depends strongly on the intensity of the acoustic waves transmitted in the bonded specimen. In the frequency region used in the present experiments, attenuation is dominated by Akhieser loss and expected to be given by the relation $\alpha_L \propto f^2$. [97-99] The departure from the f^2-dependence seems to reflect nonlinear phonon-phonon interaction of the high intensity phonons.[97,98] In the presnt method the acoustic energy density of transmitted waves in the samples is about 10^6 to 10^9 times higher than the thermal equilibrium value and thus the nonliear interaciton exists. Such a non-linear interaction of phonons is clearly seen in the case of the CdS-ZnS system (Fig. 4-11) where we found a complicated spectral dependence of the transmitted acoustic waves. Attenuation of the lower frequency phonons (0.37 - 0.56 GHz) becomes slow in the latter stage of propagation, while higher frequency phonons shows steeper attenuation at that stage. The results suggest that phonons of frequency f are converted to lower sub-harmonic phonons of frequencies, f/2, f/4, and so on, by strong non-linear effects (parametric effect).

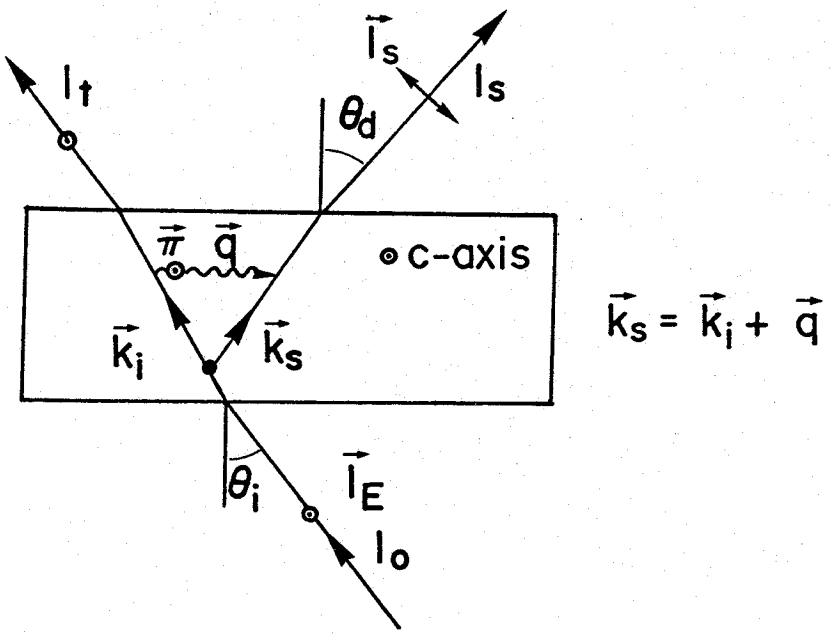

a) BRILLOUIN SCATTERING
BY BULK ACOUSTIC WAVES

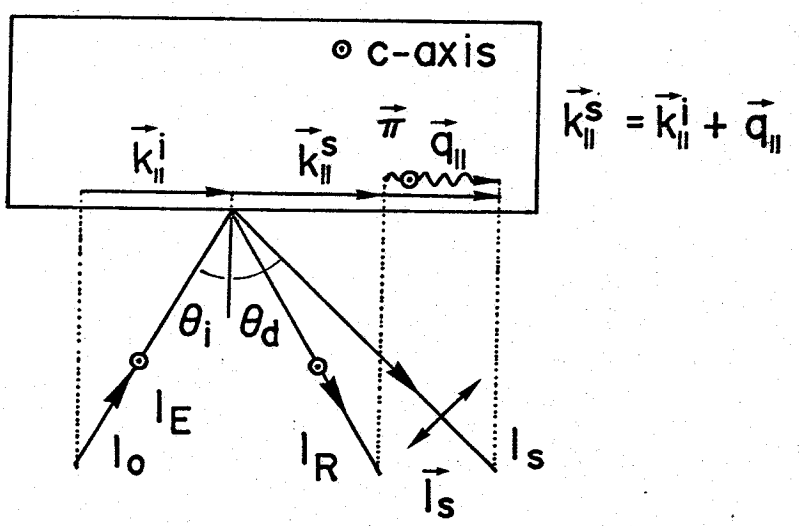

b) SURFACE BRILLOUIN SCATTERING
(REFLECTION GEOMETRY)

Fig. 4-4. Brillouin scattering by bulk acoustic waves a) and surface Brillouin scattering b).

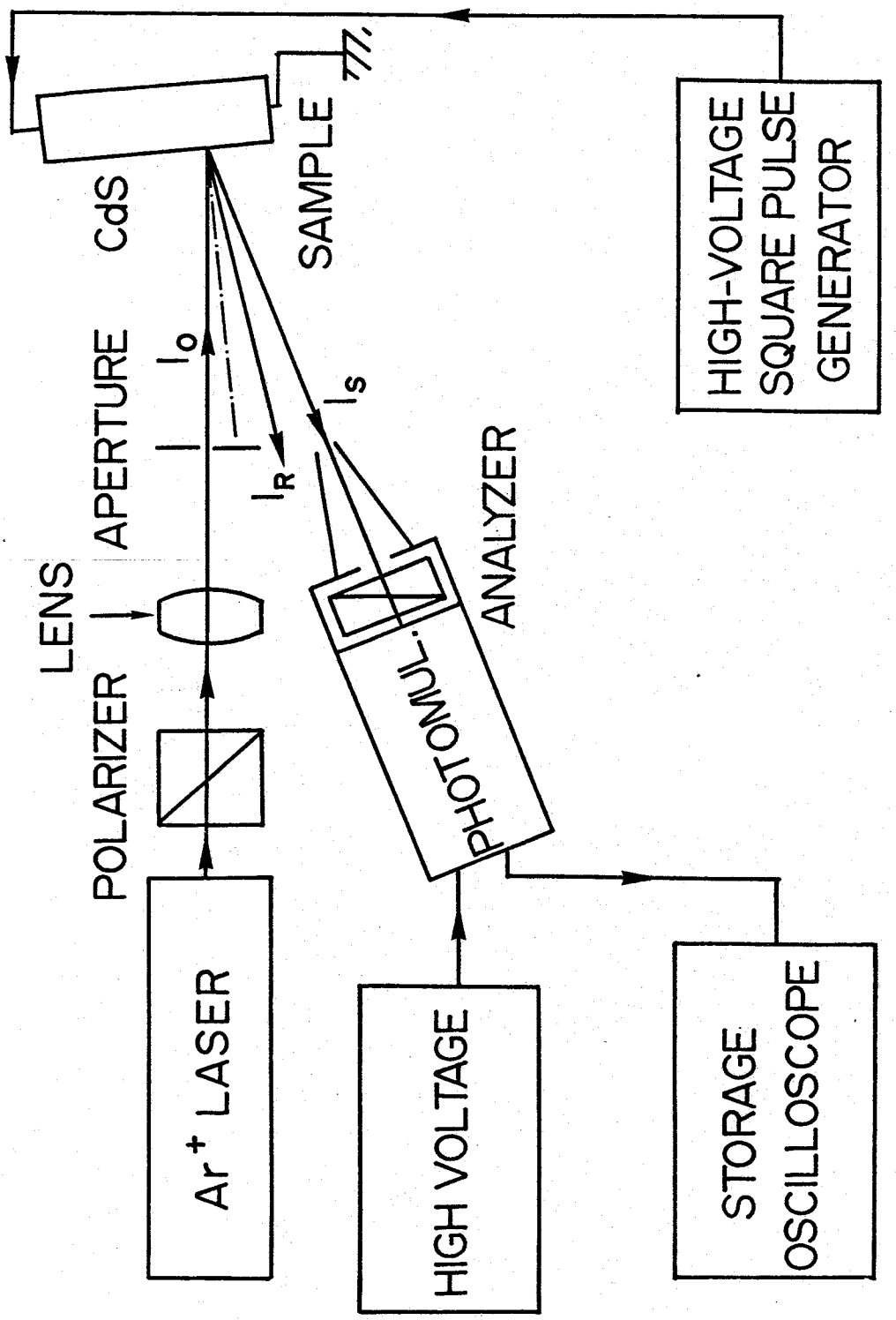

Fig. 4-5. Schematic diagram of the experimental setup used in the Brillouin scattering in the opaque region of the materials

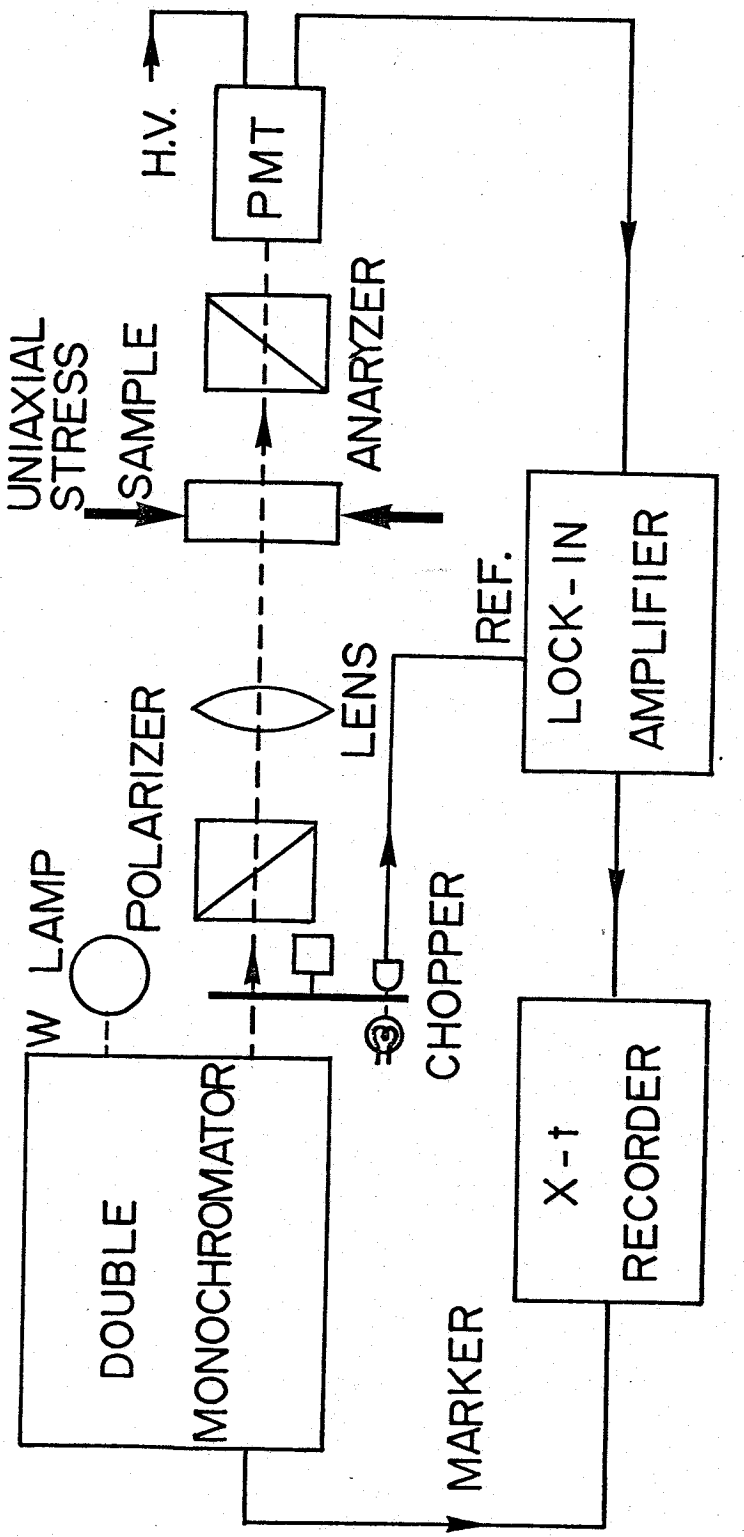

Fig. 4-6. Experimental setup for the piezobirefringence measurements. The details are shown in the text.

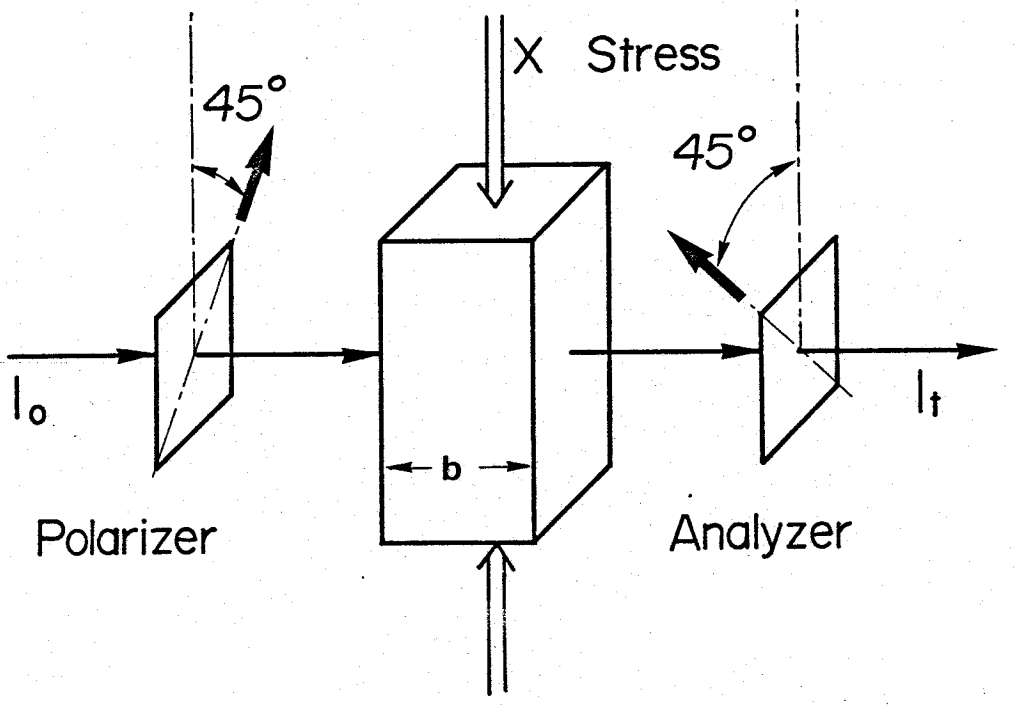

Fig. 4-7. Schematic diagram of the sample used for the piezo-birefringence experiments. Samples were placed between two crossed polarizers. Uniaxial stress was applied by the stress apparatus

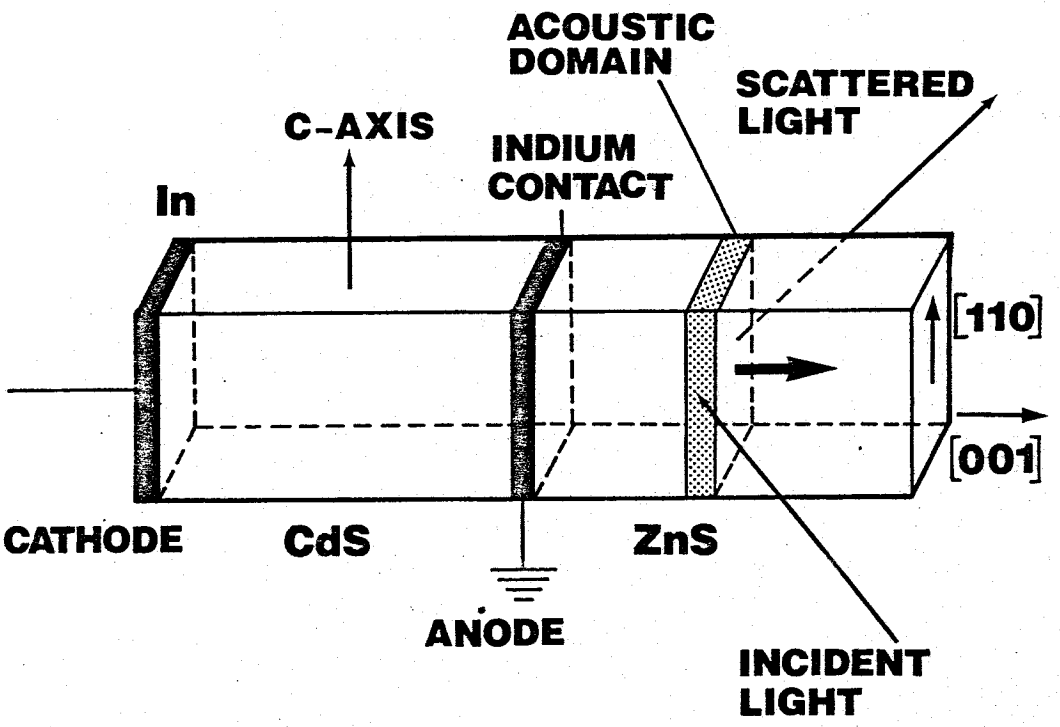

Fig. 4-8. Schematic illustration of a specimen used for the acoustic domain injection. Acoustic domains excited in a semiconductive CdS are transmitted to an insulating ZnS.

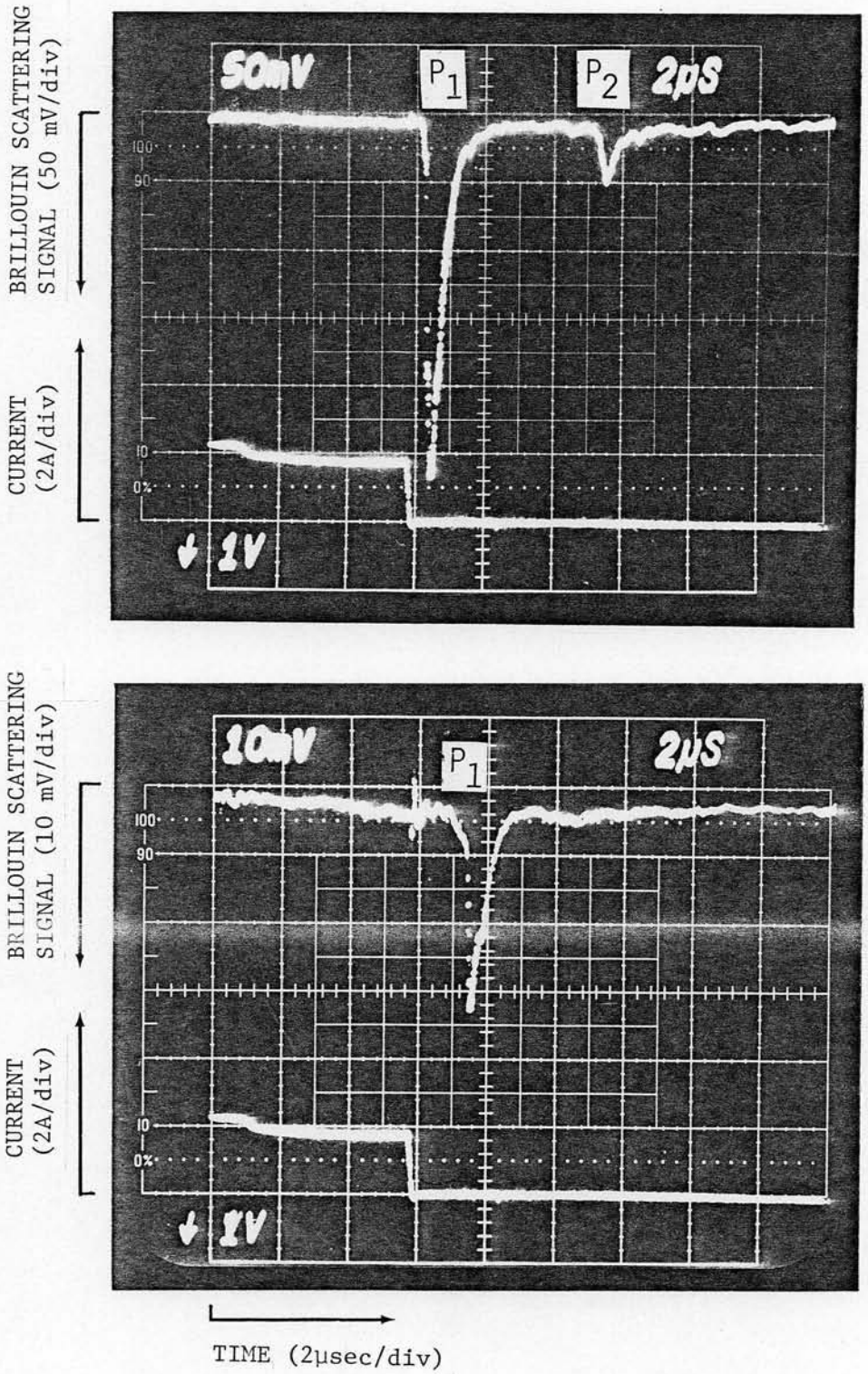

Fig. 4-9. Scope displays of the Brillouin scattering signal by injected acoustical-phonon domain obtained from the CdS-ZnS system (upper trace). The current waveform is also shown in the lower trace.

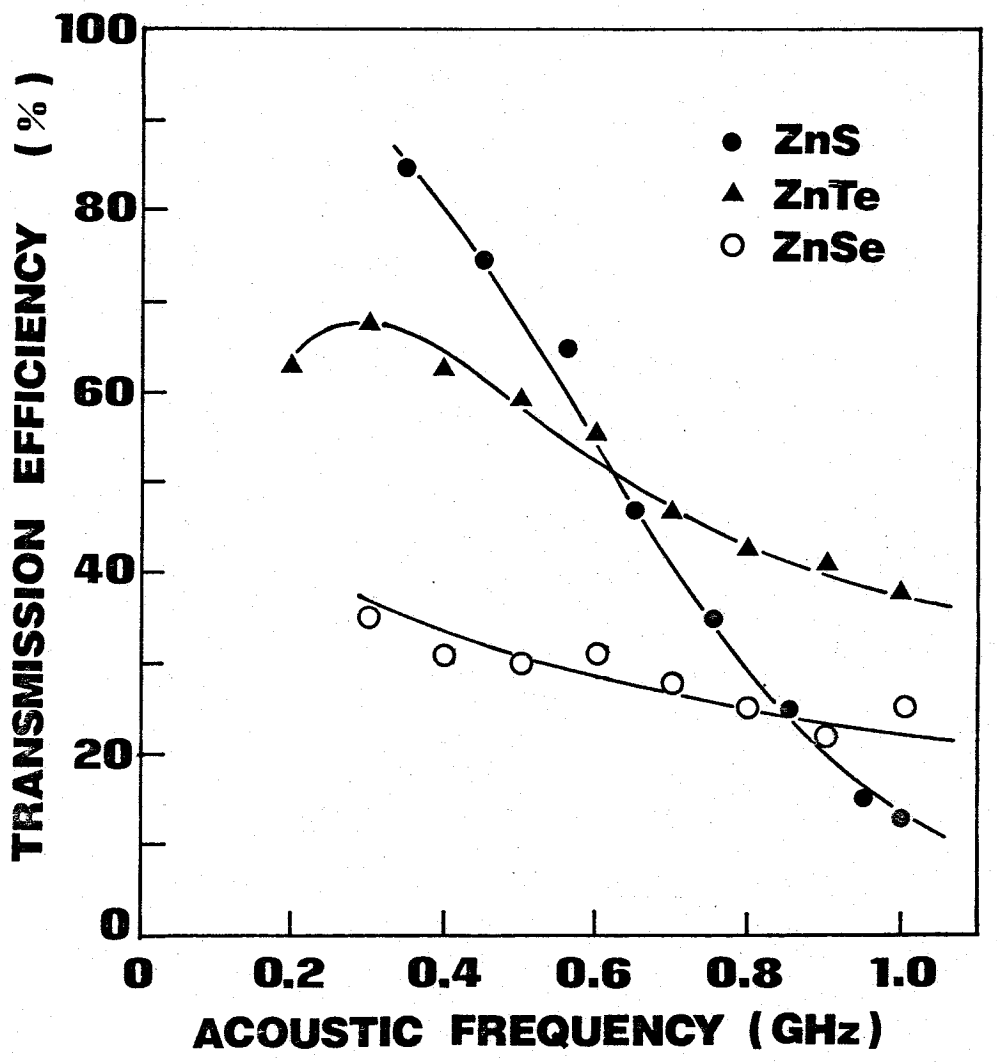

Fig. 4-10. Frequency dependence of the acoustic transmission coefficients for CdS-ZnS, CdS-ZnSe and CdS-ZnTe.

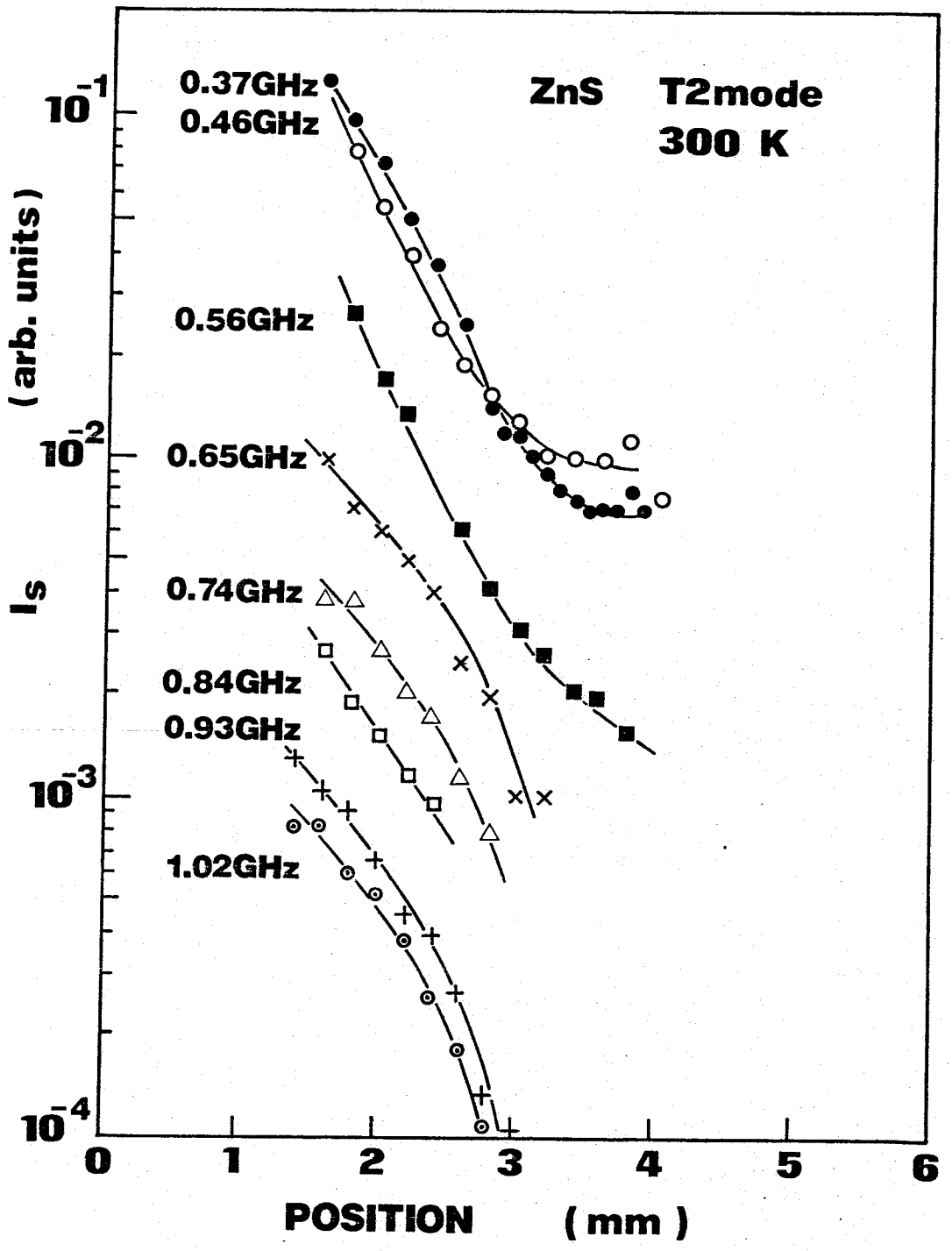

Fig. 4-11. The Brillouin scattering intensity as a function of position, from the bonded surface. The intensity I_s is proportional to the acoustic energy density in ZnS.

4.6 Summary

Experimental arrangement and sample construction used in the present work are presented. We have shown the Brillouin scattering technique by employing the acoustoelectrically amplified phonon domains and piezo-birefrinfence technique. We found that in order to obtain the Brillouin scattering signal where the incident photon energy is higher than that of the band gap, one must use reflection scattering geometry with high intensity light source. The acoustic domain injection method is also discussed and found this technique provides high transmission efficiency from CdS to other materials such as non-piezoelectric semiconductors, insulators and layered compounds.

CHAPTER 5

EXPERIMENTAL RESULTS

5.1 Introduction

Chapter 5 deals with the experimental results and discussions of the resonant Brillouin scattering and piezobirefringence in GaAs, CdS, ZnS and HgI_2. Present measurements are performed by the transmission type of experiment, where the incident photon energy is lower than that of the fundamental absorption edge. Brillouin scattering study above the fundamental absorption edge will be discussed in the following chapter. The main features of the present results are following. Steep resonant enhancement in scattering cross section is observed just below the fundamental absorption edge. Also the structure of resonant cancellation is found in the scattering cross section by transverse acoustic phonons, while a weak resonant cancellation is found by longitudinal acoustic phonons in CdS. In layered compound HgI_2, we found that the contribution of higher gaps plays an important role in the dispersion of the scattering cross seciton. It is found in comparison with the theory that the structures of resonant enhancement and cancellation are well explained by the theoretical treatment of the resonant scattering. The scattering cross sections are analyzed by the piezobirefringence theory and the dispersion of the photoelastic constants are determined. In Section 5.2, we shall analyze the scattering cross sections of GaAs. In Section 5.3, we describe the experimental results of the resonant Brillouin scattering in ZnS. In Section 5.4, the results of the resonant Brillouin scattering by T2- and LA-phonons in CdS are discussed. In Section 5.5, the results of the resonant Brillouin scattering in HgI_2 are discussed. In Section 5.6, We show the acoustic figure of merits.

5.2 Analysis of Resonant Brillouin Scattering in GaAs

In this section we analyze the Brillouin scattering cross sections in GaAs by using the Brillouin scattering theory and piezobirefringence theory.[100] The main purpose of the present section is to explain the resonant cancellation and resonant enhancement observed in the experiment of Garrod and Bray.[29]

5.2.1 Brillouin Scattering Cross Section

Figures 5-1 and 5-2 show the experimental dispersion of the Brillouin scattering cross sections for T2- and T1-mode phonons in GaAs, respectively.[29] The scattering cross sections by T2-mode phonons show a resonant cancellation (898 nm) near the fundamental absorption edge. The cancellation point by T1-mode phonons, on the other hand, is not found in the measured wavelenght region. The piezobirefringence measurements,[29,101] however, reveal that a cancellation occurs at 976 nm which is relatively far from the fundamental absorption edge as compared with the results for T2-mode phonons.

The theoretical curves shown by dashed and solid lines in Figs. 5-1 and 5-2 are calculated from eq.(2.140)($E_B = 0$;without exciton model) and eq.(2.140)($E_B = 4.2$ meV;with exciton model), respectively. The numerical parameters used in the calcualtions are listed in Table 5-1. Non-vanishing values of the matrix elements $\Xi_{\beta\alpha}$ for the deformation potential scattering are as follows:[See, eqs. (2-167) and (2-168)]

$$\left.\begin{aligned} \Xi_{AB} &= d = -4.59 \text{ eV} \\ \Xi_{CB} &= d/\sqrt{2} = -3.25 \text{ eV} \\ \Xi_{AC} &= \sqrt{6}/2 = -5.62 \text{ eV} \end{aligned}\right\} \quad \text{for T2-mode ,} \tag{5.1}$$

and

$$\left.\begin{aligned} \Xi_{AB} &= \sqrt{3}b = -3.05 \text{ eV} \\ \Xi_{CB} &= \sqrt{6}b = -4.31 \text{ eV} \end{aligned}\right\} \quad \text{for T1-mode ,} \tag{5.2}$$

Table 5-1. Parameters used in the calculation of Brillouin scattering cross section σ_B and photoelastic constants $P_{11} - P_{12}$, and P_{44} for GaAs at 295 K.

symbol		numerical value
E_{gA} (= E_{gB})	(eV)	1.422[a]
E_{gC}	(eV)	1.736[a,b]
Δ_0	(eV)	0.341[b]
F^A_{xx}	(eV^2)	7.5×10^{-4} [c]
F^B_{xx}	(eV^2)	22×10^{-4} [c]
F^C_{xx}	(eV^2)	12×10^{-4} [c]
E_B	(meV)	4.4[d]
a_0	(Å)	133[e]
μ		0.0564[f]
b	(eV)	-1.76 ± 0.1[g]
d	(eV)	-4.59 ± 0.25[g]

[a] Reference 102.
[b] Reference 103.
[c] Reference 104.
[d] Reference 105.
[e] Reference 50.
[f] Reference 106.
[g] Reference 107.

where the numerical values are estimated by using the deformation potential b and d reported in ref. 107. The matrix elements $P_{\alpha 0}$ and $P_{0\beta}$ are obtained from ref. 104.

The resonant cancellation is explained phenomenologically as follows. The scattering cross-section is proportional to the square of $|R_{is} + R_0|$, where R_{is} is the resonant contribution arising from the fundamental absorption edge and R_0 is the non-resonant contribution from the far-off critical points in the band structures. When the term R_0 is opposite in sign to R_{is}, the resonant cancellation occurs under the condition $|R_{is} + R_0| = 0$. We see in Figs. 5-1 and 5-2 that the theoretical curves calcualted from both model (free electron-hole and exciton models) show good agreement with the experimental data, and that there is no appreciable difference between the theoretical curves because of the small value of the exciton Rydberg constant. The experimental data for Tl-mode phonons by Garrod and Bray are limitted to a narrow range of wavelength and thus the cancellation is not apparent. The present analysis, however, predicts a cancellation at about 970 nm as shown in Fig. 2-2. Such a prediction is found to be consistent with the observation of the sign reversal in the photoelastic constant at 976 nm reported by Ferdman and Horowicz[101] and Higgnbotham et al.[74] as will mentioned later.

5.2.2 Photoelastic Constant

We have already shown that Brillouin scattering can be treated from a phenomenological aspect by incorporating the photoelastic constant. There are following relations between them given in eqs.(3.79) and (3.80)

$$\sigma_B(T1) = A_1 n_0^6 \omega^4 (P_{11} - P_{12})^2 \tag{5.3}$$

$$\sigma_B(T2) = A_2 n_0^6 \omega^4 p_{44}^2 \tag{5.4}$$

By using the above relations the theoretical results will be compared with the resonant Brillouin scattering cross-section reported by Garrod and Bray[29] The values of parameters used for the calculation of photoelastic constant are also given in Table 5-1. Figure 5-3 shows the theoretical dispersion of the photoelastic constant P_{44} calculated from eq.(3.51) along with the experimental data. We compared the theoretical curve with the square root of the dispersion of resonant Brillouin scattering observed by T2-mode phonons according to the relation of eq.(5.4). Figure 5-3 shows that a sign reversal exists at 898 nm which coincides with the cancellation point in the Brillouin scatteing cross section. We present in Fig. 5-4 the theoretical dispersion of the photoelastic constant $P_{11} - P_{12}$, where $P_{11} - P_{12}$ is related to the square root of the Brillouin scattering cross section by T1-mode phonons. From the analysis a sign reversal of the photoelastic constant $P_{11} - P_{12}$ can be expected to occur at 976 nm although the experimental data of the resonant Brillouin scattering in the wavelength region are lacking. However, as mentioned earlier Ferdman and Horowicz[101] and Higginbotham et al.[74] reported a sign reversal of the piezobirefringence coefficient relevant to the photoelastic constant $P_{11} - P_{12}$ at 976 nm in GaAs, which is in good agreement with the presnt analysis.

The exciton transitions in III-VI compounds are relatively weaker than those in II-VI compounds such as CdS, ZnSe, ZnTe, etc. For example the exciton Bohr radius (a_0) and exciton Rydberg constant (ecxiton binding energy; E_B) are 45 Å and 10 meV for ZnTe, and 51 Å and 19 meV for ZnSe. On the other hand, they are 133 Å [105] and 4.2 meV for GaAs.[103]

It follows from these condition that we can neglect the effect of the discrete exciton on the dispersion of the photoelastic constant in GaAs and thus the assumption of zero Rydberg ($E_B = 0$) seems to be reasonable. Such an assumption has been made by Higginbotham et al. for the analysis

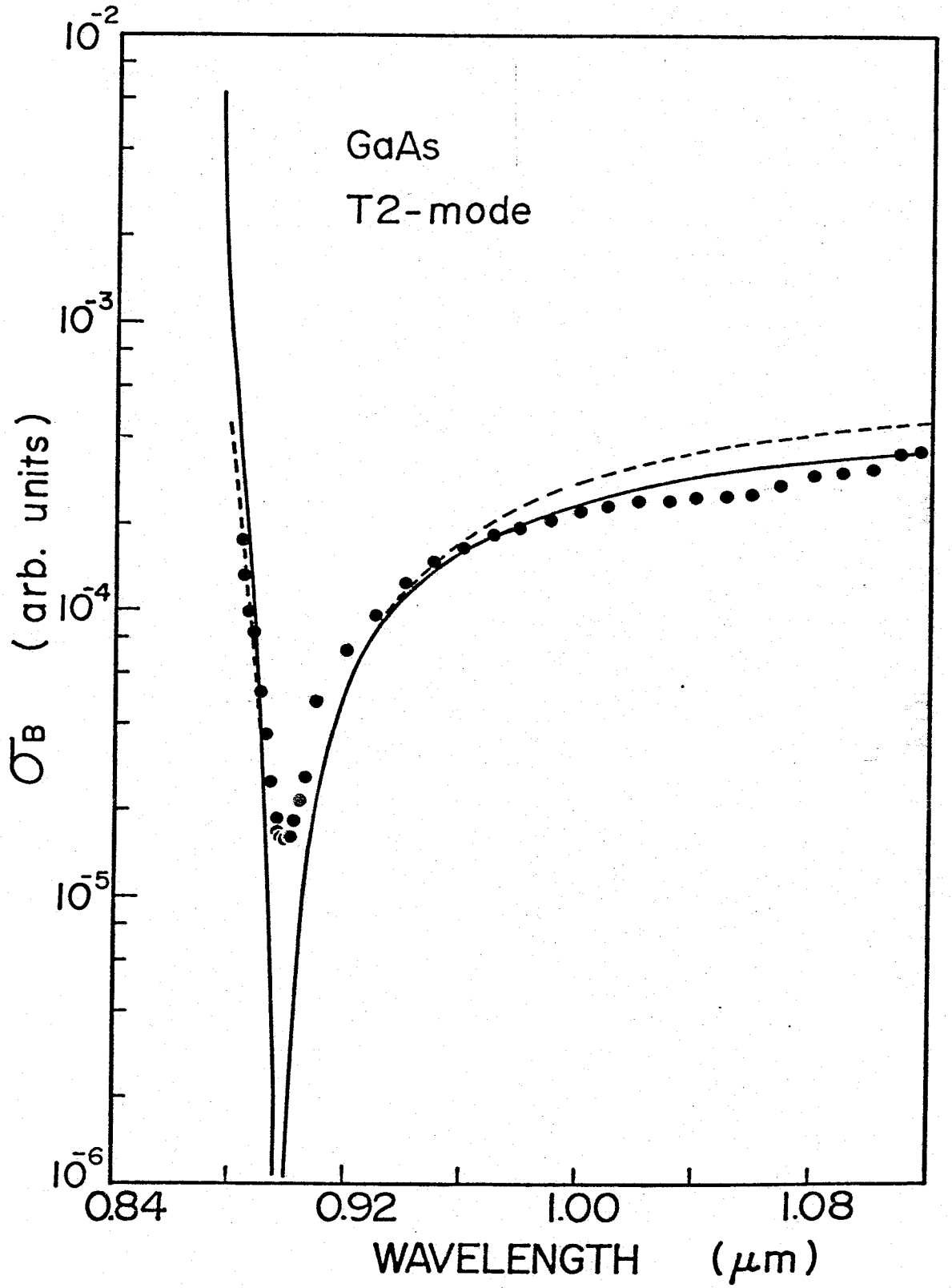

Fig. 5-1. Dispersion of Brillouin scattering efficiency by T2-mode phonon domains in GaAs at 298 K reported by Garrod and Bray. Theoretical curves were calculated from eq.(2.140); —— (with exciton;E_B = 4.2 meV), ----(without exciton;E_B=0).

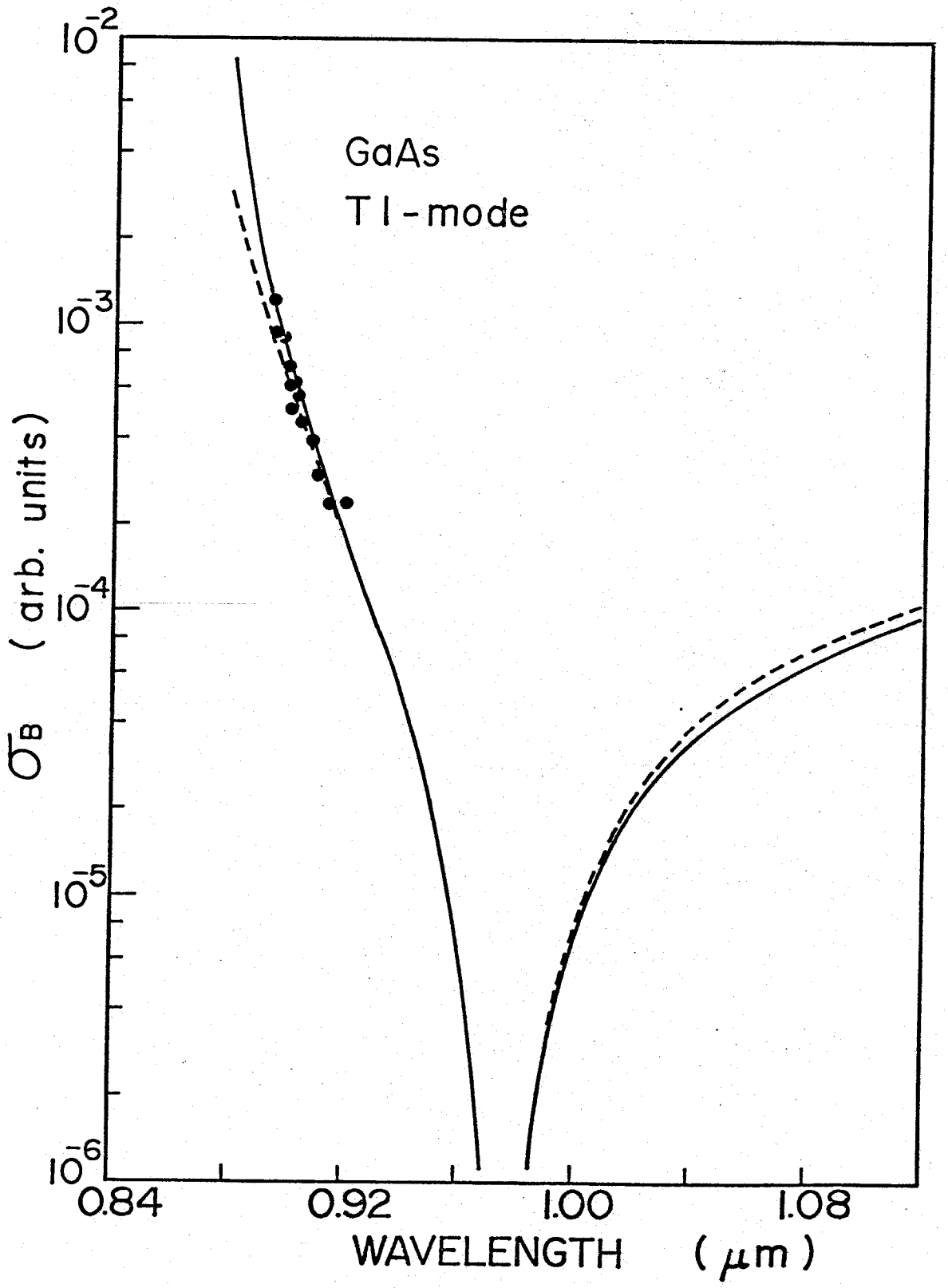

Fig. 5-2. Dispersion of Brillouin scattering efficiency by Tl-mode phonon domains in GaAs at 298 K reported by Garrod and Bray. Theoretical curves were calculated from eq.(2.140); —— (with exciton; $E_B = 4.2$ meV), ---- (without exciton; $E_B = 0$).

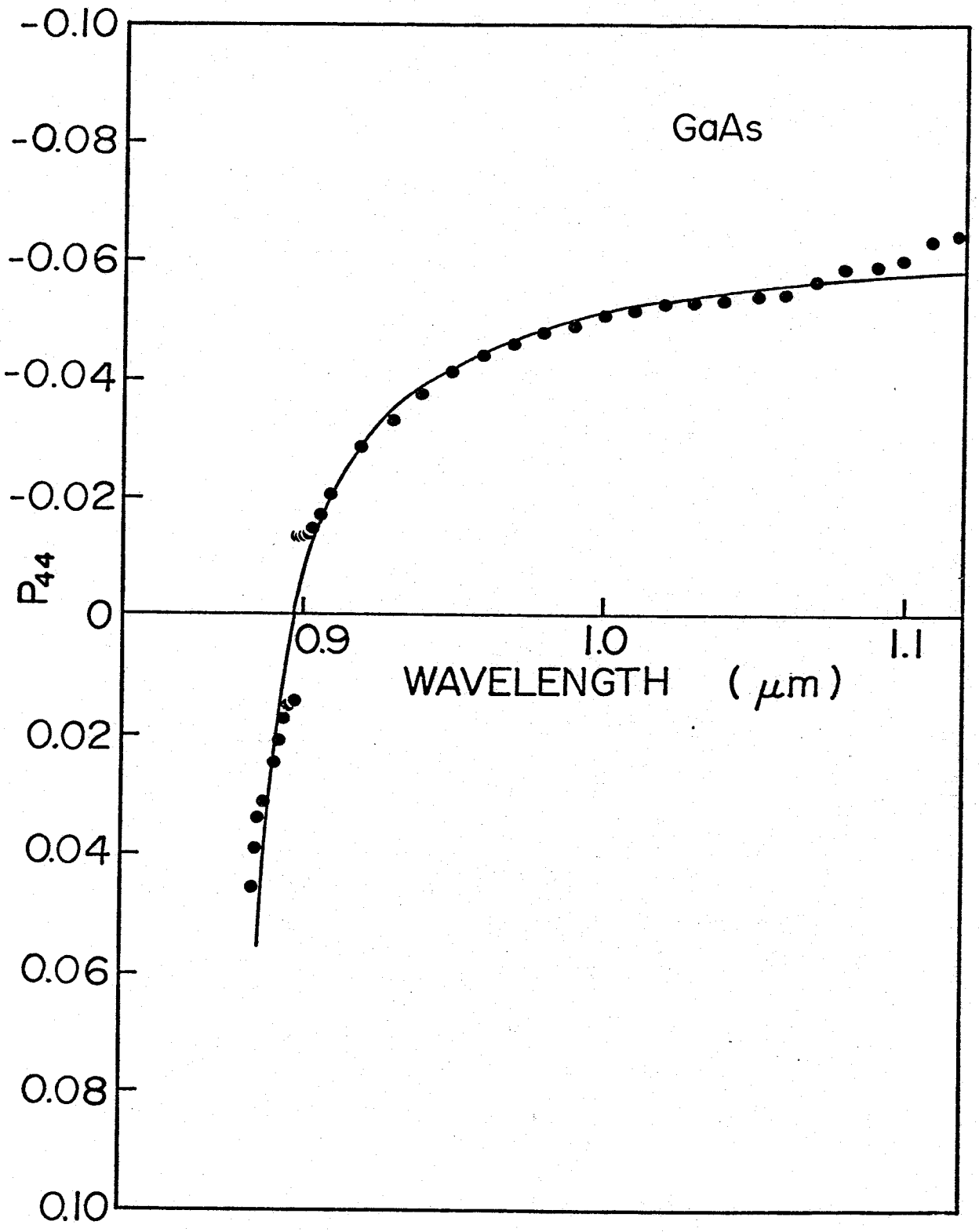

Fig. 5-3. Dispersion of photoelastic constnat P_{44}. Theoretical curve was calculated from eq. (3.51).

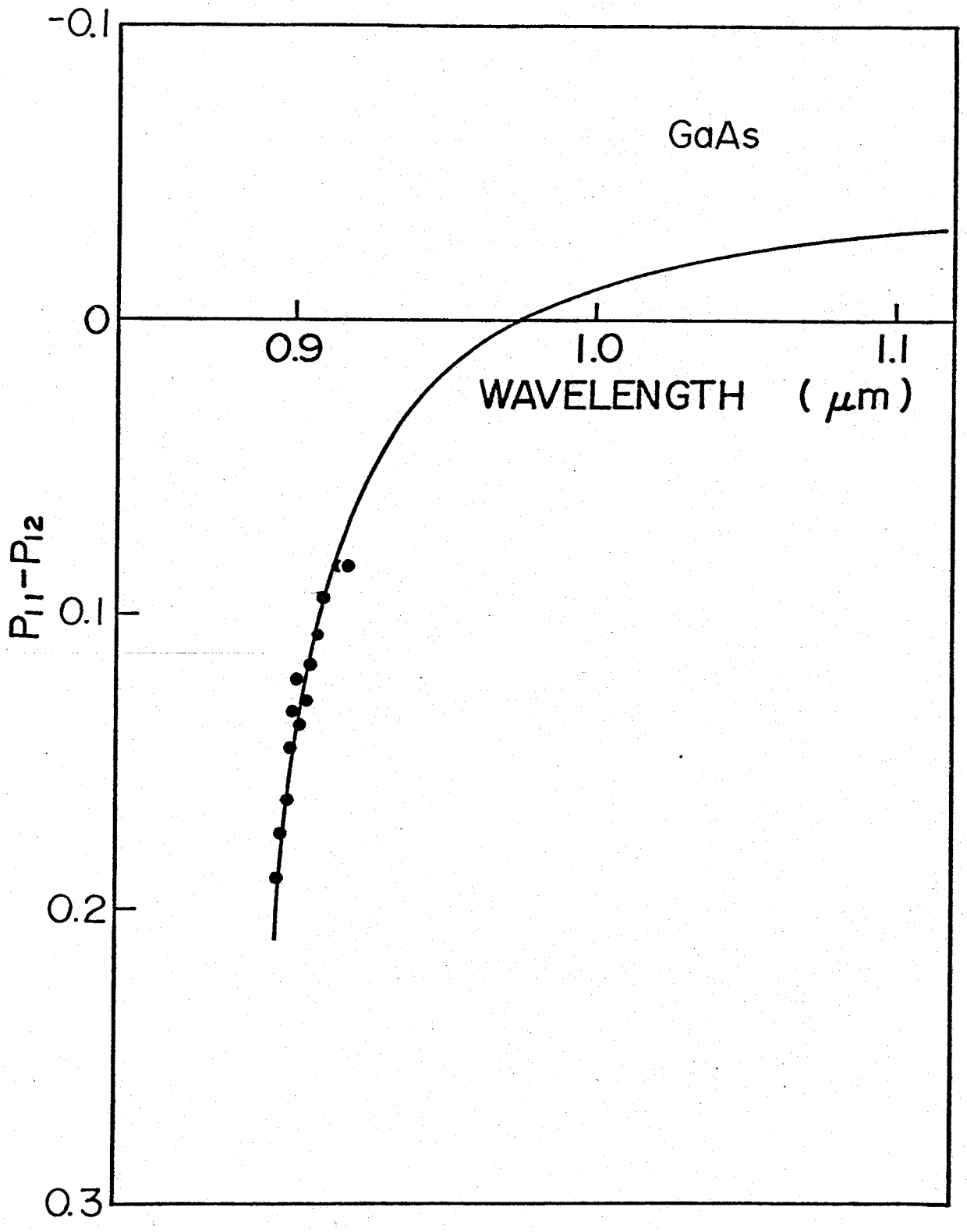

Fig. 5-4. Dispersion of photoelastic constnat $P_{11} - P_{12}$. Theoretical curve was calcualted from eq. (3.47).

of piezobirefringence. In conclusion, the resonant Brillouin scattering data obtained by Garrod and Bray are well explained by the present analysis upon the light scattering and piezobirefringence theory.

5.3 Resonant Brillouin Scattering and Piezobirefringence in ZnS

In Section 5.3, we present the results of the resonant Brillouin scattering in cubic and polytype ZnS at 300 K and 77 K for the two types of transverse acoustic waves[73,110,111] by using the acoustic domain injection method.[35,108] Also the measurements of the piezobirefingence have been performed to obtain dispersion of the photoelastic constants in the same crystals. The main purpose of the present section is to compare the spectral dependence between cubic and polytape ZnS. In Section 5.3.1 we shall discuss briefly about the crystal structure in cubic, wurtzite and polytype ZnS. In Section 5.3.2 we shall discuss the results of the Brillouin scattering cross section in the region below the fundamental absorption edge. In Section 5.3.3 we shall present the dispersion of the photoelastic constant derived by the present Brillouin scattering experiment and piezobirefingence experiment.

5.3.1. Crystal Structure and Optical Properties of ZnS

The crystal structure of the II-VI compounds consists of two types of structures. One is zincblende and other is wurtzite structure. Both structures are characterized by tetragonal coordination (sp^3) and the zincblende structure can be distinguished easily from the wurtzite structure by the structual periodicity along the <111> or <0001> axis (Miller index (hkl) stands for the cubic system, while (hkjl) represents the hexagonal

system); the zincblende (cubic) structure has a three-layer stacking (3C) as ABCABC and wurtzite structure (hexagonal) has a two layer stacking (2H) as ABAB of the closed-packed plane along the <111> or <0001> direction. All of the II-VI compounds, for example, ZnSe, ZnTe, ZnS, CdS form crystals with zincblende arrangement. Some of the II-VI compounds such as ZnS, CdS and CdSe also crystallize in the wurtzite arrangement. Figure 5-5 shows the arrangement of group II metal atoms and group VI non-metal atoms in a (a) zincblende and (b) wurtzite form. The zincblende structure is based on the cubic space group T_d^2. There are four molecules $A^{II}B^{VI}$ in a unit cell. The wurtzite structure is based on the hexagonal space group C_{6v}^4 and there are two molecules in the hexagonal units cell.

It is well known that ZnS crystallizes in both zincblende and wurtzite structures. There exists a wide variety of polytypes with stacking faults in which twinned layer of cubic alternates with wurtzite layer.[111,112] Birman[113] has performed calculation to determine the band structure of wurtzite and zincblende. Though he did not deal explicitely with ZnS polytypes, it can be concluded from his work, that the band gap will vary smoothly with α. The percentage of hexagonality of the structure α has to be defined as the percentage of close-packed planes which are in a hexagonal nearest neighbor environment. For example, if the three possible positions of the close packed planes are denoted by A, B, C, respectively,[114] then the 4H polytype is ABACABAC$\cdots$, the B's and C's are in hexagonal environments and thus 50 %. Eventually $\alpha = 100$ % for wurtzite and $\alpha = 0$ % for zincblende. For a polytype mH with m >6, knowledge of the layer sequence is essential for the determination of α. The value of α is proportional to the magnitude of the birefringence of a crystal δn and given by $\alpha = \delta n/\delta n_0$, where δn_0 is the birefringence of wurtzite.[115,116] In Fig. 5-6.(a), the degree of birefringence δn, is plotted as a function of α.

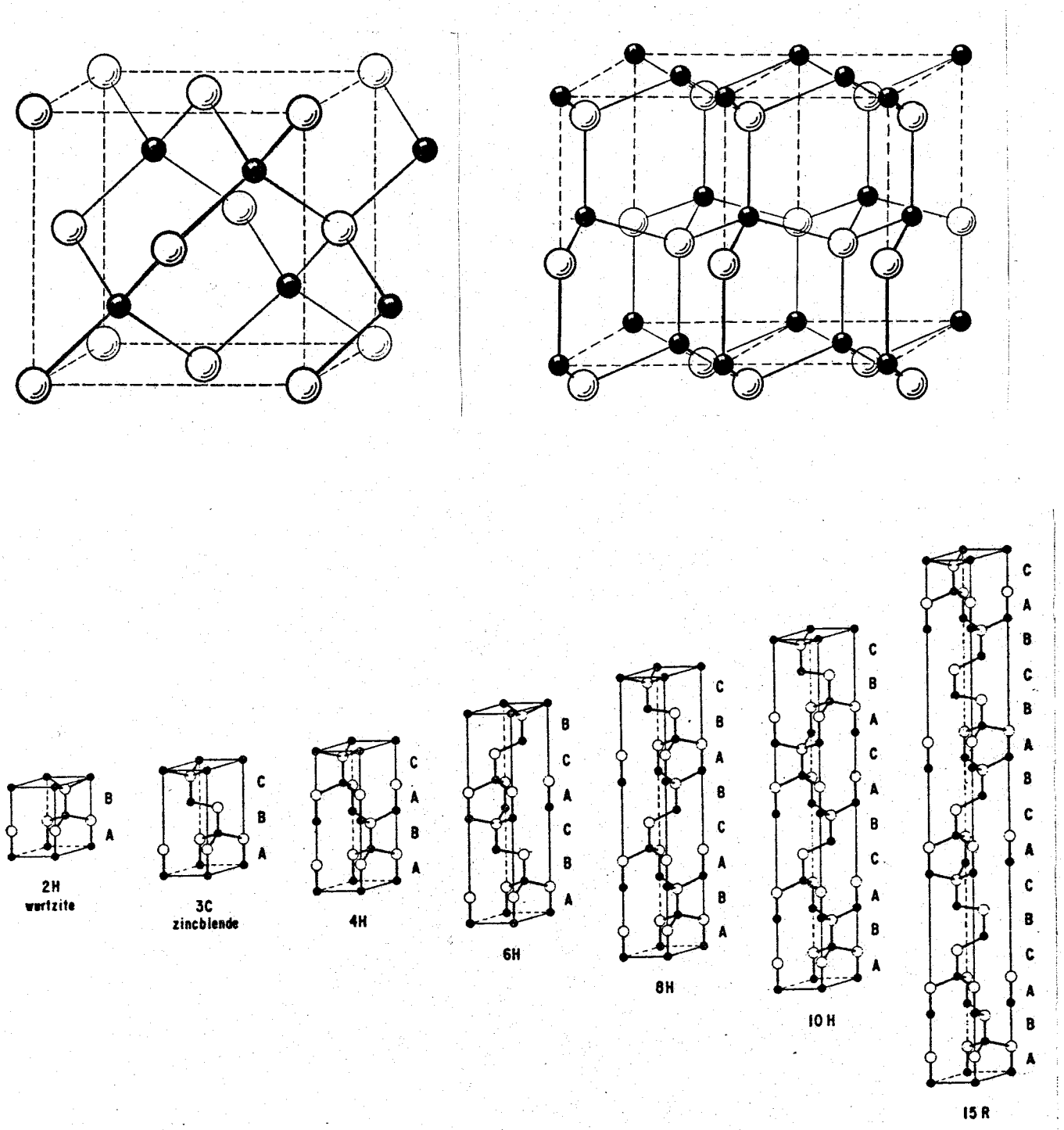

Fig. 5-5. The arrangement of Zn atoms (small filled circles) and sulfur atoms (large open circles) in a) zincblende, b) wurtzite form and c) polytype of ZnS. The letters A, B, C locate the positions of Zn-S layers.

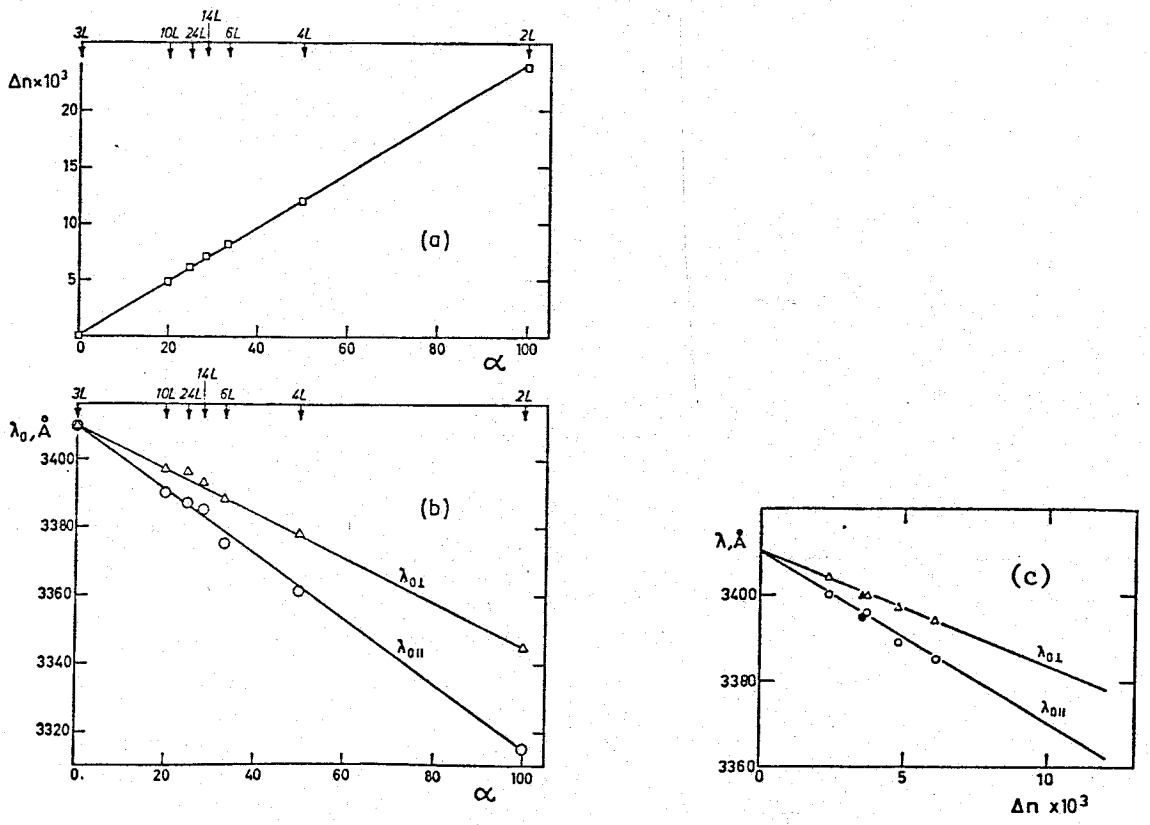

Fig. 5-6. Degree of birefringence (a) and absorption edge positions for polarization parallel and perpendicular to the c-axis (b) as a function of the percentage of hexagonality α. Absorption edge positions of 40L and 120L polytype (empty symbols) as a function of the degree of birefringence(c). (From ref. 115)

The degree of birefringence $\Delta n = n_e - n_o$, where n_e and n_o are the extreme value of the refractive index was determined at 546 nm by Brafman and Steinberger.[115] In Fig. 5-6 (b) and (c), the absorption position versus α are presented. They defined the absorption position edge as that wavelength λ_0, from which the absorption coefficient is 6 cm^{-1}. Both $\lambda_{0\parallel}$ and $\lambda_{0\perp}$ refer, respectively, to polarization parallel and perpendicular to the optical axis. It is seen that Δn, $\lambda_{0\parallel}$ and $\lambda_{0\perp}$ are linear function of α. It follows that the linear relation of Fig. 5-6, if the magnitude of birefringence Δn is known, the band gap energies of any polytypes can be determined by linear interpolation.

Most of the ZnS crystals grown from the melt shows stacking faults along the c-axis. These stacking faults arise during the grouth of crystals.[117] Stacking faults in ZnS have been investigated many times by the method of x-ray crystallography [118-120] and electron microscopy.[121-123] It has been shown that they occur as flat, practically two-dimentional formation in the <111> and <0001> plane of, respectively, the cubic and hexagonal structures.

For the purpose of determining the hexagonality and band gap energy of the polytype ZnS, we performed the natural birefringence experiment. Figure 5-7 shows a photograph of the polytype ZnS platelet placed between two crossed polarizers. The surface of the sample are parallel to the c-axis. The integer m of the stripes indicate the order of interference. Using the relations given in eqs.(3.11) and (3.13) the magnitude of the birefringence Δn and hexagonality α are determined. The relations between Δn and α are listed in Table 5-2. Figure 5-8 shows the recorded spectra of the transmitted intensity of the ZnS sample placed between two crossed polarizers. (a) and (b) indicate the measured positions of the sample shown in Fig. 5-7. From these spectra, the dispersion of the birefringence

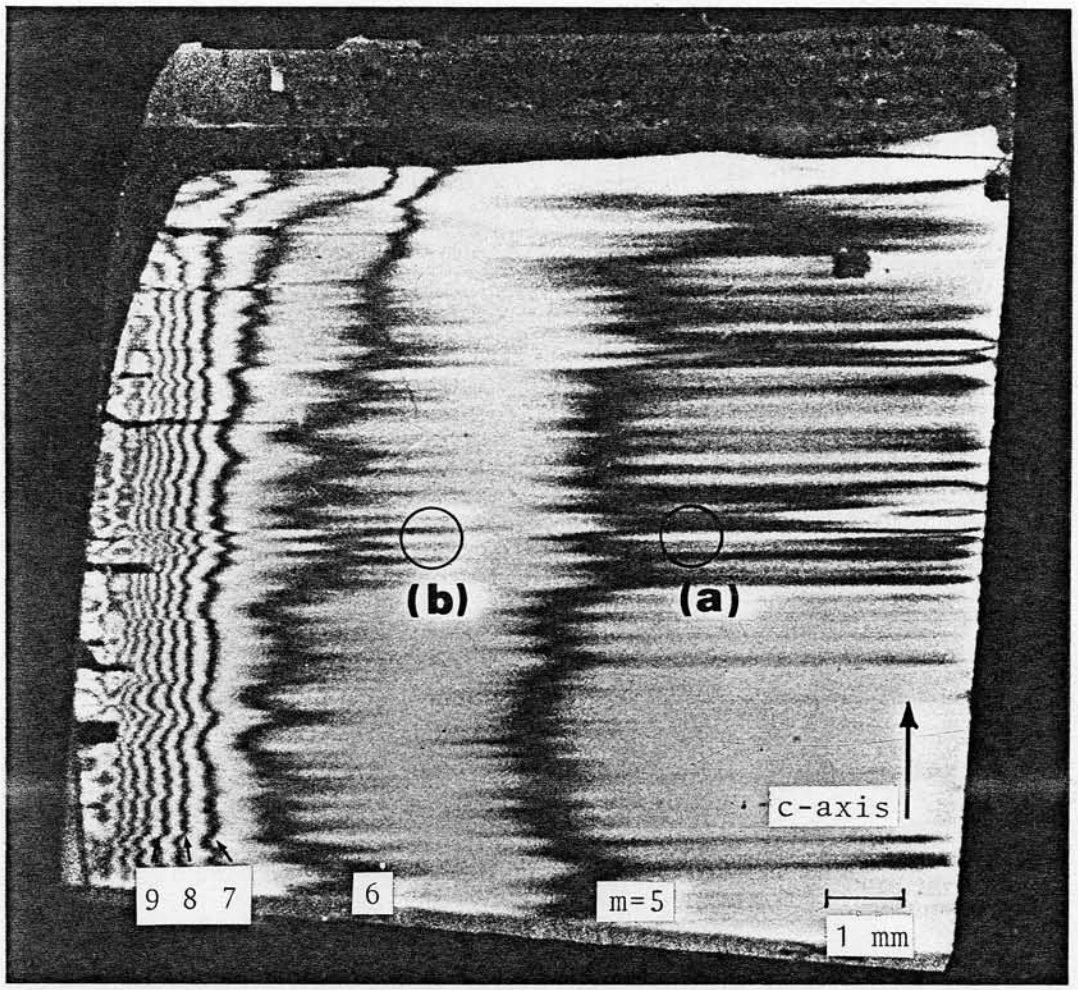

Fig. 5-7. ZnS crystal photographed between crossed polarizers. The direction of the c-axis is indicated by an arrow. The integer m indicates the order of the interference. The wavelength of the illuminated light is 650 nm and the thickness of the sample is 1.79 mm. The relation between m and the magnitude of the birefringence Δn is shown in Table 5.2. Most of the region of this sample is uniform, while the left-hand edge of the sample shows tight stripes due to variation of the birefringence.

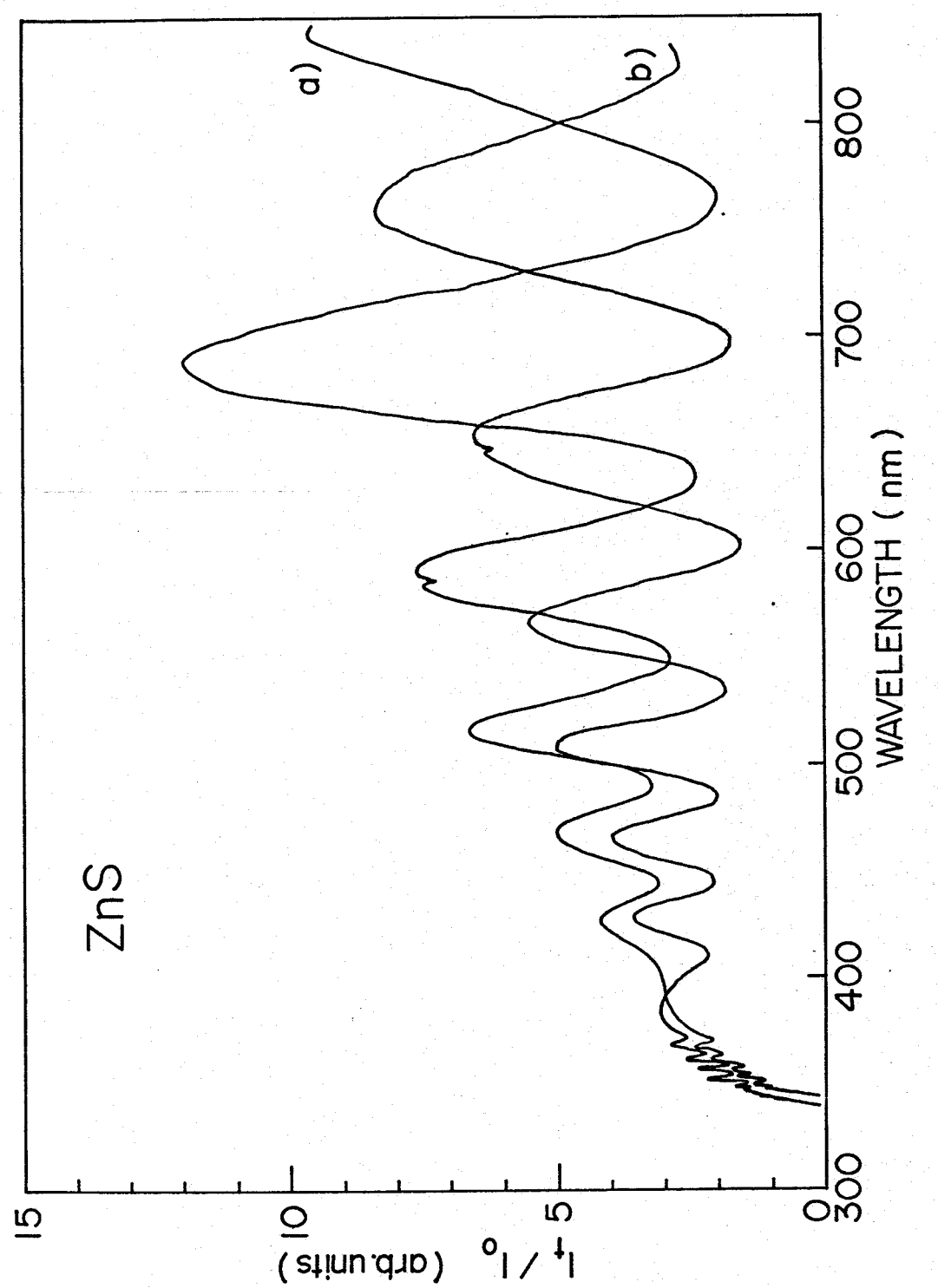

Fig. 5-8. Recorded spectra of the natural birefringence. These spectra are used to determine the hexagonality in polytype ZnS for different two positions, namely (a) and (b) shown in the photograph of Fig. 5-7.

Table 5-2. Relations among m, Δn, and α. ($d = 1.79$ mm, $\lambda = 650$ nm.)

m	$\Delta n \times 10^{-3}$	α (%)
5	1.8	7.6
6	2.2	9.1
7	2.5	10.6
8	2.9	12.2
9	3.3	13.7
10	3.6	15.2
11	4.0	16.7

can be determined by using the relation given in eqs.(3.11) and (3.13). In cubic crystals ($\alpha = 0$) the valence bands are degenerate Γ_8 and spin-orbit split off Γ_7 bands, whereas in wurtzite ($\alpha = 1$) the three valence bands (Γ_9,Γ_7,Γ_7) are completely separated. In polytipes, the band gap energies are estimated by the linear dependence of the band gap energies to the haxagonality α. The results are showin in Fig. 5-9. The numerical values used to determine the location of the band gaps are listed in Table 5-3.

5.3.2. *Brillouin Scattering Cross Sections*

In the present experiment, we performed the acoustic doamin injection method, where phonon domains amplified through acoustoelectric effect in CdS are injected into end-bonded ZnS. We used two kind of ZnS, i) synthesized by melt-grown at Eagle Picher Company (UHP grade) and ii) grown by I_2 chemical transport method, as described in Section 4.2.

Figure 5-10 shows experimental data of the transmission efficiency of the acoustic domain from CdS into ZnS samples in the frequency range of 0.3 - 1.0 GHz (90 % efficiency is achieved at 0.3 GHz in one of the

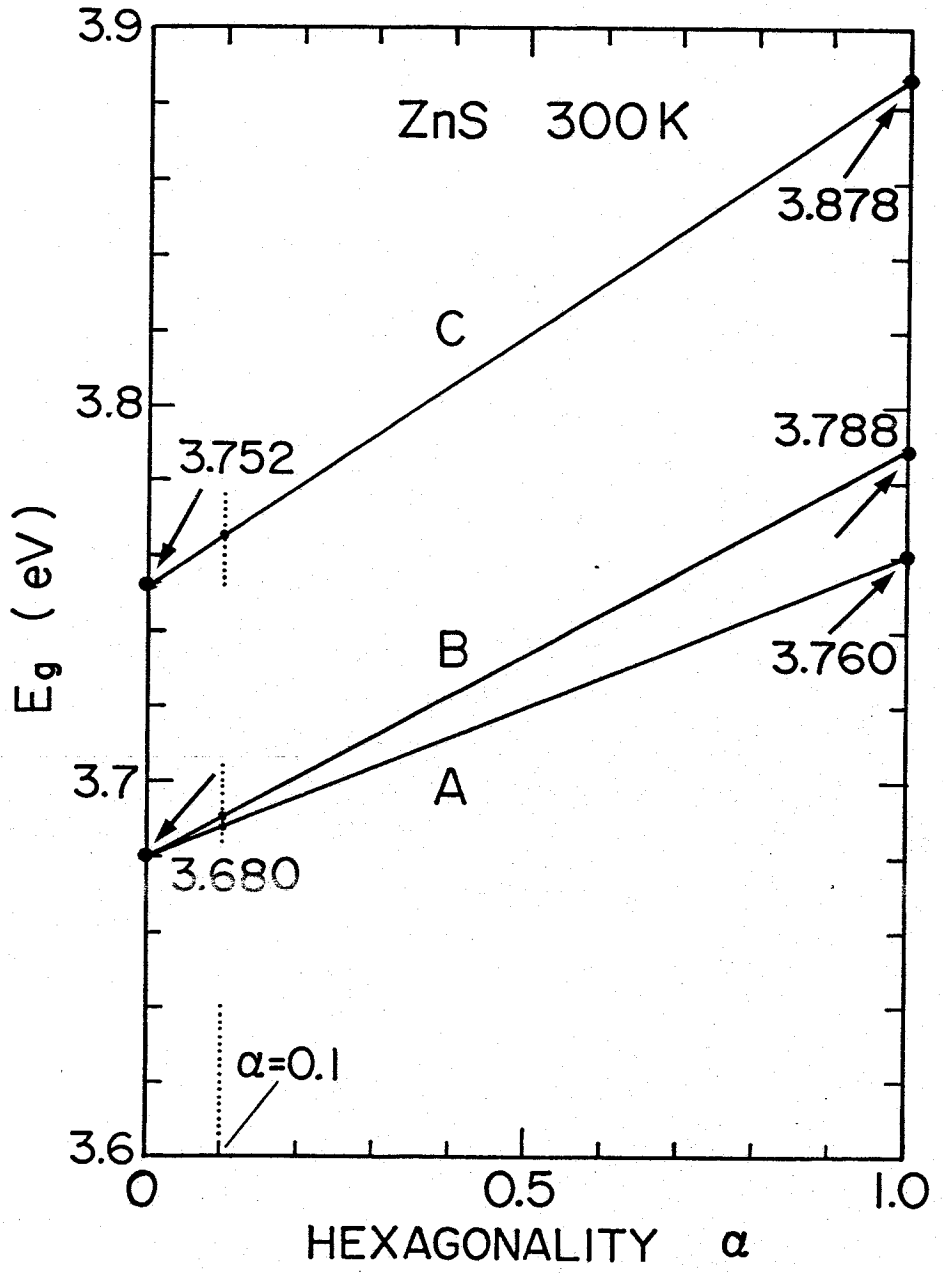

Fig. 5-9. Variation of the location of three band gaps (E_{gA}, E_{gB} E_{gC}) on the degree of hexagonality α at room temperature.

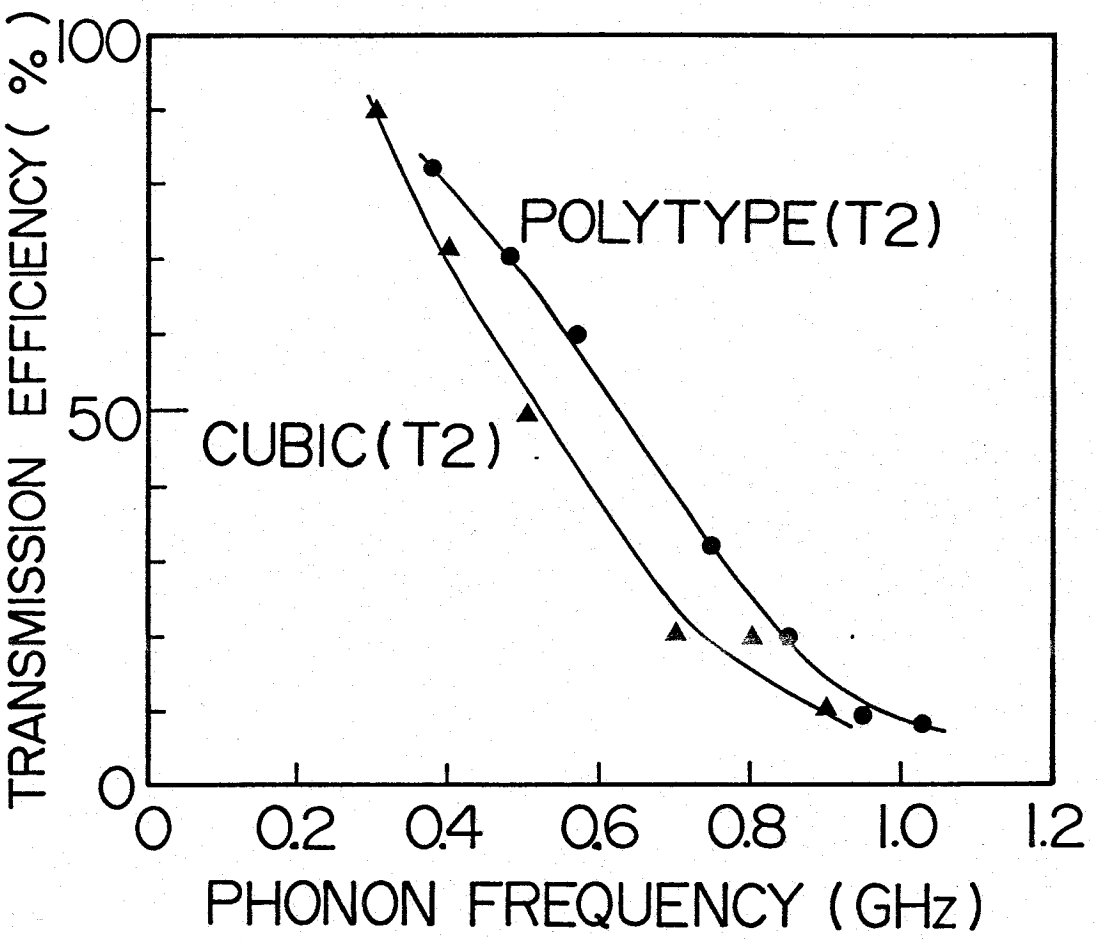

Fig. 5-10. Frequency dependence of the transmission efficiency of the acoustic phonon domains from CdS into ZnS samples.

samples). Theoretical value T_p (eq.(4.1)) of the efficiency in the higher frequency region is mainly due to the acoustic mismatch of the waves in the three layer structure CdS-In-ZnS.[109)]

The mode of the acoustic waves excited in ZnS by the acoustic domain injection method are determined by the crystal orientation as described in Chapter 4. The identification of the acoustic mode can be made by measuring the velocities of the injected acoustic waves. The slope of the curves in Fig. 5-11 give the sound velocities which are $v(T1) = 2.1 \times 10^3$ m/sec and $v(T2) = 3.4 \times 10^3$ m/sec in cubic ZnS, and the corresponding values in polytype ZnS are $v(T1) = 2.8 \times 10^3$ m/sec and $v(T2) = 2.7 \times 10^3$ m/sec. The values of the measured velocities are in good agreement with those calculated from the elastic constant reported by Berlincourt et al.[124)] and Cline et al.[125)] as listed in Table 5-3.

Figure 5-12 shows wavelength dependence of the Brillouin scattering cross section σ_B for 0.3 GHz T1-mode phonons at 77 K and room temperature for cubic and polytype ZnS.[73,109)] From the configuration for the scattering by T1-mode phonons we find that optical anisotropy (natural birefringence and dichroism in polytype crystal) does not take part in and therefore the Brillouin scattering cross seciton σ_B is propartional to I_s/I_t, where I_s and I_t stand for the light intensities scattered and transmitted through the sample. The Brillouin scattering cross sections represent a deep monimum (resonant cancellation) at around 366 nm in the cubic and 360 nm (352 nm at 77 K) in the polytype at room tenperature. At shorter wavelengths we find a resonant enhancement in polytype crystal. We have to point out here that no resonant enhancement in cubic ZnS in contrast to the case of the polytype ZnS. The disappearance of the resonant enhancement in the cubic ZnS can be ascribed to a strong absorption of the light in this region due to iodine impurities. Iodine impurities

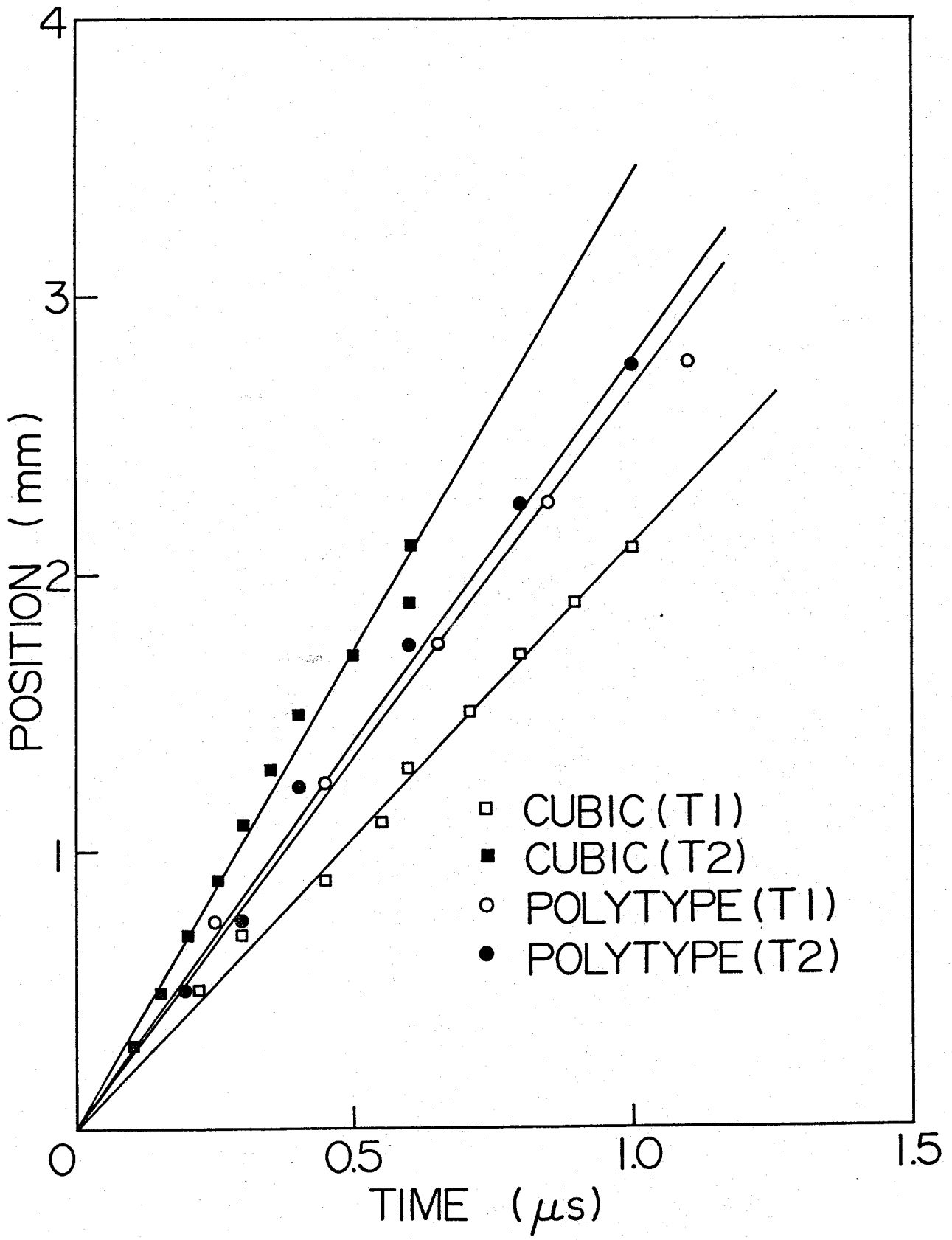

Fig. 5-11. Domain transit-time versus light-spot position for T1- and T2-mode for cubic and polytype ZnS from the Brillouin scattering measurements. The slope of each line gives the domain velocity for each mode.

Table 5-3. Values of elastic stiffness constants, density, and sound velocities for the cubic and hexagonal ZnS

Quantity		cubic	hexagonal	quasi-cubic approxinmation†	expt. value (cubic)	expt. value (polytype)
C_{44}	[10^{10} N/m^2]	4.613[a]	2.864[b]	2.898		
C_{11}	[10^{10} N/m^2]	10.46[a]	12.42[b]	13.35		
C_{12}	[10^{10} N/m^2]	6.53[a]	6.015[b]	5.792		
$C_{11} - C_{12}$	[10^{10} N/m^2]	3.93[a]	6.405[b]	7.56		
C_{33}	[10^{10} N/m^2]	——	14.00[b]	14.22		
C_{13}	[10^{10} N/m^2]	——	4.554[b]	4.913		
ρ	[10^3 Kg/m^2]	3.980[a]	4.088[b]	3.980		
$v(T1)=\sqrt{(C_{11}-C_{12})/2\rho}$	[m/s]	2222	2799	3048	2100	2750 ± 50
$v(T2)= \sqrt{C_{44}/\rho}$	[m/s]	3404	2647	2662	3400	2630 ± 50

[a]Reference 124.

[b]Reference 125.

†Defining z' =[111], y'= [$\bar{2}$11], x'=[01$\bar{1}$], the elastic constants refrred to the hexagonal axis are obtained by using the following relarions; $C'_{11} =(1/2)(C_{11} + C_{12} + 2C_{44})$, $C'_{12} =(C_{11} + 5C_{12} - 2C_{44})/6$, $C'_{13} =(C_{11} + 2C_{12} - 2C_{44})/3$, $C'_{14} = \sqrt{2}(C_{11} - C_{12} - 2C_{44})/6$, $C'_{33}=(C_{11} + 2C_{12} + 4C_{44})/3$, $C'_{44}=(C_{11} - C_{12} + C_{44})/3$ $(1/2)(C'_{11} - C'_{12})=(C_{11} - C_{12} + 4C_{44})/6$.

have been found to be about 300 ppm in the ZnS crystal prepared by the chemical transport method and measurement of optical transmission shows a strong absorption in the region below 370 nm. When we use thinner specimen ($\simeq 0.3$ mm), a resonant enhancement is observed as in the case of Brillouin scattering by T2-mode phonon which will be mentioned later. It is very interesting to point out in Fig. 5-12 that the Brillouin scattering cross section show a decrease as the wavelength increases. Such a decrease arises from the ω^4 dependence of the scattering cross section in eqs. (3.79) to (3.83).

In order to examine more precisely the ω^4 dependence in the dispersion of the Brillouin scattering cross sections, we extended the measured wavelength region to the longer wavelength region. Figure 5-13 shows the dispersion curves of the Brillouin scattering cross secitons for 0.3 GHz T1-mode phonons for 320 nm to 650 nm. We can see a decrease of the scattering cross section explicitely in the longer wavelength region. So far as our knowledge is concerned such a wavelength dependence has not been observed because earlier works are restricted to a narrow range of wavelengths. The cross section given by eq. (2.78) has an ω_s/ω_i factor appearing in the classical light scattering theory. An explicit $\omega_s^3\omega_i$ dependende can be obtained by using $\vec{E}\cdot\vec{r}$ coupling instead of $\vec{p}\cdot\vec{A}$ in the Hamiltonian.[130] Therefore we take into account the ω^4 dependence in the following calculations. In other words, we calculated R_{is} using eq. (2.134) and evaluated σ_B from eq. (2.141) including ω^4 dependence in C. Parameters used in the present calculation of the Brillouin scattering cross sections are listed in Table 5-4. The results are represented by the solid curves in Fig. 5-13.

Figure 5-14 shows the resonant Brillouin scattering cross section σ_B for 0.3 GHz T2-mode phonons at 77 K and 300 K for polytype and cubic ZnS.

Table 5-4. Parameters used in the calcualtion of the Brillouin scattering cross section and photoelastic constants of ZnS at 300 K (the values at 77 K are given in the brackets)

	Cubuc (77K)	Polztype(α=0.1)(77K)	Wurtzite
E_{gA} (eV)	3.66 (3.826[b])	3.688 (3.289[c])	3.74[a] (E‖ c)
	3.68[a]		
E_{gB} (eV)	3.66 (3.826[b])	3.691 (3.833[c])	3.78[a] (E⊥c)
	3.68[a]		
E_{gC} (eV)	3.76 (3.891[b])	3.764 (3.902[c])	3.88[a] (E‖ c)
	3.752[a]		3.87[a] (E⊥c)
E_B (meV)	31[c]	31 - 34[c]	
Δ_{so} (meV)	72[d]	74[d]	92[d]
Δ_{cr} (meV)	0[d]	3[c]	55[d]
a_0 (Å)	23.8[d]	23.8[d]	
μ	0.18[d]	0.18[d]	
a_B		0.58	0.691
a_C		0.814	0.723
	2b = -1.06[e] (eV)	———	C_1 = 2.5[f] (eV)
	2b = -3.4[b] (eV)	———	C_2 = 2.25[f] (eV)
	2b = -1.5[f] (eV)	C_3 = 0.72[g] (eV)	———
	$d/\sqrt{3}$ = -2.14[e] (eV)	C_4 = -1.07[g] (eV)	———
		C_5 = 1.09[g] (eV)	———
		C_6 = 1.57[g] (eV)	———

[a] Reference 126.
[b] Reference 127.
[c] Reference 116.
[d] Reference 128.
[e] Referenee 129.
[f] Reference 72.
[g] We evaluated this values by using b = -0.75[f] (eV), d= - 3.7[e] (eV) and eq.(4) in ref. 127.

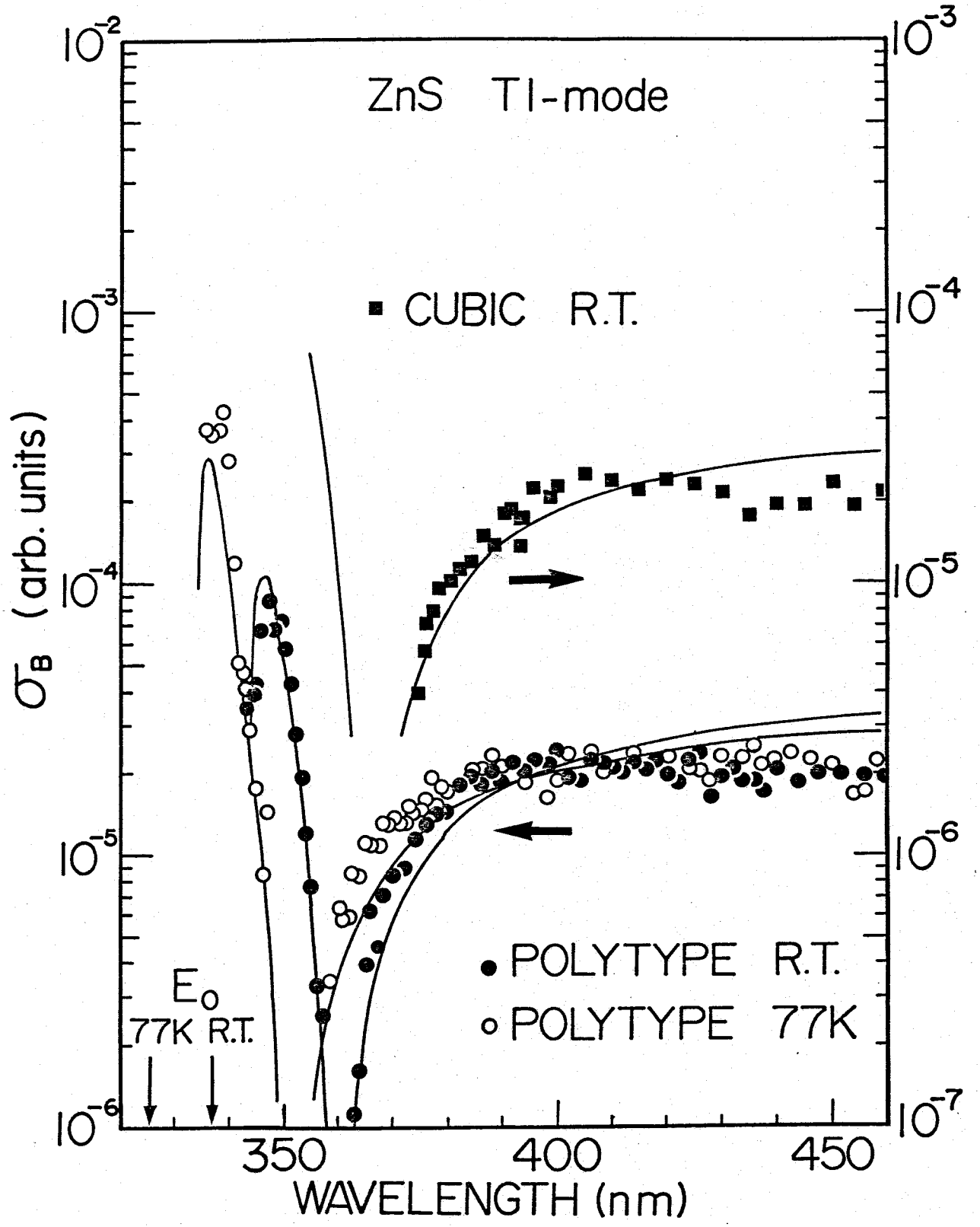

Fig. 5-12. Dispersion curves of the Brillouin scattering cross sections for 0.3 GHz TI-mode phonons measured at room temperature and 77 K. Solid curves are calculated by the Brillouin scattering theory;eq.(2.134) and (2.140). The thickness of the sample is 1.2 mm.

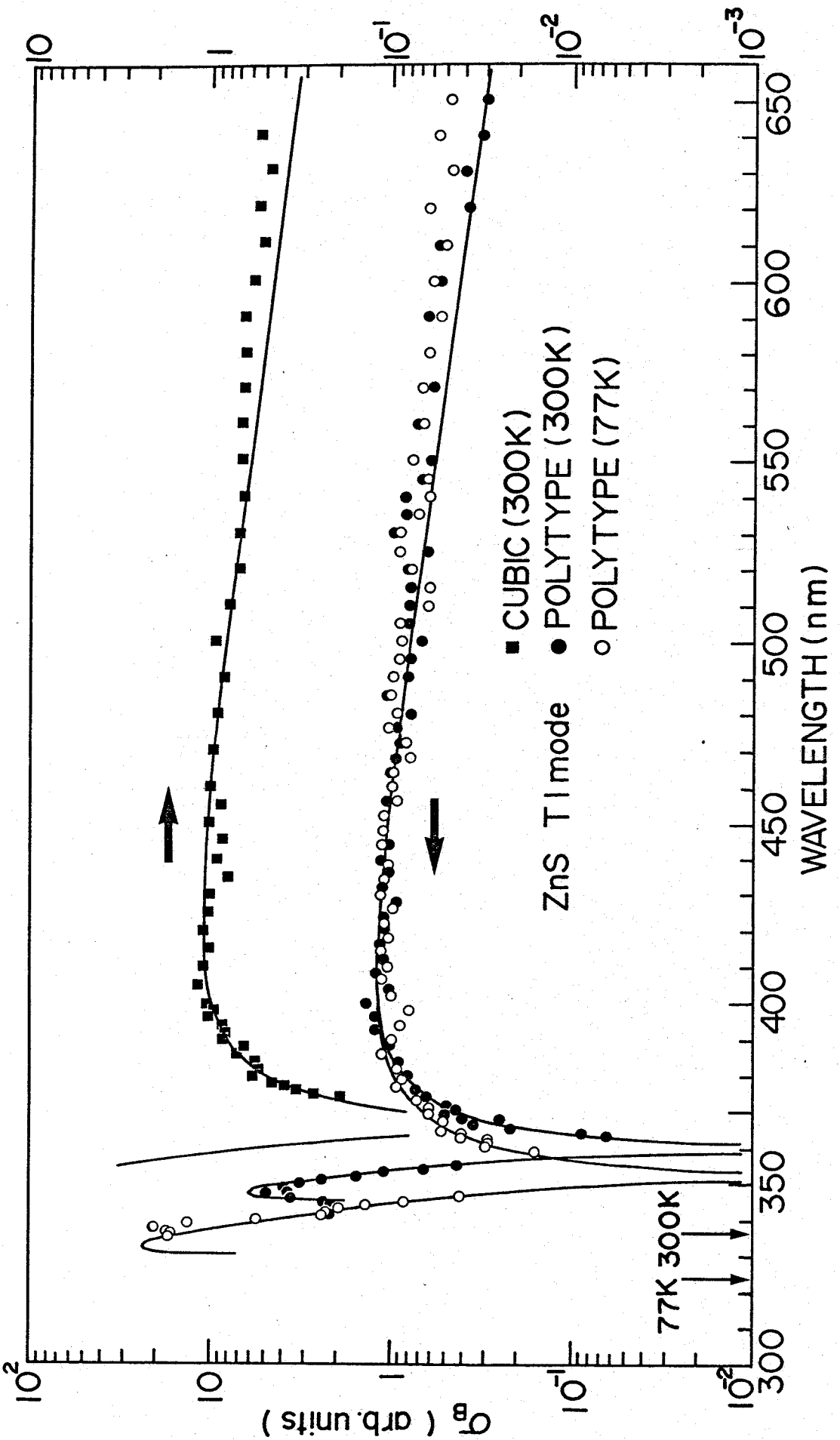

Fig. 5-13. Dispersion curves of the Brillouin-scattering cross sections for 0.3 GHz T1-mode phonons measured at room temperature and 77 K. The theoretical curves are calculated by using eqs.(2.134) and (2.140). The vertical arrows indicate the position of the band gap E_g at 300 K and 77 K.

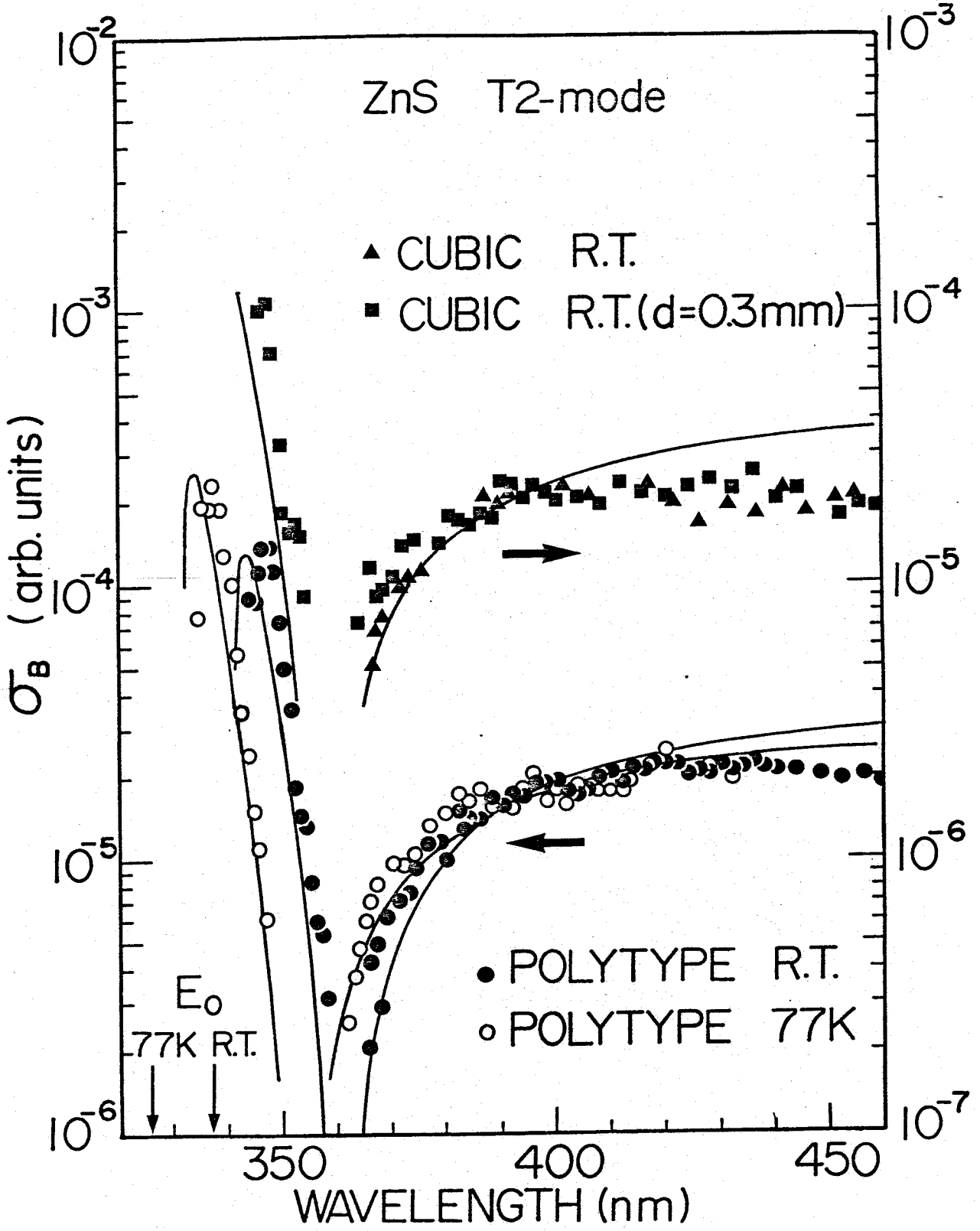

Fig. 5-14. Dispersion curves of the Brillouin scattering cross sections for 0.3 GHz T2-mode phonons measured at room temperature and 77 K. Solid curves are calculated by the Brillouin scattering theory; eqs.(2.134) and (2.140). Unless otherwise noted, the thickness of the sample is 1.2 mm.

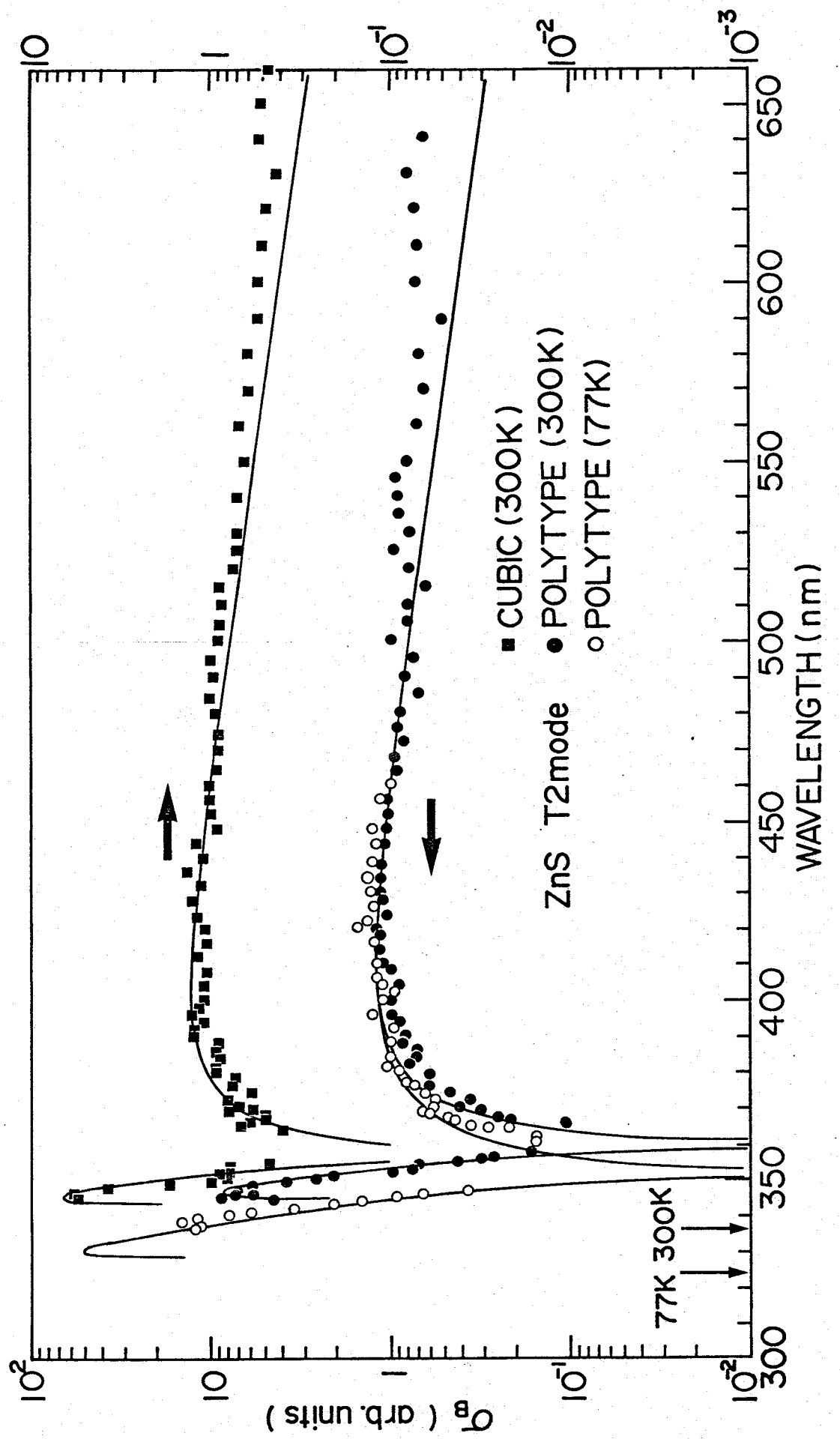

Fig. 5-15. Dispersion curves of the Brillouin scattering cross sections for 0.3 GHz T2-mode phonons measured at room temperature and 77 K. The theoretical curves are caluculated by using eqs.(2.134) and (2.140). The vertical arrows indicate the positons of the band gap E_g at 300 K and 77 K.

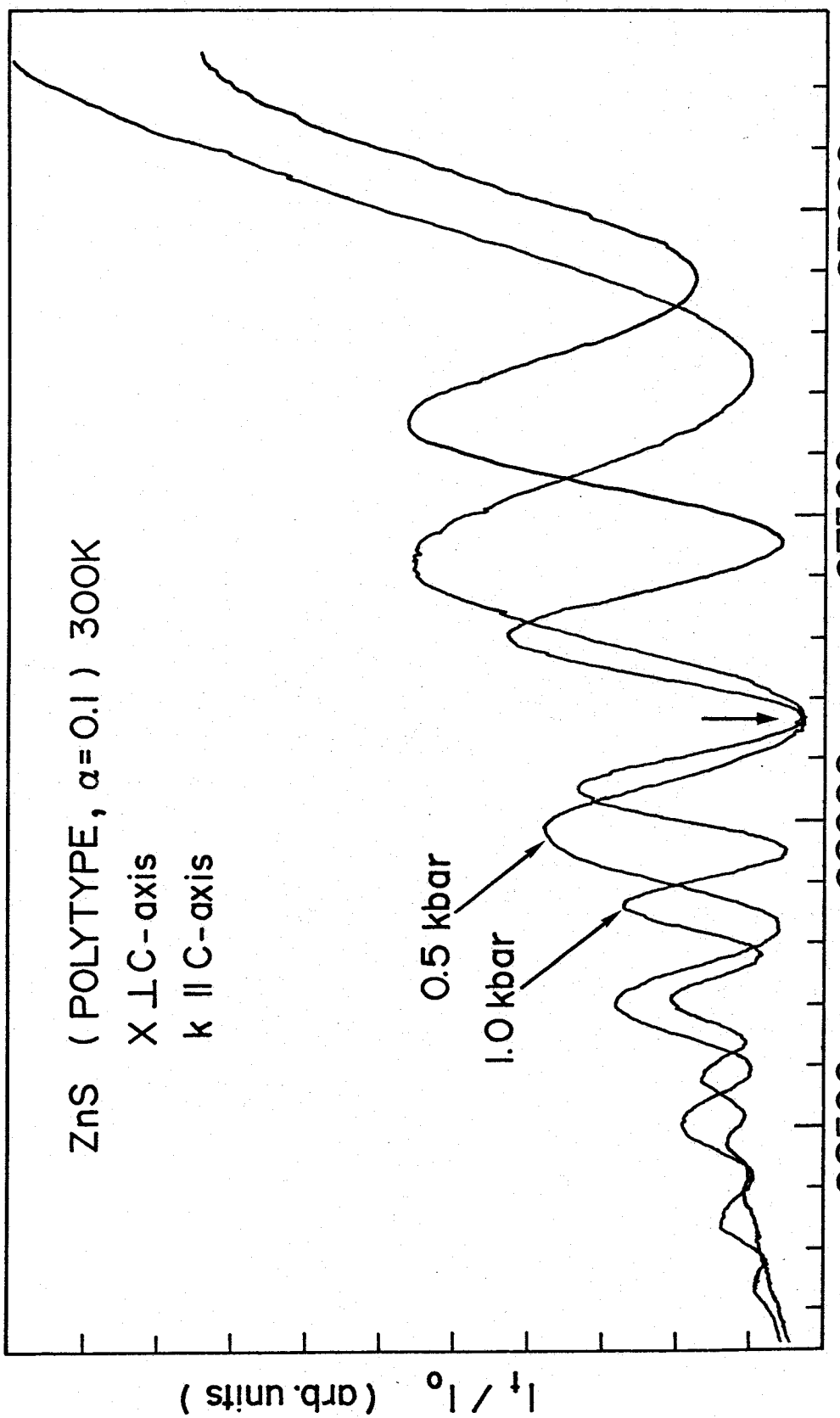

Fig. 5-16. The recorded spectra used in determination of $P_{11} - P_{12}$ on polytype ZnS ($\alpha = 0.1$). The vertical arrow indicate the position (27830 cm^{-1}) of the isotropic point.

The angles of the incident and scattered light were calculated using eqs. (2.15) and (2.16). In order to obtain the scattering cross section we have to make a correction due to the absorption as pointed by Ando and Hamaguchi.[30] In the present work we measured the transmitted light intensity $I_{t\parallel}$ and $I_{t\perp}$ for the light polarizaiton parallel and perpendicular to the c-axis and the scattering cross section was obtained from $I_s/\sqrt{I_{t\parallel} \cdot I_{t\perp}}$. The resonant feature observed here is essentially the same as that for the case of the scattering by the Tl-mode phonon domains. The cancellation points are 360 nm at 300 K and 352 nm at 77K in the polytype ZnS, while in cubic ZnS cancellation occurs at 355 nm at 300 K and thus a slight shift of the cancellation point toward the energy gap exists. We find a decrease in σ_B at larger wavelengths due to the ω^4 dependence as in the case of the Tl-mode phonons.(See Fig. 5-15) Theoretical curves of eqs. (2.134) and (2.141) are fitted to the experimental data by taking into account the ω^4 dependence.

5.3.3 Photoelastic Constants

In this subsection we state that the stress-induced birefringence (piezobirefringence) $n_{\parallel} - n_{\perp}$ is related to the photoelastic constants. In the presnet study we carried out the piezobirefringence measurement for the uniaxial stress in the [111] and [100] directions in cubic ZnS and in the $[11\bar{2}0]$ direction in polytype ZnS.

Figure 5-16 shows the recorded spectra of the piezobirefringence experiment in polytype ZnS ($\alpha = 0.1$). In this experiment, uniaxial stress perpendicular to the c-axis is applied to the sample with X = 0.5 kbar and 1.0 kbar. The vertical arrow indicate the positon (359.3 nm) of the isotropic point of the piezobirefringence. From this spectra photoelastic constant $P_{11} - P_{12}$ on polytype ZnS is determined from piezobirefringence with uniaxial stress parallel fo the c-axis and the natural and piezo-

birefringence of polytype ZnS are shown in Fig.5-17. As seen in Fig. 5-17 the compression along the c-axis of polytype ZnS reduced the magnitude of the birefringence.[131] From the piezobirefringence experiments we deduced $P_{11} - P_{12}$ in both cubic and polytype ZnS and P_{44} in cubic ZnS. The results are shown in Fig. 5-18 where we find that the photoelastic constants are negative at longer wavelengths, approaching zero at shorter wavelengths, and sign reversal occurs near the absorption edge. The spectral position of the isotropic point of the piezobirefringence corresponds to the wavelength at which photoelastic constnat becomes zero. The positions are 365 nm (by extrapolation) for $P_{11} - P_{12}$ and 365 nm for P_{44} in cubic ZnS, while the value is 359.4 nm for $P_{11} - P_{12}$ in polytype ZnS. Theoretical values of $P_{11} - P_{12}$ and P_{44} in cubic can be calculated from eq.(3.47) by adjusting the parameters C, C_{ex}, D and the results are shown by the solid curves in Fig. 5-18. The energy gaps given in Table 5-3 are used in the calculations and the best fitting parameters are shown in Table 5-4. Equations (3.66) and (3.70) reduce to eqs. (3.47) and (3.51), respectively, in the limit $E_{gA} = E_{gB}$. In the polytypes ZnS with a small α the energy separation between the A and B valence bands is quite small (3 meV for α=0.1). Therefore we can evaluate the value of $P_{11} - P_{12}$ for polytype ZnS (α= 0.1) from eqs. (3.47) and (3.51), and the result is shown by the solid curve in Fig. 5-19, where the best-fitting parameters given in Table 5-4 are used in the calcualtion.

Figures 5-20 and 5-21 show the dispersion curves of the photoelastic constants $P_{11} - P_{12}$ and P_{44}, respectively, deduced from the present Brollouin scattering measurements by using eqs.(3.79) to (3.83), where the theoretical values are adjusted to the experimental values at 460 nm in Fig. 5-19. In the analysis the dispersion of the refractive indices and ω^4 dependence are taken into account. Theoretical curves were calculated by eqs.(3.47)(for

$P_{11} - P_{12}$) and eq. (3.52)(for P_{44}), which are shown by solid curves, where the parameters used in the calcualtion are shown in Table 5-4. In all cases we find a good agreement between the experimental and calculated results. Fig 5-21 and 5-22 show the dispersion curves of the photoelastic constants $P_{11} - P_{12}$ and P_{44}, respectively, for 77 K and 300 K, deduced from the present Brillouin scattering measurements by using eqs.(3.79) and (3.83). Theoretical curves are calculated by same method as described in Figs. 5-20 and 5-21.

Piezobirefringence experiment to deduce P_{44} in polytype ZnS was not performed in the present study and therefore the magnitude of the photoelastic constant P_{44} is unknown. The value of P_{44} in the polytype crystal is estimated in the folowing way on the basis of the quasi-cubic model. It is convenient to describe atomic positions in zincblende (space group T_d^2) in terms of a Cartesian set of axis coinciding with the cubic x, y, z axis; in wurtzite (space group C_{6v}^4) or polytype (crystal symmetry C_{3v}) hexagonal axis are defined as hexagonal x´, y´, z´axis. The relations between these different system are z =[111], y =[$\bar{2}$11], x =[01$\bar{1}$].[113] The photoelastic constants referred to the hexagonal axis are then obtained by

$$P'_{44} = \frac{1}{3}(P_{11} - P_{12} + P_{44}) \quad , \tag{5.5}$$

$$P'_{11} - P'_{12} = \frac{1}{3}(P_{11} - P_{12} + 4P_{44}) \quad , \tag{5.6}$$

where $P'_{11} - P'_{12}$ and P'_{44} are photoelastic constants referred to the hexagonal axis and $P_{11} - P_{12}$ and P_{44} are those referred to the cubic axis. In order to check the validity of the quasi-cubic model we calculated $P'_{11} - P'_{12}$ from eq. (5.6) and obtained $P'_{11} - P'_{12} = -0.12$ at 460 nm which is resonable agreement with the measured value - 0.11. The value P'_{44} estimated at 460 nm from

Table 5-5. Parameters used in the calcualtion of dispersion curves of photoelastic constants from the piezobirefringence theory in eqs. (3.47) and (3.51).

Crystal structure	Photoelastic constant	$C \times 10^4$	$C_{ex} \times 10^4$	D Experiment	D[a] Theory	Dip(nm)[b]
Cubic	$P_{11} - P_{12}$	35.4	3.65	-0.0942	-0.30	366
	P_{44}	14.5	1.48	-0.0796	-0.60	355
Polytype	$P_{11} - P_{12}$	35.0	3.59	-0.127	———	360
	P_{44}	16.0	1.64	-0.0579	———	360

a) Calculated from the Penn model in eqs. (3.59) and (3.60)
b) Estimated from the present data, 'Dip' stands for the spectral position corresponding to the isotropic point of the piezobirefringence or the minimum in the Briilouin scatteing cross sections.

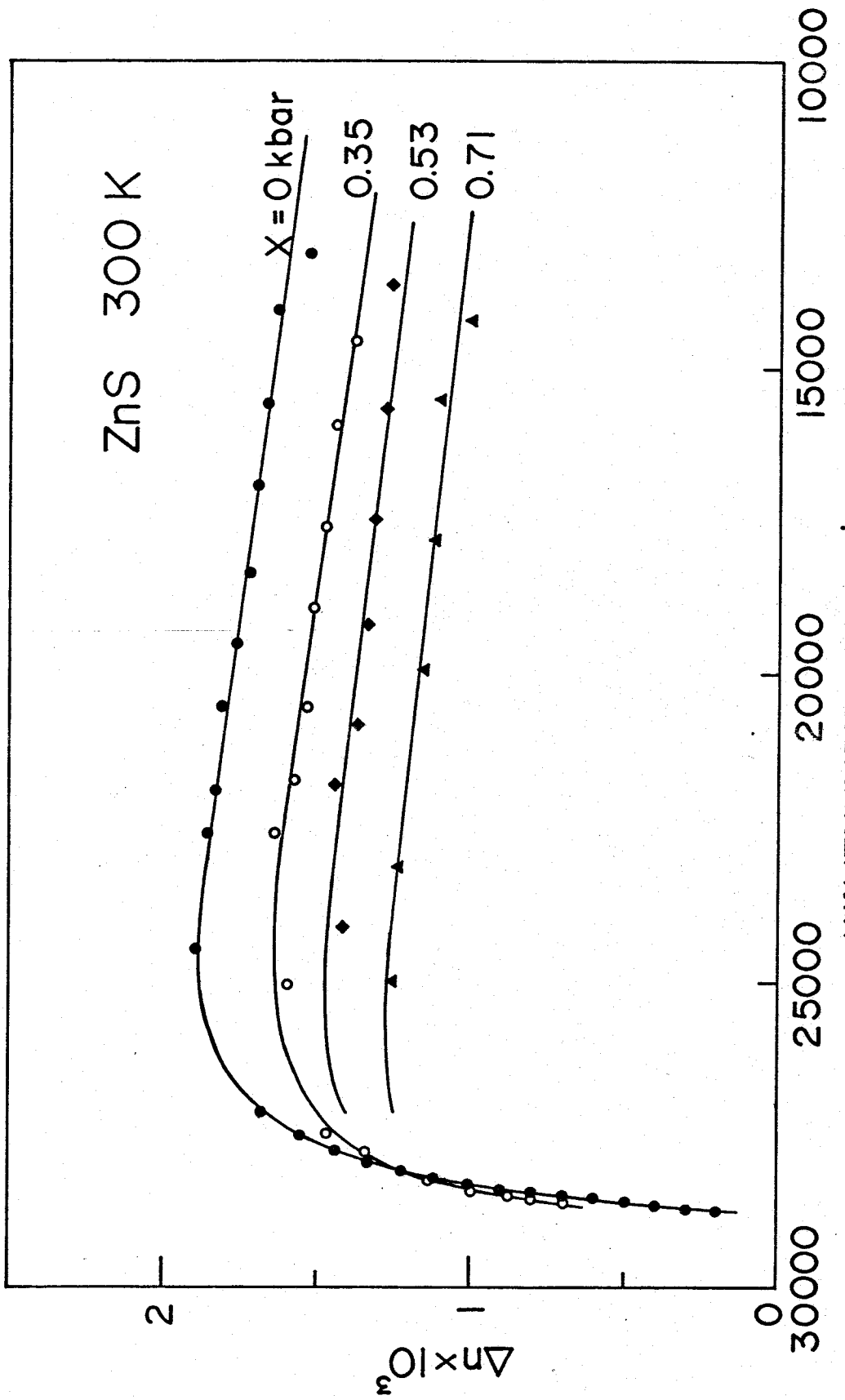

Fig. 5-17. Natural birefringence (X = 0 kbar) and piezobirefringence (X ≠ 0) in polytype ZnS (with α = 0.1) compressed along the c-axis by various stress. The wavevector of the incident light (k) is perpendicular to the c-axis.

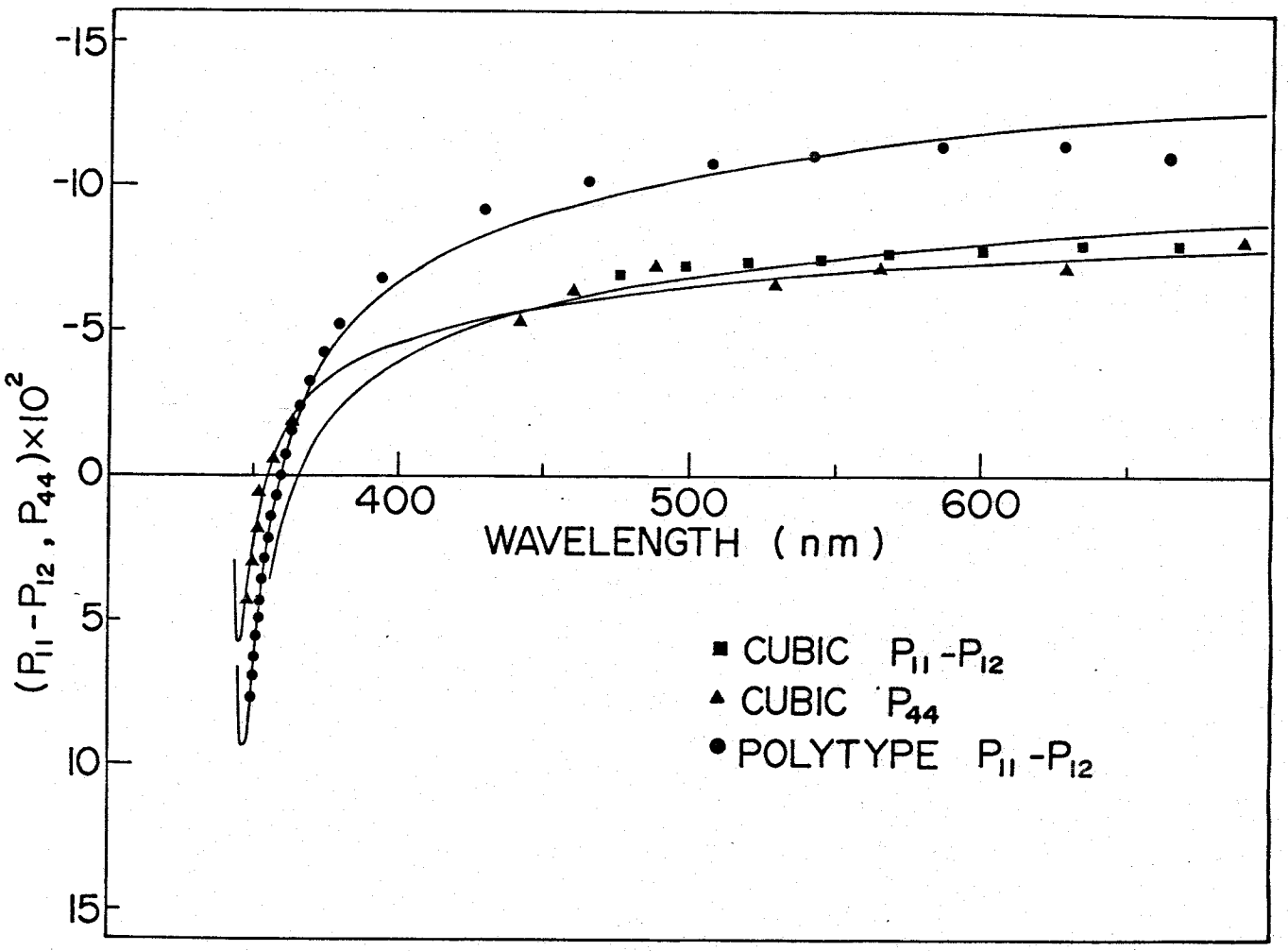

Fig. 5-18. Dispersion curves of photoelastic constants of ZnS determined by the static stress-induced birefringence measurements at 300 K. Theoretical curves were calculated from eqs. (3.47) and (3.51).

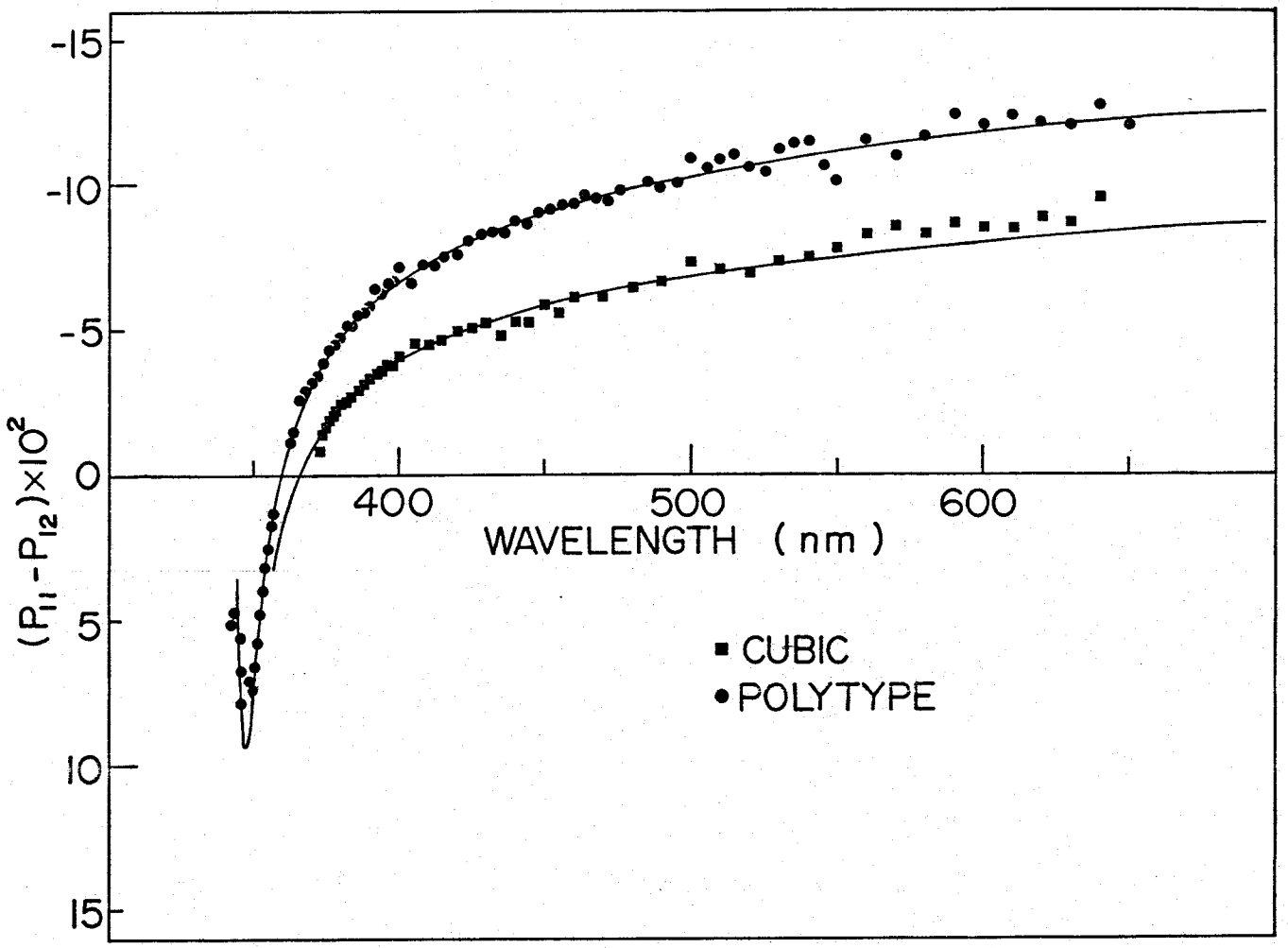

Fig. 5-19. Dispersion curves of the photoelastic constant $P_{11} - P_{12}$ of ZnS determined from the Brillouin scattering cross section in Fig. 5-13, where the sign and magnitude of the photoelastic constant is fitted to the experimental value of the piezobirefringence data at 460 nm. Theoretical curves were calculated from eq.(3.47) with the parameters given in Table 5- 5 .

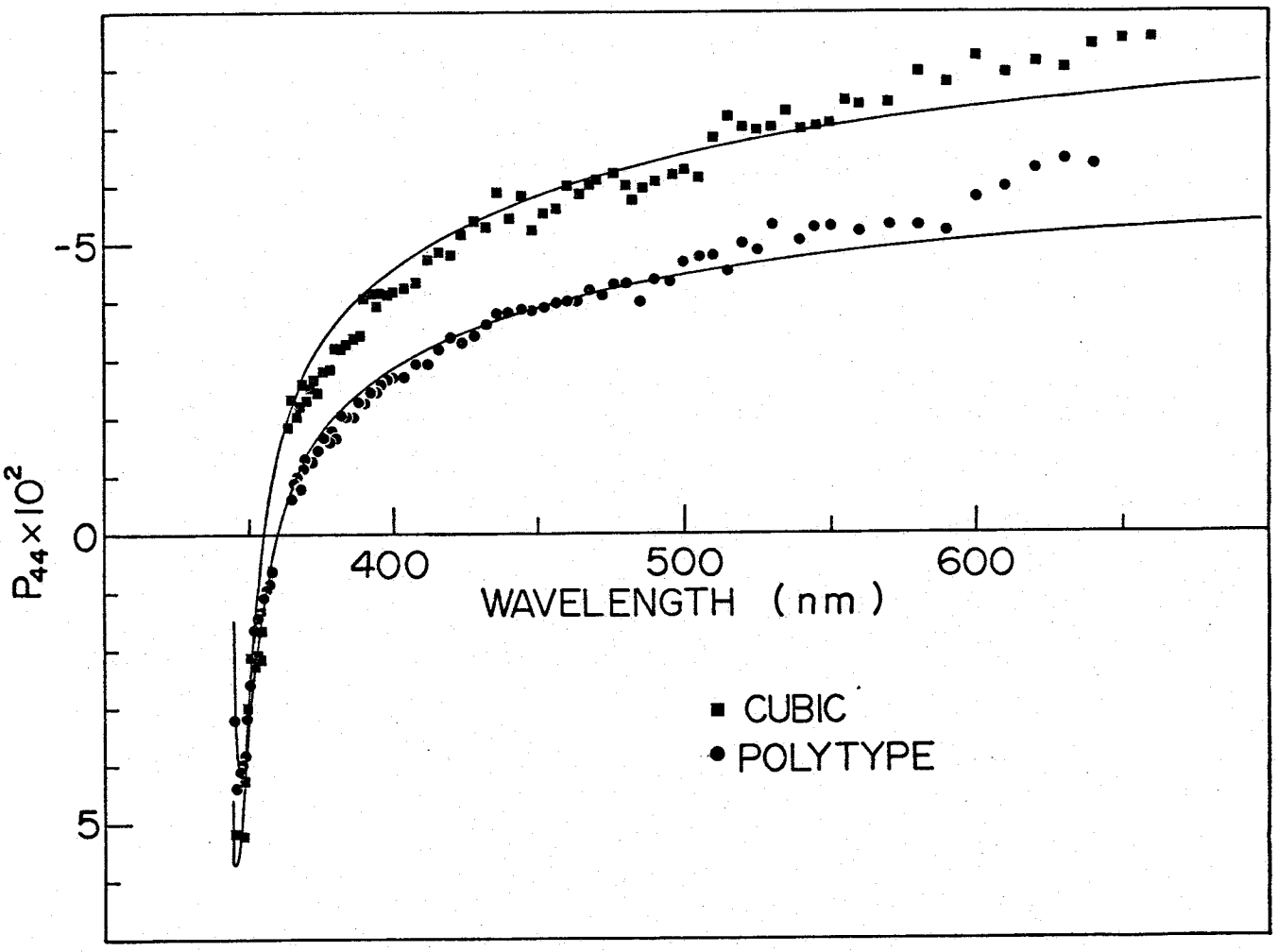

Fig. 5-20. Dispersion curves of the photoelastic constant P_{44} of ZnS determined from the Brillouin scattering cross section in Fig. 5-15, where the sign and magnitude of the photoelastic constant is fitted to the experimental value of the piezobirefringence data at 460 nm. Theoretical curves were calculated from eq.(3.51) with parameters given in Table 5-5 .

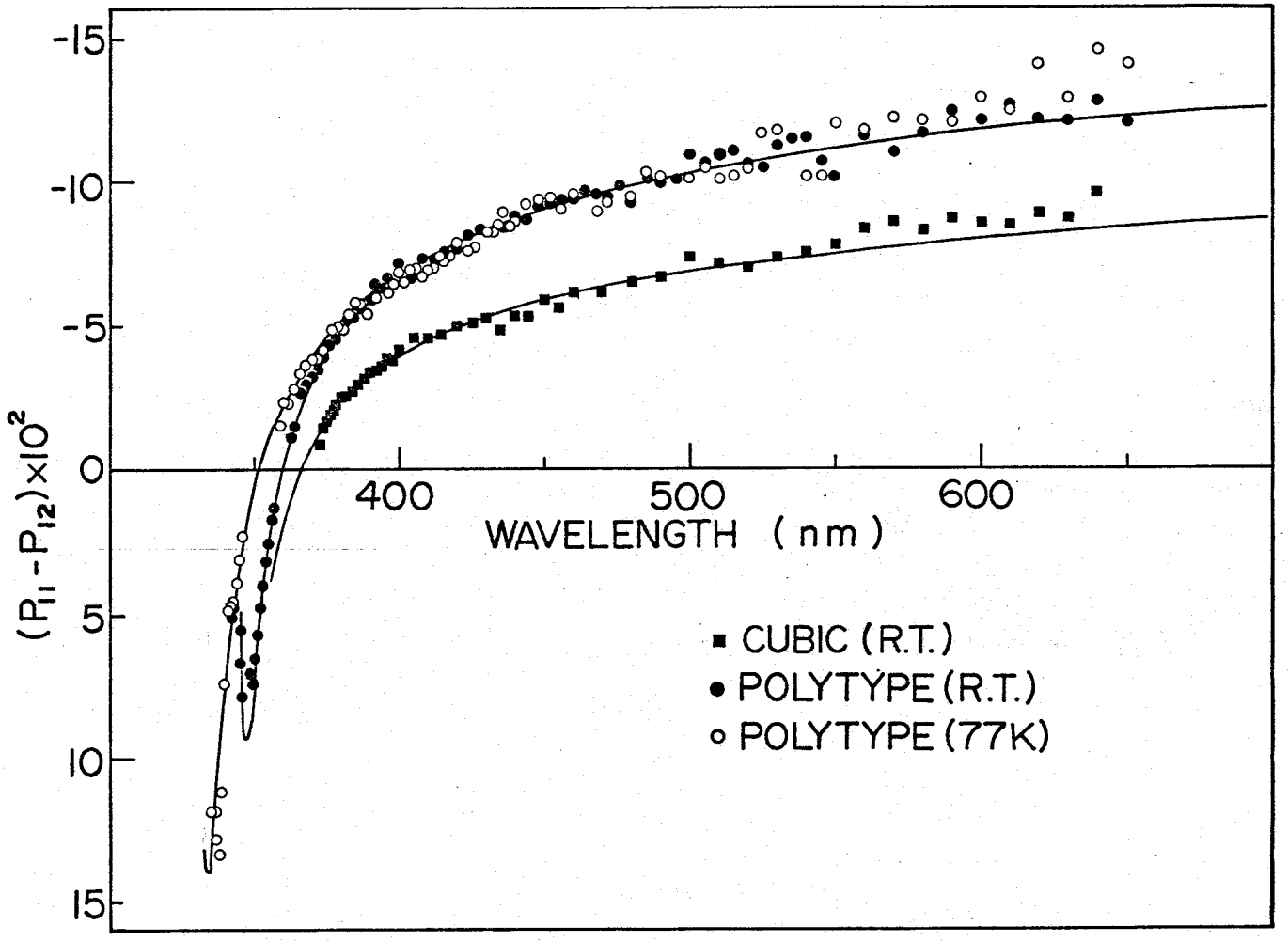

Fig. 5-21. Dispersion curves of the photoelastic constant $P_{11} - P_{12}$ of ZnS at 77 K and room temperature.

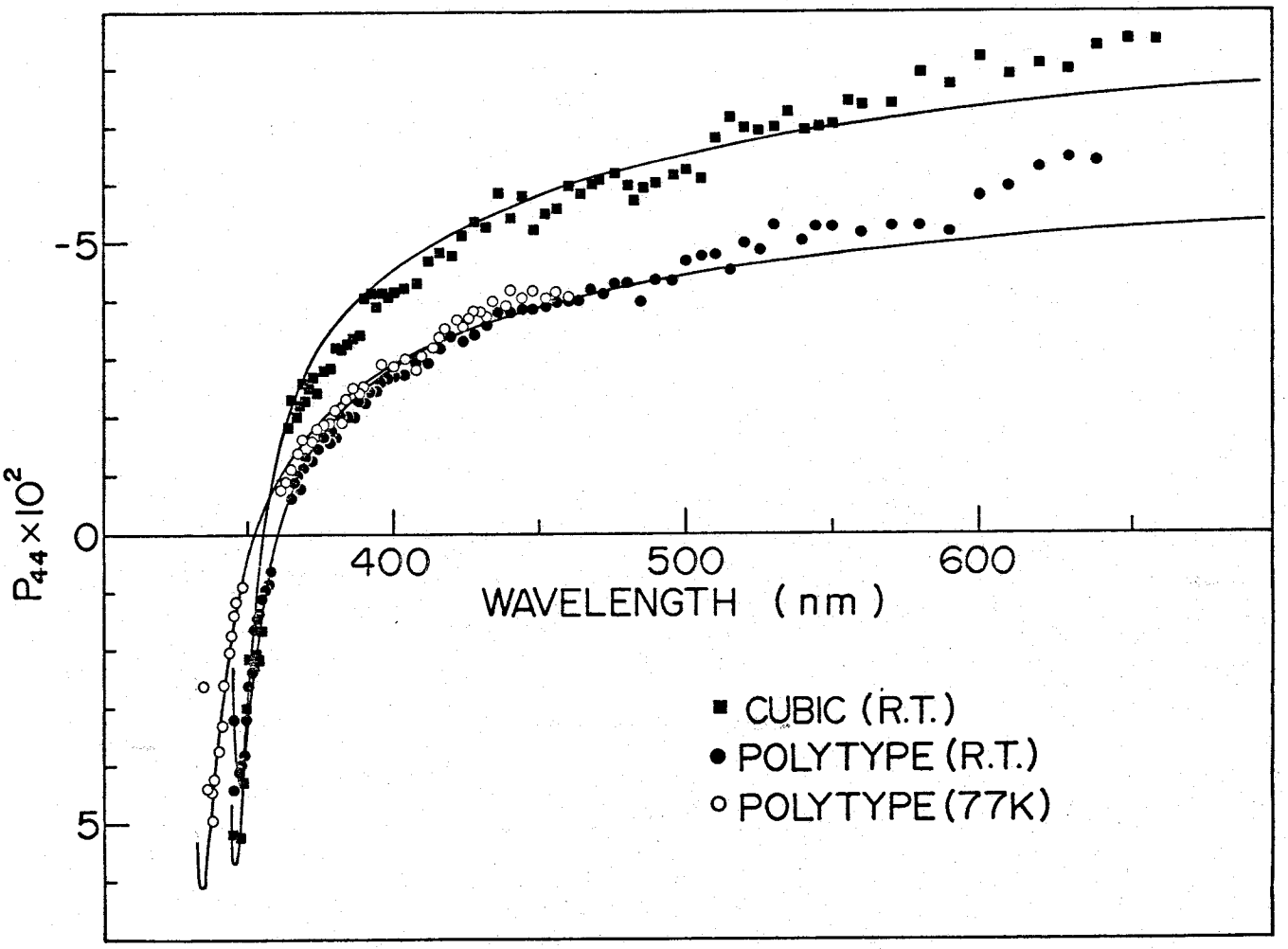

Fig. 5-22. Dispersion curves of the photoelastic constant P_{44} of ZnS at 77 K and room temperature.

eq. (5.5) is -0.040. This value is used to obtain spectral dependence of P_{44} for the polytype in Figs. 5-19 and 5-22. As mentioned in the case of $P_{11} - P_{12}$, Theoretical value of P_{44} can be calculated by eq. (3.51), which is shown by the solid curve in Fig. 5-19 and 5-22 (parameters used are shown in Table 5-5).

All the experimental data of the Briilouin scattering experiments are found to be in good agreement with the piezobirefringence theory as shown in Figs. 5-18 to 5-22.

5.4 Resonant Brillouin Scattering by T2- and LA-mode in CdS

In this section we will discuss the resonant Brillouin scattering in CdS by two kinds of phonons. In 5.4.1, dispersion of the Brillouin scattering by T2-mode phonons and photoelastic constant P_{44} is presented. In 5.4.2, dispersion of Brillouin scattering by LA-mode phonons and photoelastic constant P_{31} is presented.

5.4.1 Resonant Brillouin Scattering by T2-mode Phonons in CdS

The spectral dependence of the Brillouin scatteing cross sections for the acoustoelectrically amplified T2-mode phonon domains in CdS measured at room temperature and 77 K are shown in Fig. 5-23. The phonon frequency is selected to be 0.3 GHz. The incident and scattering angle related to the appropriate phonon frequency were obtained from eqs.(2.15) and (2.16), using the data of refractive indices[132] and natural birefringence.[133]

In the case of T2-mode phonons, the absorption coefficient of the scattered light is different from that of the incident light because the

scattered and incident light have different polarization ($e_i \| c$-axis and $e_s \perp c$-axis). Hence in order to deduce the Brillouin scattering cross section, we have to take into account a dichroism correction of absorption of light. This was first made by Ando and Hamaguchi.[30] They obtained the following relation near the fundamental absorption edge:

$$\frac{I_s}{I_0} = \frac{\sigma_B d\Omega_s}{\alpha_i - \alpha_s n_s/n_i} \exp\left(-\frac{\alpha_s b}{\cos\theta_s'}\right) \times\left\{1 - \exp\left[-\left(\alpha_i - \alpha_s \frac{n_s}{n_i}\right) \frac{b}{\cos\theta_i'}\right]\right\} , \tag{5.7}$$

where α_i and α_s are the absorption coefficents for the incident and scattered light, respectively, and b is the width of the sample in the scattering plane. The refractive indices n_i and n_d refer to the values of the incident and scattered light, and the incident angle θ_i' and the scattered angle $\theta_d' = (\theta_s' - \theta_i')$ are defined in Section 2.2. The experimental data shown in Fig. 5-23 are obtained from dichroism correction using the absorption coefficient of Dutton.[134] The experimental data show resonant cancellation at 560 nm (room temperature) and 550 nm (77 K). Above the cancellation point steep resonant enhancement is observed. The shift of the cancellation point by changing the temperature of sample corresponds to the shift of the band gap energy. The theoretical dispersions of the Brillouin scattering efficiency were calculated by using eq. (2.134) and (2.140). The numerical values used in the present calcualtion is listed in Table 5-6 . The solid curves are theoretical ones taking into account the real part of the Brillouin tensor. Imaginary part of the Brillouin tensor, which plays an important role in the region very close to the fundamental absorption edge, is omitted because the imaginaly part is negligible in the region far from the fundamental absorption edge (See

Table 5-6. Parameters used in the calculation of the Brillouin scattering cross sections and photoelastic constants in CdS

Symbol		Numerical value	
E_{gA}	(eV)[a]	2.452 (295K)	2.531 (77K)
E_{gB}	(eV)[a]	2.466 (295K)	2.545 (77K)
E_{gC}	(eV)[a]	2.525 (295K)	2.604 (77K)
E_B	(meV)[b]	28	
f_{xx}^A, f_{zz}^A	[c]	4.14×10^{-3}	0
f_{xx}^B, f_{zz}^B	[c]	2.82×10^{-3}	3.64×10^{-3}
f_{xx}^C, f_{zz}^C	[c]	1.38×10^{-3}	6.97×10^{-3}
C_2	(eV)[d]	2.9	
C_4	(eV)[d]	- 1.5	
C_6	(eV)[d]	- 2.4	
a_B		0.75	
a_C		0.66	

[a] Reference 135.
[b] Reference 70.
[c] Reference 136.
[d] Reference 72.

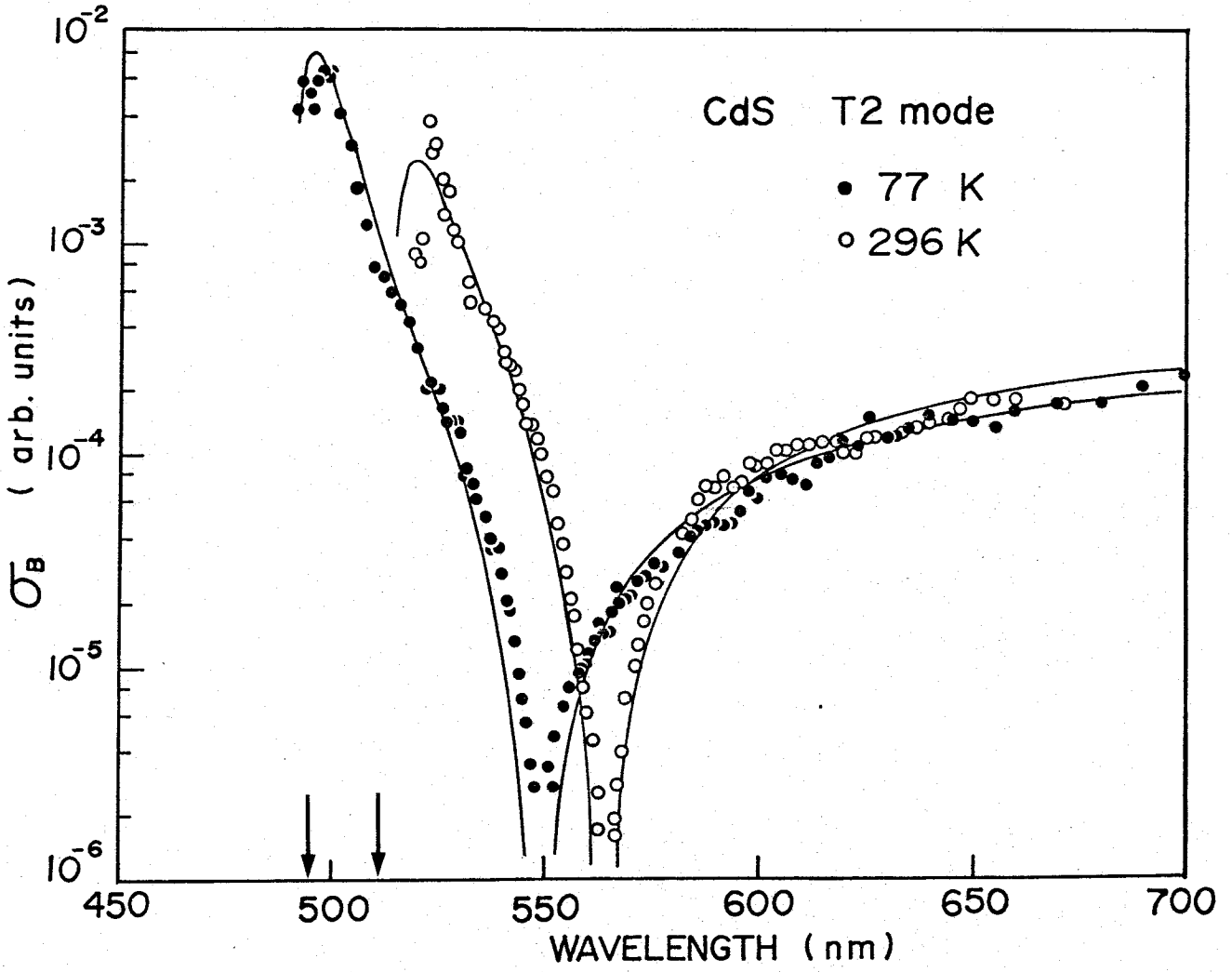

Fig. 5-23. Dispersion curves of the Brillouin scattering cross sections in CdS for 0.3 GHz T2-mode phonons measured at room temperature and 77 K. The solid curves are calculated by the Brillouin scatteirng theory given in eq. (2.134) and (2.140). The vertical arrows indicate the spectral positions of the wavelengths corresponding to the ground state levels (n = 1) of A valence band.

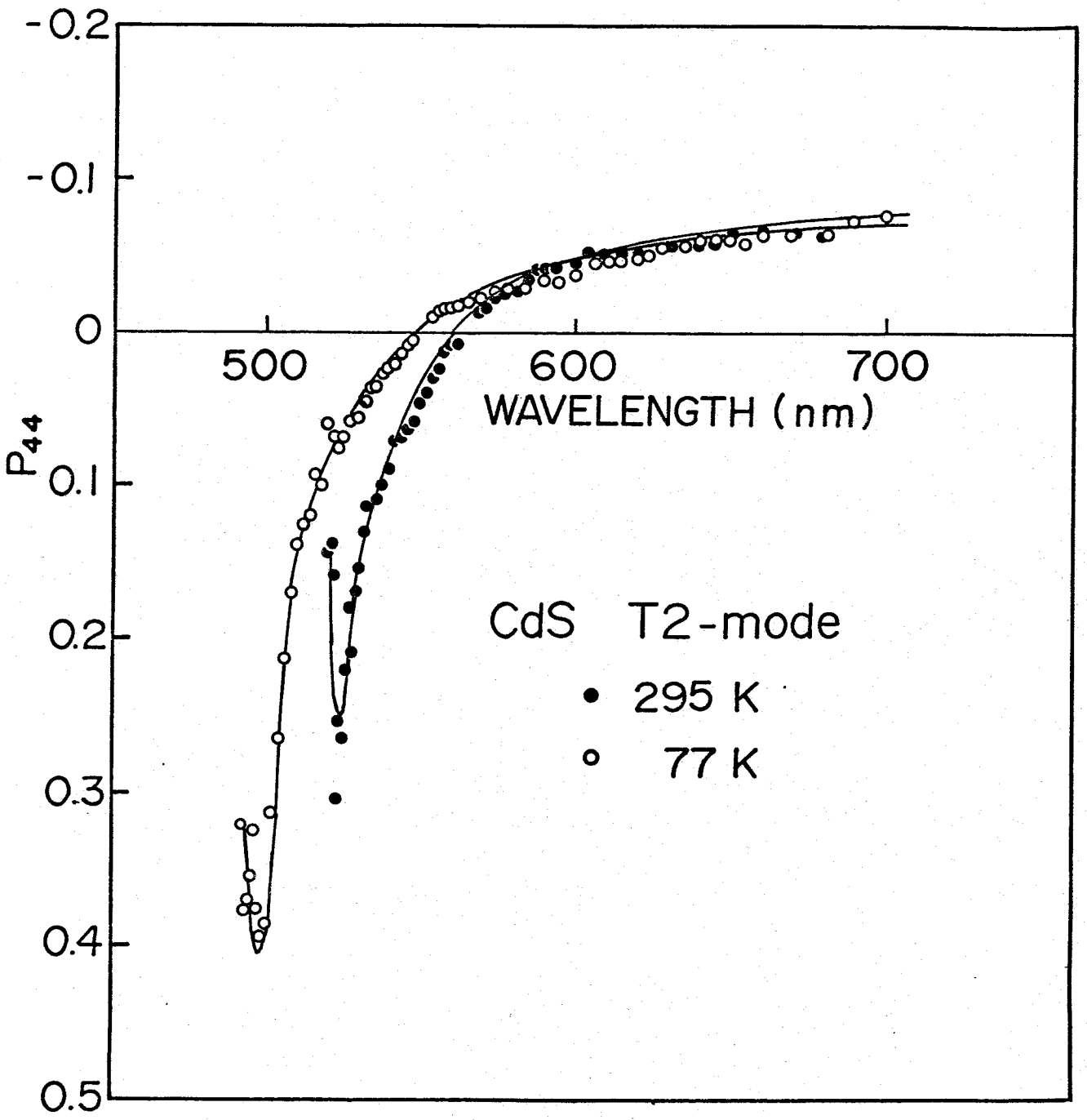

Fig. 5-24. Dispersion curves of the photoelastic constant P_{44} of CdS determined from the Brillouin scatteing cross section in Fig. 5-23, where the sign and magnitude of the photoelastic constant is fitted to the value $P_{44} = -0.075$ (at 630 nm).

Chapter 6). The experimental data show a maximum in the region very close to the fundamental absorption edge. We presume, however, this maximum arises from the experimental difficulty because both the transmitted and scattered light suffer from strong absorption. Brillouin scattering cross section is proportional to I_s/I_t, where I_s refers to the scattered light intensiry and I_t the transmitted light intensity. Near the fundamental absorption edge, the magnitude of I_S and I_t change considerably (a factor of 10^2 or more). In the strong absorption region , the S/N ratio of the factor I_s/I_t becomes bad. We conclude that this maximum of the dispersion curves comes from the low S/N ratio of the signal and no maximum peak exsists in the resonant enhancement region.

Figure 5-24 shows the dispersion of the photoelastic constant P_{44} deduced from the present Brillouin scattering measurement by using eq.(3.82), where the theoretical values are best fitted to the experimental values. The absolute value and sign are fitted to the value of P_{44} = -0.075 at 630 nm obtained by Yu and Cardona.[78] In the analysis the dispersion of the refractive indices and ω^4 dependence are neglected because the measured region of the incident light is narrow range. Theoretical curves were calculated by eq. (3.69), which are shown by solid curves, where the parameters used in the calcualtion are shown in Table 5-6. In both cases for 295 K and 77 K, we find a good agreement between experimental and theoretical results.

5.4.2 Resonant Brillouin Scattering by LA Phonons in CdS

In this subsection, we present dispersion curves of resonant Brillouin scattering by LA (logitudinal acoustic) mode in CdS at room temperature, and an analysis of the resonant behaviour by the theory based upon the Brillouin scattering theory and piezobirefringence theory.[154]

Since the first observation of the resonant Brillouin scattering in GaAs,[29] similar measurements have been carried out in various semiconductors. The measured data, however, are limitted to tansverse acoustic phonons (T1- and T2-mode phonons). Pine[27] observed a weak resonant enhancement for the scattering from LA phonons, where the scattering cross section was measured by thermally tuning the fundamental absorption edge in CdS through the incident radiation at 514.5 nm.

We report here a novel technique to observe the resonant behavior for the Brillouin scattering from LA phonons with the propagation direction and atomic displacement perpendicular to the c-axis.

The present measurement was made at room temperature by using the mode converted LA phonons which were generated by reflection of the acoustic domains at the anode of the sample. The dimensions of the sample are 1.3 mm wide, 3.9 mm thick and 6.8 mm long. We found that thicker specimens are suitable for generation of the mode converted LA phonons. This seems to be the fact that the amplified acoustelectric domains propagate with a cone angle of about 10°. Therefore various component of mode converted phonons are generated from the off axis components of the domains in thicker specimens. Polarization of the incident and scattered light are parallel to the c-axis and thus the corresponding photoelastic constant is P_{31}.

The identification of the LA phonons was made by the sound velocity $v_{LA} = \sqrt{C_{11}/\rho} = 4.34 \times 10^5$ cm/sec and the selection rule of the light polarizations. In this configuration the optical anisotropy does not take part in and therefore the Brillouin scattering cross section is proportional to I_s/I_t where I_s and I_t stand for the scattered and transmitted intensities of the light. Scattering cross sections σ_B thus obtained are plotted in Fig 5-25 along with the values estimated from the data of Tell

et al.[26] for the purpose of comparison, where the latter data are obtained from Raman-Nath experiment. We find a fairly good agreement in the data between the two different methods, and both exhibit a weak resonant enhancement near the fundamental absorption edge. It should be noted here that resonant cancellation as observed in the case of TA phonons[28-38] is not found in the photon energy range investigated. From the similar anlysis as made by Ando and Hamaguchi[30] we find that the transition of the intermediate holes between the B valence band predominates in the process and thus two band theory is possible. We evaluated the scattering cross section using the relation given in eq.(2.134) and (2.141). The result is shown by the solid curve, where we find a good agreement with the experimental data. In the analysis we find that a sign reversal of $R_{is} + R_0$ occurs at wavelength λ = 750 nm and that the non-dispersive component R_0 is very weak compared with that of transverse acoustic waves. We applied the piezobirefringence analysis to the present data and the results are shown in Fig. 2-26, where the photoelastic constant P_{31} is estimated using the relation given in eq.(3.83).

We find in Fig. 2-26 that the theoretical curve obtained from piezobirefringence analysis shows a good agreement with the experimental dispersion where the theoretical curves is adjusted to give the experimental value of $P_{31} = -0.041$ at λ = 633 nm.[137] Since the present experiment does not provide the absolute value of P_{31}, the experimental values are normalized at 550 nm so that the experimental values are best fitted to the theoretical curve by the method of least mean squares. The analysis reveals that the most dominant contribution comes from the excitation of holes in the B valence band and that the sign reversal of the photoelastic constant occurs at the wavelength about 750 nm. These results are consistent with the resonant Brillouin scattering analysis mentioned above.

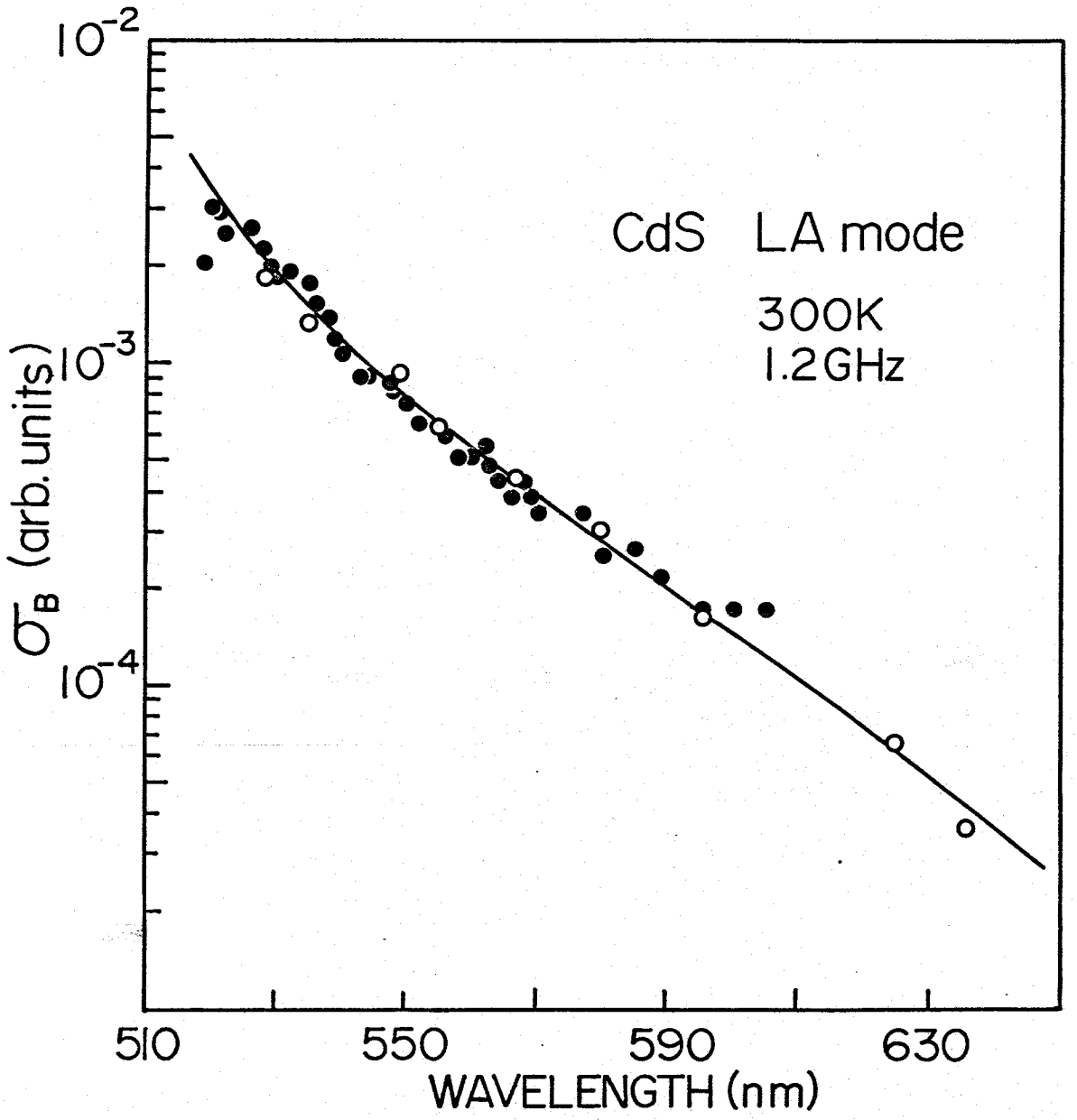

Fig. 5-25. Dispersion of Brillouin scattering cross sections (closed circles) in CdS at 300 K by 1.2 GHz LA phonos. Solid curve is calculated by taking into account the exciton effect. For comparison results of Tell et al. are plotted by open circles.

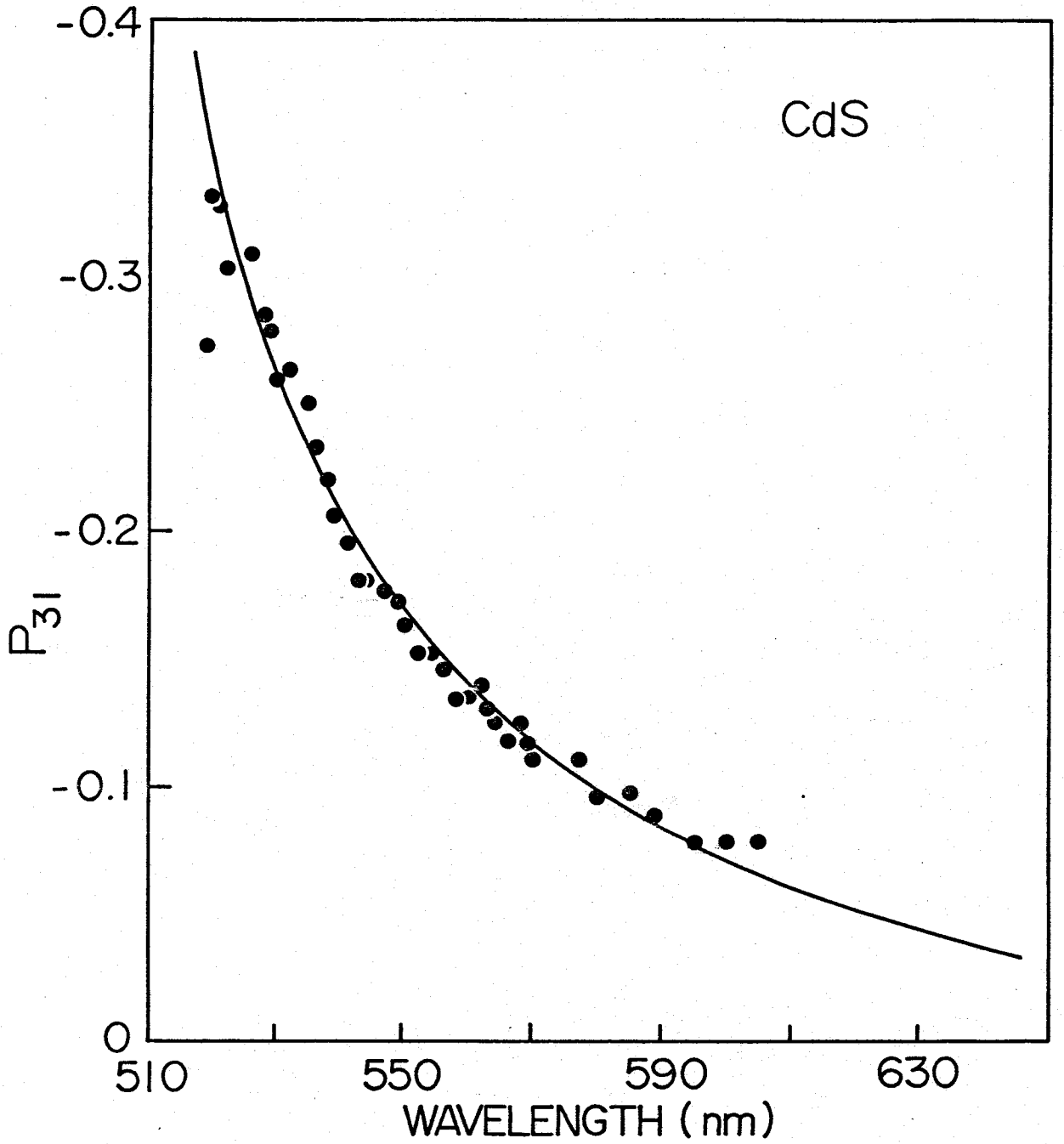

Fig. 5-26. Dispersion of the photoelastic constant P_{31} obtained from the data shown in Fig. 5-25. Solid curve is calculated by the piezobirefringence theory and the values are adjusted to give $P_{31} = -0.041$ at 633 nm.

In conclusion, the observed resonant behavior of the Brillouin scattering by LA phonons is explained by the theories of resonant Brillouin scattering and piezobirefringence theory when we assume the non-dispersive component has the different sign from the dispersive component.

5.5 Resonant Brillouin Scattering in HgI_2

In this section, we shall discuss the observation and an analysis of resonant Brillouin scattering in the layered type semiconductor HgI_2 by the pure-transverse (PT) acoustical phonons at room temperature in the photon energy of 1.45 - 2.2 eV. We performed the resonant Brillouin scattering measurement by employing the amplified acoustical domain injection method.

5.5.1. Optical Properties of HgI_2

The layered semiconductor HgI_2 gives rise to a strong anisotropic behavior of the physical properties due to the singularities of the crystal structure. At room temperature, HgI_2 occurs as red tetragonal crystal (D_{4h}^{15}) which changes to a yellow orthorombic form on heating 400 K.[138] Red tetragonal HgI_2 cleaves easily to give crystallographic plane perpendicular to the crystal c-axis. The absorption edge of HgI_2 is characterized by the direct optical transition from three p-like valence bands, which are split due to spin orbit interaction and crystal field perturabation, to an s-like conduction band. Normal incidence reflectivity measurement at 4.2 K ($E \parallel$ c-axis, $q \perp$ c-axis) shows three sharp exciton peaks at A(2.339eV), B(2.538eV), C(3.35eV), peak A being at the absorption threshold.[139] A group theoretical analysis of the band structure of the tetragonal HgI_2 in the Γ-point of the Brillouin zone has shown that the

conduction band has the symmetry Γ_6^+ and the valence band has its origin in p-orbitals of iodine and is split by the spin-orbit coupling and crystal field into three valence bands with symmetries Γ_7^-, Γ_6^- and Γ_6^- .[140] The reflection maxima A, B, and C coinside with the optical transitions into the corresponding exciton series, respectively. This band structure in the Γ point is very similar to those of wurtzite crystals such as CdS,CdSe and ZnS.

We have deduced the real and imaginary part of the dielectric constant by means of the conventional Kramers-Kronig analysis [141] of the reflection data of Kanzaki and Imai.[139] The procedure used for the extrapolation of R(E) from 6 eV to infinite energies has been described in ref.141. It is clear from Fig. 5-27 to Fig. 5-30 that the optical transitions are direct and three sharp exciton peaks are shown near the fundamental absorption edge. Various parameters related to the fundamental absorption edge is listed in Table 5-7. Figure 5-30 shows the combined density of state calculated from the data of Fig. 5-27. It should be noted that the back ground peak is very close to the fundamental absorption edge. Such a structure is in contrast to those found in III-V or II-VI compound. We assume that the background peak at around 3.5 eV of the combined density of state ($\varepsilon_2 E^2$) corresponds to direct transitions at higher bands although the characteristic of the transition is unknown. Thus it is interesting to compare the Brillouin scattering cross sections between II-VI (III-V) compounds and layered compounds since the Brillouin scattering cross section strongly depends on the band structure and density of state in higher energy region. We shall present a simple microscopic model to calculate the contribution of the broad peak to the Brillouin scattering cross sections.

5.5.2 Sample Preparation and Experimental Procedure

The HgI_2 crystal used in the presnt experiment was grown

from the solution growth by using dimethylsulfoxide (DMSO) solvent.[142] The sample is cleaved along the c-plane and used without further treatment. The sample is bonded to the end-bonded surface of the CdS single crystals through a cyanoacrylate resin (Aron Alpha) and high intensity acoustic domain was injected into the HgI_2. We found that cyanoacrylate resin is suitable material for bonding thinner or layered crystals to CdS. The HgI_2 crystal was cut and cleaved in the form of parallelepiped with dimensions of about 2 mm wide, 5 mm long, and 0.54 mm thick. The acoustical domain injected into the layered-type specimen travels in the direction perpendicular to the c-axis with shear polarization perpendicular to the c-axis (*i.e.* PT phonon domains). The identification of the injected domain was made by the sound velocity. The slope of the line in Fig. 5-31 gives the sound velocity which is $v_{PT} = 1.46 \times 10^3$ (m/sec). Theoretical value of the sound velocity is calcualted by using the existing data of the elastic constants and density of HgI_2.[143] Using the formula $v_{PT} = \sqrt{(C_{11} - C_{12})/2\rho} = 1.468 \times 10^3$ (m/sec), where $C_{11} = 3.303 \times 10^{11}$ (dyn·cm^{-2}), $C_{12} = 0.559 \times 10^{11}$ (dyn·cm^{-2}) and $\rho = 6.354$ (g·cm^{-3}). We find that the experimental and theoretical results show a good agreement.

5.5.3 Brillouin Scattering Cross Sections

Figure 5-32 shows the spectral dependence of the Brillouin scattering cross sections for pure transverse acoustic phonons in HgI_2, obtained at room temperature in the region of transparency. The following scattering configurations were used in the present measurements by taking into account their polarization selection rules[73]: $\vec{e}_i \perp \vec{c}$, $\vec{e}_s \perp \vec{c}$ and $\vec{e}_i \perp \vec{e}_s$, where $\vec{e}_i$ and $\vec{e}_s$ are the unit vector in polarization direction of the incident and scattered light, respectively. The frequency of the acoustical domains has been selected to be 0.4 GHz by properly setting the incident and scattered

angles.

The spectral dependence of the Brillouin scattering cross sections show a resonant cancellation in the vicinity of the band gap. Such a feature is in contrast to those found in other direct-gap semiconductors such as CdS,[30,38] ZnS,[73,109] ZnSe[34] and so on, where the spectral dependence shows clear resonance features (resonant enhancement and cancellation) in the region near the direct gaps. The absence of resonance features has been thought to be due to that the contribution from the direct gap in HgI_2 is rather weak so that the nonresonant contributions are dominant in the Brillouin scattering process. Such a resonant feature of HgI_2 is very similar to those found in GaSe and GaS by Adachi and Hamaguchi.[41]

The Brillouin-scattering cross section is now given by

$$\sigma_B \propto |R(\omega_i,\omega_s,\omega_q)|^2, \tag{5.8}$$

where R is the Brillouin tensor, ω_i and ω_s are the frequencies of the incident and scatterd radiations, respectively, and ω_q is the frequency of the relevant acoustical phonons. In the present analysis, we can separate the Brillouin tensor R into three independent components:

$$R = R_{is} + R'_{is} + R_0 \tag{5.9}$$

where R_{is} and R'_{is} are lowest-direct and higher-direct gap resonance terms, respectively, and R_0 is the non-resonant term arising from the other, far-off critical points in the band structure. Evaluation of R_{is} is given by eq.(2.140). For the transition at around ω_0 = 3.5 eV, we use essentially the Penn model.[80] Within this model the Brillouin tensor contribution R'_{is} can be written as

$$R'_{is} = \frac{d}{d\omega_0}\left(\frac{A}{\omega_0^2-\omega^2}\right) \simeq -\frac{2A}{\omega_0^3}\left(1+2\frac{\omega^2}{\omega_0^2}\right) \tag{5.10}$$

Table 5-7. Parameters used in the calculation of the Brillouin scattering cross sections of HgI_2

Symbol	Numerical values				
$E^{\dagger}_{eA}$ (eV)	2.339[a]	(4.2K)	2.320[a]	(77K)	2.231[b] (300K)
$E^{\dagger}_{eB}$ (eV)	2.538[a]	(4.2K)	2.505[a]	(77K)	2.426[b] (300K)
$E^{\dagger}_{eC}$ (eV)	3.35[a]	(4.2)	3.31[a]	(77K)	3.238[b] (300K)
E_B (meV)	34[c] , 41[d]				
a_B	0.76[e]				
a_C	0.64[e]				

$^{\dagger}E_{eA}$, E_{eB}, and E_{eC} are the ground state exciton energy for the valence bands, and given by $E_{e\alpha} = E_{g\alpha} - E_B$.

[a] Reference 139.

[b] Reference 144.

[c] Reference 145.

[d] Reference 146.

[e] Calculated by using eqs. (2.180) to (2.182), where we used $\Delta_0 = 0.812$.

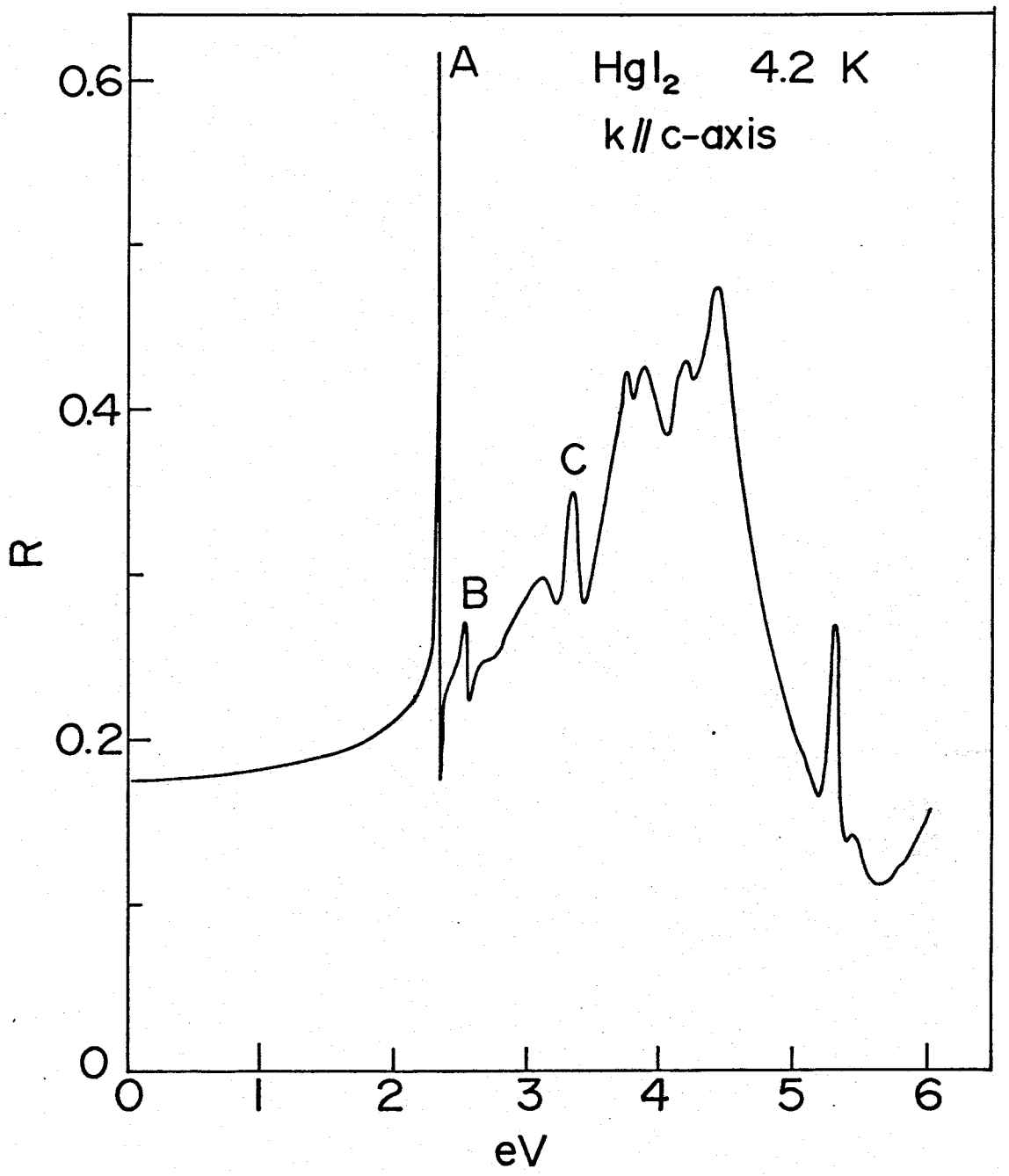

Fig. 5-27. Refrectivity spectrum of HgI_2 at 4.2 K; E⊥c-axis, k∥c-axis (From ref.139).

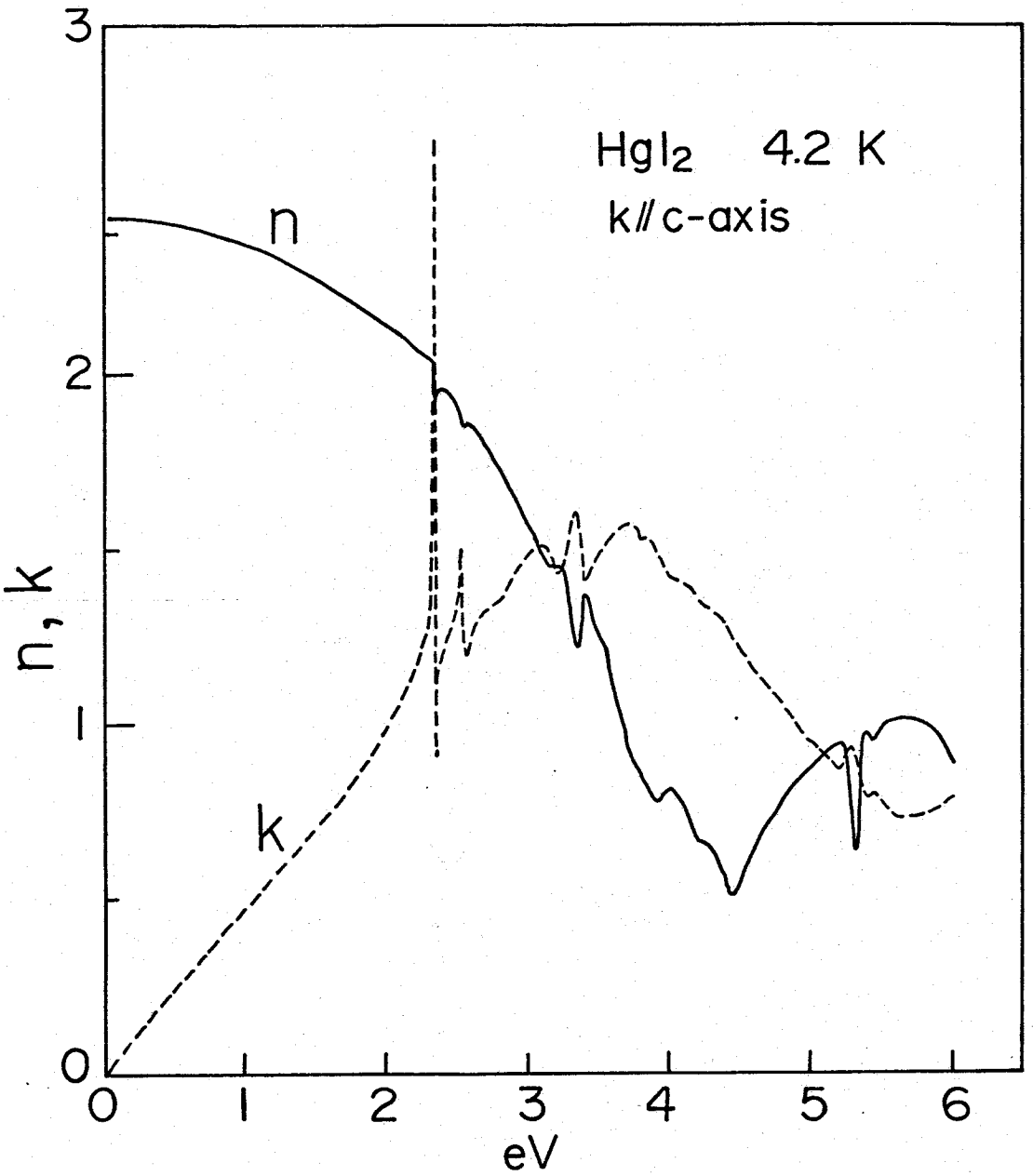

Fig. 5-28. Real and imaginary parts of the refractive index n and k of HgI_2 at 4.2 K, obtained from the Kramers-Kronig anlysis of the reflection spectrum shown in Fig. 5-27.

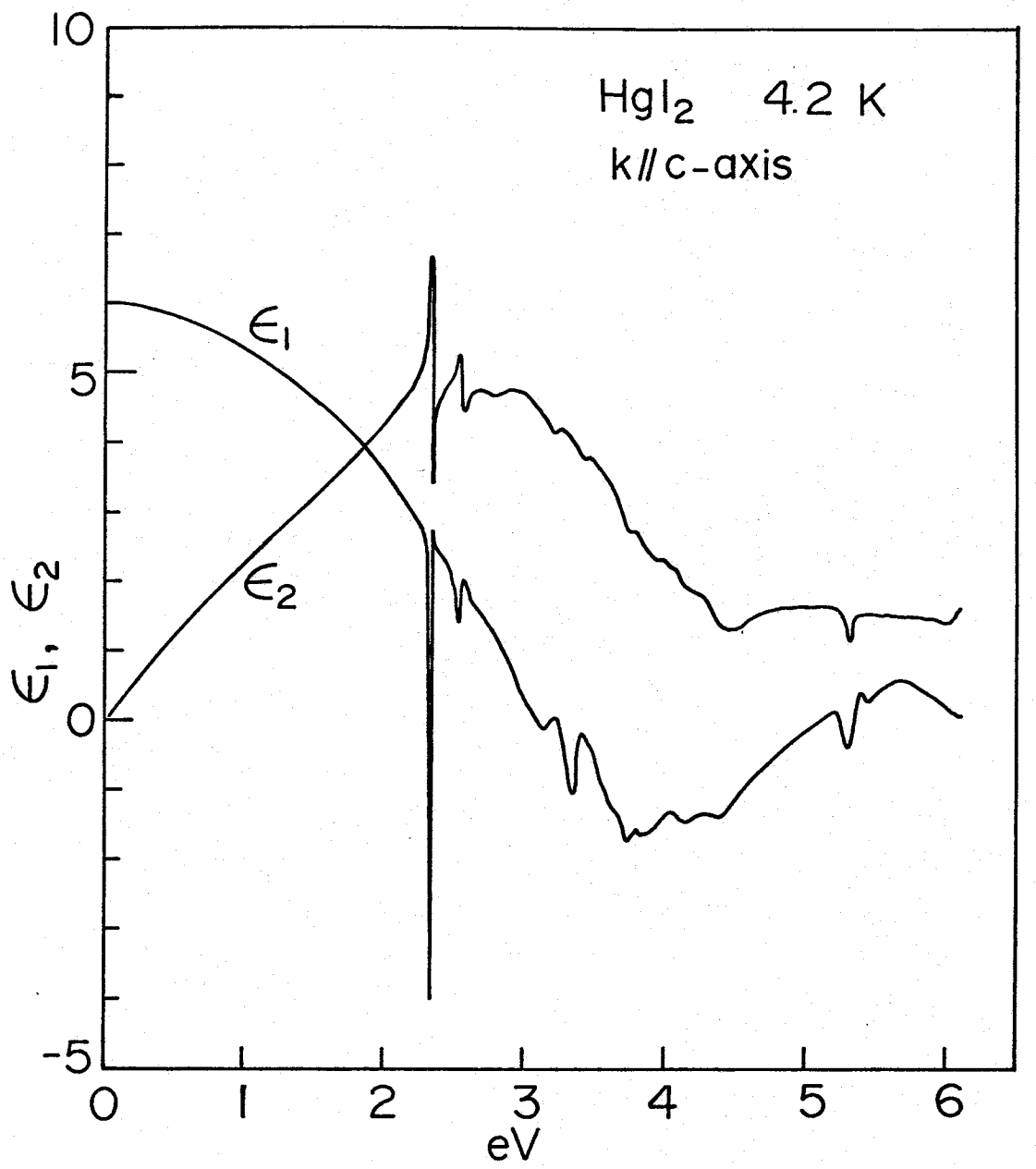

Fig. 5-29. Real (ε_1) and imaginary (ε_2) parts of the dielectric constant of HgI_2 at 4.2 K, obtained from Fig. 5-28.

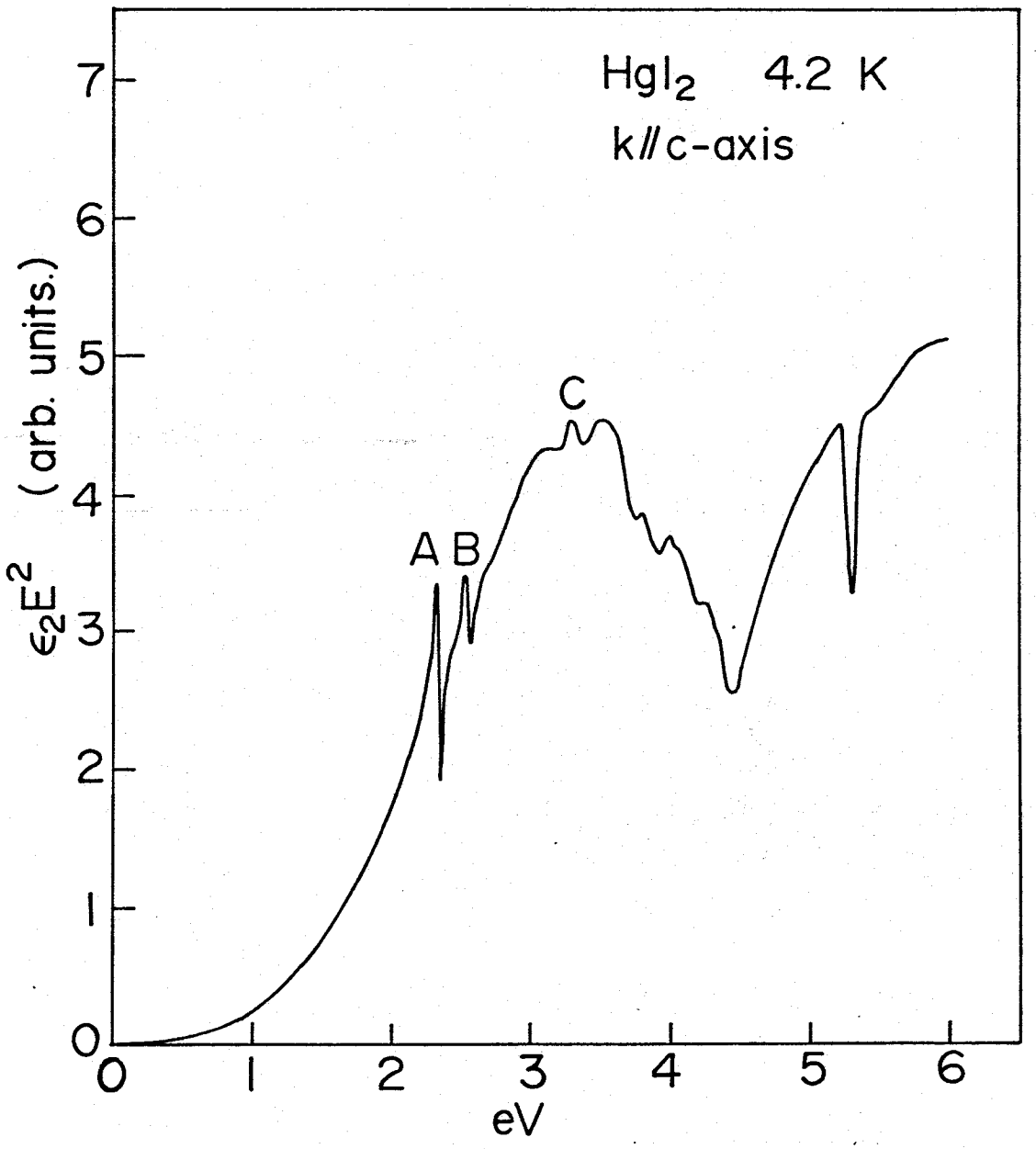

Fig. 5-30. Combined density of states function $\epsilon_2 E^2$ (in arbitrary units) for HgI_2, as obtained from the Kramers-Kronig analysis (4.2K).

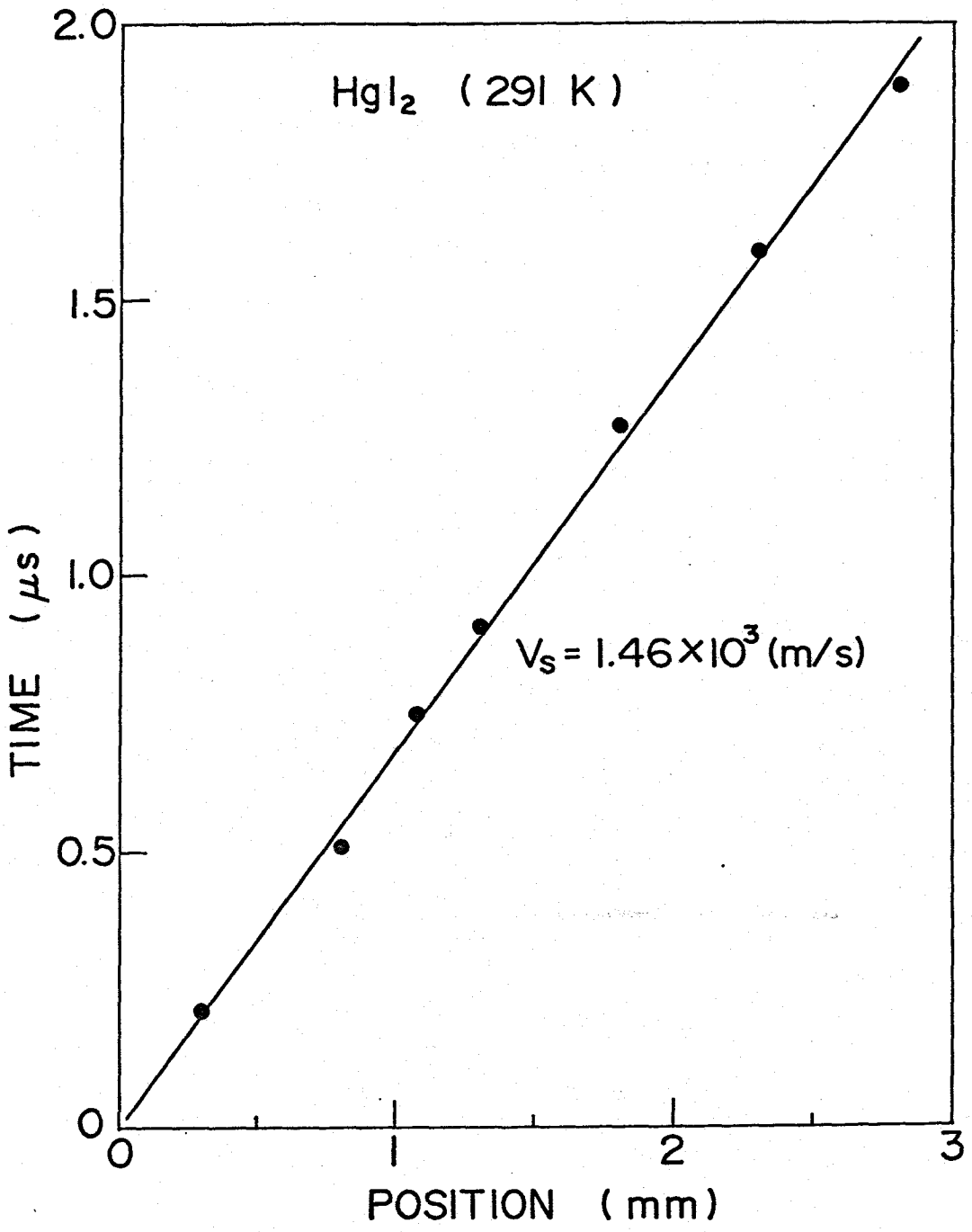

Fig. 5-31. Domain transit-time versus light-spot position for PT mode for HgI_2 from the Brillouin scattering measurements. The slope of line gives the domain velocity.

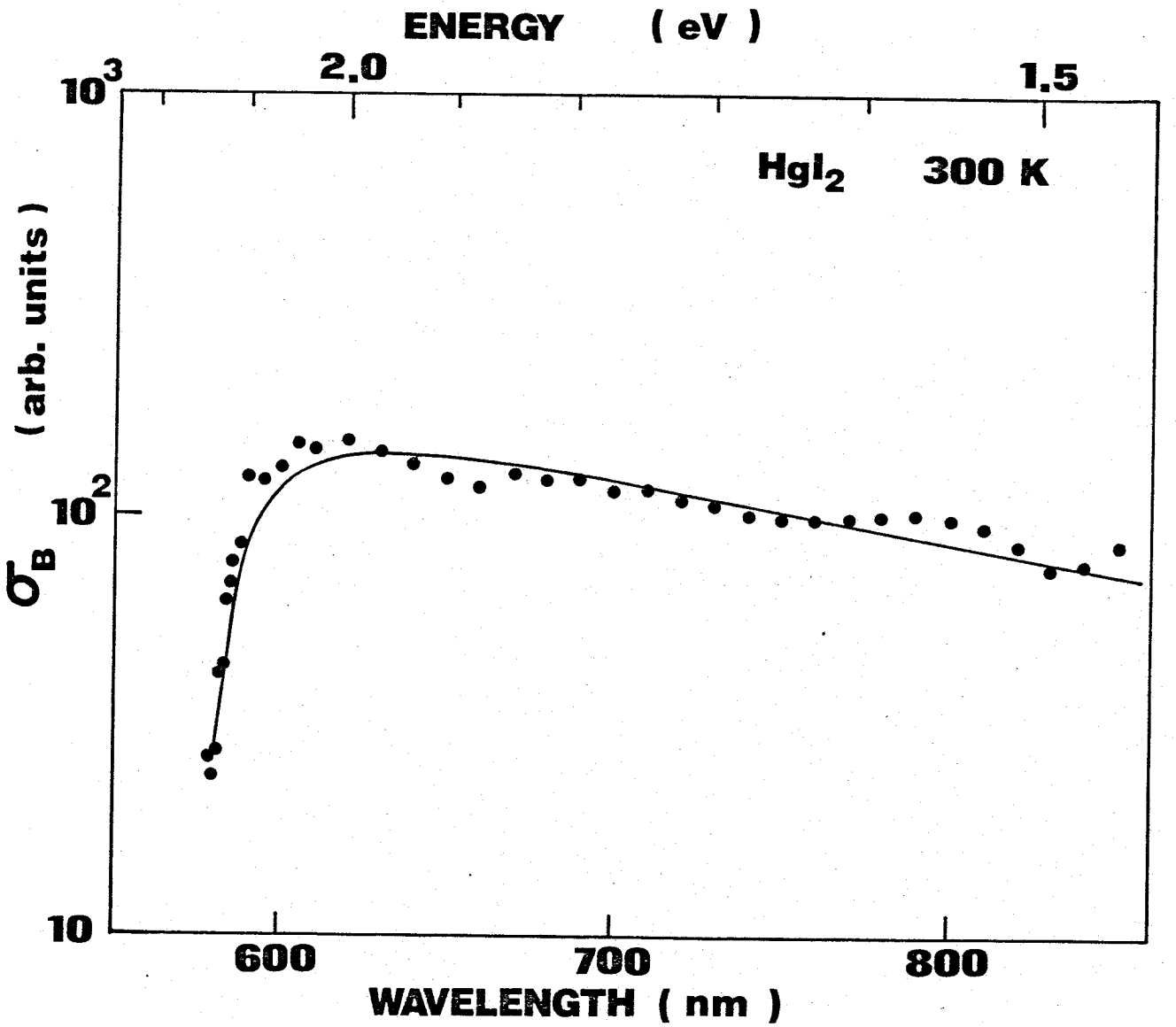

Fig. 5-32. Brillouin scattering cross section of HgI_2. Theoretical curves are calculated by using eqs. (5.8) and (5.9).

In order to calculate the Brillouin scattering cross section we have introduced the non-resonant or non-dispersive element R_0 arising from the higher gaps. The solid curve in Fig. 5-32 is calcualted from eq. (5.8). The symmetry of the Γ band in HgI_2 is same as that of the wurtzite crystals. Therefor the selection rules of the Γ point of both the momentum matrix elements $P_{0\beta}$ and $P_{\alpha 0}$, and deformation potemtial matrix elements are exactly same as those in the case of the Brillouin scattering by Tl-mode phonons in wurtzite materials. In the present PT-mode phonons, virtual A, B, and C excitons (or excitation of holes in A, B, and C valence bands) are excited. There exist two interband preocesses, namely A to B, A to C, B to A, C to A process. On the other hand intraband process is forbidden from selection rule. We used ω_0 = 3.5 (eV), A = 127.2 (arb. units), R_0 = 7.5 (arb. units). The relarive value of R_{is} = 1.18 (arb. units) at 600 nm, and R_{is} = 0.48 (arb. units) at 700 nm. According to this model given in eq. (5.8) we find that the contribution of higher band transition is not negligible and the decrease of the Brillouin scattering cross sections in the longer wavelength region is well interpreted as due to the contribution from higher lying gaps near 3.5 eV.

5.6 Acoustic Figure of Merit (M_2)

It is well known that the light scattering by ultrasonic waves is applied to the acousto-optic devices such as light modulator and scanner. This means that it is possible in principle to control light by the action of ultrasonic waves as an information carrying signal in optical data-processing devices. The great successes in recent years of applied reserch in acoustic optics have clearly shown that it is pracrically applied to a number of functionable devices, for communication system, signal processing

and other system. Therefore in order to design such an acousto-optic devices we have to take into account the precise dispersion of the photo-elastic constant of the material used in the devices because the Brillouin scattering intensity is proportional to the photoelastic constant. In particular, there exsists resonant cancellation in the vicinity of the fundamental absorption edge. Dixon[137] has pointed out, however, that the photoelastic dispersion appears to be much less important consideration for modulator design than was initialy expected. Gordon[147] has shown that for acoustic modulator there are at least three different criteria judging a material's usefulness; the center frequency f_0, the dynamic width Δf, and the scattering parameter η (the fractional light power scattered is $\sin^2\eta^{1/2}$) are under a wide variety of circumstances related by

$$f_0 \Delta f \eta \approx 9(n^7 p^2/\rho v)(\lambda_0{}^3 h \cos\theta_0)^{-1} P_a \quad , \tag{5.11}$$

in which n and p are the refractive index and photoelastic constant, respectively, λ_0 is the optical wavelength in air, θ_0 is the scattered angle, P_a is the acoustic power, and h is the acoustic-beam height. Assuming that the acoustic-beam height is held constant, the combination of material parameter $M_1 = n^7 p^2/\rho v$ constitutes a "figure of merit" by which materials for use as acoustic modulation may be compared in the usual situation in which both bandwidth and diffracted intensity are important. Since the parameter η is given by[148]

$$\eta \approx 5(n^6 p^2/\rho v^3)(\lambda_0{}^2 h \cos^2\theta_0)^{-1} W_0 P_a \quad , \tag{5.12}$$

where W_0 is the acoustic beam width. If only the scattered light intensity were important and appropriate figure of merit would be $M_2 = n^6 p^2/\rho v^3$. According to the eq. (5.12) it follows that if we wish to reduce the electrical power consumed by the device we must use a material

having a higher quality factor M_2. Figure of merit M_2 has already listed in a number of materials by Dixon.[137] These data are obtained, however, at a fixed wavelength and the dispersion of the M_2 is not presented. The developement of various types of semiconductor laser and dye lasers on the past dozen years has led to remarkable progress. Near future it will by a possibility that the acoustic-devices will be operated in a various region of wavelength. Therefore it is important to determine the detailed dispersion of M_2 over the wide range of wavelength of the materials.

In Fig. 5-33 we obtained the dispersion of M_2 in CdS, ZnS, and GaAs. It is seen from this figure that in the region far from the fundamental absorption edge the dispersion of M_2 shows less dispersive, while near the fundamental absorption edge intensity of M_2 decreases and steeply approaches zero (resonant cancellation). Finally in the region very close to the fundamental absorption edge M_2 shows resonant enhancement. The best condition for devices is achieved in the region far from the fundamental absorption edge. It is seen in Fig. 5-33 that GaAs is a good modulating materials in the infrared region. In visible and ultraviolet region, ZnS and CdS can be used as modulator, respectively.

In conclusion, to design the acousto-optic devices we must take into account the dispersion of the acoustic figure of merit.

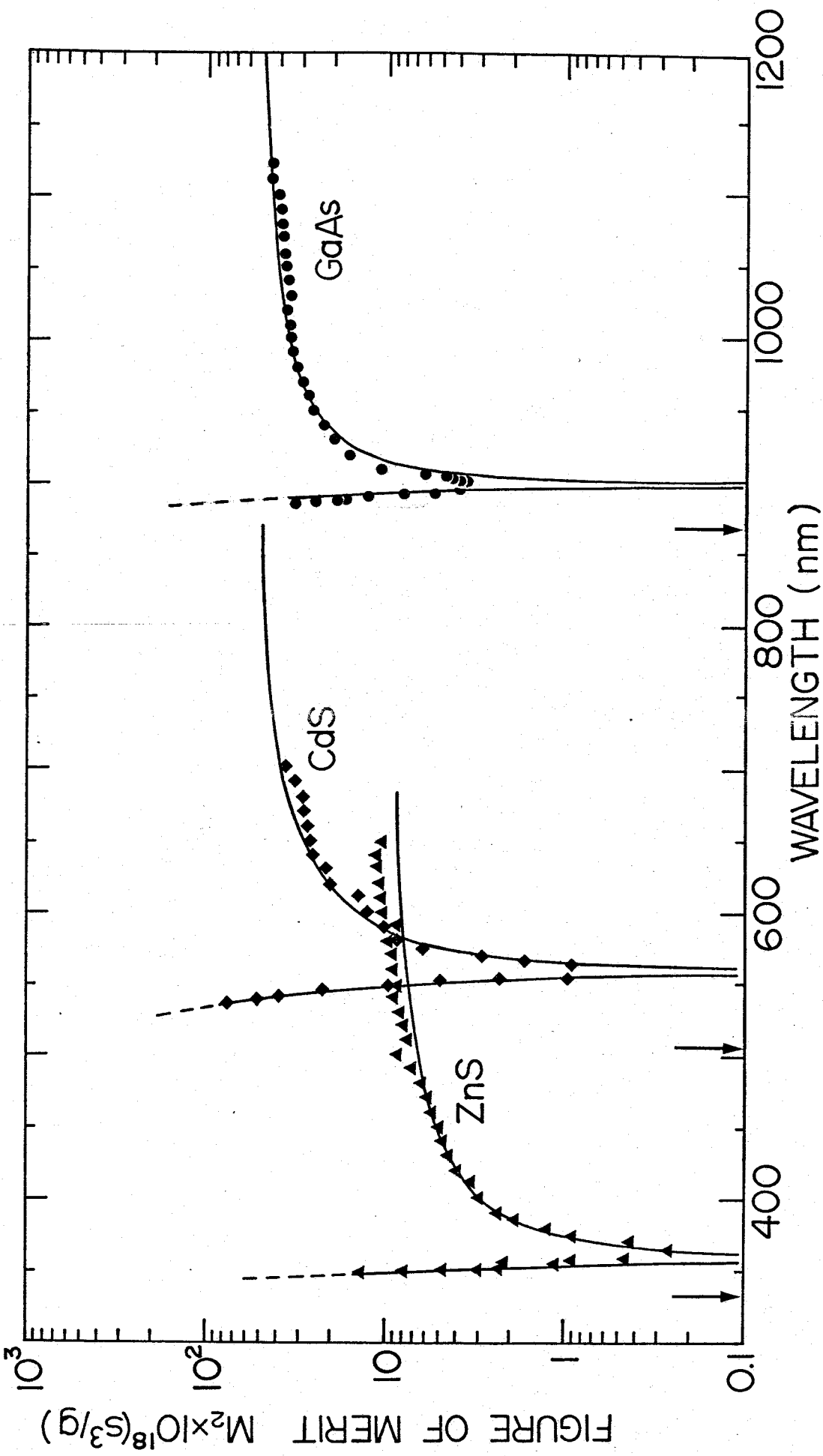

Fig. 5-33. Dispersion of the acoustic figure of merit M_2 for GaAs, CdS, ZnS. The vertical arrows indicate the spectral positions of the fundamental absorption edge for each crystal.

CHAPTER 6

Resonant Brillouin Scattering in the Opaque Region of CdS

6.1 Introduction

We have studied the resonant Brillouin scattering in several semiconductors by means of transmission type of experiments. In these experiments, however, the incident light was restricted to the transparent region because the experimental conditions that the transmitted light signal were measured. Therefore, it is difficult to obtain the dispersion of Brillouin scattering cross seciton in the opaque region due to the strong absorption. To overcome this restriction we have empolyed the reflection scattering configuration (See Chapter 4) and we have observrd resonant enhancement in the opaque side of the fundamental absorption edge.[148)]

6.2 Experimental Procedure

The samples used in the present study are single crystals (purchased from Eagle Pitcher Company, UHP grade) with ≃ 20 ohm-cm resistivity and with the scattering surface of optical flat mechanically polished and finally polish-etched by Syton. We used several lines of Ar ion laser between 457.9 nm and 514.5 nm operation at ≃ 200 mW CW as the incident light source for experiment. This laser provided light polarized vertically, and when horizontally polarized light was required, this was obtained by means of using a Rochon prism. The scattered light polarization was analyzed by placing a sheet polaroid material between the photomultiplier and sample. The reflection scattering geometry used in the present study is shown in Fig. 4-4 (b). The T2-mode phonons amplified through acoustoelectric effect

propagate in the direction perpendicular to the c-axis with shear polarization parallel to the c-axis. The laser light beam is incident on a polished surface parallel to the c-axis ($e_i \parallel$ c-axis) and the scattered plane was perpendicular to the c-axis ($e_s \perp$ c-axis). Also we measured in the scattering where the incident light polarization is perpendicular to the c-axis ($e_i \perp$ c-axis) and the scattered plane was parallel to the c-axis ($e_s \parallel$ c-axis).

The interaction length between phonon and photon is comparable to the penetration depth ($\alpha^{-1} \simeq 0.1$ μm) and restricted to the surface region because in the region above the fundamenatal absorption edge α is $\simeq 10^5$ cm^{-1}. Here the Brillouin scattering process produces a scattering light out of the propagation direction of the reflected beam. The light scattered by the ripple mechanism shows no rotaion of the polarization, but the scattering by the elasto-optic mechanism is rotated 90°. Our main interest in the present study is the latter mechanism in the opaque region. Therefore, we choose the polarization direction of the scattered light perpendicular to the incident light. It is important to point out that S/N ratio of the scattering signal is strongly dependent upon the surface condition of the sample. While the CdS is pure (UHP grade) some trouble was had in obtaining good CdS surface. The best results were obtained from Syton-etched surface, but the Rayleigh scattered light, which comes from the surface defect, causes the Brillouin scattering signal noisy. To reduce the effect of the noise, we measured the data several times and averaged thses data. The crystals were held at room temperature, but some heating of the scattering surface was inevitable. It is estimated that this heating should not have exceeded about 30 K.

The identification of the acoustic waves was made by the sound velocity $v(T2) = \sqrt{C_{44}/\rho} = (1.80 \pm 0.05) \times 10^5$ cm/sec and selection rules of the light polarization (See Fig. 4-4 (b)).

6.3 Experimental Results

In Fig. 6-1, we show the experimental results obtained from the presnt study. The scattering intensity (I_s) was normalized by the incident light intensity (I_0). This figure shows the spectral dependence of the Brillouin scattering efficiency for 0.5 GHz T2-mode phonons at room temperature. Open circles show the data obtained by choosing the incident light poralization parallel and the scattered light polarization perpendicular to the c-axis ($e_i \parallel$ c-axis, $e_s \perp$ c-axis), while the closed circles show the data obtained by choosing the incident light polarization perpendicular and the scattered light parallel to the c-axis ($e_i \perp$ c-axis, $e_s \parallel$ c-axis). Very recently, Chang et al. have reported the resonant Brillouin scattering efficiency in the opaque region by employing a Fabry-Perot interferometer, which are also shown in the figure. They obtained the signal by using the acousto-electrically amplified phonon domains with 524 MHz T2-mode phonons.[42] These two independent data were plotted by normalizing at 496.5 nm. It should be noted that these data show good agreement in spite of using different kind of instruments. The experimental data show a peak at around 500 nm and a clear resonant enhancement in the opaque region of CdS.

We have already shown that in the transparent region resonant Brillouin scattering cross section has resonant enhancement and resonant cancellation below the gap. These resonant features have been successfully explained by the Brillouin scattering theory. Thus it is interesting to consider whether the resonant enhancement in the opaque region is explained by the same theory with same parameters used in the calculation in the transparent region.

Fugure 6-2 shows the theoretical curves of the real and imaginary part of the Brillouin tensor R_{is} for T2-mode acoustical phonons in CdS at room temperature. We calculated these curves by using eqs. (2.134) and (2.140).

The numerical parameters used in the present calculation is listed in Table 5-6. In the present calculation, the contribution from the A, B and C valence bands is taken into account. Below the fundamental absorption edge, real part of R_{is} dominates the imaginary part. These facts indicate that only virtual electronic state can take place in the long wavelength region. Near the band gap, both the real and imaginaty part of R_{is} show strong resonant enhancement. In particular, the imaginary part shows a resonant peak at around 512 nm. This position corresponds to that of the ground state exciton energy associated with the A valence band (E_{ex} = 2.424 eV = 511 nm). This strong peak of the imaginary part of R_{is} shows the fact that the incident and scattered photons resonate with electron states. Above the band gaps, both the real and imaginary part of R_{is} decrease steeply and approach zero when we neglect the contribution from the higher energy critical points. The total light scattering cross section σ_B is proportional to the square of $R_{is} + R_0$ as follows:

$$\sigma_B \propto |R_{is} + R_0|^2 = |(R_{is}^r + iR_{is}^i) + (R_0^r + iR_0^i)|^2 , \qquad (6.1)$$

where R_0 ($= R_0^r + iR_0^i$) is the non-resonant term of the Brillouin tensor arising from the far off critical points in the band structure and has an opposite sign to R_{is}. The resonant cacellation ($\sigma_B = 0$) occurs when $R_{is} + R_0$ becomes zero. The spectral position of the resonant cancellation is shown at the cross point of $-R_0$ and the real part of R_{is}.

Figure 6-3 shows wavelength dependence of the Brillouin scattering cross section σ_B(in arbitray units) for 0.5 GHz T2-mode phonons at room temperature, where open circles with error bars are obtained by the reflected light scattering geometry and the solid circles are experimental data obtained by the transmission light scattering geometry. These two independent data were plotted by comparing with the theoretical curves.

According to the theory for surface elasto-optic scattering in isotropic opaque materials,[149] the cross seciton varies with absorption coefficient α, as $[1+(\alpha\lambda/2\pi n)^2]^{-1}$.[42] For CdS at room temperature, The refractive index $n = 2.8$ and α is nearly constant $\sim 10^5$ cm^{-1}, for 450 nm $< \lambda <$ 500 nm. In the region, the measured Brillouin scattering cross section is reduced by less than $\simeq 5$ %.[42] Therefore absorption correction can be neglected. We find in Fig. 6.3 a clear resonant enhancemt in the opaque region, where the three absorption edges 506 nm, 503 nm, and 491 nm exist. The resonant features (resonant cancellation and resonant enhancement) in the transparent region have been already explained by the Brillouin scattering theory. It is interesting to check whether the resonant enhancement in opaque region is explained by the same theory with same parameters. In order to clarify this problem, we calculated two kind of theoretical curves. One is calculated by using eq.(6.1), where both the imaginary and real part of R_{is} are taking into account. The other is calculated by using the following relation;

$$\sigma_B \propto |R_{is}^r + R_0^r|^2 \quad , \tag{6.2}$$

in which only the real part of the Brillouin tensor is considered. A solid curve is calculated by eq.(6.1) including both the imaginary and real part of R_{is} and R_0. On the other hand, a dashed curve is calculated by taking into account the real part only by eq.(6.2). The experimental data show a good agreement with the former results but poor agreement with the latter calculation. We measured the Brillouin scattering intensity by tuning the energy gap thermally at 514.5 nm and we find no change in the intensity. Therefore we conclude that a minimum does not exist near the band gap. From these results, we conclude that the imaginary part of R_{is} plays an important role, in particular, in the region of the absorption edge.

Figure 6.4 shows the dispersion curves of the Brillouin scatteirng

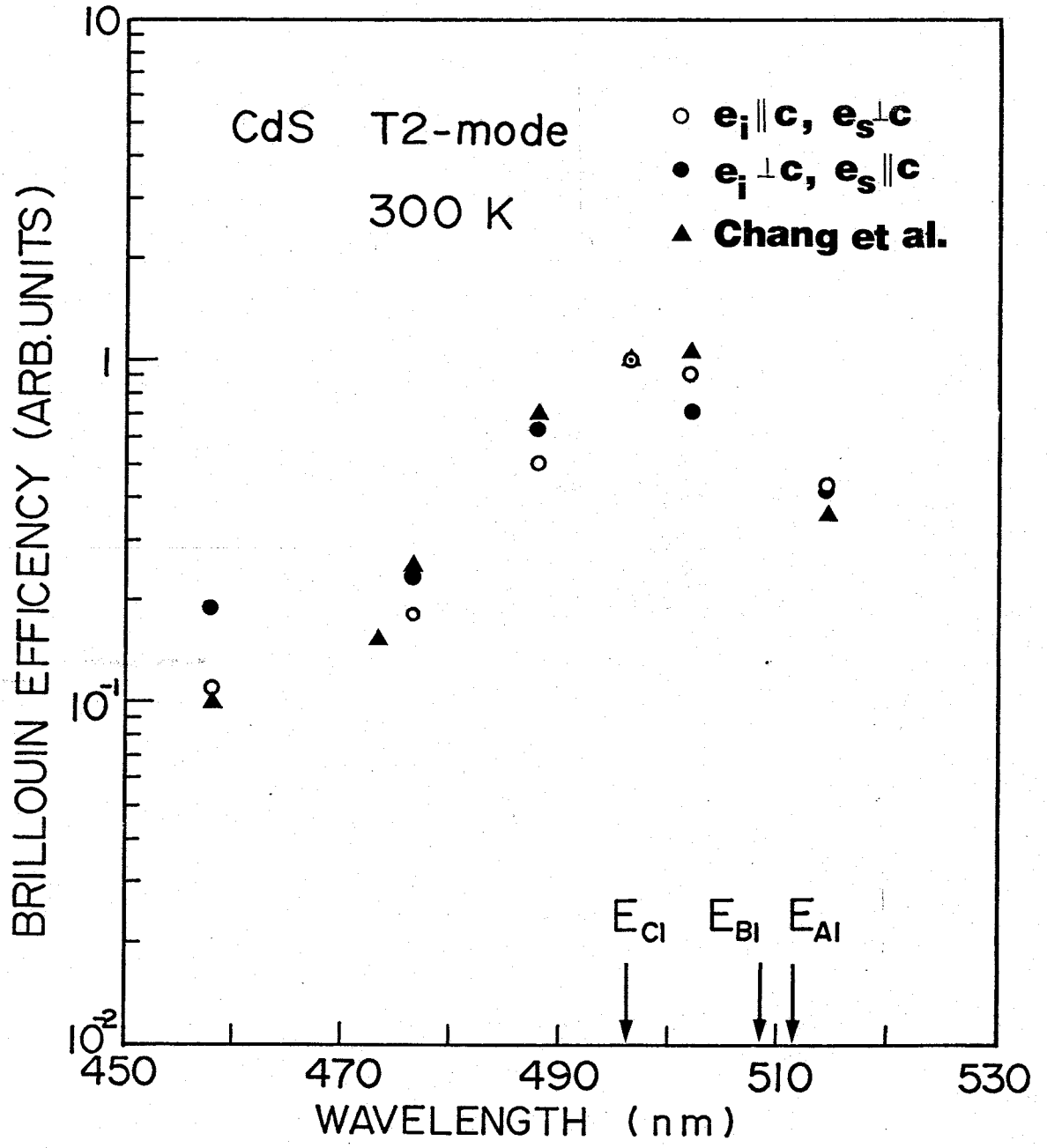

Fig. 6-1. Brillouin scattering efficiency in the opaque region of CdS at room temperature for (○) $e_i \|$ c-axis, $e_s \perp$ c-axis, (●) $e_i \perp$ c-axis, $e_s \|$ c-axis, (▲) $e_i \|$ c-axis, $e_s \perp$ c-axis, obtained by Chang et al. The vertical arrows indicate the spectral positons of the ground exciton leveles for A, B, and C valence bands.

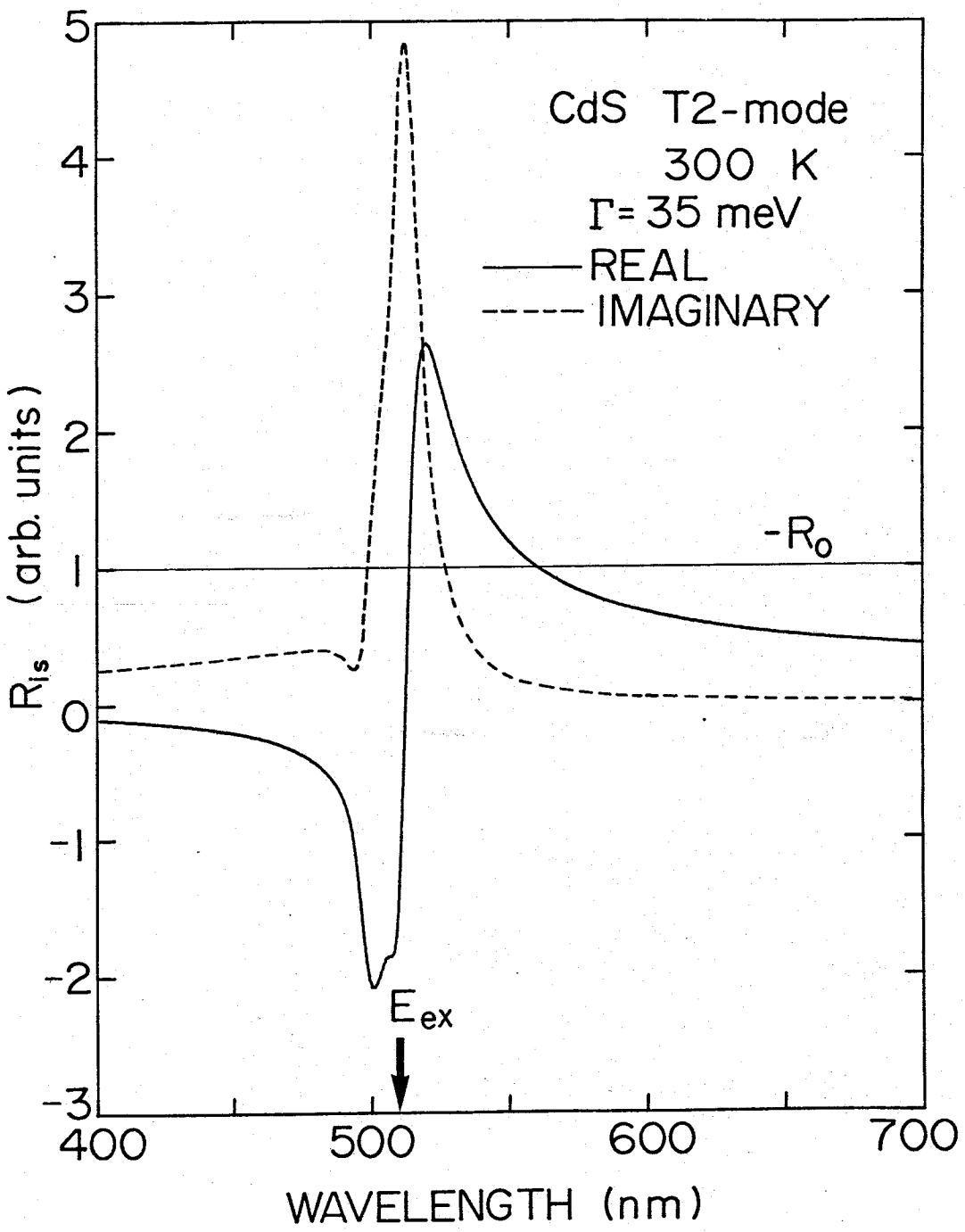

Fig. 6-2. Real and imaginary part of the Brillouin tensor for the case of T2-mode phonons in CdS at room temperature. Theoretical curves are calculated using the Brillouin scattering theory. The vertical arrow indicates the spectral position of the ground exciton energy (E_{A1}).

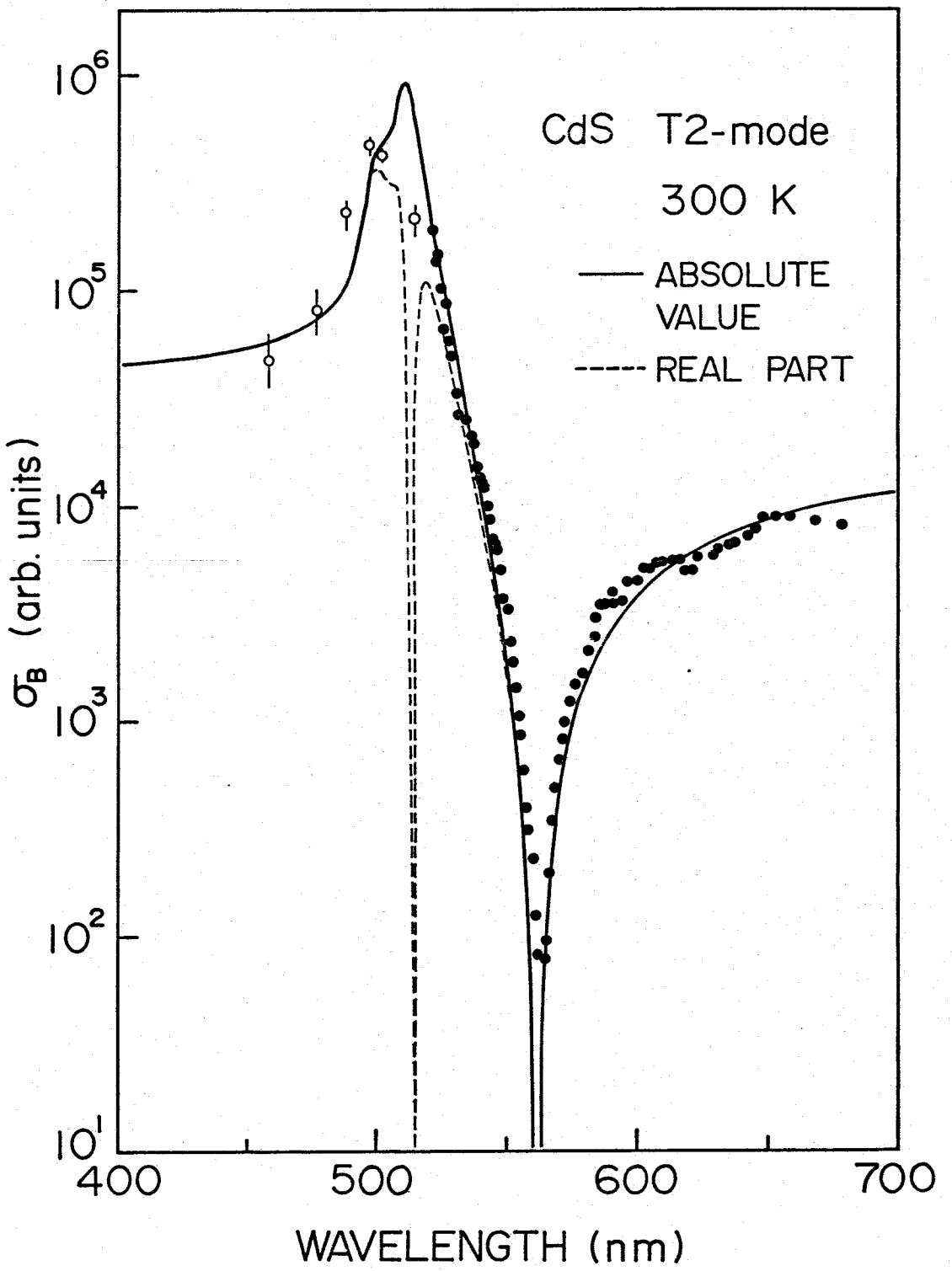

Fig. 6-3. Dispersion curves of Brillouin scatteing cross section for 0.5 GHz acoustic phonons. The present data in the opaque region is shown by open circles, while the data in the transparent region is shown by the closed circles.

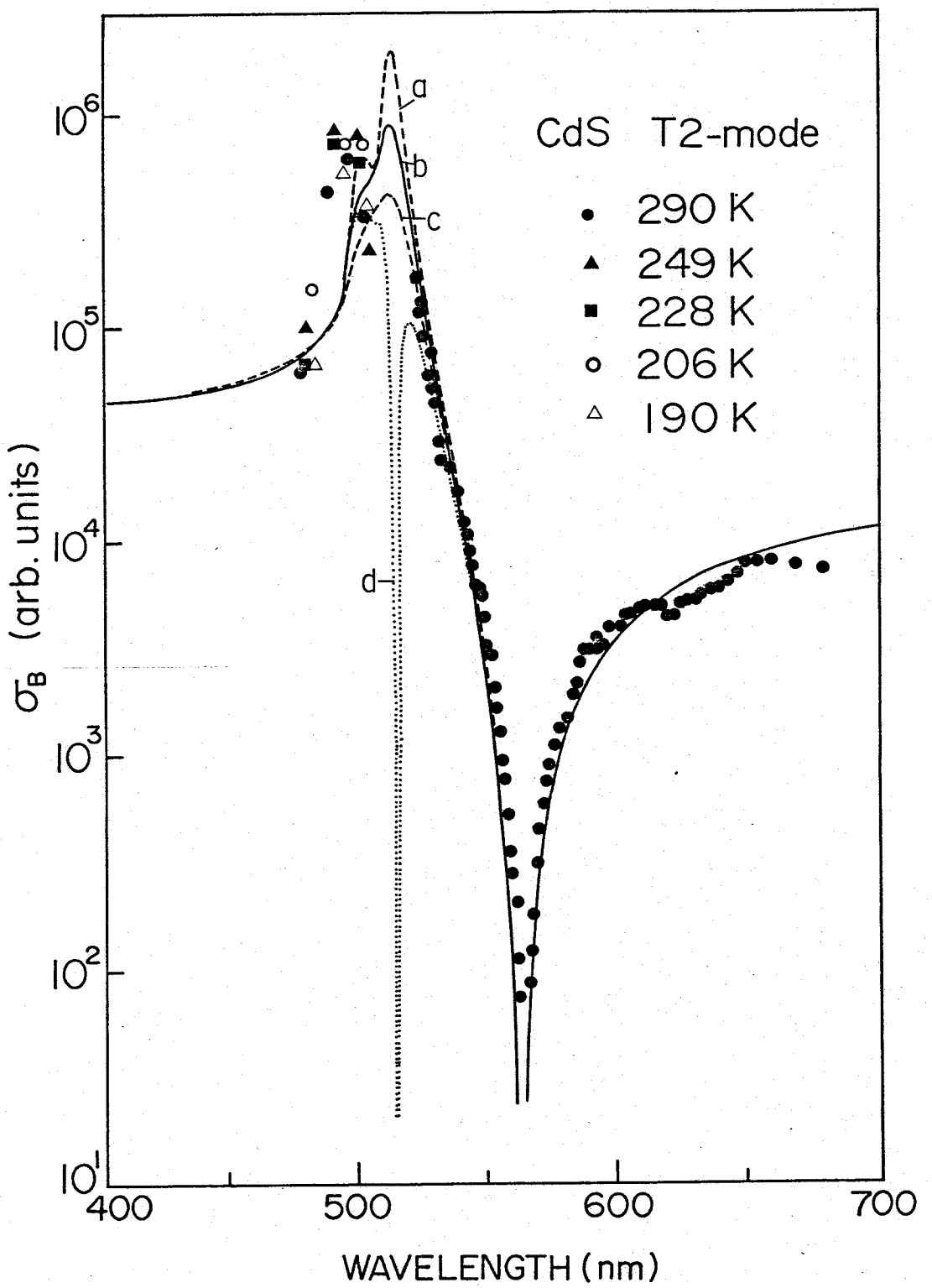

Fig. 6-4. Dispersion curves of the Brillouin scattering cross section obtained by thermally tuning the band gaps. The measured data are normalized at 300 K. Four different theoretical curves are shown; (a) Absolute value, Γ = 25 meV; (b) Absolute value, Γ = 35 meV; (c) Absolute value, Γ = 45 meV; (d) Real part only, Γ = 35 meV.

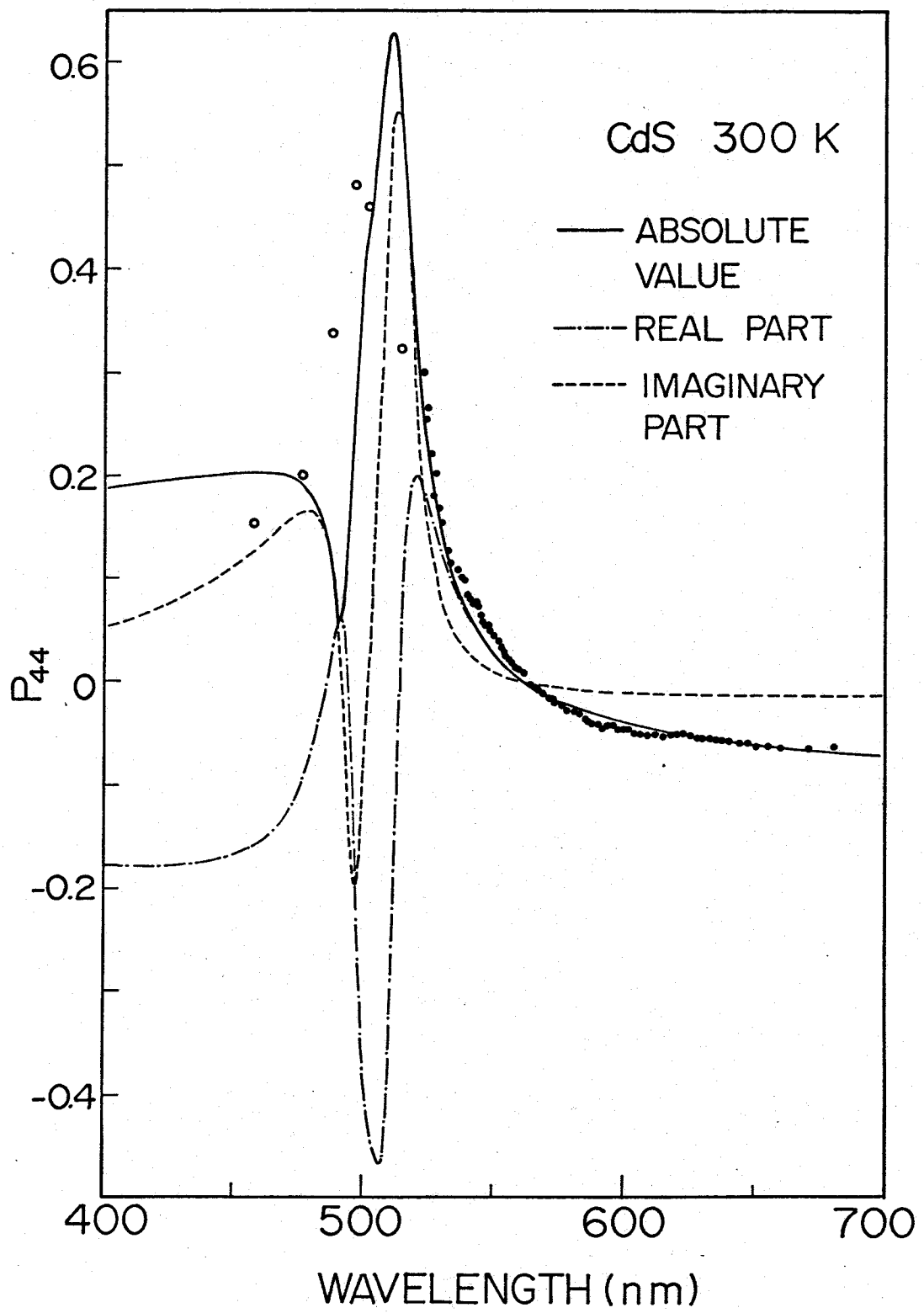

Fig. 6-5. Dispersion curves of photoelastic constant P_{44} obtained from the data shown in Fig. 6-3. The presnt data in the opaque region is shown by open circles, while the data in the transparent region is shown by closed circles.

cross sections ontained by thermally tuning band gaps. We showed here four different theoretical curves. The experimental data show a good agreement with the theoretical curves when we choose damping facter as ≃35 meV. The physical meaning of the damping factor will be discussed in Section 6.4.

It has been shown that the Brillouin scatteirng cross section is analyzed from phenomenological aspect by incorporating the piezobirefringence theory. In Fig. 6.5, we show the dispersion curves of the photoelastic constant P_{44} determined by the relation $\sigma_B \propto |P_{44}^r + iP_{44}^i|^2$, where the subscript r and i indicate the real and imaginary part of P_{44}, respectively. Since the present method does not give sign and absolute values of the photoelastic constant but relative values. they are adjusted to the values of Yu and Cardona, $P_{44}^r = -0.054$ at 630 nm.[77] The theoretical curves of the absolute value of P_{44} ($|P_{44}^r + iP_{44}^i|$) obtained from piezobirefringence analysis shows a good agreement with the experimental data in the region investigated. This indicates again that the imaginary part of the photoelastic constant plays an important role to determine the dispersion and thus the dispersion of the Brillouin scattering cross section in the resonant enhancement region.

6.4 Lifetime Broadening Effect

The damping energy Γ depends strongly on the temperature. In general the damping factor can be expressed by a sum of three independent contribution as follows;[150]

$$\Gamma(T) = \Gamma_0 + \Gamma_{ac}(T) + \Gamma_{LO}(T) \quad , \tag{6.3}$$

where Γ_0 is an independent part of temperauture T arising from the foreign nature defects, $\Gamma_{ac}(T)$ is a contribution from acoustic phonons (proportional

to T for the thermal phonons), and Γ_{LO} is a contribution from LO phonons (proportional to $[\exp(\hbar\omega_{LO}/k_BT) - 1]$ where $\hbar\omega_{LO}$ is the LO phonon energy). Bleil and Gay[151] measured the temperature dependence of Γ and shows that the dominant contribution to Γ at room temperature comes from LO phonons. From their results, Γ = 30 ∿ 50 meV at room temperature and Γ = 5 meV at 77 K. This value shows a resonable agreement with that obtaied from the present Brillouin scattering measurement in the opaque region ($\Gamma \simeq$ 35 meV).

Theoretical expression of the energy dependence near the fundamental absorption edge is proposed by Hopfield as follows:[152,153]

$$\Gamma(\omega) = \begin{cases} \Gamma_e , & \omega > \omega_e \\ \Gamma_e \exp\{C(\hbar\omega_e - \hbar\omega)\} , & \omega < \omega_e \end{cases} \qquad (6.4)$$

in which $\hbar\omega_e$ and Γ_e are the energy and broadening factor at an absorption edge, respectively, and C is a constant related to the Urbach rule. When we use a resonablt value Γ_e = 38 meV, estimated from the half-width of exciton absorption[136] and emission[151] lines at room temperature, it turns out that Γ is very small in the transparent region. Wasa et al. obtained that Γ = 0.5 meV (300 K), Γ = 0.6 meV (310 K) and Γ = 1.2 meV (350K) at 560 nm.[153] On the other hand near the band gap it is obvious that Γ becomes large and Γ is nearly constant value (Γ = 38 meV). Therefore we conclude that near the fundamental absorption edge lifetime broadening factor Γ is nerly constant and the main contribution of Γ comes from LO phonons.

6.5 Summary

We have observed the Brillouin scattering cross secitons in the opaque region of CdS by making use of the reflection scattering configuration. It

turns out that the Brillouin scattering cross section shows clear resonant enhancement above the fundamental absorption edge. The resonant enhancement in the opaque region is well explained by the Brillouin scattering theory and piezobirefringence theory when we choose same parameters used in the analysis in the transparent region of the scattering cross section. It was also found that the imaginary part of the Brillouin tensor (or photoelastic constant) is important in determining the dispersion curves near the band gap. Life time broadening factor is determined by the presnet work and found that this value (Γ = 35 meV) is nearly equal to that of the LO phonon energy.

CHAPTER 7

Conclusions

The results and conclusions obtained in the present work are summarized as follows:

1) Theoretical expression of the Brillouin scattering cross section was derived by the time-dependent third order perturbation theory. We showed that the resonant enhancement and cancellation are well explained by the resonant Brillouin scattering theory. We also presented that the Coulomb interaction causes a strong asmmetry in the Brillouin efficiency with respect to the band gap, a strong resonance occurs at the photon energy of the ground state exciton level. It also turns out that the role of the imaginary part of Brillouin tensor is of significant importance for the scattering mechanism in the vicinity of the band gap.

2) We have derived the expressions of the photoelastic constants $P_{11} - P_{12}$, P_{44} in zincblende, and $P_{11} - P_{12}$, P_{44} and P_{31} in wurtzite materials by using the model dielectric functions. We showed these formulations can be extended to the region where the incident photon energy is higher than that of the band gap energy and imaginary part of the dielectric constant plays an important role in determining the complex photoelastic constants. A simple model is also shown to explain the non-dispersive term of the photoelastic constants by using the Penn model.

3) We showed acoustic domain injection method provides great advantages in investigating phonon-phonon or electron-phonon-photon interaction, in non-piezoelectric semiconductors, insulators and layered compounds.

4) It is established that the reflection scattering configuration in the Brillouin scattering experiment with a high intensity laser provides resonant light scattering signal in the opaque region, above the fundamental absorption edge.

5) Resonant Brillouin scattering in GaAs by the transverse acoustical phonons has been analyzed by the Brillouin scattering theory and piezobirefringence theory. The resonant enhancement and cancellation are found to be well interpreted in terms of the sign reversal of the Brillouin (or photoelastic constant). A good agreement was found between the experimental data and the theoretical calculation. We found in GaAs that the effect of the discrete exciton on the dispersion of the Brillouin scattering cross seciton and photoelastic constant is negligible because the exciton Rydberg energy is small (4.2 meV) as compared to other II-VI compounds. We also predicted a cancellation of the Brillouin scattering at 976 nm for the scattering by the slow transverse (T1) acoustic mode phonons.

6) Observed dispersion spectra of the Brillouin scattering by TA-mode phonons show sharp resonant enhancement near the fundamental absorption edge in CdS, cubic and polytype ZnS. These resonant features are explained as follows: The contribution to Brillouin tensor (or photoelastic constant) from the lowest direct gap and that from higher bands have opposite sign and thus cancell at a certain energy below the gap.

7) Observed dispersion spectra of the Brillouin scattering cross sections in CdS by LA-mode acoustic phonons show only the resonant enhancement in the measured region. We have analyzed the data by the Brillouin scattering theory and piezobirefringence theory and find a good agreement between experimental data and theories. In the analysis, it turns out that a sign

reversal of Brillouin tensor (or photoelastic constant) occurs at wavelength $\lambda = 750$ nm and that the non-dispersive component R_0 is very weak compared with that of transverse acoustic waves.

8) The resonant Brillouin scattering in cubic and polytype ZnS has been investigated in the photon energy region 1.8 to 3.7 eV using two different transverse acoustic waves excited by acoustoelectric domain injection method. The results show a resonant cancellation and enhancement near the fundamental absorption edge and are in good agreement with the resonant light scattering theory. It is found that the scattering cross sections exhibit ω^4 dependence as expected from the classical light scattering theory.

9) Measurements of the stress-induced birefringence have been carried out to obtain spectral dspendence of the elasto-optical constants (photoelastic constnats) in ZnS. The results show a good agreement with the photoelastic constants estimated from the resonant Brillouin scattering data. From the present work we find that the magnitude and sign of the photoelastic constants can be determined in a wide range of photon energies when we combine the resoannt Brillouin scatteing with the piezobirefringence measurements.
It is difficult to elucidate the absolute value of the photoelastic constants only from the Brillouin scattering experiments. This difficulty may be removed by using the present method.

10) Resonant Brillouin scatteirng in HgI_2 has first been investigated at room temperature by making use of the acoustic domain injection method. The experimental data show a resonant cancellation only in the lower side of the photon energy region, while no resonant enhancement has been observed.
The spectral dependence of the cross seciton has a good agreement with the theoretical expression when we take into account the higher direct transiton.

It was also found that the contribution of higher band transiton is strong and the decrease of the Brillouin scattering cross section in the longer wavelength region is interpreted as due to the contribution from higher gaps near 3.5 eV.

11) The precise dispersion and absolute values of the acoustic figure of merit (M_2) was found to be important factor for designing acousto-optic devices. We showed the dispersion of acoustic figure of merit in ZnS, CdS and GaAs.

12) We have determined the Brillouin scattering cross sections in the opaque region of CdS by employing the reflection scattering geometry. It turns out that the Brillouin scattering cross section clearely shows resonant enhancement above the fundamental absorption edge. The resonant enhancement is successfilly explained by the Brillouin scattering theory and piezo-birefringence theory when we choose same parameters used in the analysis in the transparent region of the scattering cross section. It was also found experimentally that the imaginary part of the Brillouin tensor is important in determining the dispersion curves near the band gap. Life time broadening factor is determined by the present work and found that this value ($\Gamma = 35$ meV) is nearly equal to that of the LO phonon energy.

LIST OF REFERENCES

1. R. Loudon, Adv. Phys. *13* (1964) 423.

2. M. Cardona (ed.), *Light Scattering in Solids*, Topics in Applied Physics, Vol. 8 (Springer, Berlin, Heidelberg, New York, 1975).

3. L. Brillouin, Ann. Phys. (Paris) *17* (1922) 88.

4. A. Smekal, Naturwiss *11* (1923) 873.

5. C. V. Raman, Ind. J. Phys. *2* (1928) 387.

6. G. Lansberg and L. Mandelstam, Naturwiss *16* (1928) 57.

7. E. Gross, Nature *126* (1930) 603.

8. E. H. L. Meyer and W. Ramm, Physik. Z *33* (1932) 270.

9. P. Debye and F. W. Sears, Proc. Nat. Acad. Sci. *18* (1932) 409.

10. R. Lucas and P. Biquard, J. Phys. Radium *3* (1932) 464.

11. J. P. Russell, Appl. Phys. Letters *6* (1965) 223.

12. J. H. Parker Jr., D. W. Feldman and M. Ashkin, Phys. Rev. *155* (1967) 712.

13. J. R. Sandercock, Phys. Rev. Letters *28* (1972) 237.

14. R. C. C. Leite and S. P. S. Porto, Phys. Rev. Letters *17* (1966) 10.

15. J. M. Ralston, R. L. Wadsock, R. K. Chang, Phys. Rev. Letters *25* (1970) 814.

16. A. Pinczuk and E. Burstein, Phys. Rev. Letters *21* (1968) 1073.

17. R. C. C. Leite and J. F. Scott, Phys. Rev. Letters *22* (1969) 130.

18. F. P. Schäfer(ed.), *Dye Lasers*, Topics in Applied Physics Vol. 1, (Springer - Verlag, Berlin, Heidelberg, New York, 1977).

19. Y. M. Yarborough, Appl. Phys. Letter *24* (1974) 629.

20. M. A. Renucci, J. B. Renucci, R. Zeyher and M. Cardona, Phys. Rev. B *10* (1974) 4309.

21. J. B. Renucci, R. N. Tyte and M. Cardona, Phys. Rev. B *11* (1975) 3885.

22. J. M. Calleja, K. Kuhl and M. Cardona, Phys. Rev. B *17* (1978) 876.

23. R. Trommer and M. Cardona, Phys. Rev. B *17* (1978) 1865.

24. R. L. Schmidt, B. D. McCombe and M. Cardona, Phys. Rev. B *11* (1975) 746.

25. J. M. Calleja and M. Cardona, Phys. Rev. B *16* (1977) 3753.

26. B. Tell, J. M. Worlock and R. J. Martin, Appl. Phys. Letters *6* (1965) 123.

27. A. S. Pine, Phys. Rev. B *5* (1972) 3003.

28. D. K. Garrod and R. Bray, Phys. Rev. B *6* (1972) 1314.

29. D.K. Garrod and R. Bray, *Proc. 11th Intern. Conf. on the Physics of Semiconductors*, Warsaw 1972 (p. 1167).

30. K. Ando and C. Hamaguchi, Phys. Rev. B *11* (1975) 3876.

31. U. Gerbart and A. Many, Phys. Letters A *43* (1973) 329.

32. R. Berkowicz and T. Skettrup, Phys. Rev. B *11* (1975) 2316.

33. K. Yamamoto, K. Misawa, H. Shimizu ans K. Abe, J. Phys. Chem. Solids *37*(1976) 181.

34. K. Ando, K. Yamabe, S. Hamada and C. Hamaguchi, J. Phys. Soc. Jpn. *41* (1976) 1593.

35. K. Yamabe, K, Ando and C. Hamaguchi. Jpn. J. Appl. Phys. *16* (1977) 747.

36. S. Adachi and C. Hamaguchi, J. Phys. Soc. Jpn. *43* (1977) 1637.

37. S. Adachi and C. Hamaguchi, J. Phys. Soc. Jpn. *44* (1978) 343.

38. S. Adachi and C. Hamaguchi, J. Phys. Soc. Jpn. *45* (1978) 505.

39. M. Yamada, C. Hamaguchi amd J. Nakai, Solid State Commun. *17*(1975) 879.

40. S. Adachi and C. Hamaguchi, Physica B *97*(1979) 187.

41. S. Adachi and C. Hamaguchi, J. Phys Soc. Jpn. *48* (1980) 1981.

42. W. C. Chang, S. Mishra and R. Bray, *Proc. 15th Intern. Conf. on Physics of Semiconductors*, Kyoto 1980; J. Phys. Soc. Jpn. *59* (1980) Suppl. A, p. 711.

43. S. Mishra, G. H.Holah and R. Bray, *Proc. 3rd Inter. Conf. on Light Scattering*, Campinas, Brazil (ed. by Balkanski, Leite and Porto), Flammarion, Paris (1976) p. 198.

44. G. B. Benedek and K. Fritsch, Phys. Rev. *149* (1966) 647.

45. M. Born and K. Huang, *Dynamical Thory of Crystal Lattices*, (Clarendon Press, Oxford, 1954) Section 50.

46. D. F. Nelson, P. D. Lazay and M. Lax, Phys. Rev. B *6* (1972) 3109.

47. L. L. Hope, Phys. Rev. *166* (1968) 883.

48. C. Hamaguchi, J. Phys. Soc. Jpn. *35* (1973) 832.

49. R. Loudon, Proc. Roy. Soc. A *275* (1963) 218; J. Phys. *26* (1965) 677.

50. A. K. Ganguly and J. L. Birman, Phys. Rev. *162* (1967) 806.

51. L. N. Ovander, Fiz. Tverd. Tela *6* (1964) 361.

52. D. L. Mills and E. Burstein, Phys. Rev. *188* (1969) 1465.

53. B. Bendow and J. L. Birman, Phys. Rev. B *1* (1970) 1678.

54. B. Bendow, Phys. Rev. B *2* (1970) 5051.

55. B. Bendiw, Phys. Rev. B *4* (1971) 552.

56. R.P. Martin, Phys. Rev. B *10* (1974) 2620.

57. R.Zeyher, C. Ting and J. L. Birman, Phys. Rev. B *10* (1974) 1725.

58. K. Peuker, F. Bechstedt and R. Enderlein, *Proc. Inter. Conf. on Physics of Semiconductors,* Stuttgart, 1974, (Teubner-Verlag, Stuttgart, 1974) p.468.

59. F. Bechstedt, R. Enderlein, A. Kolpakov and K. Peuker, Phys. Stat. Sol. b *73* (1976) 141.

60. R. Loudon, Adv. Phys. *13* (1964) 423.

61. W. Heitler, *The Quantum Theory of Radiation*, (Clarendon Press, Oxford 1954) p.189.

62. K. P. Jain and G. Choudhury, Phys. Rev. B *8* (1973) 676.

63. A.Messiah, *Quantum Mechanics,* (Wiley, New York, 1965), Vol. II, p. 807.

64. A. Messiah, in ref. 63, p. 828.

65. R. Elliott, Phys. Rev. *108* (1957) 1384.

66. See, e.g., M. Abramowitz and I. A. Stegun, *Handbook of Mathematical functions,* (Dover, New York, 1970).

67. See, e.g., C. Kittel, *Quantum Theory of Solid,* (John Wiley and Sons Inc. New York, 1963).

68. G. E. Picus and G. L. Bir, Fiz. Tverd. Tela *1* (1959) 154.

69. L.I.Schiff, *Quantum Mechanics,* (McGraw-Hill, New York, 1955).

70. D. G. Thomas and J. J. Hopfield, Phys. Rev. *116* (1959) 573.

71. J. J. Hopfield, J. Phys. Chem. Solids *15* (1960) 97.

72. D. W. Langer, R. N. Euwema, K. Era and T Koda, Phys. Rev. B *2* (1970) 4005.

73. Y. Itoh, M. Fujii, C. Hamaguchi and Y. Inuishi, J. Phys. Soc. Jpn. *48* (1980) 1972.

74. C. W. Higginbotham, M. Cardona and F. H. Pollak, Phys. Rev. *184* (1969) 821.

75. M. H. Grimsditch, E. Kisela and M. Cardona, J. Opt. Soc. Am. (to be published).

76. J. F. Nye, *Physical Properties of Crystals*, (Clarendon Press, Oxford, 1960).

77. P. Y. Yu and M. Cardona, J. Phys. Chem. Solids *34* (1973) 29.

78. P. Y. Yu, M. Cardona and F. H. Pollak, Phys. Rev. B *3* (1971) 340.

79. M. Cardona, *Solid State Physics, Nuclear Physics and Particle Physics*, ed. I. Saavedra, (Benjamin, New York, 1968) p737.

80. D. Penn, Phys. Rev. *128* (1962) 2093.

81. F. H. Pollak and M. Cardona, Phys. Rev. *172* (1968) 816.

82. G. D. Dresselhaus, A. F. Kip and C Kittel, Phys. Rev. *98* (1955) 368.

83. E. O. Kane, *Physics of III-V Compounds*, ed. by R. K. Willardson and A. C. Beer, (Academic Press Inc, New York 1966), Vol. 1, p. 75.

84. J. A. Van Vechten, Phys. Rev. *182* (1969) 891.

85. M. Cardona, J. Res. of the NBS, *74A* (1970) 253.

86. N. J. Meyer and M. H. Jørgensen, *Festkörprobleme X, Adv. in Solid State Physics*, (Pergamon, 1970), p. 21.

87. R. Bray, *Proc. 10th Intern. Conf. Physics of Semiconductors*, Cambridge, Mass, (US, AEC, 1970), p. 705.

88. R.Bray, IBM J. Res. Develop. *13* (1969) 487.

89. C. Hervouet, J. Lebailly, P. L. Hugon and R. Veulex, Solid State Commun. *3* (1965) 413.

90. R. W. Smith, Phys. Rev. Letters *9* (1962) 87.

91. P. O. Sliva and R. Bray, Phys. Rev. Letters *14* (1965) 372.

92. M. Kikuchi, Jpn.J. Apple.Phys. *2* (1963) 807; *2* (1963) 812; *3* (1964) 448.

93. J. H. McFee, J. Apple. Phys. *34* (1963) 1548.

94. G. H. Schwuttke, J. Electrochem. Soc. *106* (1959) 315.

95. J. W. Edwards, *Semiconductor Products*, (1963, May) p. 30.

96. C. Hamaguchi, K. Yamabe, K. Ando and S. Adachi, *Proc. Intern. Conf. IFUAS 1977, Tokyo*, (Univ. Tokyo Press, Tokyo).

97. K.Tsubouchi, S. Kameoka and T. Arizumi, J. Phys. Soc. Jpn. *37* (1974) 1305.

98. K. Tsubouchi and N. Mikoshiba, Jpn. J. Appl. Phys. *14* (1975) 309.

99. U. Gerbart and A. Many, Phys. Rev B *7* (1973) 2713.

100. Y. Itoh, S. Adachi and C. Hamaguchi, Phys. Stat. Sol. b *93* (1979) 381.

101. A. Feldman and D. Horowicz, J. Appl. Phys. *39* (1968) 5597.

102. C. D. Thurmond, J. Electrochem. Soc. *122* (1975) 1133.

103. D. E. Aspnes and A. A. Studna, Phys. Rev. B *7* (1973) 4605.

104. P. Lawaetz, Phys. Rev. B *4* (1971) 3460.

105. M. D. Sturge, Phys. Rev. *127* (1962) 768.

106. S. Wang and M. Matsuura, Phys. Rev. B *10* (1974) 3330.

107. M.Chandrasekal and F. H. Pollak, Phys. Rev. B *15* (1977) 2127.

108. Y. Itoh and C. Hamaguchi, Jpn. J. Appl. Phys. *20* (1981) Suppl. 20-3, p. 259.

109. Y. Itoh, M. Fujii, S. Adachi and C. Hamaguchi, *Proc. Phonon Scattering in Condensed Matter*, ed. by Humphery J. Maris, (Plenum, 1980) p. 433.

110. C. Hamaguchi, S. Adachi and Y. Itoh, Solid State Electronics *21* (1978) 1585.

111. See, for example, *II-VI Semiconducting Compounds*, ed. by D. G. Thomas (Benjamin, New York, 1967).

112. G. C. Trigunayat and G. K. Chadha, Phys. Stat. Sol. a *4* (1971) 9.

113. J. L. Birman, Phys. Rev. *115* (1959) 1493.

114. L. S. Ramsdell, Am, Mineralogist *32* (1947) 64.

115. O. Brafman and I. T. Steinberger, Phys. Rev. *143* (1966) 501.

116. G. L. Bir, G. E. Pikus, L. G. Suslina, D. L. Fedorov and E. B. Shadrin, Fiz. Tverdogo Tela *13* (1971) 3551.

117. G. V. Anan'eva, K. K. Dubenskii, A. I. Ryskin and G. I. Khil'ko, Fiz. Tverdogo Tela *10* (1968) 1800.

118. H. Jagodzinski, Acta. Cryst. *2* (1949) 298.

119. H. Hartmann, Kristall und Technik *1* (1966) 27.

120. H. Hartmann, Phys. Stat. Sol.*2* (1962) 585.

121. H. Blank, P. Delavignette, R. Gevers and S. Amelinckx, Phys. Stat. Sol. *7* (1964) 747.

122. L. T. Chadderton, A. F. Fitzgerald and A. D. Yoffe, Phil. Mag. *8* (1963) 167.

123. L. T. Chadderton, A. F. Fitzgerald and A. D. Yoffe, J. Appl. Phys. *35* (1964) 1582.

124. D. Berlincourt, H. Jaffe and L. R. shiozawa, Phys. Rev. *129* (1963) 1009.

125. C. F. Cline, H. L. Dunegan and G. H. Henderson, J. Apple. Phys. *38* (1967) 1944.

126. M. Cardona and G. Harbeke, Phys, Rev. *137* (1965) A1468.

127. G. L. Bir, G. E. Picus, L. G. Suslina and D. L. Fedorov, Fiz. Tverdogo. Tela *12* (1970) 3218.

128. M. Aven and J. S. Prener, *Physics and Chemistry of II-VI Compounds* (North-Holland, Amsterdam, 1967).

129. A. Gavini and M.Cardona, Phys. Rev. B *1* (1970) 672.

130. R. Zeyher, H. Bilz and M. Cardonan, Solid State Commun. *19* (1976) 57.

131. V. B. Kulakovskii, V. I. Grinev and M. P. Kulakov, Fiz. Tverdogo.Tela. *19* (1977) 600.

132. J. M. Bieniewski and S. J. Czyzak, J. Opt. Soc. Am. *53* (1963) 496.

133. M. Nawrocki, J. A. Gaj and J. Żuk, Phys. Stat. Sol. b *68* (1975) K181.

134. D. Dutton, Phys. Rev. *112* (1958) 785.

135. M. Cardona, K. L. Shaklee and F. H. Pollak, Phys. Rev. *154* (1967) 696.

136. E. Gustsche and J. Voigt, *II-VI Semiconducting Compounds*, ed. by D. G. Thomas, (Benjamin, New York, 1967) p.337.

137. R. W. Dixon, J. Appl. Phys. *38* (1967) 5149.

138. B. L. Evans, *Optical and Electrical Properties, Vol. 4*, ed. by P. A. Lee (D. Reidel Publishing Company, Dordrecht, Holland, 1976) p.61.

139. K. Kanzaki and I. Imai, J. Phys. Soc. Japan. *32* (1972) 1003.

140. I. Akopyan, B. Novikov, S. Permogorov, A. Selkin and V. Travnikov, Phys. Stat. Sol. b *70* (1975) 353.

141. M. Cardona and D. L. Greenaway, Phys. Rev. *133* (1964) A1685; Equation (5) in this reference contains a typographical error. The term of the series expansion should by devided by $(2r+1)^2$, see ref. 126.

142. R. C. Carlston, M. M. Schieber and W. F. Schnepple, Mat. Res. Bull. *11* (1976) 959.

143. S. Haussühl and H. Scholz, Fristall und Technik, *10* (1975) 1175.

144. A. Anedda and E. Fortin, Phys. Stat. Sol. b *84* (1977) K87.

145. F. Sakuma, H. Fukutani and G. Kuwabara, J. Phys. Soc. Jpn. *45* (1978) 1349.

146. M. Sieskind, J. B. Grun and S. Nikitine, J. Phys. Radium *22* (1961) 777.

147. E. I. Gordon, Appl. Opt. *5* (1969) 1629.

148. Y. Itoh, C. Hamaguchi and Y. Inuishi, J. de Physique (to be published).

149. R. Loudon, J. Phys. C, Solid State Phys. *11* (1978) 2623.

150. B. Segall, *Proc. 9th Intern. Conf. Physics of Semiconductors*, Moscow 1968 (p. 425).

151. C. E. Bleil and J. Voigt, *II-VI semiconducting Compounds*, ed. D. G. Thomas (Benjamin, New York, 1967) p. 360.

152. J. J. Hopfield, J. Phys. & Chem. Solids *22* (1961) 63.

153. K. Wasa, T. Akiyama, K. Tsubouchi, M. Yamanishi and N. Mikoshiba, J. Phys. Soc. Jpn. *49* (1980) 589.

154. Y. Itoh, K. Yamabe, S. Adachi and C. Hamaguchi, J. Phys. Soc. Jpn *46* (1979) 542.